



HAL
open science

An Experimental Investigation on Waves and Coherent Structures in a Three-Dimensional Open Cavity Flow

Jérémy Basley

► **To cite this version:**

Jérémy Basley. An Experimental Investigation on Waves and Coherent Structures in a Three-Dimensional Open Cavity Flow. Other [cond-mat.other]. Université Paris Sud - Paris XI; Monash University (Melbourne, Australie), 2012. English. NNT : 2012PA112245 . tel-00822898

HAL Id: tel-00822898

<https://theses.hal.science/tel-00822898>

Submitted on 15 May 2013

HAL is a multi-disciplinary open access archive for the deposit and dissemination of scientific research documents, whether they are published or not. The documents may come from teaching and research institutions in France or abroad, or from public or private research centers.

L'archive ouverte pluridisciplinaire **HAL**, est destinée au dépôt et à la diffusion de documents scientifiques de niveau recherche, publiés ou non, émanant des établissements d'enseignement et de recherche français ou étrangers, des laboratoires publics ou privés.



UNIVERSITE PARIS SUD

MONASH UNIVERSITY

ECOLE DOCTORALE MIPEGE

Modélisation et Instrumentation en Physique, Energies, Géosciences et Environnement

T H E S E

pour obtenir le titre de

Docteur ès Sciences Physiques

Discipline: DYNAMIQUE DES FLUIDES

par

Jérémy BASLEY

**An Experimental Investigation
on Waves and Coherent Structures
in a Three-Dimensional Open Cavity Flow**

Thèse en co-tutelle, dirigée par

François LUSSEYRAN Luc PASTUR Julio SORIA

soutenue le **19 Octobre 2012**

en présence de

Pierre BRANCHER	- IMFT, Université Toulouse 3	<i>Rapporteur</i>
François LUSSEYRAN	- LIMSI, CNRS	<i>Directeur</i>
Frédéric MOISY	- FAST, Université Paris-Sud	<i>Examineur</i>
Innocent MUTABAZI	- LOMC, Université du Havre	<i>Rapporteur</i>
Luc PASTUR	- LIMSI, Université Paris-Sud	<i>Directeur</i>
Jean-Christophe ROBINET	- DynFluid, Arts & Métiers	<i>Examineur</i>
Julio SORIA	- LTRAC, Monash University	<i>Directeur</i>
Michel STANISLAS	- LML, Ecole Centrale de Lille	<i>Président</i>

DECLARATION

I hereby declare that the work presented in this thesis is solely my own work and to the best of my knowledge is original and contains no material previously published or written by another author, except where due reference to the other author is provided in the text of this thesis. No part of this thesis has been submitted or accepted for the award of any other degree or diploma in any university or institution.

Under the Copyright Act 1968, this thesis must be used only under the normal conditions of scholarly fair dealing. In particular no results or conclusions should be extracted from it, nor should it be copied or closely paraphrased in whole or in part without the written consent of the author. Proper written acknowledgement should be made for any assistance obtained from this thesis.

I certify that I have made all reasonable efforts to secure copyright permissions for third-party content included in this thesis and have not knowingly added copyright content to my work without the owner's permission.

Jérémy Basley

April, 2013

Foreword

This work has been undertaken in the frame of a joint affiliation (“*cotutelle*”) involving both *Université Paris-Sud* in Orsay (France) and *Monash University* in Melbourne (Australia). The research was being conducted for the main part in Orsay at LIMSI (Computer Science Laboratory for Mechanical Engineering and Information Technologies), and in Melbourne for an overall period of one year at LTRAC (Laboratory for Turbulence Research in Aerospace and Combustion).

Through such a collaboration, different approaches have become available to address the subject. That is why the thesis revolves around two aspects of the cavity flow, based on two distinct experimental campaigns, each one carried out in one of the two laboratories. Performed in parallel, both axes of the analysis combine and complete each other. The research was realised under the co-supervision of Luc Pastur (LIMSI) and François Lusseyran (LIMSI) and Julio Soria (LTRAC).

LIMSI/CNRS (UPR 3251)
Laboratoire d’Informatique pour la Mécanique et les Sciences de l’Ingénieur
Campus de l’Université Paris-Sud XI
BP 133 – 91403 ORSAY Cedex
FRANCE

LTRAC Laboratory for Turbulence Research in Aerospace & Combustion
Department of Mechanical Engineering and Aerospace Engineering
Building 31 – Clayton Campus
Monash University
VIC 3800 CLAYTON
AUSTRALIA

An Experimental Investigation on Waves and Coherent Structures in a Three-Dimensional Open Cavity Flow

Abstract: A space-time study of a three-dimensional nonlinearly saturated open cavity flow is undertaken using time-resolved space-extended experimental data, acquired in both cross-stream and spanwise planes, in incompressible air and water flows. Through multiple modal decompositions in time and space, the waves and coherent structures composing the dynamics in the permanent regime are identified and characterised with respect to the instabilities arising in the flow.

Effects of nonlinearities are thoroughly investigated in the impinging shear layer, regarding the self-sustained oscillations and their interactions with the inner-flow. In particular, the analysis conducted throughout the parameter space enlightens a global connection between the selection of locked-on modes and the amplitude modulation at the impingement and the mode switching phenomenon. Furthermore, observations of low frequencies interacting drastically with the shear layer flapping motion underline the existence of intrinsic coherent three-dimensional dynamics inside the cavity in spite of the shear layer disturbances.

Linear stability analyses have demonstrated the onset of centrifugal instabilities along the main recirculation. In the present investigation, we focus on the dynamics after saturation occurred. It reveals numerous space-time coherent structures, whose properties are quantified and classified with respect to the underlying instabilities. We observe travelling or standing spanwise waves, as well as steady structures. Finally, some patterns exhibited by the saturated structures suggest that the nonlinear mechanisms governing the mutations of the flow after the linear regime could gain more insight in the frame of amplitude equations.

Key words: open cavity, space-time dynamics, three-dimensional flows, time-resolved PIV, spectral analysis, Fourier transform, Hilbert-Huang transform, impinging shear layer, locked-on modes, Kelvin-Helmholtz, amplitude modulation, mode switching, centrifugal instabilities, Taylor-Görtler, travelling waves, interferences

Concernant la version française

Concerning the french version

Ce mémoire de thèse porte sur une étude expérimentale des ondes et structures cohérentes dans un écoulement de cavité ouverte tridimensionnel. Le manuscrit est rédigé en anglais dans le cadre de la co-tutelle de thèse entre l'Université Paris-Sud à Orsay (laboratoire LIMSI/CNRS) et l'Université de Monash à Melbourne (laboratoire LTRAC).

Un court résumé et une synthèse détaillée sont fournis en annexes pour présenter le travail en Français. Cependant, l'auteur tient à souligner que la synthèse est une version très (trop) condensée de ce mémoire et s'attache uniquement à décrire les résultats principaux. Elle ne peut en rien se substituer à la version anglaise, pleinement développée.

A mon père,
à ma mère et ma soeur.

Acknowledgements

Foremost, I would like to acknowledge the work and patience of my supervisors, Luc Pastur and François Lusseyran and Julio Soria. Through their skills and knowledge and experience, their support has been constant for years. Learning with them has been, above all, a rewarding experience which will greatly help me in the future. Working alongside three supervisors in two different laboratories is indeed enriching but could have become challenging. This has been kept simple because they have always been understanding and patient, especially when I needed time for personal matters.

I would like to express my deepest thanks to Luc, who has played an important part during several decisive moments of my career path. Through advice or support, his assistance has been priceless in my professional choices since 2004, from Orsay to Toulouse to Melbourne. Ever since I came back to Orsay to work with him at LIMSI, Luc has never stopped pushing me forward and has been consistently invested in my work. There is more about our conversations than work. On countless occasions, we spent hours talking about philosophy, culture, arts or politics. With time, our care and respect for each other have turned into a mutual affection for which I am grateful.

I would like to thank François who made me a full member of the team and valued my opinion from the very beginning. On top of his eclectic experience in various scientific subjects, his views and knowledge in general matters are always insightful. More personally, I have quickly realised that we share, in many aspects, similar traits and sensitivity.

I sincerely thank Julio who has given me the opportunity of working both in his laboratory at Monash University (Australia) and with the people of Universidad Politecnica in Madrid. His enthusiasm has always been both inspiring and stimulating. I acknowledge Julio's ability to mix his impressive wisdom with a dynamic pragmatism. His advices have been especially useful to keep me on tracks in many occasions. I also would like to thank Julio for the time spent in handling the mountains of paperworks implied by the joint-award. Without his help, the administration would have rapidly overwhelmed me.

Someone else played a key role in the directions of this work: Nathalie Delprat. Until now, I have not sufficiently acknowledged her priceless involvement in this research and I would like to express my sincere and profound respect and affection towards her. Her unique perspective and original views have enlightened the work of the whole team at LIMSI and most primarily the studies presented in this thesis. The group meetings were always exciting but I think I can say that the stubbornness shared by Nathalie and I made our debates undoubtedly the warmest of all. They were also the loudest according to my office neighbours (my apologies) but I would not change any of such moments of which I especially enjoyed the enthusiasm and richness.

I feel really honoured to have gathered such a outstanding panel of academics for my defence. I have very much appreciated hearing different perspectives on the subject of my work. Fresh eyes will obviously help me to extend and deepen my analyses in a broader context. In particular, I want to acknowledge the thorough study of the thesis by the reviewers Pierre Brancher and Innocent Mutabazi. Their reviews have been of great interest to me.

I would like to mention how much I have enjoyed working alongside my fellow "LTRACians" in Melbourne, Dan, John, Varun, Omid, Sophie, Nicolas, Ivy, Daniel, Callum, Yoshi, Navid, Paul, Damon, etc. Everyone has always been kind and thoughtful. They definitely have made my life easier and happier in the times of anguish and grief I had to overcome during my stays in Australia. I will not forget Lydia Wong whose kindness and positive attitude were always refreshing. Working beside such an adorable office neighbour was a pleasure.

With all my heart, I would like to thank Daniel Mitchell for being such a precious friend. His empathy and support have been invaluable both morally and materially. His generosity equals his wisdom, and that is saying something.

*To my friends down under: I do not know where and when
but we will meet again.*

I want to acknowledge the pleasing atmosphere I found at LIMSI. Above all, I would like to thank the supporting staff who endeavours to bring the best working conditions for students and academics, indiscriminately. Notably, I can mention Pascal and Romain, the AMIC team, Vincent Bourdin and his team, Nadine and the secretaries.

I also would like to acknowledge the help of Yann Fraigneau, Thierry Faure, Ivan Delbende, Claudine Dang Vu Delcarte, Patrick Le Quéré in multiple occasions.

I thank Thomas Duriez for the chocolate bars when they were the most needed, for the helpful advices given with dark but extremely relaxing humour, and for the proof-reading during the dull weekends of summer 2012.

I thank all my fellow doctorate students for the friendly spirit which prevails in our group. With time, we sometimes have become more than colleagues – Francky, Julie, Lyes, Benoît or Charles...– and I am thankful for that. Some of them were more involved in my work. I want to thank in particular Christelle Douay for our passionate discussions concerning Taylor-Görtler vortices among other things. I am sure those exchanges have been mutually fruitful and inspiring. I thank Florimont Guéniat, whose enthusiasm and dynamism were refreshing. His original skills brought new perspectives to the group.

I deeply thank the staff of the Department of Applied Mathematics at the Universidad Politecnica in Madrid for being such kind and welcoming hosts during the two stays among them. I have very much appreciated working with Javier de Vicente and Fernando Meseguer and hope for many more years of collaboration. Their generosity and friendship have supported me both in my research and personally.

I have not yet mentioned the people from outside the professional circle but I would like to acknowledge their patience and comfort for the past few years. Doctorate studies surely constitute a long and demanding endeavour which one has to take up with no compromises. This has a great influence on the day to day life and requires much indulgence from closest ones. I want to thank my dear friends, Mathieu, Bérengère, William, Pauline, Marina, Francky, Sabrina, Gazou, Samayar, Arnaud,... who supported me in so many ways. For instance, they have been generous enough to feign interest when listening to hours of fluid mechanics talking.

Above all, I would like to dedicate this work to my family. If my motivation and energy has never dried up until now, it has undoubtedly to do with their inexhaustible trust and comfort. Since childhood, my parents have always had faith in me and this has given me great confidence, so essential to overcome difficulties and doubts arising in a scientific career.

Funding

This work was primarily funded by both DGA and CNRS through a doctor/engineer scholarship during three years. I also want to acknowledge the ANR contracts HiSpeedPIV and CORMORED for the experimental equipment and mission expenses.

I acknowledge the financial support of the Region Île-de-France. A SETCI scholarship (for cotutelle) paid the travel expenses between France and Australia.

I am grateful for the scholarship from the Australian Research Council, which funded the living expenses during four months at Melbourne.

Nomenclature

C_*	Streamwise phase velocity associated with the shear layer mode (*).
c_*	Spanwise phase velocity associated with the inner-flow spanwise mode (*).
D	Cavity depth
D/θ_0	Dimensionless cavity depth
f_a	Dominant frequency of the self-sustained oscillations of the shear layer
f_{ah}	Harmonic of frequency f_a such that $f_{ah} = h f_a$
f_b	Edge modulating frequency
f_{h+}, f_{h-}	Right, Left side-band frequency of f_{ah} associated with f_b
f_ℓ	Left side-band frequency of f_a associated with f_Ω
f_+, f_-	Right, Left side-band frequency of f_a associated with f_b
f_Δ	Very low frequency in cross-stream experiments
f_Ω	Secondary modulating (low) frequency
$\mathcal{F}^z, \mathcal{F}^t$	Spanwise, Time Fourier transform
\mathcal{F}^{zt}	Time-spanwise Fourier transform (in practice, $\mathcal{F}^{zt} = \mathcal{F}^z \circ \mathcal{F}^t$)
$\mathcal{H}^z, \mathcal{H}^t$	Spanwise, Time Hilbert transform
$\mathcal{H}\mathcal{H}^z$	Spanwise Hilbert-Huang spectrum (from Hilbert-Huang transform)
HH^z	Spanwise wavenumber distribution ($\mathcal{H}\mathcal{H}^z$ integrated so as to get a (z, β) map)
hh^z	Spanwise Hilbert-Huang marginal spectrum
k_*	Streamwise wavenumber associated with the shear layer mode (*)
L	Cavity length
L/θ_0	Dimensionless cavity length
Re_L, Re_D	Reynolds number based on cavity length (resp. depth) and external velocity U_0
S	Cavity span
St	Strouhal number (dimensionless frequency)
T	Total acquisition time of one recording
\mathbf{U}	Three-dimension-three-component (3D-3C) velocity field
\mathbf{U}_{xy}	Velocity field in xy -plane (2D-2C)
\mathbf{U}_{zx}	Velocity field in zx -plane (2D-2C)
\mathbf{U}_B	Steady base flow for linear stability analysis
\mathbf{U}_B^{2D}	Two-dimensional steady base flow
U_0	Farfield velocity at separation (leading edge of the cavity)
U_1, U_2	Upper, Lower velocity in shear layers
U_m	Mean velocity in shear layers

u, v, w	Streamwise, Crosswise, Spanwise velocity components
u', v', w'	Streamwise, Crosswise, Spanwise velocity fluctuations
$u_\varphi, v_\varphi, w_\varphi$	Streamwise, Crosswise, Spanwise slopes in space-time diagrams
x	Streamwise coordinate relatively to separation (leading edge of the cavity)
y	Crosswise coordinate relatively to separation (leading edge of the cavity)
y_{piv}	Crosswise position of the laser-sheet in spanwise experiments (LTRAC)
z	Spanwise coordinate relatively to mid-span
z_{piv}	Spanwise position of the laser-sheet in cross-stream experiments (LIMSI)
β	Spanwise wavenumber normalised by cavity depth
γ	Corrective coefficient in aeroacoustic feedback equation
Δt	PIV inter-frame delay (between the two frames of an image pair)
δt	Time step in a time-resolved dataset
δ^{99}	Incoming boundary layer thickness (99%)
δ_0^{99}	Incoming boundary layer thickness (99%) at separation (leading edge)
δ^*	Incoming boundary layer displacement thickness
δ_0^*	Displacement thickness at separation (leading edge of the cavity)
δ_ω	Vorticity thickness of the shear layer
$\delta_{\omega 0}$	Vorticity thickness at separation (leading edge of the cavity)
ζ_*	Streamwise growth rate associated with the shear layer mode (*)
κ	Velocity ratio U_m/U_0 in aeroacoustic feedback equation
Λ_*	Streamwise wavelength associated with the shear layer mode (*)
λ_*	Spanwise wavelength associated with the centrifugal instability mode (*)
θ	Incoming boundary layer momentum thickness
θ_0	Incoming boundary layer momentum thickness at separation (leading edge)
ω_y	Crosswise vorticity (out of 2D-velocity fields in zx -planes)
ω'_y	Crosswise vorticity fluctuations (out of 2D-fluctuation fields in zx -planes)
ω_z	Spanwise vorticity (out of 2D-velocity fields in xy -planes)
ω'_z	Spanwise vorticity fluctuations (out of 2D-fluctuation fields in xy -planes)

Contents

1	Introduction	7
1.1	State of the art	7
1.1.1	On free shear layers: Kelvin-Helmholtz instability	7
1.1.2	Case of impinging flows: the pressure feedback loop	9
1.1.3	The cavity locked-on frequencies	9
1.1.4	Shear layer mode switching	12
1.1.5	Amplitude modulation at the impingement	13
1.1.6	3D-effects & centrifugal instabilities	13
1.2	Open issues and aims of the study	17
1.3	Outline	18
I	Tools and methodologies	19
2	On the experimental data	21
2.1	Experiments at LIMSI	21
2.1.1	Wind-tunnel facility	21
2.1.2	Laser Doppler Velocimetry	21
2.1.3	High frame rate acquisition	22
2.2	Experiments at LTRAC	25
2.2.1	Water-tunnel facility	25
2.2.2	Particle image acquisition	27
2.2.3	Data merging	28
2.3	PIV algorithms	28
2.3.1	MCCDPIV: cross-correlation algorithm	28
2.3.2	Optical flow processing	29
2.3.3	Discussion	30
3	Decomposing the saturated dynamics of a real flow	39
3.1	The Fourier transform	39
3.1.1	The Discrete Fourier Transform	39
3.1.2	On Power Spectral Densities	40
3.1.3	Transfer Functions	44
3.1.4	The Global Fourier Modes	45
3.1.5	Motivations for another approach	48
3.2	The Hilbert-Huang Transform	48
3.2.1	The Hilbert transform	48
3.2.2	Instantaneous/local properties of an analytic signal	49
3.2.3	The Empirical Mode Decomposition	50
3.2.4	The Hilbert-Huang Spectrum	58

II	Flow Analysis through Space and Time	61
4	Cross-stream dynamics	63
4.1	Overview and context	63
4.1.1	Preliminary remarks	63
4.1.2	Inflow characteristics	67
4.1.3	Statistical moments	71
4.1.4	Spectral signature	71
4.1.5	Local stability in the shear layer	74
4.1.6	Nonlinear dynamics of the self-sustained oscillations	78
4.2	Self-sustained oscillations and harmonic families	79
4.2.1	Space-time structures of self-sustained oscillations	79
4.2.2	Wave properties	81
4.2.3	Spatial structure of the shear layer modes	86
4.3	Amplitude modulation	91
4.3.1	Side-band peaks and low frequencies	91
4.3.2	Wave properties of the side-band peaks	93
4.3.3	Modulating and side-band frequencies in the parameter space	94
4.3.4	Space-time dynamics	96
4.3.5	Spatial structure of the amplitude modulated shear layer	99
4.3.6	Main remarks on the amplitude modulated regime	103
4.4	Mode switching and overmodulation	104
4.4.1	Time-frequency dynamics	104
4.4.2	Saturation of the second locked-on mode: two harmonic families	107
4.4.3	Wave properties of the two competing families	108
4.4.4	Spatial structures of the two harmonic families	109
4.4.5	Critical stability region for self-sustained oscillations	109
4.5	Inner flow and very low frequencies	112
4.5.1	Secondary feedback	113
4.5.2	Three-dimensional structures in the inner-flow	115
4.5.3	Another drastic amplitude modulation	115
4.5.4	Spatial structures associated with very low frequencies	116
5	Spanwise dynamics	121
5.1	Preliminary remarks	121
5.1.1	PIV datasets	121
5.1.2	Spanwise boundary conditions	123
5.2	Spanwise wavelengths analysis	125
5.2.1	Space Fourier transform	125
5.2.2	Space Hilbert-Huang transform	126
5.3	Space-Time structures in the inner flow	130
5.3.1	Dataset coherence	130
5.3.2	Space-Time diagrams	132
5.4	Space-time modal decomposition	136
5.4.1	Characteristic Strouhal numbers	136
5.4.2	Associated spatial modes	137
5.4.3	Identifying space-scales	138

5.4.4	Results	138
5.4.5	Synthesis	157
6	Discussion on centrifugal instabilities	159
6.1	Nonlinear regime	159
6.2	Linear regime	161
6.2.1	Direct numerical simulations in an open square cavity	161
6.2.2	Linear stability analysis	162
6.3	Concluding remarks	168
7	Conclusions	169
	Appendix A Résumé en Français	173
	Appendix B Synthèse détaillée en Français	175
B.1	Introduction	175
B.2	Sur les données expérimentales	176
B.3	Décomposer la dynamique saturée d'un écoulement réel	176
B.4	Les interactions non-linéaires dans la dynamique principale	178
B.5	La dynamique transverse de l'écoulement intra-cavitaire	184
B.6	Conclusions	187

Introduction

1.1 State of the art

1.1.1 On free shear layers: Kelvin-Helmholtz instability

One of the major issues encountered in fluid mechanics is the stability of shear flows, such as jets or shear layers. These features are actually the core of all processes involved in noise and drag production, in fluid/structure interactions and also in the transition to turbulence. In ideal fluids, shear flows can be modelled as singularities (or separations) of the flow (the momentum thickness tends to zero). More precisely, free shear flows exhibit an inflexion point in their velocity cross-profile, which makes them always unstable against Kelvin-Helmholtz modes.

In the incompressible inviscid approximation, linear stability analysis carried out around a stationary basic state of the form of a hyperbolic tangent velocity profile can predict the mode against which the basic state is the most unstable and the range of the destabilising modes (Betchov and Szewczyk, 1963; Michalke, 1964, 1965). Linear stability analysis is performed locally on the basic velocity profile in an initially parallel flow. Growth rates and frequencies of unstable modes are determined as functions of mean velocity $U_m = (U_1 + U_2)/2$ (where U_1 and U_2 are the two farfield velocities) and local vorticity thickness δ_ω . The most temporally unstable wavenumber, based on vorticity thickness, has been obtained by Michalke (1964) in the incompressible case using a dichotomy method:

$$k_{\text{kh}} = \frac{0.4446}{\delta_\omega/2} = 0.1415 \frac{2\pi}{\delta_\omega}. \quad (1.1)$$

The associated frequency is expressed using the mean velocity U_m

$$f_{\text{kh}} = \frac{0.4446}{\pi} \frac{U_m}{\delta_\omega}, \quad \text{that is } \text{St}_{\text{kh}} = f_{\text{kh}} \delta_\omega / U_m = 0.4446 / \pi. \quad (1.2)$$

Note that the purpose here is not a review of the numerous investigations and extensions related to that celebrated relation. Regarding free shear layer instability, the author refers to the works by Betchov and Szewczyk (1963); Michalke (1964, 1965); Williams and Hama (1980); Monkewitz and Huerre (1982); Huerre and Monkewitz (1985, 1990); Monkewitz et al. (1993); Amram (1995); Huerre and Rossi (1998).

Evolution from *convective* to *absolute* instability has been investigated by Huerre and Monkewitz (1985). Determining whether the shear layer is going to be convectively or absolutely unstable pertains to the chosen reference frame. In other words, disturbances will grow spatially when both streams move in the same direction or, if counterflow exists, as long as counterflow U_2 is such as $|U_2/U_1| < 0.136$ (Huerre and Monkewitz, 1985). In other cases, one observes temporal growth yielding an absolute instability.

What remains of the free shear layer inviscid linear stability theory in the case of a non-free shear layer? How does a forcing affect stability properties of the shear layer?

The first effect to be seen comes from flow conditions at separation. Monkewitz and Huerre (1982) investigated parallel shear flows with different velocity profiles, other than the “classic” hyperbolic tangent. They showed that in the case of laminar boundary layer separating from the wall, the Blasius profile of the incoming boundary layer directly impacts the shear layer thickness and thus, the shear layer critical frequency. Indeed, vorticity contained in the incoming boundary layer is passed on to the shear layer, through the relation at separation,

$$\delta_{\omega 0} \simeq 4\theta_0. \quad (1.3)$$

where θ_0 and $\delta_{\omega 0}$ are the momentum and vorticity thicknesses at separation ($x = 0$). If the farfield velocity is noted $U_1(x = 0) = U_0$ at separation and the lower velocity is considered as $U_2 = 0$. From Equations 1.3 & 1.2, the maximum growth rate of a free shear layer just after separation occurs for the frequency f_{kh0} which can be expressed as a Strouhal number based on incoming boundary layer momentum thickness θ_0 . It comes

$$St_{kh0} = \frac{f_{kh0}\theta_0}{U_0} \approx \frac{f_{kh0}\delta_{\omega 0}/4}{2U_m} \approx \frac{0.4446/\pi}{8} \approx 0.018. \quad (1.4)$$

Unsteady conditions can force the shear layer more drastically by injecting frequencies from the start. Miksad (1973) investigated experimentally the impact of disturbances upstream of the shear layer on the spectral structure of the flow in order to bring to light the transition to turbulence. Two frequencies were picked up at various values around the critical frequency f_{kh} and acoustically injected in the developing shear layer. He demonstrated that such a *coloured* disturbance is primarily enhanced to the detriment of any other frequency of the natural broad-band spectrum. Then, while the shear layer spreads and energy of the oscillations grows, non-linear interactions between existing frequencies induce new spectral components — linear combinations of the two initial frequencies. Eventually, initial forcing fades out and broad-banded dynamics is rebuilt. In brief, upstream conditions can only have a spatially-limited influence on the spectral signature of the shear layer due to the convective nature of the instability.

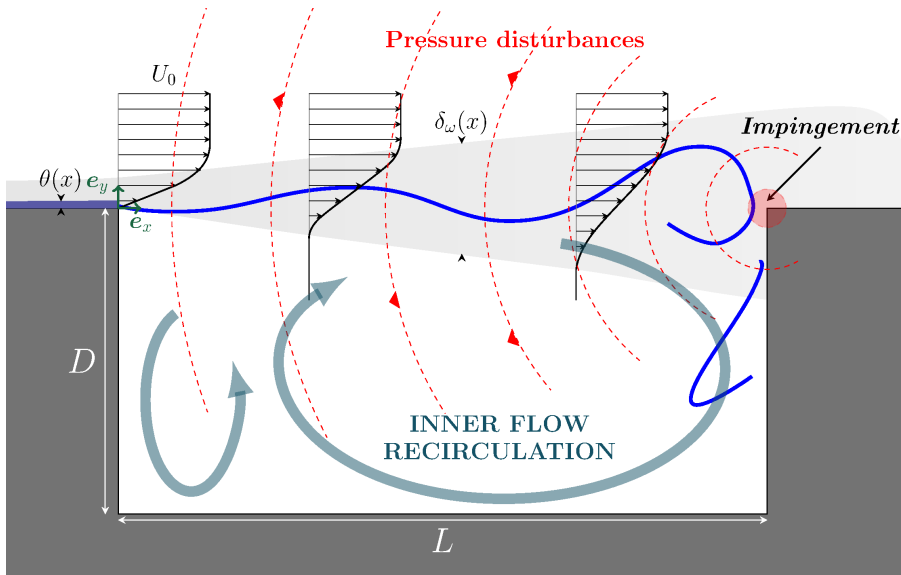


Figure 1.1: Schematic description of an open cavity flow

1.1.2 Case of impinging flows: the pressure feedback loop

Another source of forcing for a shear flow is the impingement onto a bluff body. This is the case for a shear layer above a cavity or towards a bevelled edge as well as a jet hitting a plate or a ring. By bringing supplementary boundary conditions to constrain dynamics, those geometries constitute an *acoustic resonator*, which enhances characteristic vibrations in the presence of a shear flow. Such an assertion was first correctly put forward by Lord Rayleigh himself (Powell, 1990, 1995; Gloerfelt, 2009), intuitively from his observations.

Only long after these good old days were conducted the first systematic and extensive studies focusing on the fascinating properties of impinging flows: Powell (1953, 1961); Rossiter (1964) and then, Rockwell (1977); Rockwell and Naudascher (1978, 1979), among others. They characterised and modelled the rise of *self-sustaining oscillations* in the impinging shear layer. The underlying mechanism can be understood as follow. When impinging, the flapping motion of the shear layer at the edge is responsible for pressure variations, which are fed back to the leading corner, enhancing Kelvin-Helmholtz vortex shedding. As a result, this *aeroacoustic feedback* selects and reinforces shear layer oscillations of frequencies f_n satisfying the *feedback equation*

$$\frac{n}{f_n} = \frac{L}{U_{kh}} + \frac{L}{c_s} \quad \text{with } n \in \mathbb{N}^{+*}, \quad (1.5)$$

where L is the cavity length, U_{kh} is the convection velocity of the Kelvin-Helmholtz disturbances along the shear layer and c_s is the speed of sound. The integer n represents the number of wavelengths contained between separation and impingement. The spectrum hence contains only a few modes: it is no more broad-banded as in a free shear layer.

In fact, Huerre and Monkewitz (1990) asserted that a flow exhibiting self-sustained oscillations is by definition absolutely unstable since it requires energy from a disturbance to travel both downstream and upstream. That was verified by Colonius et al. (1999); Rowley et al. (2002) with numerical simulations in the compressible regime. The feedback mechanism thus participates in sustaining the highly organised oscillations of the cavity-flow by making the system become globally unstable. The first consequence of that absolute instability is the shear-layer associated frequencies becoming common to the entire flow, such as pointed out in Basley et al. (2011).

1.1.3 The cavity locked-on frequencies

The early studies mentioned above dealt first with the compressible regime (Powell, 1953, 1961; Rossiter, 1964) and then for low Mach configurations (Rockwell, 1977; Rockwell and Naudascher, 1978, 1979; Rockwell and Knisely, 1979; Knisely and Rockwell, 1982). Their common aim was to predict *locked-on* frequencies of the self-sustained oscillations through lumped simple models based on Equation 1.5, *ie.* depending on cavity length L and external flow velocity U_0 .

In the compressible regime, the locked-on spectral distribution can usually be matched by the well known experimentally-based empirical *Rossiter's* formula (Rossiter, 1964; Delprat, 2006, 2010). It models the delayed acoustic feedback, which results in a non-harmonic series of peaks corresponding to the so-called *Rossiter* modes

$$\text{St}_n = \frac{f_n L}{U_0} = \frac{n - \gamma}{M + 1/\kappa} \quad \text{with } n \in \mathbb{N}^{+*} \quad (1.6)$$

where $\kappa = U_{kh}/U_0$ is the velocity of travelling vortices relatively to incoming external velocity. The corrective coefficient γ has been asserted to model the time delay between the vortex impact

and the emission of an acoustic wave. In practice, κ and γ are determined empirically and were originally set to

$$\kappa = 0.57 \text{ and } \gamma = 0.25 \quad (1.7)$$

for a rectangular cavity of length/depth ratio $L/D = 4$ (Rossiter, 1964; Delprat, 2006). More generally, these empirical values must be tuned accordingly to the configuration under study to match the results. Typically, one finds

$$0.3 \leq \kappa \leq 0.6 \text{ and } \gamma = 0.2. \quad (1.8)$$

In the incompressible case, when the Mach number $M \ll 1$, information from the impinging condition travels instantaneously ($c_s \rightarrow \infty$) through pressure (Rockwell, 1977; Rockwell and Naudascher, 1978, 1979). The frequencies of self-sustained oscillations hence satisfy the relation

$$\text{St}_n = \frac{f_n L}{U_0} = (n - \gamma) \kappa = (n - \gamma) \frac{U_{kh}}{U_0}. \quad (1.9)$$

The coefficient γ is however far less predictable. It cannot be set to a constant value as in the compressible regime. Many empirical models have been proposed over the years, such as in Rockwell (1977) (see Figure 1.2). Providing reasonable matching with experiments, none could actually predict all features of the self-sustained oscillations. Practically, the first order model assuming $\kappa \simeq 0.5$ and $\gamma \ll n$ is always quite helpful for it provides a simple and general scaling to approximate the locked-on frequencies (Equation 1.10).

$$\text{St}_n \approx \frac{n}{2} \quad f_n \approx n \frac{U_0}{2L} \quad (1.10)$$

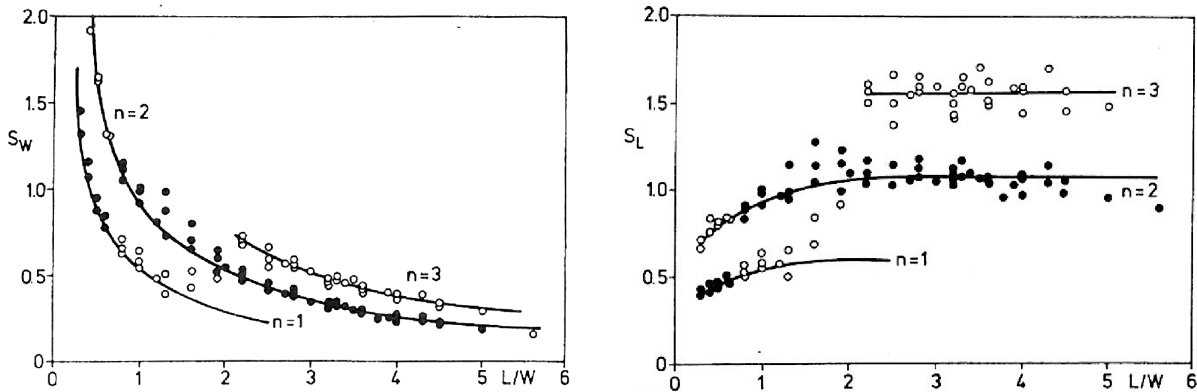


Figure 1.2: Extracted from Rockwell (1977) (*Figures 6 & 7*). Comparison of empirically-based theory with experimentally determined frequencies as functions of L/D (L/W in Rockwell (1977)); (left) L -based Strouhal numbers, (right) D -based Strouhal numbers (S_L and S_W in Rockwell (1977), respectively). Filled point represent frequencies with largest amplitudes.

The transition from one natural mode n to another can be either sub- or super-critical depending on the geometry of the impinging configuration (Rockwell and Naudascher, 1979; Kuo and Jeng, 2003). Contrary to other types of impingement — jet ring, bevelled edge, etc. (Knisely and Rockwell, 1982; Ziada and Rockwell, 1982; Howe, 1997) — hysteresis has never been observed in cavity flows.

As pointed out already by Rockwell and Naudascher (1979), changes in shape of the averaged-velocity profile and gradient along the shear layer make difficult the estimation of the actual critical frequency. It is anyway questionable to apply the free shear layer theory – based either on upstream conditions at separation only or on locally convective instability – to a globally unstable system. More particularly, one can find in Rowley et al. (2002) numerical results for which is given the evolution of the vorticity thickness δ_ω along the impinging shear layer. For various Mach numbers and cavity geometries in the compressible regime, it is shown that shear layer spreads faster for long cavities than for shorter ones. This is likely due to self-sustained oscillations of larger amplitude when cavity length L is increased. Similar results have been obtained for experimental data, in the incompressible case, for various cavity lengths, see Section 4.1.5. In the 90's, much has been accomplished in order to take into account the absolute instability of the flow. Beginning with pioneer work by Monkewitz et al. (1993) concerning weakly non-parallel shear flows, it has become possible to consider the stability properties of a spatially extended stationary basic state, with respect to which perturbations may either be amplified or not. Since then, spatially extended linear stability analysis has been applied to many configurations, including cavity flows (Mamun and Tuckerman, 2009; Colonius et al., 2001; Theofilis, 2003; Theofilis and Colonius, 2003; Ehrenstein and Gallaire, 2005; Sipp and Lebedev, 2007; Ehrenstein and Gallaire, 2008; Dergham et al., 2008; Brès and Colonius, 2008; Barbagallo et al., 2009). Those numerical studies have confirmed the global nature of cavity flow stability and the selection of a few well-defined spectral components. However, the mechanisms leading to self-sustained oscillations in the nonlinearly saturated state are by definition out of the scope of linear stability analysis. Physically, apparition of self-sustained oscillations can be explained by the coupling of two effects:

- i)* the intrinsic (Kelvin-Helmholtz) instability, depending on shear layer characteristics,
- ii)* the pressure feedback-loop caused by impingement.

In practice, the regime of the self-sustained oscillations in an impinging flow is mainly determined by both length Λ and thickness δ of the shear layer. That is why versions of the ratio Λ/δ have been used as suitable control parameters since pioneer work on *edge tones* by Powell (1953, 1961). For impinging jets, Λ corresponds to impingement distance and δ to orifice diameter; for bevelled edges, the ratio becomes impingement distance over boundary layer thickness, and so on. In the case of a cavity flow, regimes of self-sustained oscillations are ruled by the ratio cavity length over momentum thickness at separation L/θ_0 , hereafter called *dimensionless cavity length*.

The influence the boundary layer thickness at separation is mostly lost when dealing with shear layers initiated by priorly established turbulent incoming flows. For instance, Rockwell et al. (2003); Oshkai et al. (2005) recently investigated turbulent flows passing over shallow cavities. They performed parametric studies over a wide range of axisymmetric cavity configurations with the aim of describing emergence of self-sustained oscillations (called *flow tones*) from a broad-band upstream flow. The scaling obtained from their results showed no connection with the incoming flow, depending only on pressure feedback loop parameters. Other experiments (Chatellier et al., 2004; Ashcroft and Zhang, 2005; Haigermoser et al., 2008) and numerical simulations (Larchevêque et al., 2004; Gloerfelt, 2006, 2008; Lee et al., 2010) have also studied the impact of incoming turbulent structures on the impinging shear layer. Self-sustained oscillations are generally weakened by the adjunction of incoming perturbation but overall the dynamics are unchanged without respect to incoming boundary layer thickness.

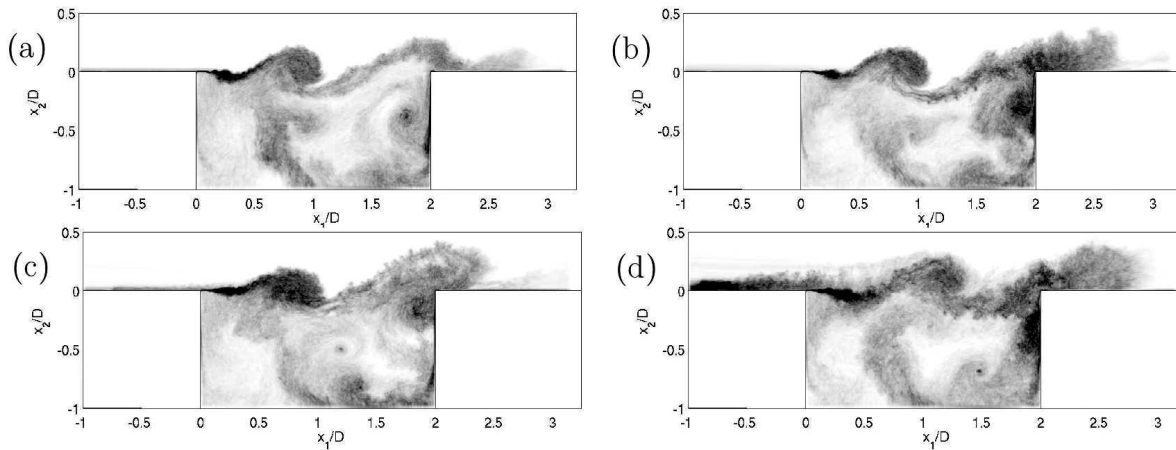


Figure 1.3: Figure extracted from Gloerfelt (2006). Large-eddy simulations are performed for a $L/D = 2$ cavity at a Mach number of 0.4. Snapshots of instantaneous vorticity modulus averaged over spanwise direction, depicting little or no influence of incoming boundary layer thickness at high Reynolds number. With laminar inflow, (a) $\delta_{ini} = 3.5$ mm, (b) $\delta_{ini} = 6.1$ mm; with turbulent inflow, (c) $\delta_{ini} = 3.5$ mm, (d) $\delta_{ini} = 6.1$ mm.

1.1.4 Shear layer mode switching

Impinging shear layers past a cavity do not necessarily exhibit a single regime of self-sustained oscillations. In many cases, multiple frequencies statistically coexist in the spectrum. This signature corresponds either to amplitude modulations, as discussed in the next section, or to the selection of two distinct modes of self-sustained oscillations. In the latter case, the locked-on frequency is not permanent but jumps in time from one stage to the other. That transition between two locked-on modes of oscillation is not a periodic phenomenon. It occurs suddenly and erratically. That intermittency is named *mode switching* or *mode competition*. It has been observed in compressible cavity flow experiments (Garg and Cattafesta III, 2001; Kegerise et al., 2004) and numerical simulations (Gloerfelt et al., 2003a,b), as well as in the incompressible limit (Lusseyran et al., 2008; Pastur et al., 2008).

Such a phenomenon calls for a dynamical analysis to investigate transition sequences between the two modes at the smallest time-scales (first-return applications). Using symbolic dynamics based on local time-series of streamwise velocity (Laser Doppler anemometry measurements), Lusseyran et al. (2008) showed that successive transitions are unlikely. They rather observed sequences corresponding to several returns in the same vicinity of the first-return map. In other words, once a mode has been selected, the system tends to exclude the other.

When using the spectral approach, drastic changes of regime corresponding to time-scales as short as only a few oscillations are difficult to study. The inherent averaging of spectral analysis implies less precision and the dispersion due to flow complexity makes the distinction between the two modes less clear. Nonetheless, Pastur et al. (2008) manage to quantify the transition and the existence probability of the two modes in competition. Hilbert transform was performed on band-filtered local time-series to provide an amplitude-based criterion for the presence of mode of oscillation. This study revealed that periods of transition can last for a few oscillations during which both modes are present.

1.1.5 Amplitude modulation at the impingement

One of the most interesting features of open cavity flows is the amplitude modulation of the shear layer flapping motion. On top of the locked-on frequency, some regimes deal with the creation of secondary frequencies resulting from a nonlinear interaction between shear layer self-sustained oscillations and trailing edge. In order to explain such a process, Rockwell and Knisely (1980b) proposed a descriptive model based on four classes of vortex-edge interactions (clipping, partial clipping, partial escape, escape). Using phase visualisations (hydrogene bubbles) and time-series issued of pressure measurements, they asserted scenarios matching with emergence of secondary peaks $0.4f_a$ and $0.6f_a$, beyond a threshold at $L/\theta_0 = 90$. More phenomenology concerning vortex-edge interaction can be found in Ziada and Rockwell (1982); Tang and Rockwell (1983), based on dye-streakline observations and pressure measurements.

An alternative point of view to such a mechanical description relies upon a spectral approach, that is an amplitude modulation of the self-sustained oscillations. Indeed, nonlinear interactions between two modes can be seen as amplitude modulation of one by the other, corresponding to linear combination of frequencies in spectral space. Hence the secondary peaks are *side-band* peaks produced from a *carrier* frequency f_a corresponding to self-sustained oscillations and a *modulating* frequency f_b , which yields the effect of the impingement. Amplitude-modulated regimes are commonly encountered in literature regarding impinging flows. Coming back to Rockwell and Knisely (1980b), the regime presenting multiple frequencies consists in fact in an amplitude modulation of the dominant mode f_a , called β in Rockwell and Knisely (1980b), by $0.4f_a$, resulting in the emergence of the side-band frequency $0.6f_a$. More side-band peaks at $0.2f_a$ $0.8f_a$ were encountered in a similar configuration in Knisely and Rockwell (1982).

As for initially turbulent cavity flows, (Larchevêque et al., 2003; Grace et al., 2004; Oshkai et al., 2005), or the compressible regime (Garg and Cattafesta III, 2001; Colonius et al., 1999; Rowley et al., 2002; Gloerfelt, 2008), amplitude modulations often come up as well, inducing secondary peaks. In general, modulating frequencies correspond to L -based Strouhal numbers between 0.25 and 0.4. Delprat (2006) introduced an original point of view by modelling compressible cavity flows in regards to low (modulating) frequencies observed in various experiments. In Delprat (2010), a relationship was asserted connecting acoustic ‘‘Rossiter’’ modes to low frequencies through a nonlinear mechanism at the impingement, without respect to the pressure feedback-loop.

All references point out a two-dimensional phenomenon, this amplitude modulation relying on the flapping motion of the shear layer at the impingement. However, the underlying mechanism responsible for this versatile flapping motion as well as for the selection of low frequencies still remains unclear.

1.1.6 3D-effects & centrifugal instabilities

Modulations at far smaller frequencies than f_b have also been observed in open cavity flows. Contrary to nonlinear interactions occurring at the impingement, these modulating frequencies are generally imputed to 3D-effects, or in other words, to *spanwise* dynamics. For instance, though Rockwell and Naudascher (1979) were mainly dealing with 2D-dynamics implied by the self-sustained oscillations of the shear layer, the three-dimensional organisation of the flow was briefly mentioned (Figure 1.4). Using the very same experimental data, Rockwell and Knisely

(1980a) focused on that streamwise vorticity introduced in the shear layer, disturbing the Kelvin-Helmholtz vortices. As well, the experimental observations in Koseff and Street (1984a,b,c) are frequently mentioned regarding three-dimensional dynamics in cavity flows. Low span/depth ratio cavities ($S/D \leq 3$) were used in order to focus on endwall effects. Neary and Stephanoff (1987) published experimental results in which a regime was showing a side-band peak, located at $f_2 \simeq 0.9f_1$, with f_1 the dominant peak. They related appearance of that side-band peak to a spanwise modulation of cavity main recirculation by a low frequency $f_1 - f_2$.

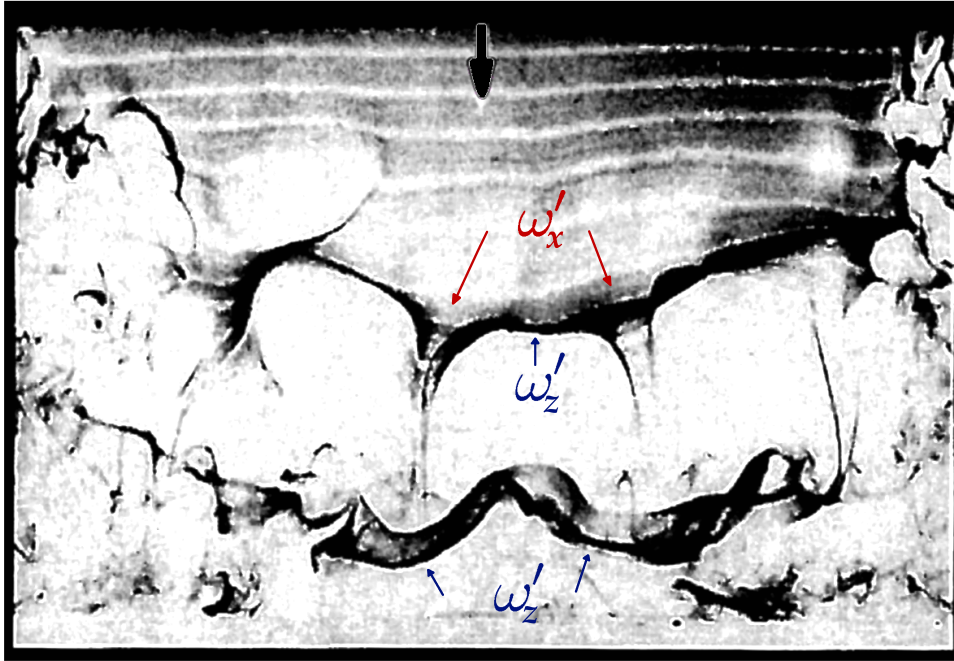


Figure 1.4: Extracted from Rockwell and Naudascher (1979) (*Figure 7*). Topview of oscillating cavity flow ($Re_{\theta_0} = 106$, $L/\theta_0 = 142$), illustrating three-dimensionality. Interaction between primary vorticity ω'_z and streamwise vorticity ω'_x produces severe distortion of primary vortices. Phase visualisation is obtained through hydrogen bubbles generated by a spanwise wire.

More detailed descriptions of the three-dimensional dynamics in cavity flows came out recently with other experimental works using laser techniques. Mainly based on streaklines observations, they brought to light a well-defined spanwise organisation for the inner-flow. Investigating an incoming turbulent flow past a square cavity with dye observations, Djenidi et al. (1999) pointed out versatile three-dimensional coherent structures arising inside the cavity.

In Podvin et al. (2006), numerical data processed by Proper Orthogonal Decomposition revealed interesting three-dimensional modulation of the dominant modes in the shear layer. In Larchevêque et al. (2007), numerical simulations modelling an asymmetric incoming flow exhibited inner-flow three-dimensional structures, which in turn modulated the shear layer oscillations. In the laminar regime, Faure et al. (2007, 2009) relied on smoke visualisations for various geometries and Reynolds numbers to observe vortical structures winding onto the main recirculation and periodically distributed along the span. They reported coherent pairs of rolls either steady or drifting towards the end-walls, depending on the cavity geometry.

For low dimensionless cavity lengths L/θ_0 , the shear layer above open cavities experiences little or no self-sustained oscillations. The outflow is roughly steady, so the dynamics

basically reduces to the inner-flow. It can be inferred that lid-driven cavities, for which the boundary conditions are more easily characterised and controlled, present analogous properties. In Chiang et al. (1998), direct numerical simulations of a square lid-driven cavity flow were presented. One could observe 3D-vortical structures arising at mid-span and travelling towards the endwall. Note that the simulations were forcing the symmetry since only half a domain was computed. Pioneer work by Albensoeder et al. (2001) (see Figures 1.5.a & 1.6) and then Guermond et al. (2002); Migeon (2002); Migeon et al. (2003); Albensoeder and Kuhlmann (2005, 2006) brought more insight concerning the origin of the so-called *Taylor-Görtler-like* vortices. Developing between the main recirculation and the cavity walls in the induced boundary layers along the walls, such vortical structures indeed suggested centrifugal instabilities (Figure 1.5.b). Meanwhile, Vogel et al. (2003) performed dye-visualisations in a periodically-driven cavity. By characterising the space-time dynamics of the flow within the forcing period, they demonstrated the rise of spanwise structures organising in both standing and travelling waves. This work was supported by direct numerical simulations in Blackburn and Lopez (2003). One may consider such a configuration yielding unsteady boundary conditions as a connection with shear layer driven cavities.

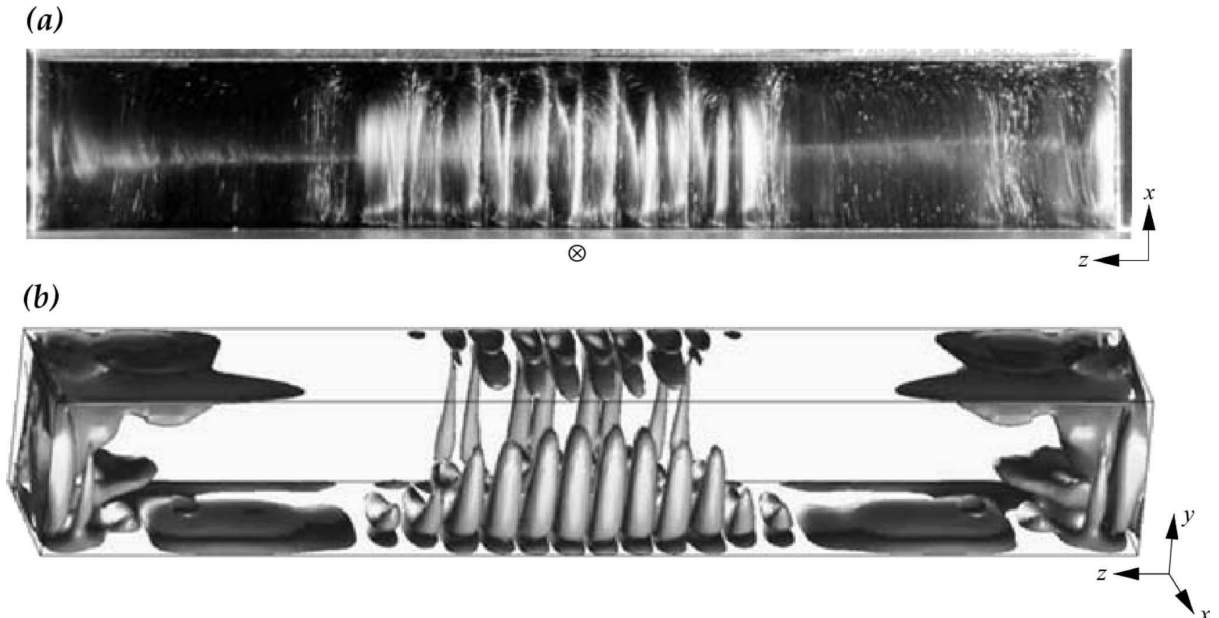


Figure 1.5: Extracted from Albensoeder et al. (2001): (a) Steady three-dimensional cellular flow for $L/D = 1$ at $Re_D = 850$. The lid is located at the bottom of the figure and move into the plane. The flow was visualised by aluminium flitters and illuminated in the plane $y/D = 0.5$. Extracted from Albensoeder and Kuhlmann (2006): (b) Numerical simulation of the flow for the same parameters. Shown are vorticity iso-surfaces $|\omega_x| = 210$.

Remark that experimental studies have been almost exclusively based on streaklines observations. In open cavity flows in particular, obtaining quantitative (velocity) measurements regarding the spanwise features is a challenging task. Three-dimensional dynamics involves steady or slow-moving coherent structures, which thus imply characteristic time-scales one or two orders of magnitude greater than those corresponding to shear layer oscillations. Furthermore, in the saturated regime, spanwise dynamics are usually overwhelmed by the primary dynamics of the flow, namely the oscillations of the shear layer and the main recirculation. As a result, implementation of Particle Image Velocimetry (PIV) in a spanwise plane is difficult

due to large out-of plane velocity components and to low signal over noise ratio.

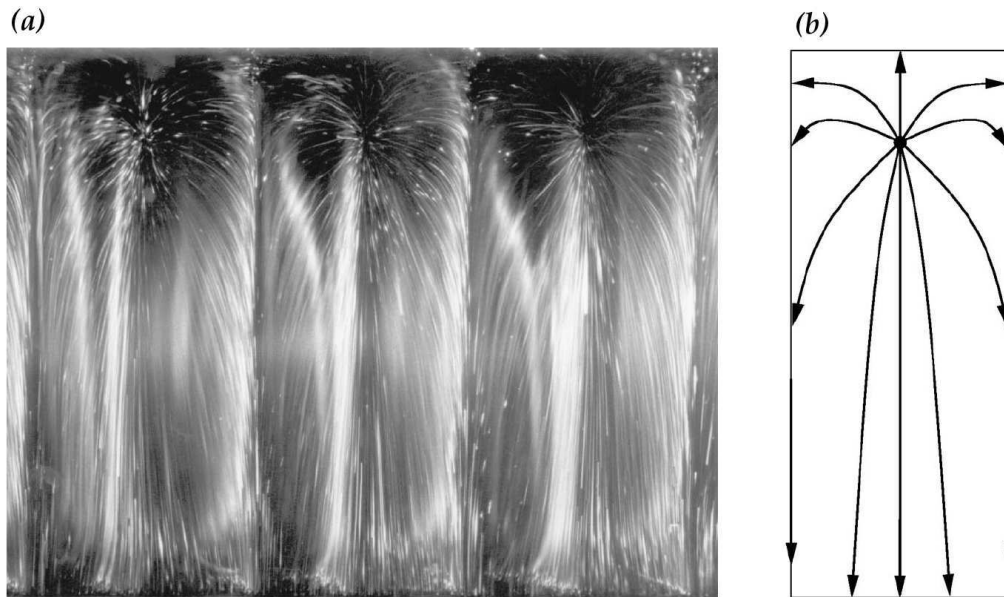


Figure 1.6: Extracted from Albensoeder et al. (2001) (*Figure 15*): (a) Close-up of Figure 1.5.a (steady three-dimensional flow pattern for $L/D = 1$ at $Re_D = 850$); (b) a sketch of the streakline topology for a single wavelength.

Another point of view consists in investigating the dynamical system just after bifurcation and before onset of the saturation. In other words, this comes down to studying the stability of the steady base flow against small perturbations. In practice, this is generally achieved through numerical simulations using three-dimensional periodic perturbations upon a two-dimensional base-flow. Such a methodology is sometimes referred to as *(Bi-)global* stability analysis. Spanwise instabilities in the linear regime have been intensively studied over the past ten years, especially in lid-driven cavities (Ramanan and Homay, 1994; Poliashenko and Aidun, 1995; Albensoeder et al., 2001; Blackburn and Lopez, 2003; Theofilis et al., 2004; Chicheportiche et al., 2008; Boppana and Gajjar, 2010; Gonzalez et al., 2011).

In open flows, the more complex boundary conditions imply a much larger computation domain and continuity issues to overcome, see for instance Theofilis (2003); Theofilis and Colonius (2003); Alizard et al. (2010) and the review in Theofilis (2011). In particular, Brès and Colonius (2007, 2008) used direct numerical simulations and linear stability analysis to characterise centrifugal instabilities arising in the cavity inner flow in the compressible regime. They have shown that those centrifugal instabilities organise themselves as spanwise waves whose wavenumbers scale on cavity depth D almost regardless of Mach number and fairly match experimental results cited above. Frequencies associated with resulting spanwise structures also scale on D such as $0.011 \leq fD/U_0 \leq 0.026$. Among other parameters, Strouhal numbers actually depend on cavity aspect ratio L/D and dimensionless cavity length L/θ_0 . Recently, de Vicente (2010) and Meseguer-Garrido et al. (2011) have notably confirmed and extended such results to open cavities of various aspect ratios and for a large range of control parameters D/θ_0 and L/D .

1.2 Open issues and aims of the study

After this review, one realises the extensive literature concerned with impinging flows and especially flows past open cavities. In particular, the main features of the shear layer self-sustained oscillations, modelled using the two-dimensional approximation, have been overall understood and characterised for decades, which makes this system a good benchmark. However, the origin of some features still needs to be addressed.

To begin with, a precise comprehension of the evolution of locked-on modes in the shear layer remains out of reach since one usually relies on empirically-based models, whose parameters must be tuned accordingly to match reference datasets. The present study notably provides a law of evolution for locked-on frequencies as a function of the control parameter (dimensionless cavity length), based on parametric experimental data.

Other questions relate to the nonlinear interactions at the impingement. For instance, what mechanism underlies the selection of low frequencies involved in amplitude modulation of the self-sustained oscillations? New insight into the space-time dynamics of the flow at the impingement can be gained through space-extended time-resolved quantitative data, made available by high-speed Particle Image Velocimetry (PIV).

Moreover, intermittency or mode switching has been observed only recently and it would be worthwhile studying mode transitions more thoroughly. In particular, intermittency has been investigated without respect to the amplitude modulation process. Starting from space-time analysis, we adopt an original point of view involving *overmodulation* to highlight a connection between the two phenomena. A practical criterion is also proposed for distinguishing mode-switching dynamics relying on power spectrum alone.

Although the three-dimensional organisation of the flow in the incompressible regime has been mentioned long ago, to our knowledge only few investigations concern its influence on the shear layer flapping motion when the Reynolds number increases. Indeed, the inner-flow in open cavities is the source of very low frequencies believed to be responsible for great amplitude modulation of the self-sustained oscillations.

Furthermore, the literature review has emphasised the common ground shared with lid-driven cavities. Shear- and lid-driven cavities alike can exhibit centrifugal instabilities arising from an originally two-dimensional basic flow. In that context, one strikingly needs new insights regarding the organisation and temporal evolution of the three-dimensional dynamics in the permanent regime. Notably, this consists in identifying quantitatively time and space scales after saturation, by means of space-time analysis and multiple modal decompositions applied to experimental data.

1.3 Outline

The questions raised hereinbefore are addressed in this thesis organised in two parts.

The first part deals with the tools and methodologies employed to process and analyse the experimental data. In Chapter 2 are presented the two experimental campaigns. Spatially extended time-resolved datasets have been acquired, respectively, at LIMSI in a cross-stream (wall-normal) plane and at LTRAC in a spanwise plane (parallel to the bottom of the cavity). The facilities as well as experimental protocols and acquisition characteristics are first described in Sections 2.1 & 2.2. Follows a characterisation of the performance of the PIV algorithms utilised to process particle images (Section 2.3).

The analysis of the experimental results relies primarily on modal decomposition methods, based on Fourier and Hilbert-Huang transforms. The reader may find details on such methodologies helpful. To that aim, a description of those modal decompositions and their application to a spatially extended time-resolved dataset is provided in Chapter 3.

The second part of this study concerns the analysis of the results obtained in both experimental campaigns. Chapter 4 focuses on the impinging shear layer and the wall-normal dynamics of the flow. After an overview and a parametric study (Section 4.1), we emphasise the space-time dynamics of the nonlinear interactions both inside the shear layer itself (Sections 4.2-4.4) and in relation to the inner-flow (Section 4.5).

In Chapter 5, the three-dimensional dynamics in the permanent regime are investigated with respect to centrifugal instabilities. Sections 5.2-5.4 focus on identifying the space and time scales of the inner-flow in a spanwise plane. Then, in Chapter 6, the organisation of the inner-flow is discussed by referring to the insightful frame of linear stability analysis. To extend the scope of the study our results are also considered with amplitude equations.

Chapter 7 summarises the thesis and provides some perspectives.

Part I

Tools and Methodologies

On the experimental data

2.1 Experiments at LIMSI

2.1.1 Wind-tunnel facility

The present work is mainly based on two experimental investigations. The first campaign was carried out at LIMSI by using an open wind-tunnel described in Figure 2.1. The experimental facility is composed of a centrifugal fan providing stationary volume flow upstream of the wind-tunnel, a settling chamber and a honey-comb panel, placed at the inlet of the contraction, in order to laminarise the flow. In the measurement region, the boundary layer develops above a $A = 300$ mm-long plate with profiled leading edge. Wind-tunnel spans over $S = 300$ mm. Distance between top and bottom walls is $F = 75$ mm, so that the top boundary layer meets the bottom flow largely downstream of the cavity. Cavity depth is $D = 50$ mm and cavity length L varies from 50 to 100 mm. Complete optical access is made available using reflection-treated glass walls for the wind-tunnel as well as for the cavity setup. Available incoming velocities range from 0.7 m/s to 5.0 m/s. At such low Mach numbers ($M \simeq 10^{-2}$), the flow can be considered as incompressible. In addition, at the frequencies of the flow – typically 20 Hz – acoustic modes have wavelengths λ_{acoust} much larger than the cavity length L . The pressure-based feedback mechanism can be seen as instantaneous (Rockwell and Naudascher, 1979). Vein noise has been estimated based on Laser Doppler Velocimetry measurements. Background turbulence is less than 1%. The wind tunnel forces frequencies mainly distributed from 0 to 10 Hz, with a maximal power around 1 Hz three orders of magnitude smaller than the cavity flow spectrum for the same frequency range.

2.1.2 Laser Doppler Velocimetry

Local streamwise velocity u measurements, based on laser Doppler velocimetry (LDV), were performed in the shear layer, 5 mm upstream of the trailing corner, 5 mm above the cavity top plane, in the very same conditions as the PIV measurements. The light source is a continuous Argon-ion laser (power 1 W, wavelength 488 nm). The beam is split into two coherent beams by a beam splitter. They cross each other at the LDV point with an angle $\Theta_{LDV} = 9^\circ$, generating an interference pattern of interfringe $d = 3.11 \mu\text{m}$. The measuring volume is 1.3 mm in length and 0.1 mm in diameter. One of the two beams travels through a Bragg cell where it is frequency shifted to reduce fringe bias and get rid of direction ambiguity. The first diffracted beam is frequency modulated at $\Delta f_{\text{Bragg}} = 40$ MHz. Consequently, the interference fringes scroll at velocity $V = d\Delta f_{\text{Bragg}} \simeq 120$ m/s, such that V is opposite to the inflow velocity. A convergent lens - photomultiplier system is focused on the LDV control volume and detects the intensity variation of the light diffused by the seeding particles passing through the interference pattern. Photomultiplier signal is processed by a Doppler signal analyser, and the digitised data are stored on a PC computer. As the LDV point is located near the trailing corner, shear layer oscillations as well as low frequencies are of highest amplitude. LDV can provide long

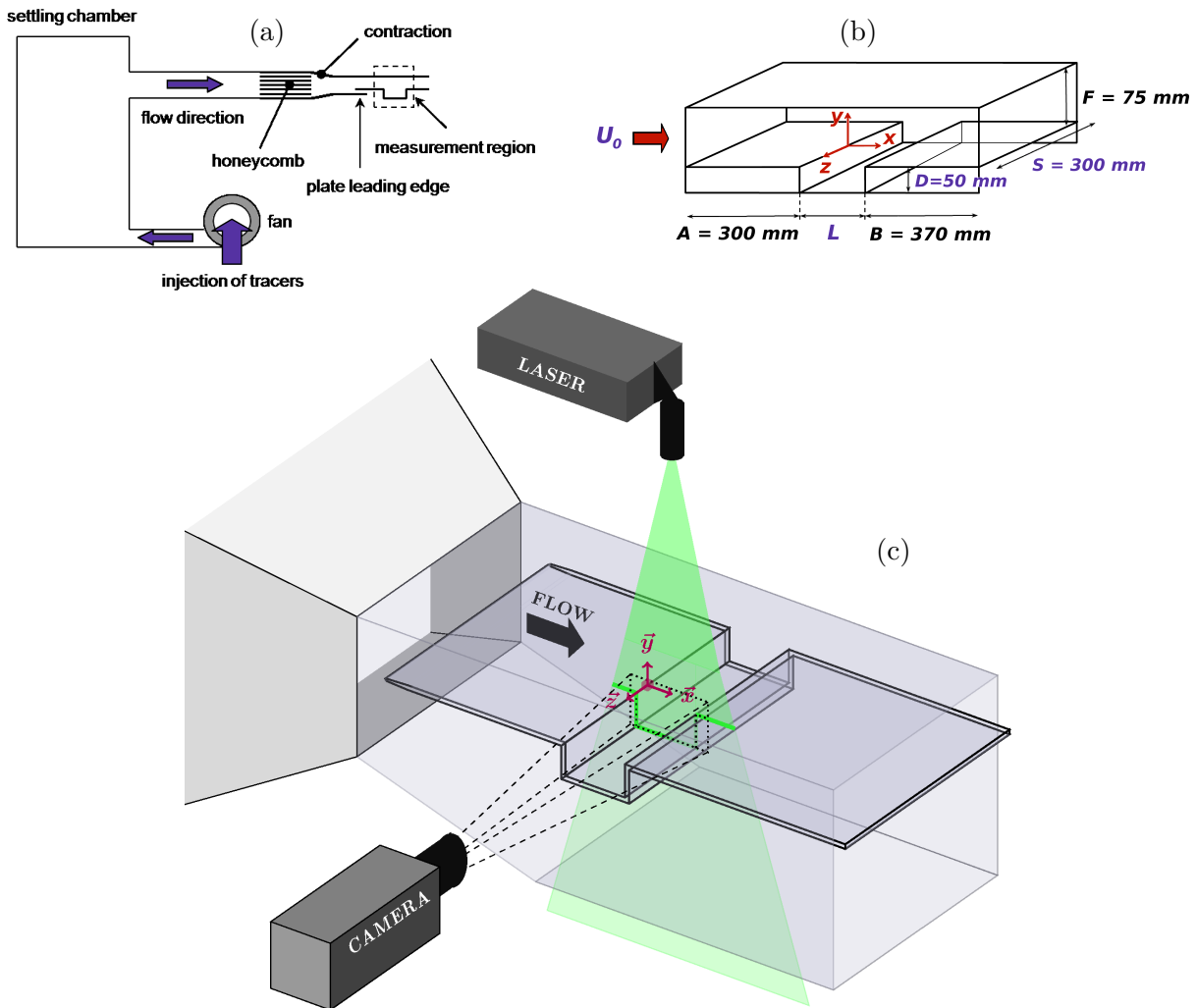


Figure 2.1: Wind-tunnel facility (a) and test section in close-up (b). PIV setup (c) for the high frame rate campaign at LIMSI.

records (typically 4 minutes, that is two orders of magnitude above the largest time scales of the flow). It is indeed useful for compensating TR-PIV limitations in length of time series. LDV count rates are of the order of 2 kHz. Time-series are then equally resampled at the mean particle-sampling frequency by linear interpolation before performing any analysis. For each working point $(L/D, U_0)$ of the parameter space, three to six different LDV measurements were performed.

2.1.3 High frame rate acquisition

Equipment: Through the ANR contract *HiSpeed PIV*, collaborating research teams from FAST, LIMSI, ENSTA, and LadHyX, located in Orsay and Palaiseau (France, Essonne), were entrusted with the means to purchase high repetition rate equipment as pooling resources to perform time-resolved Particle Image Velocimetry (TR-PIV).

A New Wave Pegasus laser was chosen to deliver the light source. The Pegasus is a dual-head, high repetition rate, diode-pumped Nd:YLF laser system specifically designed for high-speed PIV. Each head can be triggered independently and can operate from 1 to 10 000 pulses per

second allowing camera frame rates up to 20,000 frames per second. According to the technical sheet, 1 kHz is the optimal repetition rate. At 1 kHz pulse duration is less than 180 ns and each laser head supplies about 10 mJ per pulse. Beam diameter is 1.5 mm and divergence is less than 3 mrad. Laser wavelength is $\lambda_{pegasus} = 527$ nm.

In order to acquire frames at high rate, a CMOS camera Photron FASTCAM-APX RS was selected. Its full resolution – 1024×1024 pixel – is available for repetition rates up to 3 kHz. Images are encoded over 8 bits. Camera on-board memory is 2.6 GB, filled up in about 2.5 s at full resolution and repetition rate of 1 kHz. The Photron camera allows the user to define two time steps, one being equal to 2^n times the other (with $n = 0, 1, \dots, 5$). The Photron camera was associated with a 60 mm Micro-Nikkor lens, with an aperture set to $f_{\#} = 2.8$.

Seeding: For PIV experiments, seeding particles were liquid droplets of mineral oil DEHS – di(2-ethylhexyl)sebacate –, sprayed at the fan entrance. DEHS density is 0.9 and droplet diameters are of the order of $1 \mu\text{m}$, which provides a relaxation time around $3\mu\text{s}$, *ie.* far shorter than any time scale of the flow. Moreover, DEHS surface energy is particularly high, curbing the settling of micro-droplets. This is quite a useful property when dealing with an open wind-tunnel. The lab is then equipped with a ventilation system which removes the seeding particles before they settle down. Measurements only start after the seeding particle distribution is uniform inside the cavity.

On the contrary, visualisations require the seeding not to be non uniformly disseminated within the cavity, light contrast revealing coherent structures of the flow. With that aim, liquid droplets of glycerol (theatre smoke) were used to provide burst of dense seeding.

Acquisition parameters: Planar PIV measurements were conducted at high repetition rate in a xy -plane (cross-stream); providing thereby time-resolved two-dimensional-two-component (2D-2C) velocity fields such as

$$\mathbf{U}_{xy}(x, y, z_{piv}, t) = u(x, y, z_{piv}, t) \mathbf{e}_x + v(x, y, z_{piv}, t) \mathbf{e}_y. \quad (2.1)$$

The laser sheet was set up at the spanwise position $z_{piv} = 0.07S$, such as to avoid symmetry planes of the flow.

As in any experimental campaign, many compromises must be dealt with when adjusting image acquisition characteristics. Particle image quality is a primary prerequisite. It depends on the amount of energy provided by the light source and seeding diffraction properties and the optical setup. Power requirement is particularly demanding in wind-tunnels where particles must be small enough to show a short relaxation time in air. Particle size and brightness are enhanced by a greater magnification. However, image resolution is limited when acquiring time-resolved data. Indeed, a balance must be found between image size and available number of frames stored in camera on-board memory, from which depends the overall acquisition time. In that context, the light supply was greatly raised by synchronising both laser heads to their optimal repetition rate (1 kHz). Remark that firing simultaneously (a single laser burst) now imposes frames to be uniformly sampled. In other words, PIV *inter-frame delay* Δt will be driven only by camera frame rate.

To increase the dynamic range in PIV images, the laser sheet had to be carefully adjusted. Light intensity measurements were performed by using a Photometer. As expected, they revealed a Gaussian-shaped profile. By spreading the laser sheet over 40 cm in the region of investigation, the effective width for usable particle images was about 15 cm, *ie.* from $1.5L$ to

$2L$ depending on cavity shape-ratio. Light sheet thickness was reduced as much as possible: the laser sheet was thinner than 1 mm. Such a thickness is available because the flow is mainly two-dimensional. In fact, out-of-plane velocity component is known to be at least one order of magnitude smaller than in-plane velocity.

Another compromise must be reached between the smallest and largest time scales to be resolved in the experiments. The smallest time-scale first corresponds to PIV inter-frame delay Δt , constrained by particle displacement inside an image pair. Cavity flows are challenging in regards to the wide range of velocities they exhibit. Indeed, cavity inner-flow typically scales on velocities 20 times smaller than incoming velocity. PIV inter-frame delay Δt was adjusted so as to resolve the inside and shear flow displacements. This lets inner-flow displacements of the order of at least 1 pixel but implies free stream displacement from 10 to 25 pixels depending on the case under study. The outflow is however mainly two-dimensional: spanwise velocity component almost negligible relatively to streamwise component. Longer Δt could thus be undertaken, such as to guarantee enough precision for the inside flow velocity field. Computation of large displacements will be discussed in Section 2.3. In addition, the highest frequency in the flow imposes the minimal sampling frequency available without producing spectral aliasing. From LDV experiments, characteristic frequencies (including their harmonics) have been observed as up to about 100 Hz for the investigated cases. According to the Shannon-Nyquist criterion, it comes

$$f_s \geq 200 \text{ Hz} \quad (2.2)$$

where f_s is the sampling frequency of the TR-PIV datasets. This implies that δt , the time-step between two successive velocity fields, must be smaller than 5 ms.

On the other hand, cavity flows also exhibit low frequencies two orders of magnitude lower than highest frequencies. The lowest resolved frequency, which is also the frequency step, depends on the total length of the recording, T . When window-averaging is used for spectral analysis, getting down to 0.1 Hz requires a recording time of $T = 20$ s. That period increases with δt and N_f the number of samples (velocity fields).

$$T = N_f \delta t \quad (2.3)$$

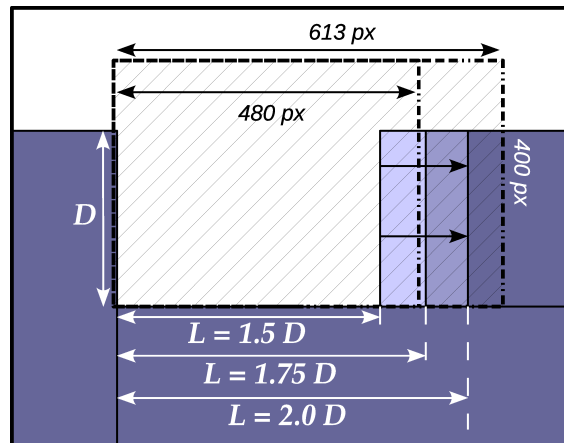


Figure 2.2: Various PIV image configurations for LIMSI High-Speed campaign.

Since δt cannot be increased without damaging high frequency identification, T is limited by on-board memory. Image resolution hence has to be reduced in order to get longer records. Depending on whether the shape ratio L/D is 2 or 1.5, image size has been lowered to 640×400 or 512×400 pixel (see Figure 2.2). In all cases, images cover at least an area $0 \leq x/L \leq 1.1$ by $-1 \leq y/D \leq 0.4$, with a magnification of $\mu = 0.176$ mm/pixel. As a result, records consist of 8192 to 10484 successive equally sampled images, depending on the experimental configuration. Reducing image size has a positive side-effect for image optical quality. By using only the central part of the CMOS array – a surface smaller than 11×7 mm² – parallax distortions are almost completely avoided.

In brief, camera repetition rate was set to $f_{piv} = 500$ Hz, that is $\Delta t = 2$ ms. $\delta t = 2\Delta t = 4$ ms was chosen so as to maximise recording time while satisfying the Shannon criterion – $f_{Nyquist} = f_s/2 = 125$ Hz. Recording times T range from 16 s to 21 s, which still do not provide high resolution in regard to very low frequencies. In order to improve statistics on events occurring at large time scales, at least fifteen PIV records were performed for every configuration under study.

Displacement fields are computed using an optical flow algorithm (OPFLOW) which relies on an orthogonal dynamical programming. This kind of algorithm has been originally developed to help in image processing for information technology applications. It has been adapted and optimised to be used in PIV (Quénot, 1992; Quénot et al., 1998). Such an algorithm is particularly suitable for the present study because it can deal with low resolution images while providing with high quality velocity fields nonetheless. By using OPFLOW, it has become possible to work with large reproduction ratio (object size over image size) – typically 10 –, necessary to achieve full field acquisition at high frame rate as well as maintained for long durations. More detail about OPFLOW algorithm will be given in Section 2.3.2.

2.2 Experiments at LTRAC

With the aim of studying spanwise dynamics of the cavity inner-flow, PIV experiments were carried out in the Laboratory for Turbulence Research for Aerospace & Combustion (LTRAC), in Melbourne. Spanwise dynamics investigation do not call for high frame rate experiments. In place of a large range of time-frequencies, spanwise dynamics implies a large range of space-scale. Indeed, the inner-flow investigated in a spanwise zx -plane is almost free of shear layer activity and involves large time scales only. The challenge hence rather concerns spatial resolution. Since centrifugal instabilities are involved, images of high reproduction ratio are required to give access to fine structures. On the other hand, spectral analysis and side-wall effects would require the entire span to be considered. Furthermore, out-of-plane velocity component, though limited by the choice of a plane at $y/D = -0.1$, remains strong. Such system rather requires high quality images to optimise PIV robustness than high repetition experiments.

2.2.1 Water-tunnel facility

Using a water-tunnel is valuable to optimise particle images. Larger particles with better diffraction properties ease PIV computation. The experiments were conducted in a 500 mm cross-section recirculating water tunnel. The tunnel has a 5 m long test section and is capable of free-stream speeds up to 1 m/s. Velocity turbulence intensity in the core region of the test

section is less than 0.5 %, as seen in Parker et al. (2007). Furthermore, water high kinematic viscosity induce lower frequencies in the flow if Reynolds number is kept constant. This is particularly useful for acquiring time-resolved datasets, in spite of low frame-rate cameras.

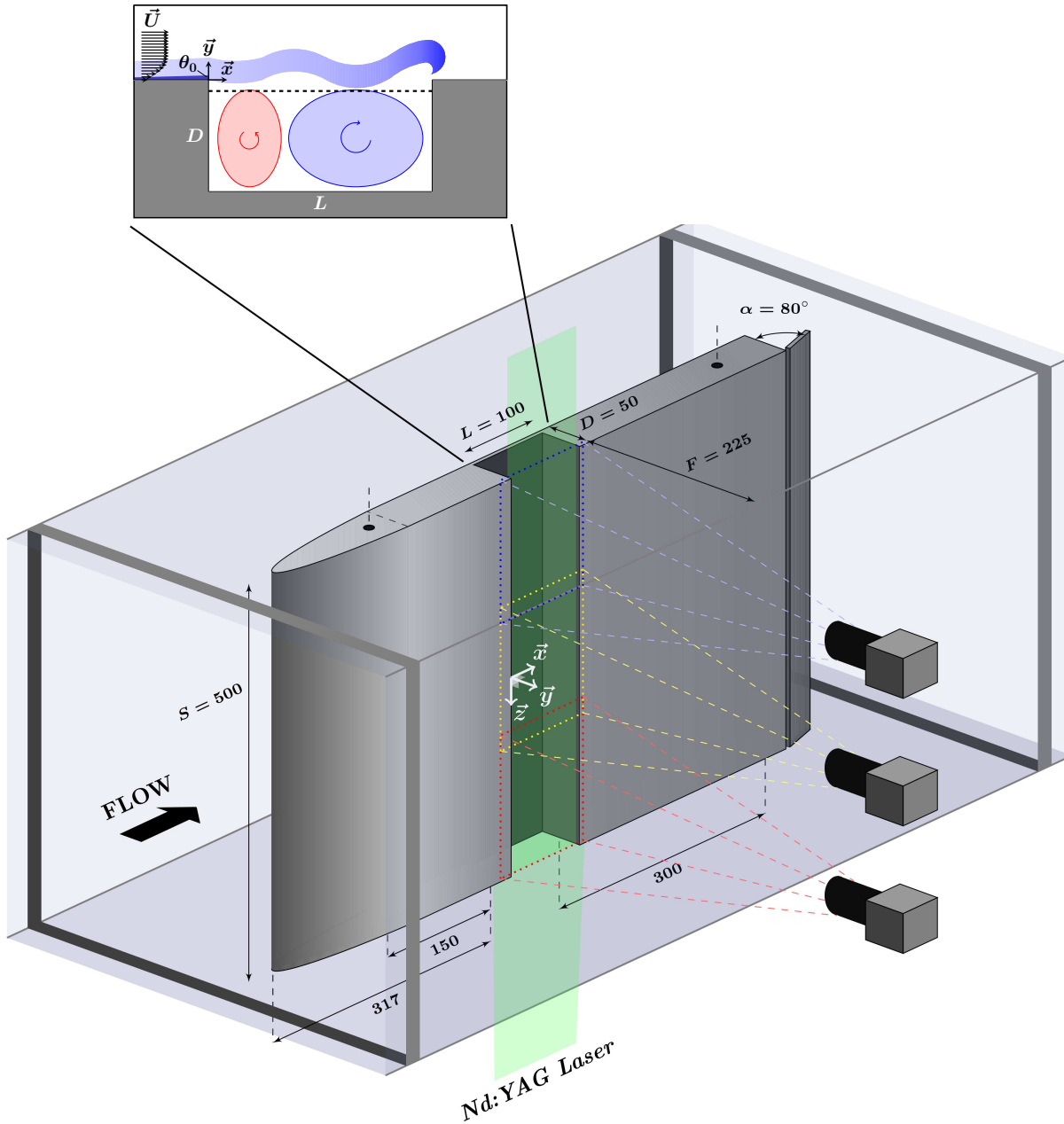


Figure 2.3: Scheme of the experimental set-up. Dimensions are given in millimetres. In a close-up on the $L = 2D$ – shaped cavity, the location of the laser sheet is displayed ($y = -0.1D$). For high resolution images, three cameras are actually required to cover entirely the cavity span, their respective fields of view overlapping in pairs.

The experimental set-up is described in Figure 2.3. The test plate, which has a 6:1 semi-elliptical leading edge, was mounted vertically in the middle of the test section 1 m downstream of the contraction exit. The 50 mm deep, D , 100 mm long, L , cavity spans the water tunnel and is

located $6.34 D$ from the leading edge of the plate. For these experiments the distance from the plate surface to the water-tunnel walls is nominally $F = 225$ mm resulting in a ratio $F/D = 4.5$. The water-tunnel was uniformly seeded with $11 \mu\text{m}$ diameter glass hollow spheres whose density is 1100 kg/m^3 , implying a particle relaxation time of $8 \mu\text{s}$. Error intervals have been carefully estimated by taking into account systematic errors – calibration, temperature measurement and geometry precision –, as well as uncertainties related to computation and statistics – turbulence rate, PIV precision, etc.

The results presented later in Section 5 have been obtained for three mean free-stream velocities $U_0(A) = 29.5 \pm 0.8$ mm/s and $U_0(B) = 47.0 \pm 0.9$ mm/s and $U_0(C) = 107.5 \pm 3$ mm/s, corresponding to Reynolds numbers based on cavity depth (Re_D) around 1500 and 2400 and 5550, respectively. Inflow characteristics for these three cases are provided in Table 2.1. Temperature conditions at the time of each acquisition have been measured to be taken into account in kinematic viscosity calculation. The incoming boundary layer is characterised through the displacement and momentum thicknesses at separation ($x = 0$), δ_0^* and θ_0 , respectively.

Table 2.1: Characteristics of the wall bounded laminar inflow at the leading edge.

	U_0 (mm/s)	δ_0^* (mm)	θ_0 (mm)	Re_D	Re_{θ_0}	D/θ_0
<i>A</i>	29.5 ± 0.8	5.59 ± 0.28	2.16 ± 0.11	1500 ± 43	65 ± 4.9	23.2 ± 1.2
<i>B</i>	47.5 ± 0.9	4.27 ± 0.18	1.70 ± 0.07	2400 ± 51	81 ± 5.0	29.4 ± 1.3
<i>C</i>	107.5 ± 2.8	2.61 ± 0.13	1.07 ± 0.05	5550 ± 161	119 ± 9.2	46.6 ± 2.4

2.2.2 Particle image acquisition

Spanwise (zx)-planes In order to obtain high spatial resolution, PIV single-exposed images were generated using three *ImperX B4820* CCD cameras each with an array of 4904×3280 pixels and equipped with 105 mm Micro-Nikkor lenses set at a reproduction ratio of 5. Such a configuration was required for a field of view spreading over the cavity span ($S = 500$ mm). The three imaged regions, each corresponding to $3.62 D \times 2.42 D$, overlap so as to enable us to merge them in a single velocity field such as

$$\mathbf{U}_{zx}(z, x, y_{piv}, t) = w(z, x, y_{piv}, t) \mathbf{e}_z + u(z, x, y_{piv}, t) \mathbf{e}_x. \quad (2.4)$$

The pulsed illumination to acquire the single-exposed image pairs was obtained using a NewWave dual cavity Nd:YAG laser with a maximum energy per pulse of 120 mJ. A suitable light sheet of nominally 1 mm thickness was produced using appropriate spherical and cylindrical lenses. The light sheet forming a zx -plane, thus parallel to the cavity bottom, was located at $y = -0.1 D$, that is 5 mm below cavity top-plane spanning its width. Far from the source, brightness was increased by doubling the laser sheet with a mirror placed at $z/S = -0.5$ – on top of the rig perpendicularly to the cavity. The free stream was validated by acquiring images in another plane at $y = 0.3 D$. Image acquisition and laser pulse synchronisation were controlled by a timing computer operating on a Real Time Application Interface (RTAI) linux operating system.

Cross-stream (xy)-plane Supporting acquisitions were also performed in a cross-stream plane at $z/S = 0.06$ with the aim of obtaining incoming flow characteristics in cases B and C . The camera used for those acquisitions was a *pc0-4000* presenting a 4008×2672 CCD array and coding images on 14 bits. It was equipped with a 4 GB on-board memory.

2.2.3 Data merging

The single exposed image pairs from LTRAC campaign were analysed using multigrid cross-correlation digital particle image velocimetry (MCCDPIV), for which details can be found in Soria (1994, 1996); Soria et al. (1999). Characteristics and performance are discussed further in Section 2.3.1.

Once velocity fields have been processed for each of the three cameras — left, centre and right areas — they have to be merged into a global field spanning the entire cavity. The merging is performed through a two-dimensional interpolation of the three velocity fields on a single global grid. Then, inside overlap regions is used weighted averaging in order to take into account contributions of both cameras according to their local relevance. Indeed, the closer a pixel is to the image edge, the larger local distortion is. Consequently, weight of contributions of the two overlapping velocity fields was decreased when closing in image edge. Furthermore, as distortion is mainly in opposite directions in both images, its effect is largely removed after merging.

2.3 PIV algorithms

2.3.1 MCCDPIV: cross-correlation algorithm

For the PIV campaign carried out at LTRAC, the single exposed image pairs were analysed using multigrid cross-correlation digital particle image velocimetry (MCCDPIV). The code, described in Soria et al. (1999), has its origin from Soria (1994) and Soria (1996). It uses an iterative and adaptive cross-correlation algorithm to increase the velocity dynamic range and reduce the random and bias error. The performance, accuracy, and uncertainty of the algorithm with applications to the analysis of a single-exposed PIV and holographic PIV (HPIV) images have been reported in Soria (1998) and von Ellenrieder et al. (2001). The MCCDPIV algorithm also incorporates a local cross-correlation function multiplication method Hart (2000) to improve the search for the location of the maximum value of the cross-correlation function. For the sub-pixel peak location calculation, a two-dimensional Gaussian function model is used to find the location of the maximum of the cross-correlation function using the least mean square value Soria (1994). A dynamic mean value operator test Westerweel (1994) is applied to validate the MCCDPIV data field. Following data validation, the in-plane velocity components in the coordinate directions are computed by dividing the measured MCCDPIV displacement in each interrogation window by the time between the exposures of the image pair and the optical magnification.

An uncertainty assessment based on the methodology outlined in Moffat (1988) was conducted in Soria et al. (1999). The uncertainty in the PIV processing algorithm is 0.032 pixels at the 95% confidence level. The RTAI timing system has an uncertainty of $0.15\mu\text{s}$. The uncertainty in measuring the magnification factor is 2 pixel over the length of the CCD array used. Based on these values, the largest uncertainties in deduced length scales from the PIV measurement at the 95% confidence level is 0.3% of the imaged region (*i.e.* $3.62 D$) with an uncertainty in the velocity of 1% of the full scale range (FSR) at the 95% confidence level.

2.3.2 Optical flow processing

For the high frame rate images acquired at LIMSI, velocity fields were processed by using an optical flow algorithm (OPFLOW), which relies on an orthogonal dynamical programming (Quénot, 1992; Quénot et al., 1998). Over the years, this algorithm had been successfully employed at LIMSI for cavity flow experiments, in spite of the low resolution of input images (typically less than 1 Megapixel). Based on the minimisation of optical intensity difference between two images, the code has been shown to be one of the most efficient in shear layers, boundary layers or more generally in strong gradient area with respect to other algorithms. Characterisation and comparison with various cross-correlation codes are provided in Quénot et al. (2001); Stanislas et al. (2005, 2008). The particle relative motion is estimated by minimising the norm of the gray level difference,

$$\delta r^*(r) = \min_{r, \delta r \in \mathcal{D}} \|I(\mathbf{r} + \delta \mathbf{r}, t + \delta t) - I(\mathbf{r}, t)\|, \quad (2.5)$$

between the images under study. This process is carried out iteratively on horizontal (and vertical) stripes \mathcal{D} of decreasing height (and width). Each new iteration uses the estimation of the previous iteration as an initial condition, and the computation ends up with an estimation of the displacement x -(y -)component at any pixel of the grid.

One could rightfully argue that no PIV image hold that much information. Indeed, only particles carry information which makes it locally discrete and sparse. Then, how does OPFLOW algorithm provide information at any given pixel of the image? By definition, the minimisation takes into account larger areas (stripes of decreasing width) by fulfilling continuity laws inside. Of course, those laws are obviously not related to flow dynamics in any way. However they produce a similar effect which brings coherence to a reconstruction relying on sparse information. In that sense, we understand that this “full-resolution” field is not extracted from local information exclusively. From that interpolated nature comes a greater robustness to high gradients and discontinuities in the flow. On the other hand, if calculation divergence occurs nonetheless, for instance due to a lack of particles, error propagation can be encountered: appearing as partially *exploded* fields.

When calculation fails (exploded fields or large area of false vectors), three successive images, instead of two, are used, which helps in stabilising the minimisation process, though smoothing the displacement field. At last, it remains less than 1% of incorrect displacement fields. The search for those errors is based on the temporal continuity rather than spatial gradients. The validation process applies to every displacement time-series at a given point in space. Outliers are detected when the displacement vector is beyond either one of the thresholds: *i*) a threshold value defined relatively to the mean displacement, at the same spatial point, over a finite-time slipping window, *ii*) a maximal slope allowed in the rate of change of the displacement vector, relatively to the time-series standard deviation. When detected, outliers are replaced by linear interpolation between the previous (past) and next (future) displacement values, at the spatial point under consideration. Detection/interpolation procedure is then pursued iteratively until no more incorrect vectors are detected.

As usual, the displacement field is then mapped into a velocity field using a calibrated image (rule) and the time delay between both images, the inter-frame delay Δt .

2.3.3 Discussion

The present section aims to provide a basic validation of PIV computations performed on the two experimental campaigns at LTRAC and LIMSI. Though both optical flow and MCCDPIV codes have already been largely characterised and validated (see references above), we discuss here their performances and limitations when applied to the present datasets. Examples of processed velocity fields are confronted with a reference code *PIVview2C*. The latter is an advanced cross-correlation-based-PIV software developed at the German Aerospace Centre (DLR). It is available at LTRAC and a demo version can be found at <http://www.pivtec.com>. For the sake of comparison, we choose to display vorticity fields and colour scales are designed to highlight any detail and defect in processed data.

***zx*-plane data at LTRAC** Considering spanwise images from LTRAC experimental campaign, high spatial resolution was a primary requirement. It was necessary to enable the identification of centrifugal instabilities (small structures), while embracing the entire span of the cavity to maximise the number of wavelengths. Furthermore, the out-of-plane component being at least as large as in-plane displacement, the inter-frame delay Δt had to remain small. High magnification was therefore useful to maintain suitable displacements – recall that $\delta x \geq 1$ pixel corresponds to a signal over noise ratio (S/N) higher than 30. Thus, cameras with large arrays were required (three *ImperX* cameras 4904×3280). An example from a single camera is provided in Figure 2.4, for both MCCDPIV and PIVview computations.

Particle images are pre-processed prior to any cross-correlation computation: 3×3 kernel Gaussian smoothing is first applied in order to remove peak-locking. Then, particle images are normalised using a 7×7 kernel *min-max* filter, such that at pixel (a, b) :

$$I'_{ab} = \frac{I_{ab} - I_{\min}}{I_{\max} - I_{\min}} \quad (2.6)$$

with $I_{\min} = \min[I_{ij}]$ and $I_{\max} = \max[I_{ij}]$ for $a - 3 \leq i \leq a + 3$, $b - 3 \leq j \leq b + 3$.

Both MCCDPIV and PIVview computations are performed with 32×32 pixel windows overlapped at 50 %. In this case, displacements are homogeneous enough so that multigridding is not required. MCCDPIV uses cross-correlation based correction (Hart, 2000) to improve sub-pixel resolution and increase robustness while PIVview makes use of image deformation with B-spline interpolation of degree 3. Overall time for loading and processing each image pair is around 30 seconds for both methods.

As shown in Figure 2.4.(c-d), results from both MCCDPIV and PIVview are very close. In vorticity fields, one can remark that MCCDPIV results reveal a far lower S/N ratio. This good performances constitute a validation of this campaign. In fact, an undemanding computation was expected since the experiment was designed exclusively towards a single purpose: getting high quality velocity fields. This was achieved notably by acquiring high magnification water-flow images – so as to supply optimised seeding and brightness – across a plane minimising out-of-plane velocity ($y = -0.1D$). More difficulties rise when investigating the flow in a cross-stream plane.

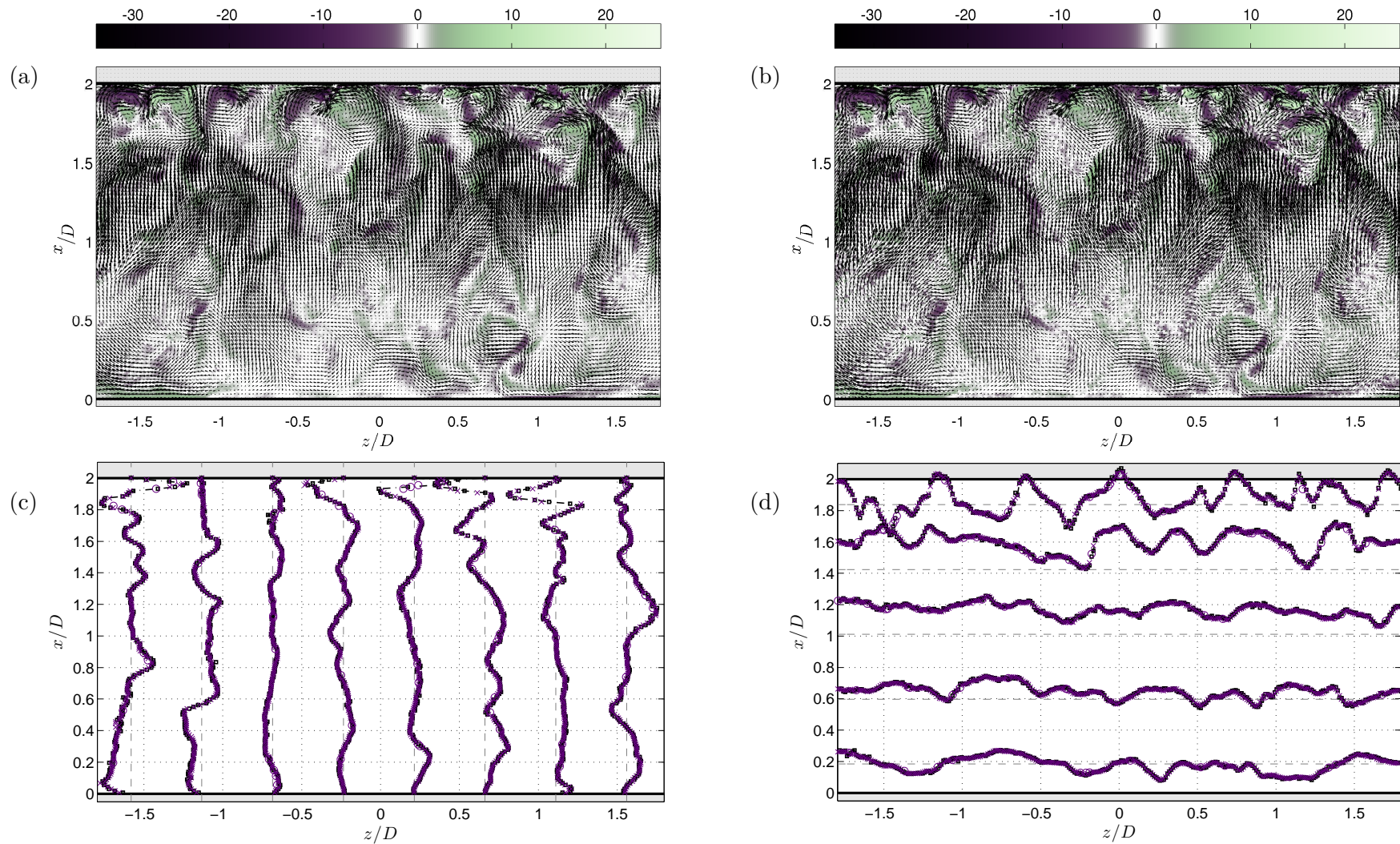


Figure 2.4: A snapshot obtained from one of the three cameras (central part of the cavity in the zx -plane at $y/D = -0.1$), for $Re_D = 5550$ and $D/\theta_0 = 46.6$. Instantaneous velocity field, (a) MCCDPIV and (b) PIVview computations. One vector out of two are displayed, colours encode dimensionless vorticity $\omega_y D/U_0$. Profiles of dimensionless velocity, (c) spanwise component w/U_0 and (d) streamwise component u/U_0 , for MCCDPIV – (\times) and interpolated outliers (\circ) – and for PIVview (\square)

xy -plane data at LTRAC Observed in a cross-stream plane, an open cavity flow exhibits high gradients of velocity primarily due to the shear layer. Such high disparities in displacement represent a strong limitation for PIV computation. Indeed, adjusting the displacement (through Δt) to better resolve free stream displacements (outflow) would pull down inner-flow displacements, decreasing drastically their S/N ratio. On the contrary, optimising the computation for low velocities inside the cavity by increasing Δt lowers the correlation coefficients in the outflow. With PIV algorithms using interrogation windows one can make use of multigridding methods to deal with large displacements. Large windows in the first iteration allow to identify high velocities in order to shift interrogation window accordingly for next iteration, and so on. However, multigridding cannot improve cross-correlation when dealing with high gradients inside the interrogation window itself: the “local” assumption is no longer valid. This is a major issue for images at large reproduction ratios: structures cannot be resolved properly. In the last decade, image deformation algorithms have been introduced in the most advanced PIV codes to increase the robustness to higher gradients. More detail can be sought in Raffel et al. (2007) and the extensive review therein.

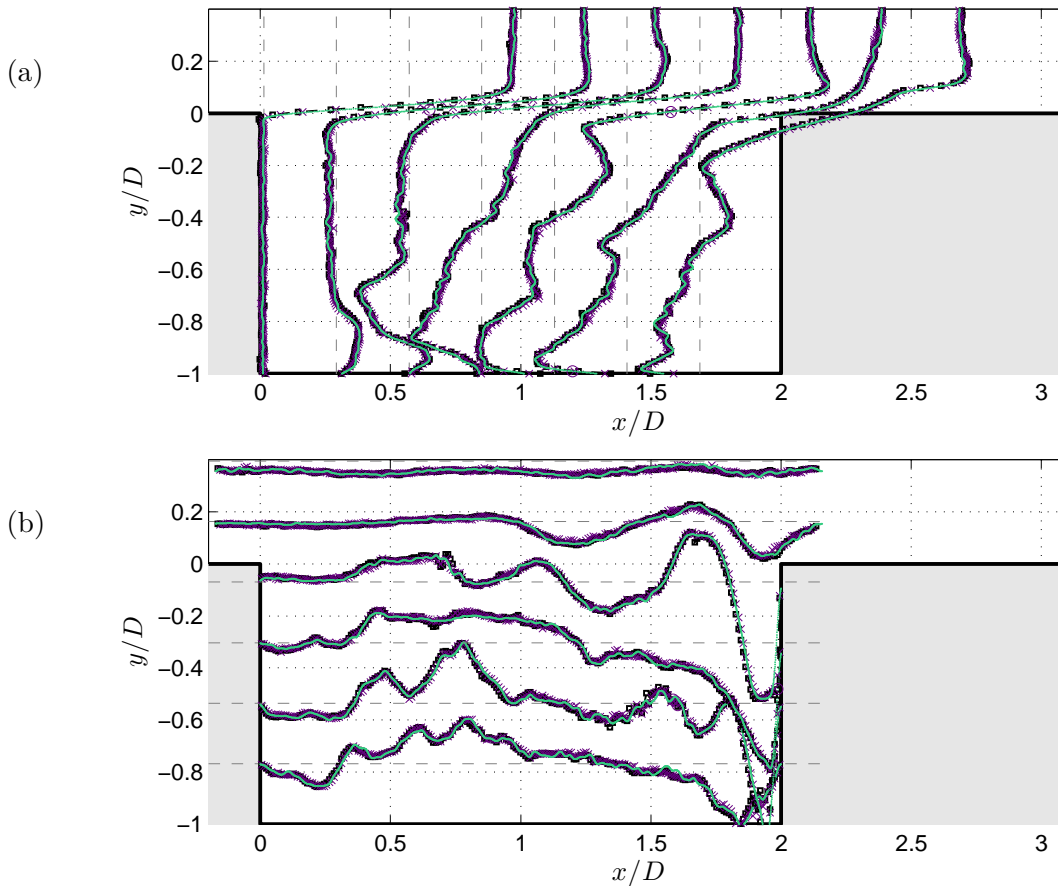


Figure 2.5: Same snapshot as Figure 2.5. Profiles of dimensionless velocity, streamwise component u/U_0 (a) and cross-stream component u_y/U_0 (b), for MCCDPIV – (\times) and interpolated outliers (\circ) –, for PIVview ($-\square$) and for OPFLOW (\cdot).

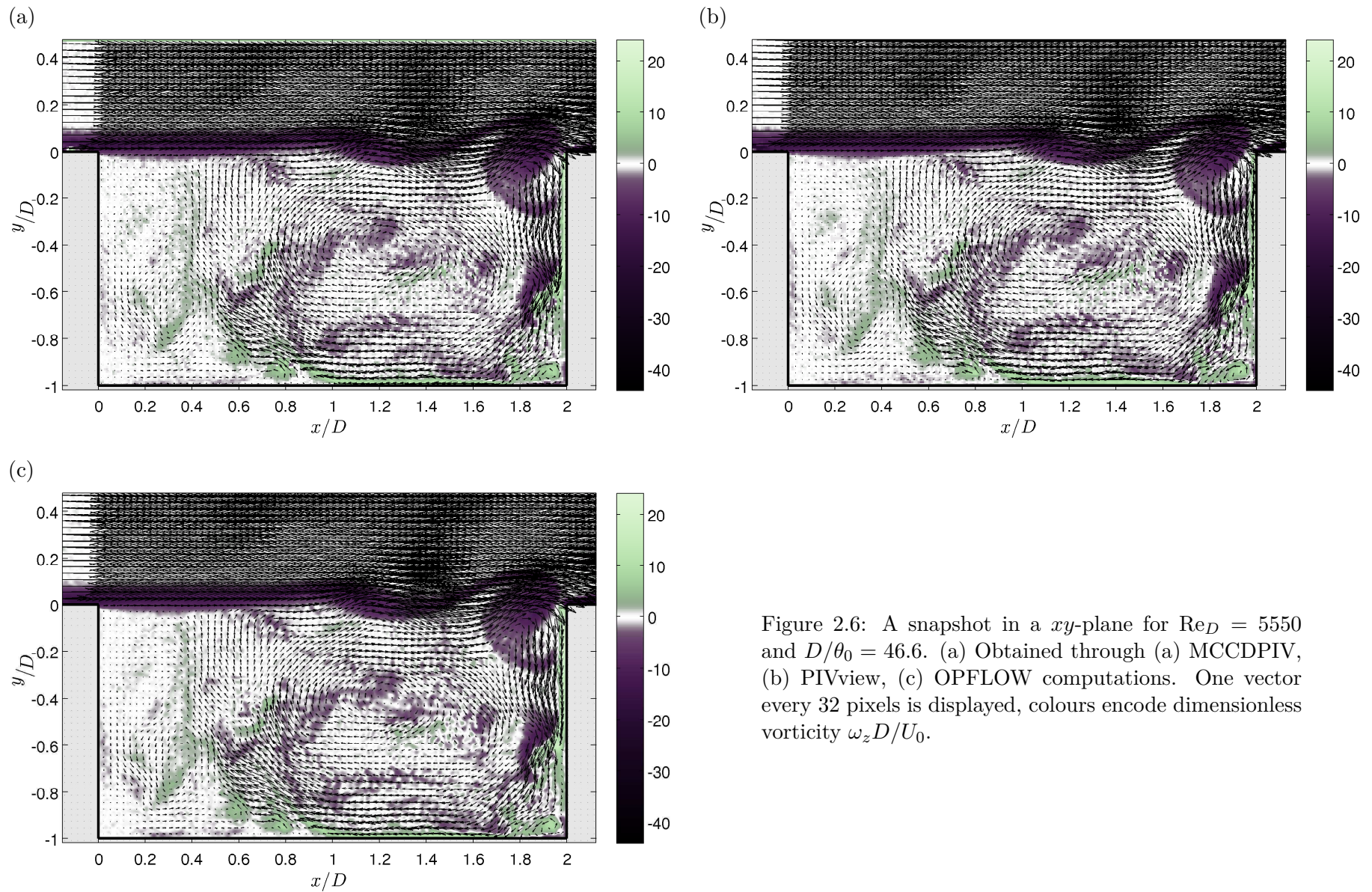


Figure 2.6: A snapshot in a xy -plane for $Re_D = 5550$ and $D/\theta_0 = 46.6$. (a) Obtained through (a) MCCDPIV, (b) PIVview, (c) OPFLOW computations. One vector every 32 pixels is displayed, colours encode dimensionless vorticity $\omega_z D / U_0$.

Cross-stream plane experiments carried out at LTRAC have been processed using all three algorithms (MCCDPDV, PIVview and OPFLOW), as shown in Figures 2.5-2.6. MCCDPDV and PIVview computations are performed using multigriding from 64×64 to 32×32 pixel interrogation windows with a 50% overlap. Similarly to zx -planes, MCCDPDV and PIVview rely on cross-correlation based correction and image deformation with B-spline interpolation of degree 3, respectively, to improve precision and robustness. Performances are similar for both cross-correlation techniques. The number of outliers is below 0.8 %. In particular, large gradients observed inside the shear layer and at the impingement are kept under control thanks to multigriding and high magnification. Spatial resolution is indeed high enough for the structures to be largely bigger than interrogation windows. On the other hand, the S/N ratio in the inner-flow is unavoidably low, so as to keep reasonable displacements in the out-flow (22 pixels at the most)

Processing large images with OPFLOW is rather costly in terms of computation time. For instance, it takes about 50 minutes to process a 4008×2672 pixel image pair. Such a duration makes difficult any massive dataset computation for large images. The example given for the sake of comparison in Figures 2.5-2.6 has been downgraded to match resolution of PIVview and MCCDPDV fields. Scales smaller than PIVview and MCCDPDV grid (one out of 16 pixels) are Fourier-filtered. The resulting velocity field is equivalent but without hardly any outlier to be seen, contrary to cross-correlation methods. On the other hand, using full resolution field directly would reveal more noise, probably due to a lack of information at these scales. Indeed, seeding density was adjusted to get about 10 to 15 particles in a 32×32 window. In that particular case, full resolution, so costly in computation time when dealing with large images, helps in satisfying the continuity rather than accessing smaller scales, often polluted with noise. Note that such a long computation time is likely due to a lack of optimisation to take into account the increasing size of camera images. CCD arrays were rarely larger than 640×480 pixels when OPFLOW was originally designed.

***xy*-plane at LIMSI: high speed acquisition** On top of the high gradients existing in the shear layer, the experiment conducted at LIMSI presented important restrictions, both due to requirements in time-frequency resolution and to equipment limitations. As explained earlier in Section 2.1, Δt was not let independent from frame rate, making impossible to adjust precisely the displacements to be resolved. Also, image size had to be minimised (around 1/4 Megapixels) to increase acquisition duration. The resulting magnification of 5.67 pixel/mm hence yields 100 pixels along the length of the cavity. Finally, the high-speed camera only codes grey-levels on 8 bits, *ie.* providing a dynamic range of only 256 levels.

With those restrictions deteriorating image data quality, PIV processing becomes difficult. In Figures 2.7-2.8, results from OPFLOW computation are compared with PIVview and MCCDPDV in the same harsh conditions. Because of the low magnification, multigriding for cross-correlation methods is pushed down to 16×16 pixel interrogation windows, with drastic oversampling to reach one vector every 4 pixels (75 %-overlap). In that case, OPFLOW computation time for one field, cropped over a 613×400 pixel sub-domain, is of the order of 80 s, on a 2.4 GHz processor. Processing each velocity field using both MCCDPDV and PIVview lasts only a few seconds. Once again, a low-pass filter has been applied to OPFLOW-processed vorticity fields in order to divide by 4 its resolution, down to cross-correlation algorithms.

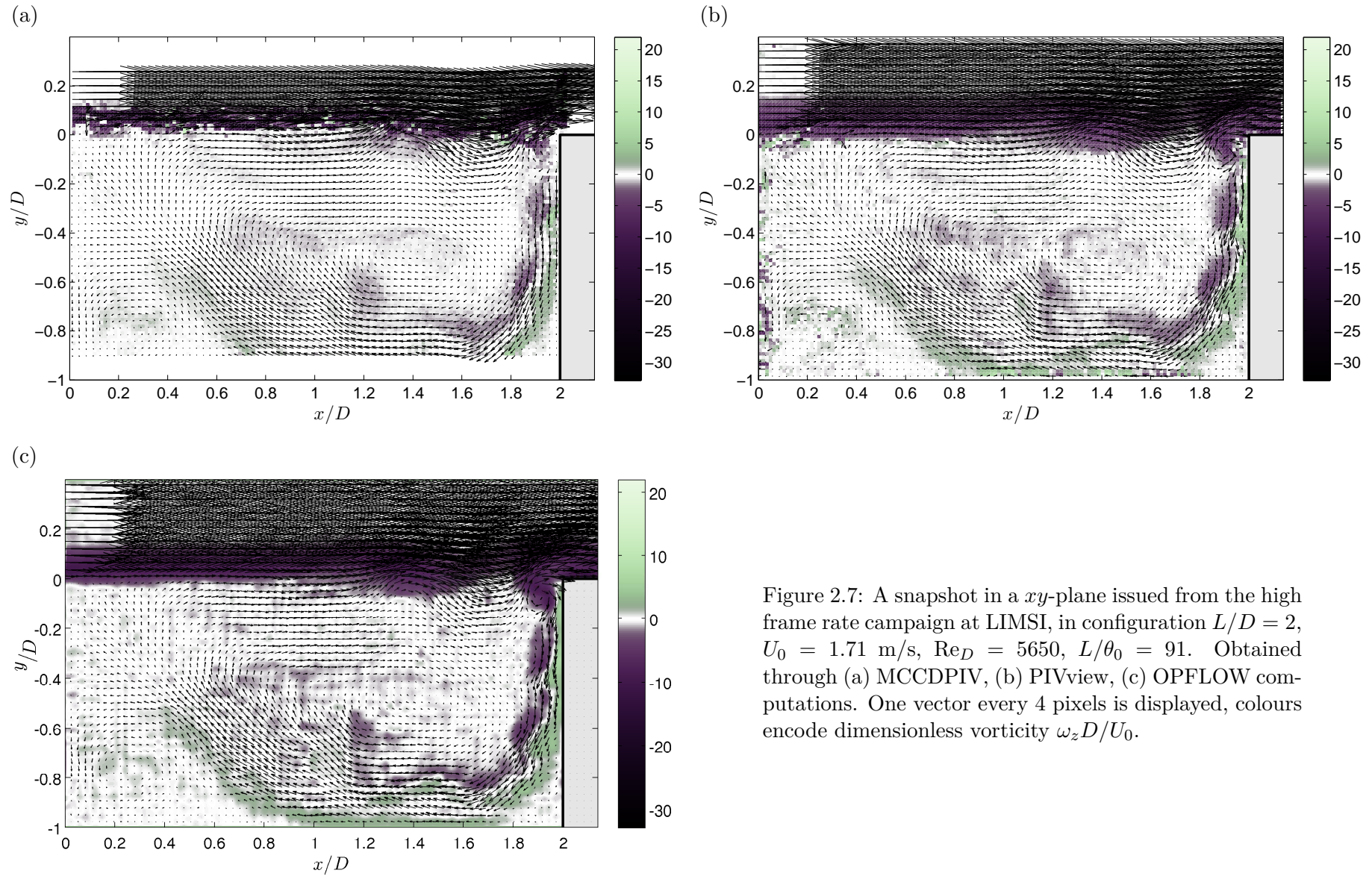


Figure 2.7: A snapshot in a xy -plane issued from the high frame rate campaign at LIMSI, in configuration $L/D = 2$, $U_0 = 1.71$ m/s, $Re_D = 5650$, $L/\theta_0 = 91$. Obtained through (a) MCCDPIV, (b) PIVview, (c) OPFLOW computations. One vector every 4 pixels is displayed, colours encode dimensionless vorticity $\omega_z D/U_0$.

As expected, the main issue with results from cross-correlation techniques concerns the correlation drop in high gradient region inside the shear layer and at the impingement. With such small images, relative window size increases too much to be handled by multigridding only. While PIVview relies on image spline deformation process, thereby preserving a decent robustness, MCCDPIV diverges dramatically. Induced damage is beyond repair: the starting shear layer explodes and the impinging vortex at the downstream corner of the cavity is missing, see Figures 2.7.a and 2.8. Similarly, inflows along the downstream wall are diminished relatively to PIVview and OPFLOW calculations.

Velocity fields from PIVview and OPFLOW appear globally coherent. It is a fair match for both snapshot and mean flow. However, contrarily to previous cases, artefacts are clearly visible. For instance, cross-correlation techniques are particularly sensible to background noise. Even when using pre-processing, that is background subtraction and min-max filtering, both PIVview and MCCDPIV results exhibit many outliers close to the walls, likely due to reflexions. OPFLOW appears to be far more robust to image defects.

On the other hand, one may note that intrinsic noise is revealed for OPFLOW results by small S/N ratios existing at the centre of the main recirculation in the cavity. OPFLOW errors are shown by high RMS levels in the incoming outflow in Figure 2.8.d. From time to time, computation is destabilised due to incoming (new) particles combined with large velocities. Those exploded regions are removed through time-continuity validation, as explained in Section 2.3.2.

Another shortcoming to interrogation window algorithms is the loss of image boundaries. When processing low resolution images, non-treated perimeter expands drastically, in particular for MCCDPIV, for which there is no window modification to overcome that loss. In general, both instantaneous and averaged streamwise velocity profiles – in Figure 2.8.(a,c) – show that boundary layers are better identified with OPFLOW.

Finally, OPFLOW resolution (4 pixel width stripes) is greater than PIVview and MCCDPIV algorithms, for which decreasing interrogation window size below 16×16 pixel causes too much deterioration to correlation coefficient.

In conclusion, OPFLOW and MCCDPIV algorithms provide satisfying results in different configurations, for which they have been respectively designed and calibrated. On one hand, MCCDPIV offers equivalent performance to one of the most advanced commercial software PIVview when applied to high quality images. It is therefore perfectly suitable for LTRAC experiments using an optimised PIV set-up. On the other hand, OPFLOW shows an increased robustness to image defects, notably encountered in restricted quality small size images issued from high frame rate experiments, such as conducted at LIMSI.

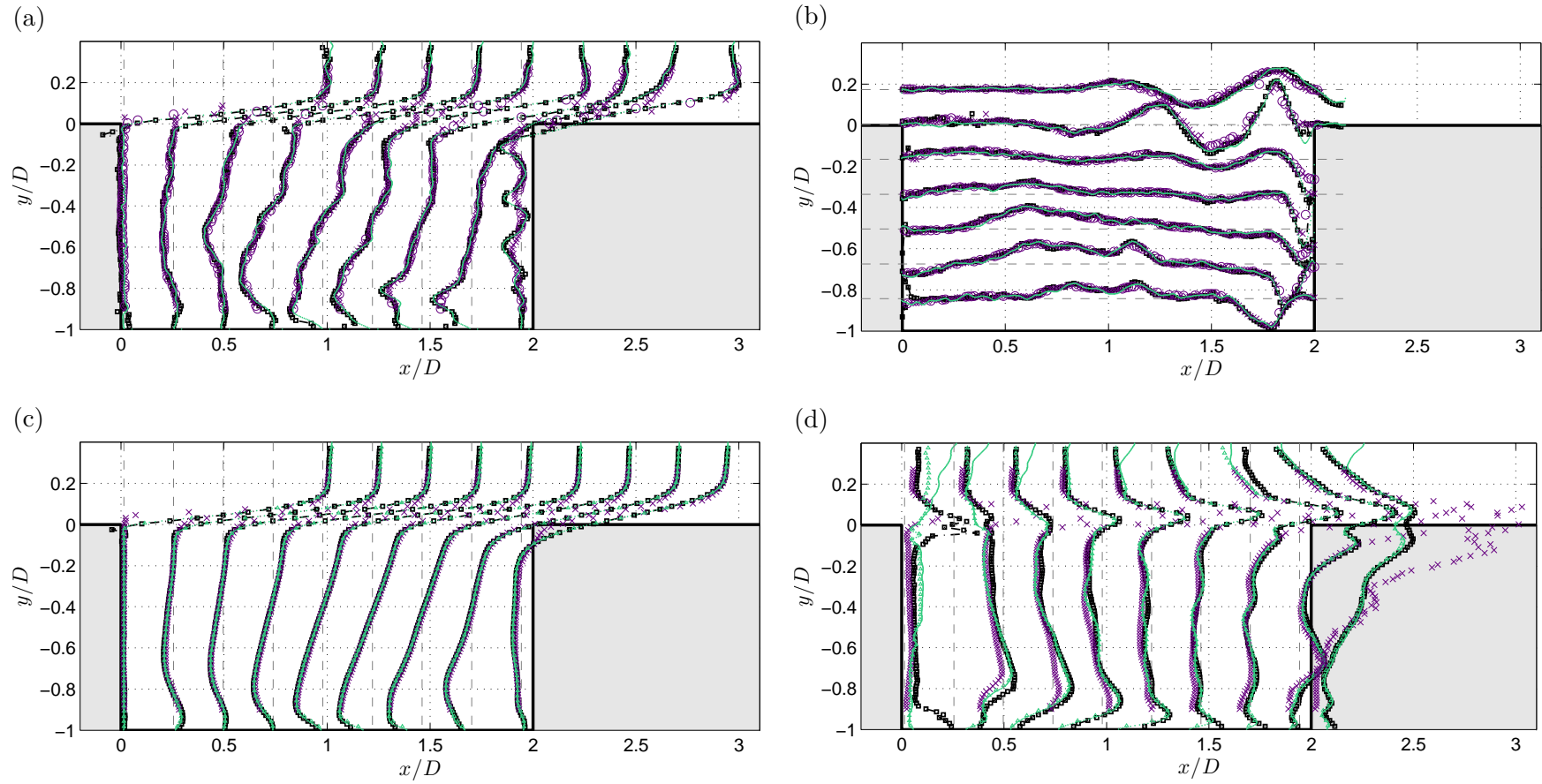


Figure 2.8: Same snapshot as previous Figure. Profiles of dimensionless velocity, streamwise component u/U_0 (a) and cross-stream component u_y/U_0 (b). Statistics of one dataset of 4096 time-resolved velocity fields: streamwise mean velocity \bar{u}/U_0 (c) and streamwise RMS $\overline{u'u'}/U_0$ (d). Markers are for MCCDPIV – (\times) validated, and (\circ)interpolated outliers –, for PIVview ($-\square$) and for OPFLOW – (\cdot) validated, and (\triangle) time-interpolated vectors.

Decomposing the saturated dynamics of a real flow

Once time-resolved space extended datasets have been obtained from experimental campaigns detailed in previous chapter, it now becomes possible to apply modal decomposition methods to identify time or/and space scales at stake in the flow under study. Decomposing the flow is particularly relevant when studying impinging flows since such systems are known to concentrate their energy in only a few peaks in spectral components. It is therefore possible to reduce the analysis to a few characteristic modes out of modal decompositions.

Below are described the methodologies employed to perform the forthcoming analyses. In particular, the modal decomposition is primarily applied time-wise to sets of xy and zx -plane velocity fields. For spanwise datasets in Chapter 5, modal decompositions are also performed spanwise – *ie.* along the dimension z . The reader may acquaint himself with the present chapter either now or gradually, when it becomes a prerequisite for the analysis.

3.1 The Fourier transform

The first tools described here rely on Fourier transform, that is the projection of the dynamics on a basis of complex sinusoidal functions. The principle of discrete Fourier transform is briefly recalled in the next section.

3.1.1 The Discrete Fourier Transform

Consider a discrete scalar N -long 1D signal

$$\{\mathbf{v}_j\} = \{\mathbf{v}_0, \mathbf{v}_1, \dots, \mathbf{v}_{N-1}\}, \quad (3.1)$$

such as a time-series issued of a local measurement of the dynamics, consisting for instance of a velocity component $v(\mathbf{x}_p, t)$ at a given point $\mathbf{x}_p = (x_p, y_p, z_p)$

$$\mathbf{v}_j \equiv v(x_p, y_p, z_p, j\delta t) \quad \text{with} \quad j = 0, 1, 2, \dots, N - 1 \quad (3.2)$$

where δt is the time step of the time-series. Period of acquisition and sampling frequency are thus given by

$$T = N \delta t \quad \text{and} \quad f_s = \frac{1}{\delta t}. \quad (3.3)$$

The discrete (time) Fourier transform \mathcal{F}^t associates elements $\{\mathbf{v}_j\}$ of the *physical domain* to Fourier modes $\{\nu_k\}$ with $k = 0, 1, \dots, N - 1$ in the *spectral domain*.

$$\{\mathbf{v}_j\} \xrightarrow{\mathcal{F}^t} \{\nu_k\}$$

The (scalar) Fourier modes ν_k are defined as

$$\nu_k = \frac{1}{\sqrt{N}} \sum_{j=0}^{N-1} v_j \exp(-2i\pi \frac{jk}{N}) \quad (3.4)$$

with $i^2 = -1$. Mathematically, the Fourier mode ν_k represents the projection of the time-series $\{v_j\}$ on the discrete complex sinusoid function

$$\Psi_{jk} = \exp(2i\pi \frac{jk}{N}) \quad (3.5)$$

yielding the dimensionless angular frequency ω_k

$$\omega_k = \frac{2\pi k}{N} \in [0, 2\pi] \quad (3.6)$$

Of course, Ψ_{jk} is defined modulo 2π , such that

$$\Psi_{jk} = \exp(i\omega_k) = \exp(i(\omega_k - 2\pi)) \quad (3.7)$$

This translates the *aliasing* which occurs for time scales smaller than $2\Delta t$. Spectral components such that $\omega_k > \pi$ are folded onto smaller negative frequencies $\omega_{k-N} = \omega_k - 2\pi$.

That is the reason why the input signal must satisfy the *Shannon-Nyquist* criterion,

$$f < \frac{f_s}{2} \quad (3.8)$$

where f stands for any frequency carrying energy in the signal. Note $f_s/2$ is named *Nyquist* frequency. In practice, the Fourier modes are hence associated with dimensionless angular frequencies

$$\omega_k = \pm \frac{2\pi k}{N} \in [-\pi, \pi] \quad \text{with } k = 0, 1, 2, \dots, N' \quad (3.9)$$

such that $N = 2N'$ (even) or $N = 2N' + 1$ (odd). In the case of a real input signal $\{v_j\} \in \mathbb{R}$, $|\nu_k| = |\nu_{-k}|$. As a result, the only physical frequencies are positive:

$$f_k = \frac{k}{T} = f_s \frac{k}{N} \quad \text{with } k = 0, 1, 2, \dots, N' \quad (3.10)$$

and cumulate the contributions of both complex conjugate modes $\nu_{\pm k}$.

3.1.2 On Power Spectral Densities

This section concerns the computation of averaged power spectral densities (PSD) through discrete Fourier transform and window averaging process (*Welch* algorithm). It also provides the parameters used for power spectral densities computation of Laser Doppler Velocimetry and time-resolved PIV time-series. One estimates the *power spectral density* as

$$\text{PSD}(\omega_k) = \lim_{N \rightarrow \infty} \mathbf{E}[|\nu_k|^2] \quad (3.11)$$

where ν_k is the Fourier mode referring to previous section, and $\mathbf{E}[\cdot \cdot \cdot]$ is the expectation of the function between brackets.

Welch algorithm

The estimation of power spectral density tends to the real value through its expectation (Equation 3.11). Therefore, averaging over a rising number n of statistically equivalent acquisitions is usually required since it reduces confidence interval by a factor of $1/\sqrt{n}$.

This can be achieved by splitting up the signal into shorter segments of length N_w elements. One computes the Fourier transforms out of the n segments – or *computation windows* – providing n estimations of PSD, over which the averaging is performed. The *computation windows* are usually overlapped to increase further the number of estimations.

Note however that shorter segments imply that one loses precision in frequency since the frequency step becomes

$$\delta f = \frac{1}{N_w \delta t} \quad \text{with } N_w < N \quad (3.12)$$

Also, one must take into account that window length $T_w = N_w \delta t$ should remain such as $T_w \gg \tau$, with τ the longest characteristic time scale in the dynamics, so as to preserve the approximation $T_w \rightarrow \infty$.

In order to reduce edge effects due to abrupt truncation, each window is multiplied by a *window function*, prior to Fourier computation (Welch, 1967). That window function forces the signal into a gradual decay when closing the edge of the dataset. For the computation of power spectral densities in the present work, a *Hanning* function was chosen:

$$\Pi_j = \frac{1}{2} \left[1 - \cos \left(\frac{2\pi j}{N_w - 1} \right) \right] \quad \text{with } j = 0, 1, \dots, N_w - 1 \quad (3.13)$$

This operation leads to a loss of information contained in a computation window, but it is counterbalanced by window overlapping. Finally, considering the segments $\{v_{\ell j'}\}$ ($1 \leq \ell \leq n$), extracted from the time-series $\{v_j\}$, the converged power spectral density finally writes

$$\text{PSD}(\omega_k) = \frac{1}{n} \sum_{\ell=1}^n \frac{1}{N_w} \left| \sum_{j'=0}^{N_w-1} v_{\ell j'} \exp(-2i\pi \frac{j'k}{N_w}) \right|^2 \quad (3.14)$$

Normalisation

In the forthcoming analyses, power spectral densities are usually normalised and expressed in dB units, noted as functions of frequency f :

$$\underline{\text{PSD}}(f) = 10 \cdot \log_{10} \left(\frac{\text{PSD}(f)}{\max_f[\text{PSD}(f)]} \right), \quad (3.15)$$

such that PSDs are non-dimensionalised with respect to the dominant frequency. A set of PSDs computed from LDV measurements (streamwise velocity) are plotted in Figure 4.5.

Time spectra across the entire velocity field

When processing time-resolved PIV datasets, time power spectral densities can be processed at various locations in the field, for both velocity fluctuation components (or vorticity), since we are dealing with two-components-space-extended data. The expression 3.14 rewrites as a

function of the considered position $\mathbf{r} = (x, y, z)$ in the flow

$$\text{PSD}(\mathbf{r}, \omega_k) = \frac{1}{n} \sum_{\ell=1}^n \frac{1}{N_w} \left| \sum_{j'=0}^{N_w-1} v_{\ell j'}(\mathbf{r}) \exp(-2i\pi \frac{j'k}{N_w}) \right|^2 \quad (3.16)$$

where $v_{\ell j'}(\mathbf{r})$ is the variable under study, namely u' , v' , w' , ω'_z or ω'_y , *etc.*

PSDs are now normalised relatively to the entire field and expressed in dB units according to

$$\underline{\text{PSD}}(\mathbf{r}, f) = 10 \cdot \log_{10} \left(\frac{\text{PSD}(\mathbf{r}, f)}{\max_{\mathbf{r}, f}[\text{PSD}(\mathbf{r}f)]} \right), \quad (3.17)$$

such that the spectra are normalised, among all frequencies and over any spatial point, with respect to the highest amplitude of the dominant frequency. Power spectra calculated at different spatial points, out of TR-PIV velocity fields acquired in a cross-stream plane (xy), is depicted in Figure 3.1. The dominant frequency has the same value everywhere in the flow, $\text{St} = fL/U_0 = 1.04$ ($f = 19.7$ Hz). Only the amplitude of the peak actually varies in space. In fact, this feature is common to any frequency in the spectrum. It confirms that the flow organisation persists along the entire length of the cavity shear layer and inside the cavity. That signature of a globally unstable flow is characteristic of self-sustained oscillations (Rockwell and Knisely, 1979; Basley et al., 2011). PSDs can also be integrated in space to improve statistics. This is done for instance in Figures 4.9 & 4.20.

Computation parameters

Laser Doppler velocimetry (LDV): local measurements performed during the experimental campaign in the wind-tunnel at LIMSI have been used for studying the parametric evolution of the spectral signature of the flow. Acquisitions typically last for about 5 minutes with a sampling frequency of 2 kHz. Segments of approximately 10 s in order to get a frequency step of $\delta f \simeq 0.1$ Hz, with a 90 %-overlap. This leads to about 310 samples available for *Welch*-averaging. As a result, the 99 %-confidence interval is $[-0.62 \ 0.66]$ dB. Note that confidence intervals are computed using χ^2 -distributions of probability.

Time resolved Particle Image Velocimetry (TR-PIV): performed in a cross-stream plane (xy). The sampling frequency was $f_s = 250$ Hz, which fully satisfies the Shannon-Nyquist criterion. Length of TR-PIV recordings varies accordingly to the cavity aspect ratio L/D . Indeed, since the size of the dataset was limited by camera on-board memory, a greater L/D would imply larger images and therefore a smaller number of available snapshots. Hence, recordings last from $T = 16.4$ s for the $L/D = 2.0$ geometry to $T = 21.0$ s for $L/D = 1.5$ geometry. Without window averaging, the frequency step for Fourier transforms is $0.048 \text{ Hz} \lesssim \delta f \lesssim 0.061 \text{ Hz}$. For power spectral densities, computation windows represent half the acquisition time. The frequency step becomes $0.095 \text{ Hz} \lesssim \delta f \lesssim 0.122 \text{ Hz}$. Segments are overlapped at 95%. Furthermore, typically 15 statistically independent recordings were performed, which provides 300 windows and a 99 %-confidence interval of $[-0.63 \ 0.67]$ dB.

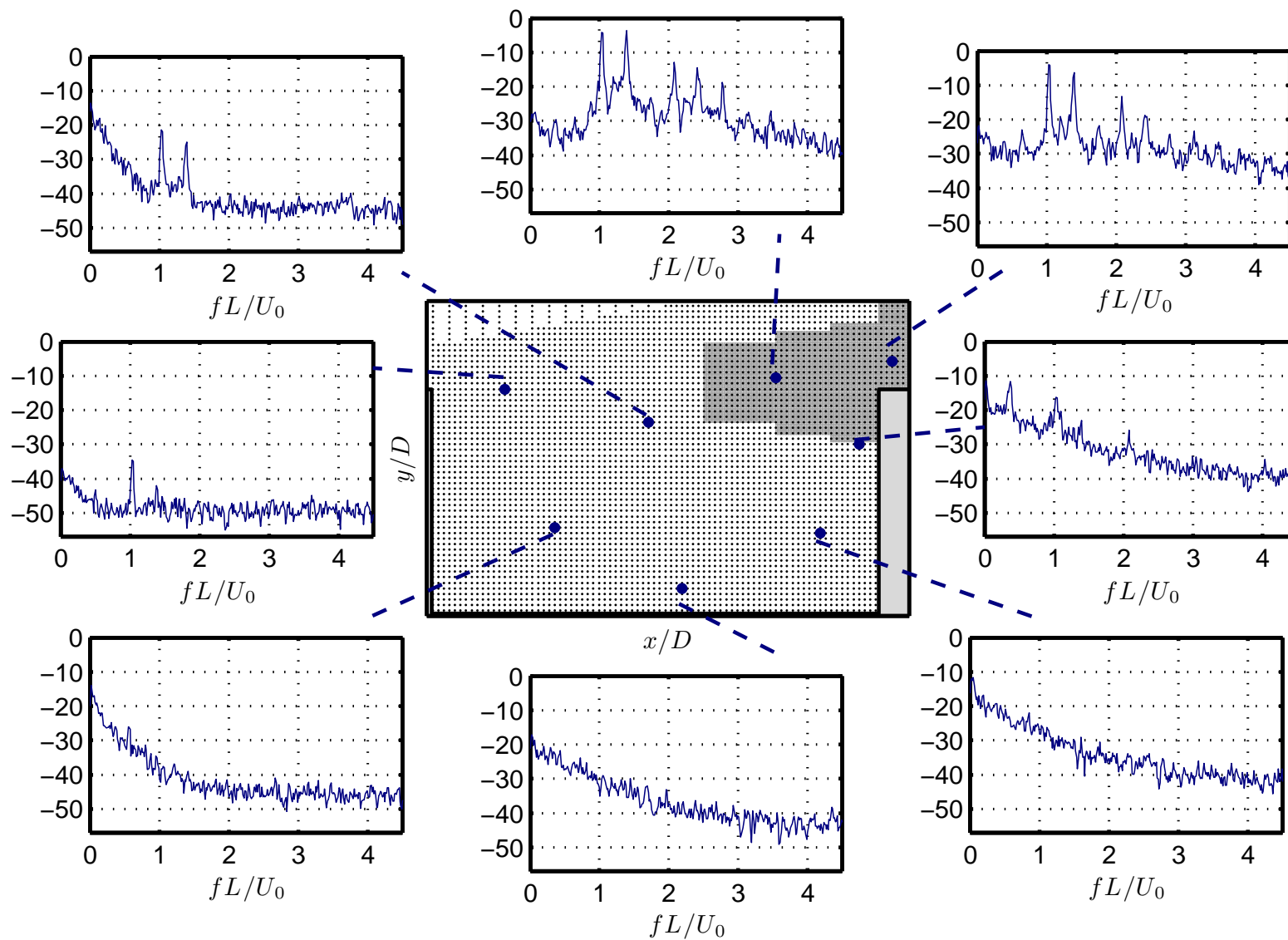


Figure 3.1: Normalised power spectral densities, in dB at various locations of the cross-stream (xy) velocity field, for $L/D = 2.0$, $\text{Re}_L = 12670$ ($U_0 = 1.89$ m/s). Contributions of both velocity fluctuations u' et v' are summed up. Extraction points every 7×7 pixels (dots) and full resolution near the impingement (grey region).

3.1.3 Transfer Functions

Cross-correlation

Time resolved space-extended datasets also make it possible to use spectral analysis time cross-correlation between distant locations in the flow. As an application, the forthcoming procedure was implemented with the aim of getting the shear layer *wave properties* in Chapter 4. Considering two points along the direction of propagation of the wave, at x_u (upstream position) and x_d (downstream position), respectively, $\Delta x = x_d - x_u$ apart, the *transfer function* $T_{ud}(\omega)$ between the two points can be determined for any frequency $f = \omega/(2\pi)$.

A good estimate for this transfer function, between an input signal $v_u(t)$ (velocity at point x_u) and an output signal $v_d(t)$ (velocity at point x_d), can be defined as:

$$T_{ud}(\omega) = \frac{P_{du}(\omega)}{P_{uu}(\omega)} \quad (3.18)$$

where $P_{du}(\omega)$ is the cross spectral distribution between signals v_d and v_u :

$$P_{du}(\omega) = \sum_{m=-\infty}^{+\infty} R_{du}(m) \exp(-i\omega m), \quad (3.19)$$

which involves the cross-correlation function R_{du} :

$$R_{du}(\tau) = \mathbf{E}[v_d(t + \tau)v_u^*(t)] = \mathbf{E}[v_d(t)v_u^*(t - \tau)] \quad (3.20)$$

where the considered correlation period is $\tau = 1/f$, and a^* the conjugate transpose of a . In the case of an equally sampled signal, the expectation $\mathbf{E}[\cdot \cdot \cdot]$ of the function under brackets can simply reduce to the time average operator (Rockwell, 1983). Then it comes

$$T_{ud}(\omega) = G(\omega) \cdot \exp(i\phi(\omega)), \quad (3.21)$$

The transfer function T_{ud} , with gain G and phase shift ϕ , must be used with some care. Indeed, at frequencies $f = \omega/(2\pi)$ where the spectral density is vanishing, that is, when $P_{uu}(\omega) \rightarrow 0$ in Eq. (3.18), the quantity $T_{ud}(\omega)$ is not well defined and only frequencies that significantly contribute to the spectrum should be considered.

It must be noted that this method has been described in the continuous case for the sake of clarity. It applies to discrete signals the same as power spectral densities seen in Section 3.1.2.

$$\left\{ \begin{array}{l} v_{uj} = v_u(j\delta t) \\ v_{dj} = v_d(j\delta t) \end{array} \right\} \quad \text{with } j = 0, 1, 2, \dots \quad (3.22)$$

Estimation of wave properties

The aim is now to obtain the properties of a travelling wave under study. By estimating the transfer function between a *reference* point and measurements acquired at various locations widely distributed along the direction of propagation of the wave, one can build the function

$$T(x, \omega) = G(x, \omega) \cdot \exp(i\phi(x, \omega)), \quad (3.23)$$

with x the coordinate along the direction of propagation of the wave and x_0 the reference point where the transfer function is identically initialised:

$$\forall \omega, \quad T(x_0, \omega) = 1, \quad \phi(x_0, \omega) = 0, \quad G(x_0, \omega) = 1. \quad (3.24)$$

Therefore, $T(x, \omega)$ yields the gain $G(x, \omega)$ and the phase $\phi(x, \omega)$ as functions of the position x and corresponding to the frequency $f = \omega/2\pi$, as long as the cross spectral distribution $P(x, \omega)$ is large enough, as mentioned earlier.

In Chapter 4, transfer functions are used to estimate the wave properties of the locked-on modes in the shear layer. The variable under investigation is the crosswise component of velocity fluctuations $v'(x, t)$ observed along the axis of the shear layer. The reference point is set to $x_0 = L/2$ (cavity mid-length). From the estimation of the phase $\phi(x, \omega)$ comes the associated wavelength Λ . Space-shift Δx matches with wavelength when the phase difference $\Delta\phi = 2\pi$, which occurs for:

$$\Lambda(\omega) = \frac{2\pi}{\left(\frac{\partial\phi}{\partial x}\right)_{\text{mean}}} \quad (3.25)$$

Moreover, the phase velocity C of the wave writes as

$$C(\omega) = \frac{\omega}{\left(\frac{\partial\phi}{\partial x}\right)_{\text{mean}}} \quad (3.26)$$

Gain of the transfer functions distributed along the shear layer gives access to an estimation of spatial growth $\zeta(x, \omega)$ of the propagating wave.

$$\zeta(x, \omega) = \left(\frac{\partial \ln |G(x, \omega)|}{\partial x} \right) \quad (3.27)$$

3.1.4 The Global Fourier Modes

Before dealing with the particular case of the *global Fourier decomposition*, let us introduce the general scope of the modal decomposition of a multi-dimensional dataset.

Modal decomposition of a multidimensional system

Consider a \mathcal{D} -dimensional system

$$v(x_1, x_2, \dots, x_{\mathcal{D}}) \quad (3.28)$$

evolving in the domain $(\mathbf{e}_1, \mathbf{e}_2, \dots, \mathbf{e}_{\mathcal{D}})$.

One can define a modal decomposition along the dimension \mathbf{e}_1 as an operator which projects the dynamics on a set of *basis vectors* (or *functions*) $\Upsilon_k(x_1)$, where $k \in [0, 1, 2, \dots, N-1]$ with N the dimension of the basis. The resulting projections or *modes*, associated with Υ_k are contained in the subdomain $(\mathbf{e}_2, \dots, \mathbf{e}_{\mathcal{D}})$ such that

$$\mu_k(x_2, \dots, x_{\mathcal{D}}) = \langle v \mid \Upsilon_k(x_1) \rangle \quad (3.29)$$

where $\langle a \mid b \rangle$ is the scalar product such that

$$\langle a \mid b \rangle = \int_{x_1} a b^* dx_1 \quad (3.30)$$

Physically, the modal decomposition has identified the x_1 -scales in the basis $\{\mathcal{T}_k\}$ and separated them from the rest of the dynamics, which ends up contained in the set of associated modes μ_k .

The case of Fourier functions

In the case of Fourier decomposition, functions \mathcal{T}_k become complex sinusoidal functions writing as follow:

$$\Psi_k(x_1) = \exp(2i\pi x_1 k/N) \quad (3.31)$$

with $i^2 = -1$. The mode μ_k is hence defined as

$$\mu_k(x_2, \dots, x_{\mathcal{D}}) = \langle v \mid \Psi_k(x_1) \rangle \quad (3.32)$$

$$\mu_k(x_2, \dots, x_{\mathcal{D}}) = \int_{x_1} v(x_1, x_2, \dots, x_{\mathcal{D}}) \exp(-2i\pi x_1 k/N) dx_1 \quad (3.33)$$

In practice, global Fourier decomposition is applied to a discrete dataset $v(x_1, x_2, \dots, x_{\mathcal{D}})$, such that $x_{1j} = x_1(j\delta x_1)$, with $j = 0, 1, 2, \dots, N - 1$ and N the size of the dataset in the \mathbf{e}_1 direction. This implies the functions Ψ_k now write as in Expression 3.5

$$\Psi_{jk} = \exp(2i\pi \frac{jk}{N}),$$

and the scalar product logically becomes

$$\langle a \mid b \rangle = \sum_j a_j b_j^*. \quad (3.34)$$

Hence, the discrete extended Fourier modes are expressed as

$$\mu_k(x_2, \dots, x_{\mathcal{D}}) = \sum_j v(j\delta x_1, x_2, \dots, x_{\mathcal{D}}) \exp(-2i\pi \frac{jk}{N}) \quad (3.35)$$

When applied to spatially extended time-resolved velocity fields, the *global* time Fourier decomposition provides a set of spatial structures (or *global Fourier mode*), each of them associated with one temporal frequency (see Rowley et al. (2002); Basley et al. (2011)).

Figure 3.1 displays the distribution of locations where time-series are extracted across the entire velocity field, in a cross-stream plane (xy), acquired during the high-framerate PIV campaign at LIMSI. An example of global Fourier mode computed from vorticity fluctuations ω'_z is provided in Figure 3.2. It is associated with the dominant frequency $f_a = 19.7$ Hz ($St = f_a L/U_0 = 1.04$), in the case $L/D = 2.0$, $U_0 = 1.89$ m/s.

Remark that only the tip of the peak is selected for describing the spatial dynamics. One could argue that it appears more relevant to take into account the whole peak to reconstruct a spatial mode. This has been notably realised by Duriez (2009) for the spectral decomposition of a flow past a descending ramp. Presently, tests using such a methodology have been carried out and the physics depicted by the reconstructed field is obviously very similar to the global Fourier mode associated with the dominant frequency alone. However the signal over noise ratio is clearly decreased, which leads to a loss of information regarding the second order structures. Consequently, the spatial structures shown in the forthcoming analyses (in Chapter 4 and 5) are obtained using the tip of the peak under consideration.

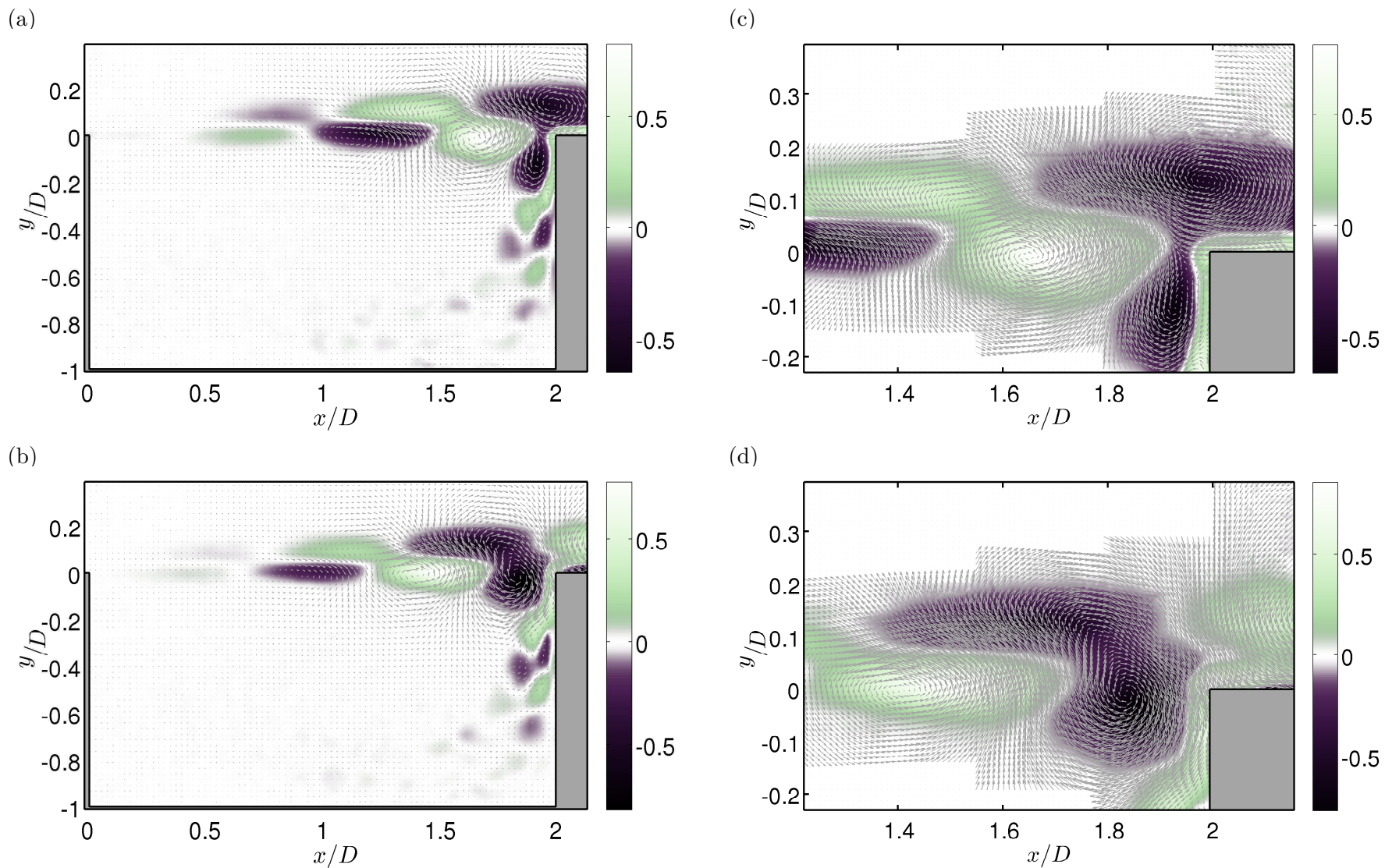


Figure 3.2: Global Fourier mode associated with $f_a = 19.7$ Hz in the case $L/D = 2.0$ & $Re_L = 12670$ ($U_0 = 1.89$ m/s). Real part (top) and imaginary part (bottom) are displayed both in overview (from dots in Figure 3.1) and close-up at the impingement (grey part in Figure 3.1). Colours encode vorticity and vector fields represent velocity.

Successive modal decompositions

One may finally note that Fourier decomposition can be applied in turn to the newly obtained $\mu_k(x_2, \dots, x_D)$ along another direction, for instance e_2 in order to continue with the separation of x_2 -scales.

As an example, the 2D-Fourier transforms are commonly used in image processing: an image represented by the matrix A_{ij} can be processed into spectral space (k_i, k_j) through the double operation $\mathcal{F}^i\{\mathcal{F}^j\{A\}\}$.

In this thesis, successive Fourier transform is performed in Section 5.4 for datasets such as $S_{5.4} = v(t, z, x)$, with a time-Fourier decomposition first ($x_1 = t$) and then a spanwise Fourier decomposition ($x_2 = z$).

3.1.5 Motivations for another approach

The analysis carried out in Chapter 5 deals with centrifugal instabilities arising in the inner-flow. Different spanwise waves are at play therein, simultaneously or successively, spanning the entire cavity or restricting only to a limited region of the inner-flow. The properties of these waves may change drastically. In particular, the spanwise waves can be strongly modulated in space. Applying space Fourier transform to those data is useful but only provides statistic (integrated) information since it relies on a scalar product. On the other hand, estimating locally the wave properties of such a signal would give more detail regarding the spanwise location of the identified coherent structures. In that context, the Hilbert-Huang Transform could be of great help.

3.2 The Hilbert-Huang Transform

The *Hilbert-Huang Transform* (HHT) was developed by N. E. Huang (Huang et al., 1998, 1999) to describe more precisely the nonlinear distorted signals implied by water waves and other non-permanent systems (Huang et al., 1996). Indeed, on top of amplitude modulations related to multi-scale dynamics, nonlinearly saturated waves also yield intrinsic frequency modulations. In other words the instantaneous frequency varies within one period of oscillation. Instead of a deterministic linear operator, such as the Fourier transform, the Hilbert-Huang transform provides a data-based set of modes without any *a priori* model. More specifically, HHT consists in applying the *Hilbert transform* on oscillatory components extracted beforehand from the flow by means of the *Empirical Mode Decomposition* (EMD). A very detailed discussion can be found in Huang et al. (1998). The present section only aims to provide the reader with the basic principle of that methodology, in order to prepare the analysis that is to come in Chapter 5. First, the Hilbert transform is briefly recalled, as well as the distinctive properties of an analytic signal. Then, Section 3.2.3 is concerned with the EMD method.

3.2.1 The Hilbert transform

The Hilbert-Huang transform partly relies on the application of Hilbert transform to obtain the local estimations of the phase and amplitude. The Hilbert transform enables building an *analytic signal* from real data by providing an imaginary part in quadrature of phase relatively

to this input signal. Formally, the Hilbert transform of the 1D-signal $v(t) \in \mathbb{R}$ writes

$$\mathcal{H}^t\{v(t)\} = \mathcal{H}_v^t = \frac{1}{\pi t} * v(t) \quad (3.36)$$

with $a * b$ the convolution product of a and b . Another way of describing the Hilbert transform is obtained through the spectral space and Fourier transform:

$$\mathcal{F}^t\{\mathcal{H}_v^t\} = -i \operatorname{sign}(\omega) \mathcal{F}^t\{v\} \quad (3.37)$$

with \mathcal{F}^t the Fourier transform in time, and $\operatorname{sign}(x)$ the function equal to $+1$ when $x > 0$, -1 when $x < 0$ and 0 when $x = 0$. Physically, one remarks the positive part of the signal spectrum is multiplied $-i = \exp(-i\pi/2)$, that is rotated by $-\pi/2$, while its negative part is multiplied by $i = \exp(i\pi/2)$, thus rotated by $\pi/2$.

3.2.2 Instantaneous/local properties of an analytic signal

The analytic signal $\tilde{v}(t)$ can be build as follow

$$\tilde{v}(t) = v(t) + i\mathcal{H}_v^t(t) = \mathcal{A}(t) \exp(i\Phi(t)) \quad (3.38)$$

with the *instantaneous amplitude* of the analytic signal \tilde{v}

$$\mathcal{A}(t) = \sqrt{(v)^2 + (\mathcal{H}_v^t)^2} \quad (3.39)$$

and its phase

$$\Phi(t) = \arctan\left(\frac{\mathcal{H}_v^t}{v}\right). \quad (3.40)$$

From the phase gradient can be calculated the *instantaneous angular frequency* ω

$$\omega(t) = \frac{\partial\Phi}{\partial t}. \quad (3.41)$$

Note that if one considers a signal $s(z)$, evolving in space along the axis (z), the angular frequency logically becomes the *local wavenumber*

$$k(z) = \frac{\partial\Phi}{\partial z}. \quad (3.42)$$

Obtaining such instantaneous/local properties is obviously quite appealing. However, the notion of instantaneous or local frequency is highly controversial as explained in Huang et al. (1998). In general, it requires some limitations for the data to which the Hilbert transform is applied. One considers an estimation of the local frequency as valid if the signal is narrow-banded and such that any given local extremum is followed by a zero-crossing before another extremum is reached. In other words, the signal must not yield a non-zero mean: it has to be a pure oscillatory function. Not satisfying these conditions leads to paradoxes: multiple frequencies can be defined simultaneously because of riding waves.

In order to overcome such an issue, one has often recourse to narrow-band filtering, as in Pastur et al. (2008). The signal is filtered around one considered frequency. Unfortunately, filtering

causes distortion by stripping the waves of their harmonics. Another strategy is available with the Empirical Mode Decomposition.

3.2.3 The Empirical Mode Decomposition

The Empirical Mode Decomposition (EMD) has been developed to provide suitable oscillatory functions out of the data in order to perform the Hilbert transform. Therefore, it is aimed to be applied to 1D-datasets, such as time-series or, as seen in the following, space arrays, extending along one direction of the reference frame.

The originality of EMD comes from its *a posteriori*-defined basis. The decomposition relies entirely and directly on the data, without any pre-requirement for the modes resulting from the process. In fact, one only assumes that the data can be decomposed into a set of simple oscillatory modes, called *Intrinsic Mode Functions* (IMF).

On the Intrinsic Mode Functions

An intrinsic mode function corresponds to oscillations, non-necessarily sinusoidal, which may yield various length scales and amplitudes but are such that the local mean is always null. One can thus appreciate that such an oscillatory function would meet the requirements for the application of Hilbert Transform.

How can we obtain an IMF?

To begin with, it is important to specify what a length scale is. The aim here is to use the most basic definition, free from any *a priori* model, such as Fourier decomposition relying upon sinusoidal functions. Consequently, we simply consider a characteristic length scale as the lapse between two successive local extrema. Using that definition, it comes that an intrinsic mode function should verify the following:

- (i) all local maxima are positive and all local minima are negative,
- (ii) the mean value of *top* and *bottom envelopes* tends to zero at any given time (position).

In order to extract such intrinsic mode functions out of the data, Empirical Mode Decomposition is based on an iterative/recursive procedure called *sifting process* and detailed in next section.

The sifting process

In principle, Intrinsic Mode Functions are obtained by subtracting from data a *running average* defined as the local mean value of the envelopes of the signal. Applying recursively the same process, that running average eventually tends to zero, with oscillations ending up properly centred.

The first issue concerns the construction of top and bottom envelopes at each step of the recursive process. Consider a sample dataset evolving in the z direction, $s(z)$. To be consistent with the above-stated definition of space scales, it is reasonable to define the top and bottom envelopes e_{max} and e_{min} as the “*neutral*” curves passing through the maxima and embracing the whole data between them. The term *neutral* means that an envelope should not bring more scales. In other words, it must not yield more local extrema than the underlying data $s(z)$.

Formally, this writes

$$\begin{cases} e_{max}(z) \geq s(z), \forall z & \& e_{max}(z) = s(z) \text{ if } \frac{ds}{dz} = 0, \frac{d^2s}{dz^2} < 0 & \& \mathcal{N}_{ext}[e_{max}] \leq \mathcal{N}_{ext}[s] \\ e_{min}(z) \leq s(z), \forall z & \& e_{min}(z) = s(z) \text{ if } \frac{ds}{dz} = 0, \frac{d^2s}{dz^2} > 0 & \& \mathcal{N}_{ext}[e_{min}] \leq \mathcal{N}_{ext}[s] \end{cases} \quad (3.43)$$

where $\mathcal{N}_{ext}[f(z)]$ is the number of local extrema of the function $f(z)$.

In practice, the envelope e_{max} (resp. e_{min}) is built from the maxima (resp. minima) only, connecting those points by means of an interpolation. Of course, extensive research on the construction and optimisation of the envelopes has been ongoing for years, in particular regarding the edge effects. A basic *cubic spline interpolation* is yet usually used for it has revealed quite satisfying results with a simple implementation. It is not without shortcoming, but the iterative process described below is actually robust enough to overcome the defects of the estimated envelopes.

Once the envelopes have been obtained, their expression of the running average to subtract is straightforward, for it corresponds to the mean value

$$m(z) = \frac{e_{max}(z) + e_{min}(z)}{2} \quad (3.44)$$

An example of signal $s(z/D)$ enclosed by the two envelopes, along with its resulting running average, is plotted in Figure 3.3.

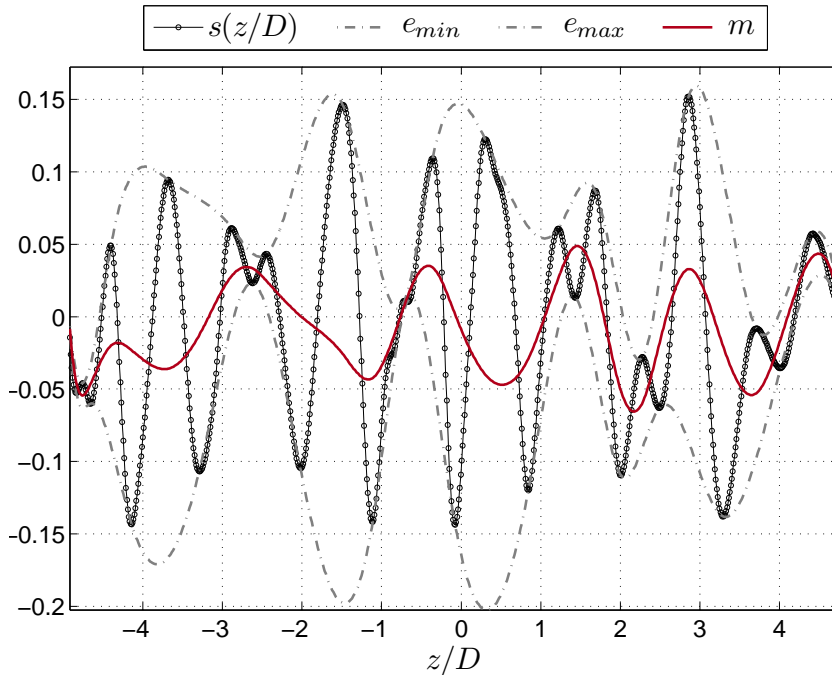


Figure 3.3: A given signal $s(z/D)$ enclosed by the two envelopes e_{min} and e_{max} . Its running average is defined as $m = (e_{min} + e_{max})/2$. The space coordinate z is non-dimensionalised by the length scale D .

The first Intrinsic Mode Function $IMF_1(z)$ is obtained after a recursive process bringing into play the variable functions $p_1(z)$, named *proto-IMF*, and $m_1(z)$ the running average. The

recursion starts with initialising the variables $p_{1,0}$ and $m_{1,0}$ ($i = 0$) with the data, as shown in Expression 3.45.

$$\begin{cases} p_{1,0} &= s(z) \\ m_{1,0} &= (e_{max,0} + e_{min,0}) / 2 \end{cases} \quad (3.45)$$

Note that $m_{1,0}$ is the running average of the signal $s(z)$, using the envelopes $e_{max,0}$ and $e_{min,0}$, constructed so as to fulfil the conditions in Expression 3.43 and Figure 3.3. Then, $m_{1,0}$ is subtracted to provide the first proto-IMF $p_{1,1}$, and a new running average can be obtained:

$$\begin{cases} p_{1,1} &= p_{1,0} - m_{1,0} \\ m_{1,1} &= (e_{max,1} + e_{min,1}) / 2 \end{cases} \quad (3.46)$$

The same operation is repeated recursively as follow:

$$\begin{cases} p_{1,i} &= p_{1,i-1} - m_{1,i-1} \\ m_{1,i} &= (e_{max,i} + e_{min,i}) / 2 \end{cases} \quad (3.47)$$

where $p_{1,i}$ and $m_{1,i}$ are the proto-IMF and running average at the i^{th} iteration. The envelopes $e_{max,i}$ and $e_{min,i}$ are based on the proto-IMF $p_{1,i}$. Ultimately, one converges towards the first intrinsic mode function IMF_1 , such that

$$\text{IMF}_1 = p_{1,n_1-1} - m_{1,n_1-1} \quad (3.48)$$

with n_1 the number of iterations required for convergence. The stoppage criterion is obviously a crucial point in the EMD. It will be further discussed in Section (*Stoppage criteria*).

As an example of data to be processed by Hilbert-Huang transform, we consider a randomly picked-up span array out of PIV data obtained during the LTRAC campaign. More specifically, the data signal $s(z)$ becomes the normalised fluctuating vorticity $\omega'_y D/U_0$, extracted from a zx -plane ($y_{piv}/D = -0.1$) at the streamwise coordinate $x_e/D = 1.86$ out of a single snapshot, with the control parameters $\text{Re}_D = 2400$, $D/\theta_0 = 29.4$.

The sifting process for the first Intrinsic Mode Function IMF_1 is illustrated in Figure 3.4. The number of iterations before convergence is $n_1 = 10$. One remarks that this first IMF concentrates the smallest space scales measured in the span array.

Successive Intrinsic Mode functions

Now that the smallest scales of the dataset have been, the empirical mode decomposition can go on after removing the first IMF from the data:

$$r_1 = s(z) - \text{IMF}_1 = p_{1,0} - \text{IMF}_1 \quad (3.49)$$

The residue r_1 (orange curve in Figure 3.4) is used as new dataset from which the sifting process for the second mode, IMF_2 , is carried out. The proto-IMFs $p_{2,i}$ lead to IMF_2 using a recursive

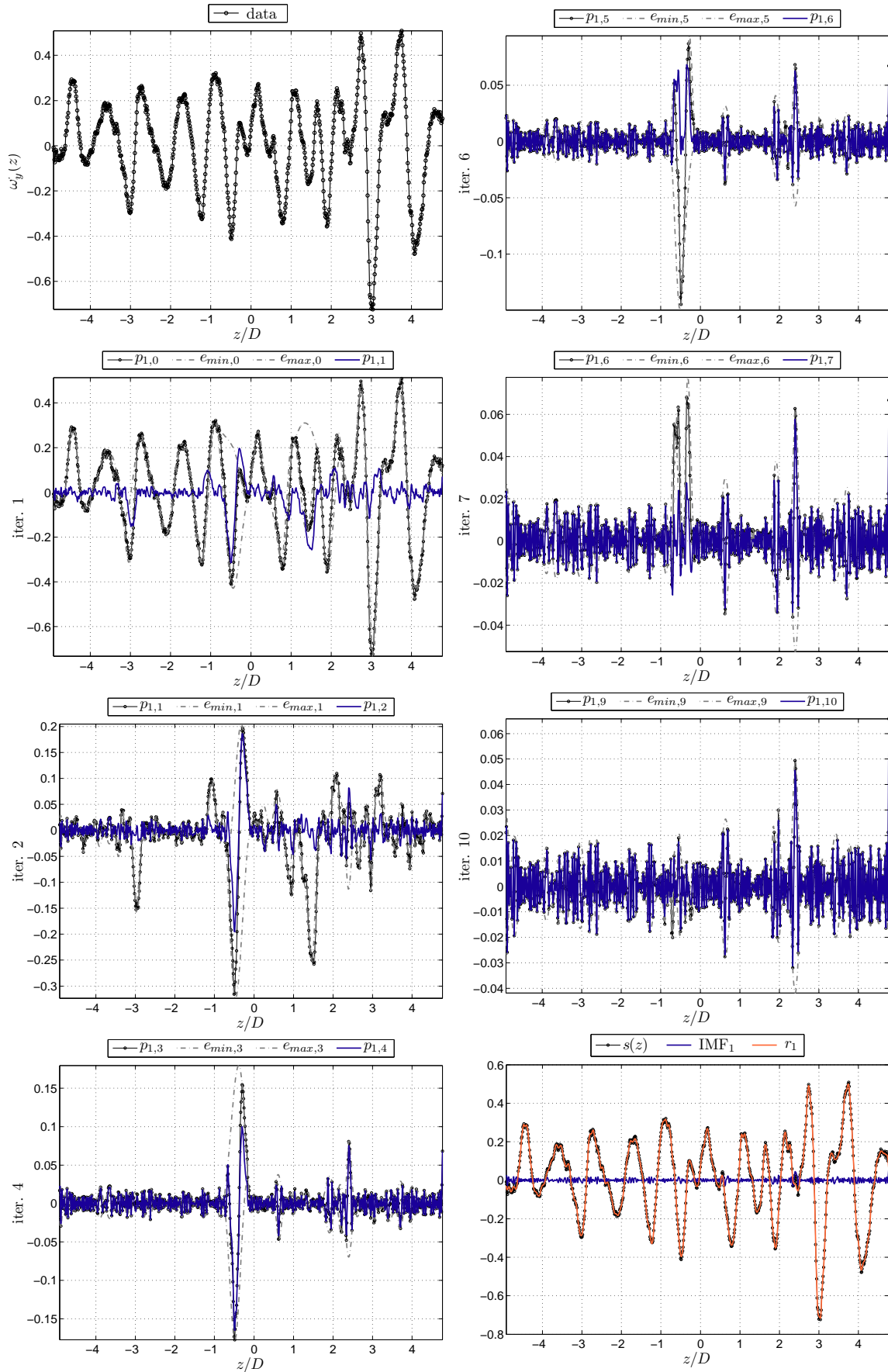


Figure 3.4: Sifting process for the first Intrinsic Mode Function, IMF_1 , extracted from a span array of normalised fluctuating vorticity $s(z) = \omega'_y(z, x_e, t_e)D/U_0$, randomly picked-up in the dataset $Re_D = 2400$, $D/\theta_0 = 29.4$ (at the streamwise position $x_e/D = 1.86$ of a given snapshot).

relation similar to Equation 3.47 – as seen in Figure 3.5.

$$\text{IMF}_2 = p_{2,n_2-1} - m_{2,n_2-1} \quad (3.50)$$

Obtained after $n_2 = 7$ iterations, the second IMF still exhibits low-energy small scales along the main part of the span but several more energetic *bursts* arise. They are composed of a few oscillations yielding larger wavelengths and larger amplitudes than the rest of the mode. Similarly to Equation 3.49, the second residue can be obtained:

$$r_2 = r_1 - \text{IMF}_2 \quad (3.51)$$

The decomposition continues the same way: with each new IMF_j , the signal is stripped of larger scales, resulting in a residue r_j ; each step j implies a sifting process which consists in recursive iterations $i = 1, 2, \dots, n_j$ providing proto-IMFs $p_{j,i}$ until converging to IMF_j . That double-recursion can be written as

$$\left\{ \begin{array}{l} p_{j,0} = r_{j-1} \\ \left\{ p_{j,i} = p_{j,i-1} - m_{j,i-1} \right\} \text{ with } i = 1, \dots, n_j \\ \text{IMF}_j = p_{j,n_j-1} - m_{j,n_j-1} \\ r_j = r_{j-1} - \text{IMF}_j \end{array} \right\} \text{ with } j = 1, \dots, N \quad (3.52)$$

Note the residue is initialised to $r_0 = s(z)$.

The Intrinsic Mode Functions IMF_3 to IMF_6 are displayed in Figures 3.6 & 3.7. Physically, note that the length scales are mostly well separated between the different modes and that the highest amplitude is obtained for IMF_3 . Eventually, only remains in the residue r_N a function yielding no length scale. In other words, $r_N(z)$ is either a monotonic or a parabolic function, that is a function with at the most one local extremum.

Completeness

One can wonder if the basis of Intrinsic Mode Functions is complete. This is true if the residue r_N , remaining after all Intrinsic Mode Functions have been extracted, is negligible against the sum of IMFs.

$$s(z) = \sum_{j=1}^N (\text{IMF}_j) + r_N \quad (3.53)$$

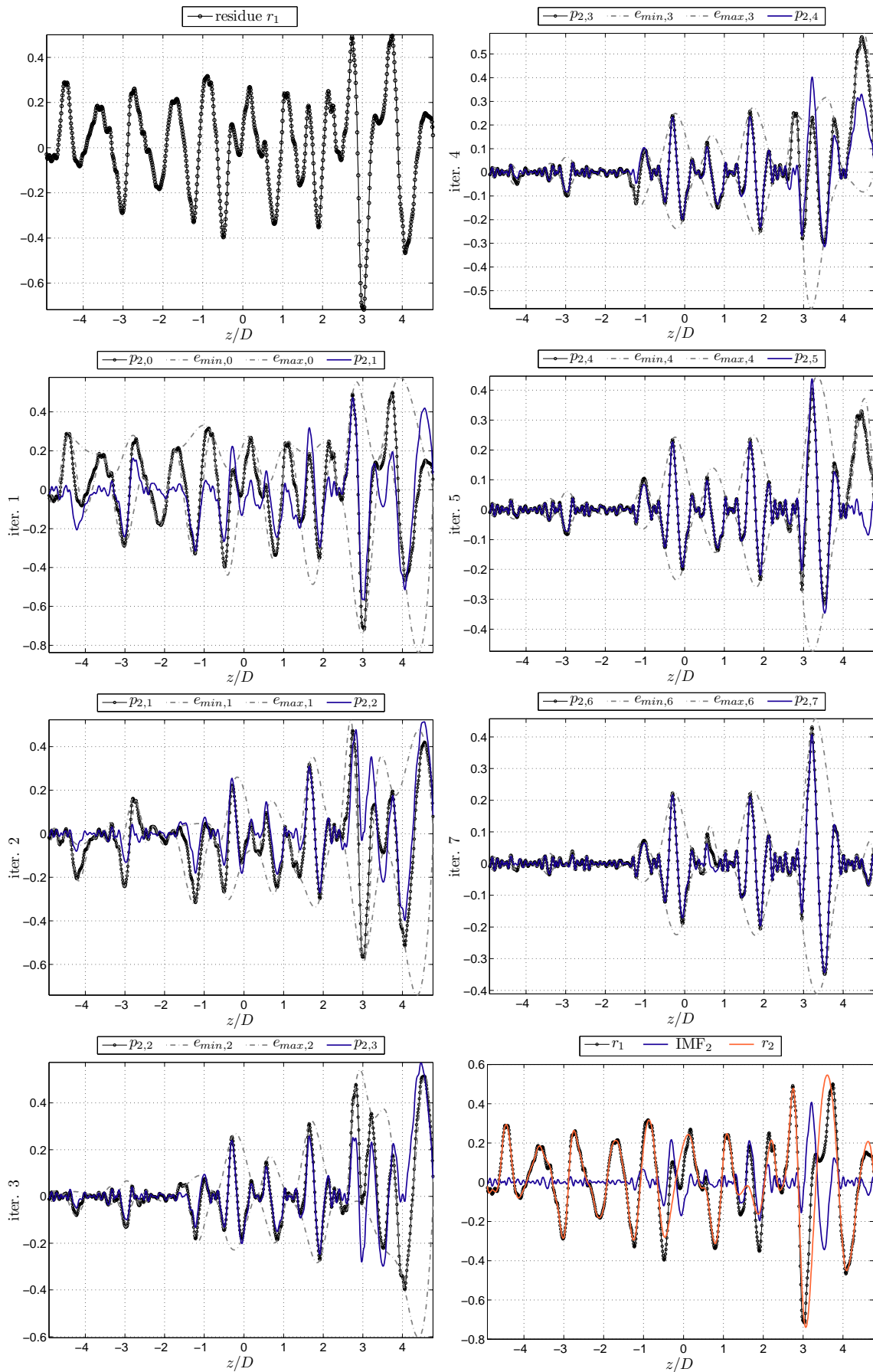


Figure 3.5: Sifting process for the second Intrinsic Mode Function, IMF₂, extracted from the same span array as Figure 3.4.

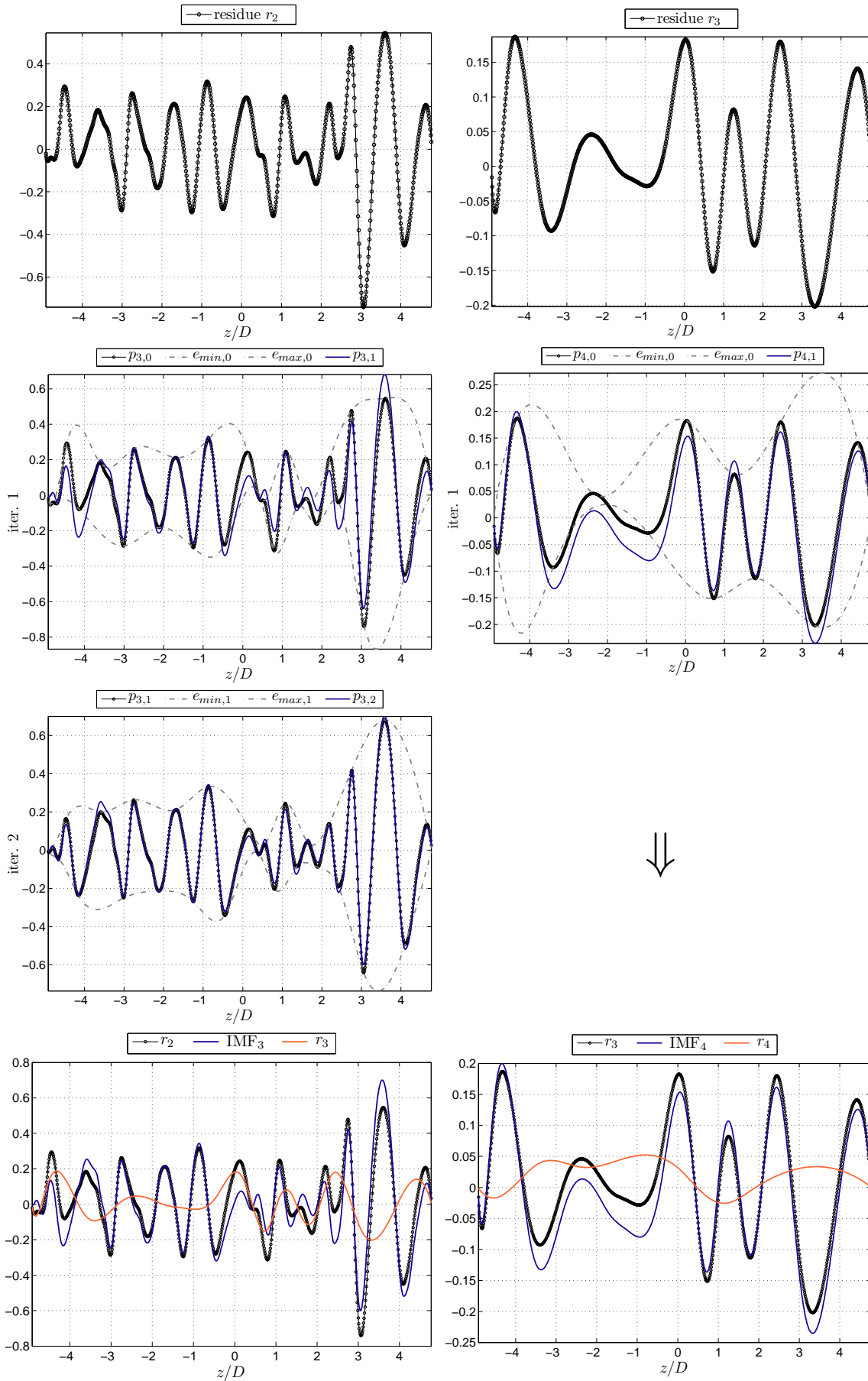


Figure 3.6: Sifting processes for the Intrinsic Mode Functions (left) IMF₃ and (right) IMF₄, extracted from the same span array as Figure 3.4.

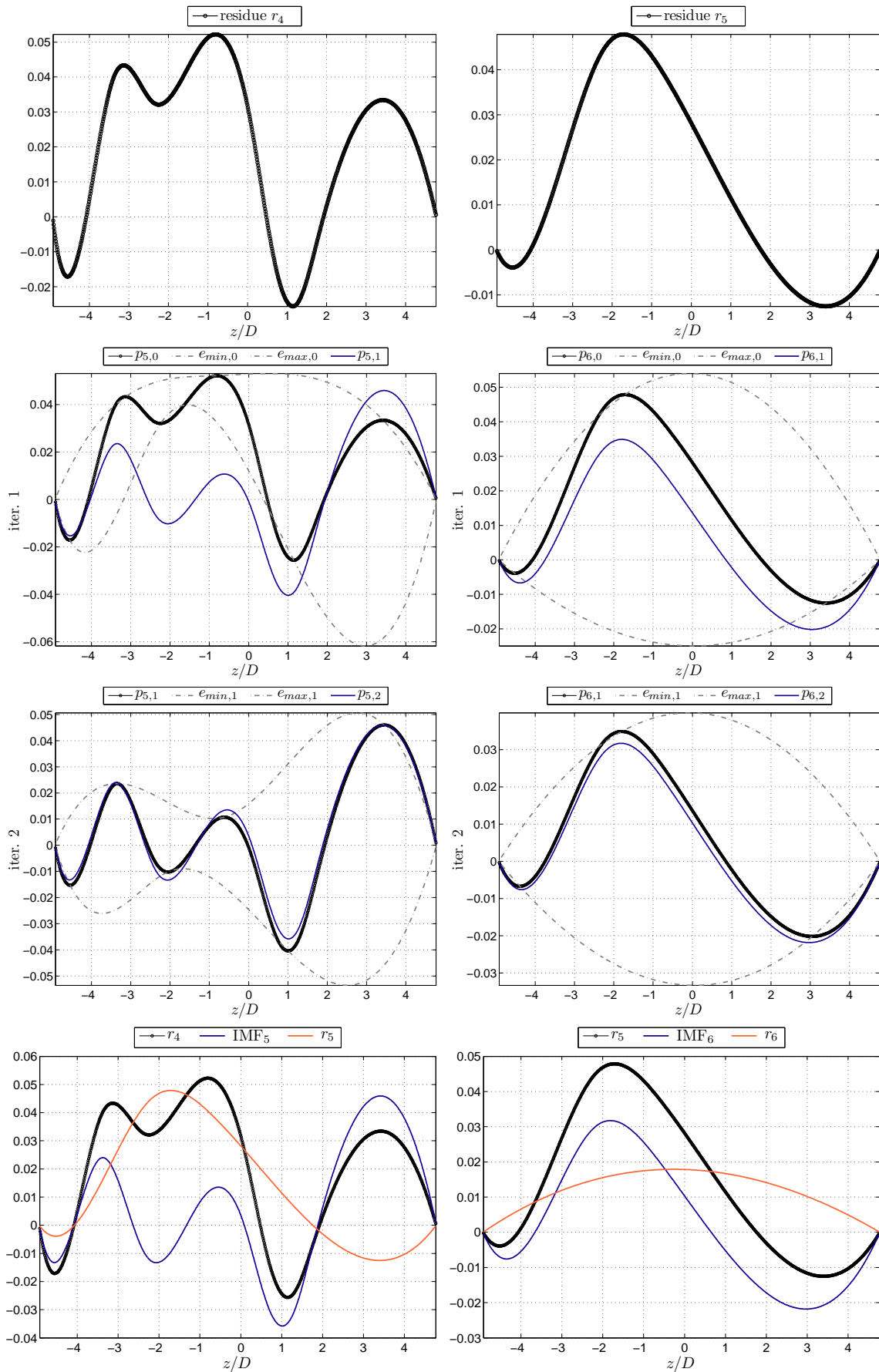


Figure 3.7: Sifting processes for the Intrinsic Mode Functions (left) IMF₅ and (right) IMF₆, extracted from the same span array as Figure 3.4.

Stoppage criteria

The choice of the stoppage criterion for ending the sifting process remains an open issue, subject of many studies, notably in Huang et al. (2003). However, the object here is not to debate about the various available methodologies. As a first approach, the simple criterion proposed by Huang et al. (1998) provided fairly satisfying results.

The sifting process stops if one of the next two conditions is fulfilled:

- (i) The numbers of *zero-crossings* and *local extrema* differ at the most by 1
- (ii) $SD < \alpha_s$ where SD is the normalised *squared difference* between two successive proto-IMFs defined in Equation 3.54 and α_s is an arbitrary threshold.

Considering the Intrinsic Mode Function IMF_j ,

$$SD_i = \frac{\int_z |p_{j,i-1} - p_{j,i}|^2 dz}{\int_z p_{j,i-1}^2 dz} \quad (3.54)$$

The first condition (i) corresponds to the definition of an IMF but in practice, it can reveal too strict to allow convergence by itself, likely because of the cubic spline defects. That is why a second condition (ii) representing the degree of convergence of the sifting process is brought along. In the present work, the threshold was set to

$$\alpha_s = 0.1. \quad (3.55)$$

The code used for that computation is initially based on the open-access code by Alan Tan: (http://www.mathworks.com/matlabcentral/fileexchange/19681-hilbert-huang-transform/all_files)

3.2.4 The Hilbert-Huang Spectrum

The Hilbert Transform can now be applied to IMFs, as described in Section 3.2.1. The resulting analytic signals are plotted in Figure 3.8. Then, local properties of each mode are estimated, as in Section 3.2.2, and the Hilbert-Huang Spectrum \mathcal{HH}^z becomes available. In this case where a single 1D-data array was considered, the Hilbert-Huang spectrum corresponds directly to the distribution $\mathcal{HH}^z(z, k_j)$ weighted by local amplitude $\mathcal{A}_j(z)$ as in Equation 3.39, with $k_j(z)$ the local wavenumber of the mode IMF_j , defined as in Equation 3.42. \mathcal{HH}^z integrates the contributions of all IMFs and is shown in Figure 3.9.

As a result, continuous and precise information on wavenumbers (wavelengths) is available for every extracted mode. This means that multiple length scales are locally defined simultaneously, yet without creating a paradox thanks to the decomposition into Intrinsic Mode Functions.

In addition, by weighting the wavenumbers with their associated amplitudes, one reveals only the relevant information, that is where the phase is properly defined. For instance, the high wavenumbers yielded by the mode IMF_1 were too small to show up on the plot. Similar distributions are used for analysing the data in Chapter 5.

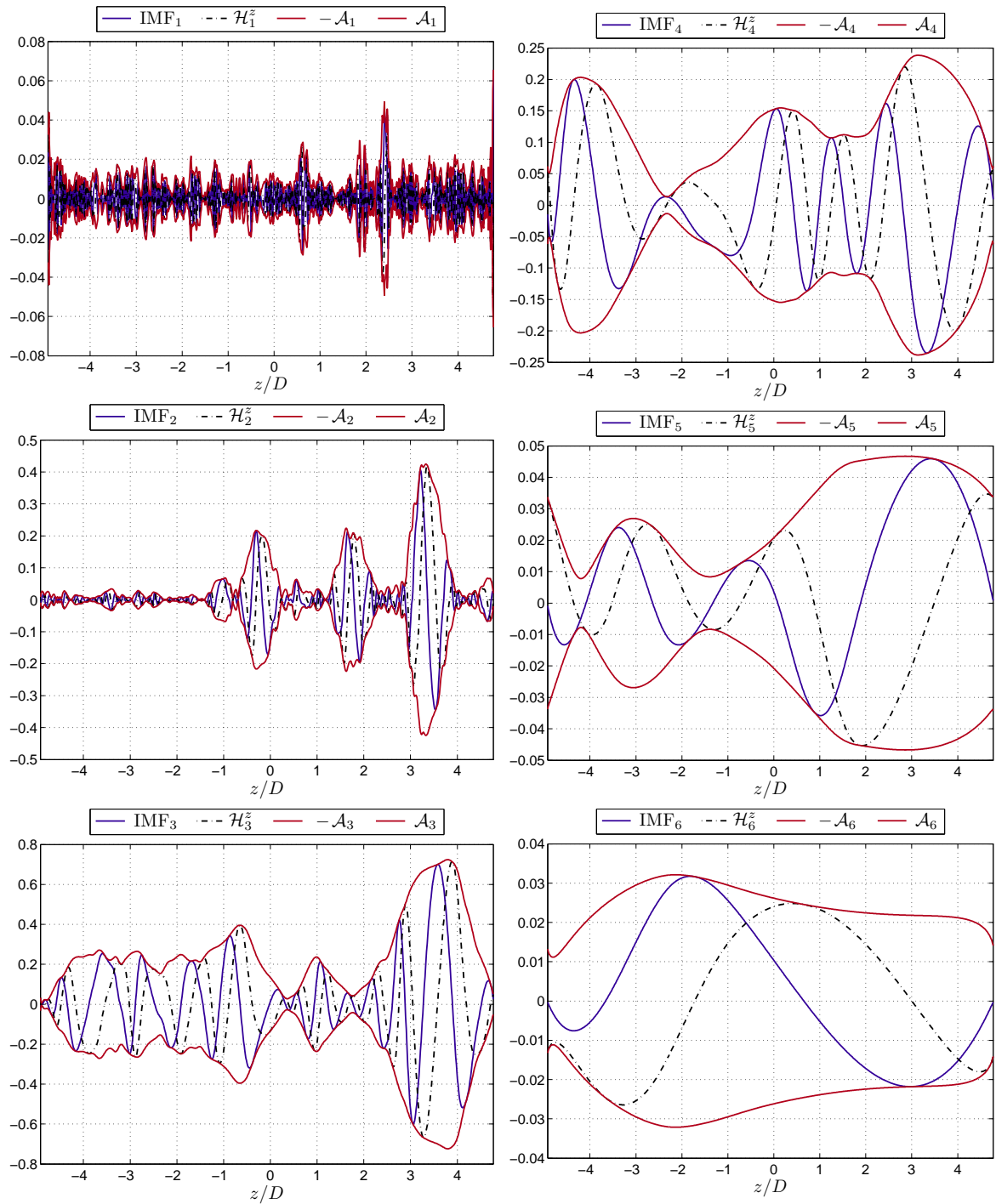


Figure 3.8: Analytic signals produced from Intrinsic Mode Functions IMF_j by means of the Hilbert transform. The resulting envelope (amplitude $\mathcal{A}_j(z)$ of the intrinsic mode) is simply the modulus of the analytic signal (Equation 3.39).

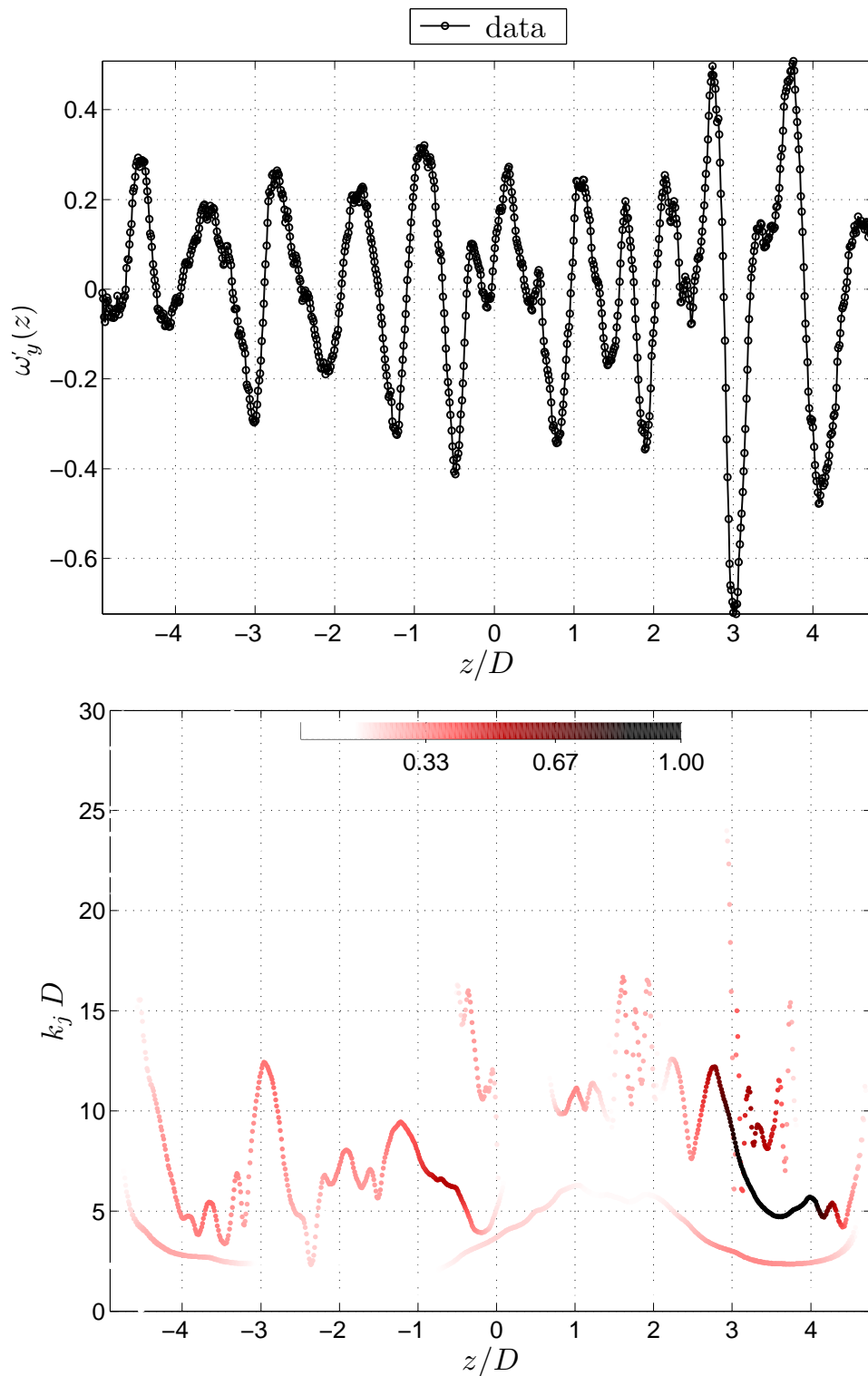


Figure 3.9: Hilbert-Huang Spectrum produced from the set of analytic signals based on Intrinsic Mode Functions IMF_j . Colours encode the local amplitude $\mathcal{A}_j(z)$ associated with the local wavenumber $k_j(z)$. Local amplitude is normalised by its maximum value. The original data series is recalled at top.

Part II

**Open Cavity Flow
Analysis through Space and Time**

Cross-stream dynamics

4.1 Overview and context

Open cavity flows are primarily driven by the (unstable) impinging shear layer, notably responsible for noise generation or structure damage. As described in the review (Section 1.1), from the nested shear layer rise travelling waves enhanced by a pressure feedback-loop to produce self-sustained oscillations or locked-on modes.

At the leading order, the symmetries of the shear layer hence impose a spanwise z -invariance to the flow. Consequently, investigating a cross-stream (xy) plane gives access to the main characteristics of the shear layer impinging onto the trailing edge and to the first order organisation of the inner-flow.

Though the main features of this system have been long studied, analyses have often been limited to locked-on modes and to parametric considerations. Moreover, for decades, studies were based on local measurements (pressure sensors, hotwire, *etc.*) or direct observations (schlieren in the compressible regime, and also streaklines through smoke, dye or bubbles), but nowadays quantitative space-extended time-resolved measurements are available by means of high-speed particle image velocimetry (TR-PIV). Space-time global evolution of the system is thereby available in the saturated regime.

The present work relies on TR-PIV to confirm and complete results from literature. Then, a thorough analysis of coherent structures is performed through space and time modal decomposition. We aim to identify the nonlinear mechanisms responsible for amplitude modulations and mode switching, as well as the complexity induced by interactions between the inner-flow and the shear layer waves.

4.1.1 Preliminary remarks

The results discussed in this chapter are based on time-resolved data, issued from High-frame-rate PIV campaign (LIMSI – ANR-contract *HiSpeedPIV*). Description and characterisation of experimental work can be found in Section 2.1.

As a first approach, smoke visualisations are particularly useful to emphasise the flow dynamics through aesthetically pleasing images. A set of smoke-snapshots are provided in Figure 4.1 for various geometries and incoming velocities. When looking at the entire recordings, it has been noticed that the mixing logically strengthens when incoming velocity or/and cavity length are increased. Part from that, it would be unwise to assert any parametric evolution of the flow by relying only on those pictures. Indeed, aspect of the flow varies a lot depending on relative time to seeding startup. In addition, observations based on streaklines must be considered with caution in an unsteady flow. Streaklines actually cumulate the dynamics in time, which may result in confusing features, such as cellular structures in a shear flow Hama (1962); Williams and Hama (1980).

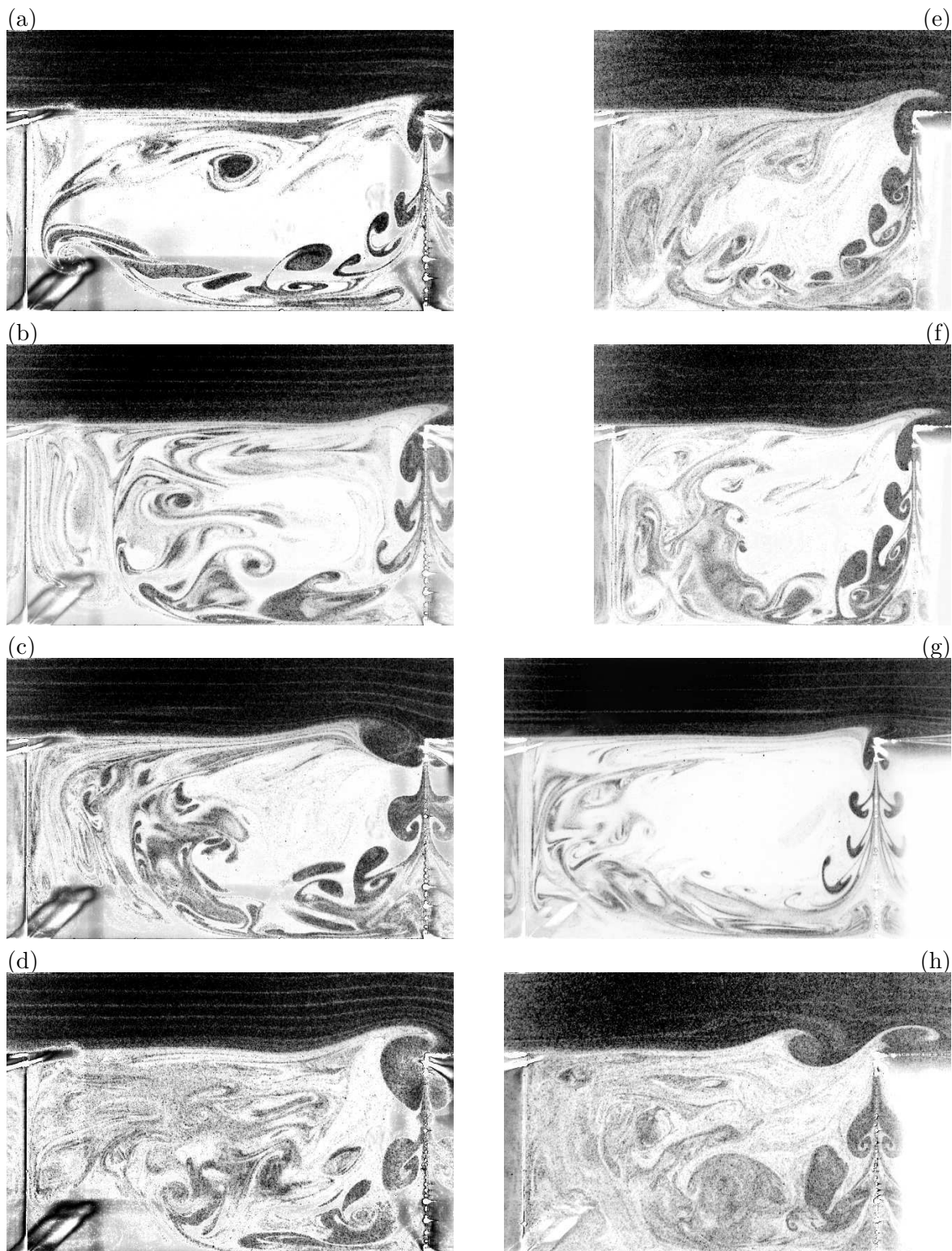


Figure 4.1: Smoke visualisation snapshots extracted from TR-PIV data, in a cross-stream plane (x, y) . On the left-hand side, (a,b), $L/D = 2.0$, $U_0 = 1.1$ m/s; (c), $L/D = 2.0$, $U_0 = 1.4$ m/s; (d), $L/D = 2.0$, $U_0 = 1.9$ m/s. On the right-hand side, (e), $L/D = 1.5$, $U_0 = 2.3$ m/s; (f), $L/D = 1.5$, $U_0 = 2.9$ m/s; (g), $L/D = 1.75$, $U_0 = 1.5$ m/s; (h), $L/D = 1.75$, $U_0 = 2.5$ m/s

Nonetheless, there are many important properties that can be deduced from the pictures in Figure 4.1. In all cases, the shear layer experiences self-sustained oscillations, whose amplitude grows along the top cavity plane. Eventually, nonlinear saturation occurs, as indicated by wave breaking near the impingement. Driven by the outflow, the inside-flow is put into motion, generating a main fluid recirculation inside the cavity, from the trailing edge over about the cavity length. For some shape ratios, a secondary, smaller, counter-rotating vortex forms upstream of the main vortex, close to the backward-facing step.

In addition, the flapping motion induced by shear layer waves generates *mushroom-like* inflows into the cavity. Those inflows travel down the forward-facing step and then, along the main recirculation. The mushroom-like shapes represent the Lagrangian signature of advected vortex pairs, resulting from injected vorticity at the impingement. Inflow strength is directly influenced by the amplitude of the shear layer oscillations. Concerning the incoming flow, parallel streaklines are observed above the shear layer. This is due to the honey comb. When seeding particles hit the honey comb between two cells, seeding density is decreased downstream along the issued streakline. Hence, homogeneous density would only be restored either by diffusion or/and velocity fluctuations. Being able to observe those streaklines 700 mm downstream implies an especially low turbulence rate. In other words, the incoming flow is actually parallel. Inside the cavity, various events are depicted, representing available scenarios for the system. For instance, Figures 4.1.(a,b) are two snapshots extracted from the same recording but they show two different paths for advected vortices inside the cavity. In Figure 4.1.a, inflows travel all the way back upstream to coil themselves up around the secondary vortex. Snapshot shown in Figure 4.1.h exhibits shear layer oscillations of smaller wavelength, which likely corresponds to another mode of self-sustained oscillations.

In order to acquire quantitative results, a high repetition-rate PIV campaign was carried out, as described in Section 2.1. Let us recall that the cartesian coordinate system $(\mathbf{e}_x, \mathbf{e}_y, \mathbf{e}_z)$ is set mid-span at the cavity leading corner. The cross-stream plane under study is located at $z/D = 0.4$. Examples of snapshots are provided in Figure 4.2. A scalar function $a(x, y, t)$ extracted from PIV datasets splits up into mean flow (time-averaged field) and fluctuations as follow:

$$a(x, y, t) = \bar{a}(x, y) + a'(x, y, t) \quad (4.1)$$

For normalised velocity fields and underlying normal vorticity, it comes

$$\frac{\mathbf{U}_{xy}}{U_0} = \frac{\bar{u} + u'}{U_0} \mathbf{e}_x + \frac{\bar{v} + v'}{U_0} \mathbf{e}_y \quad (4.2)$$

$$\frac{\omega_z D}{U_0} = \frac{\partial v/U_0}{\partial x/D} - \frac{\partial u/U_0}{\partial y/D} = \frac{(\bar{\omega}_z + \omega_z') D}{U_0} \quad (4.3)$$

They are displayed for two different geometries $L/D = 1.5$ and $L/D = 2$. As expected, spanwise vorticity ω_z is perfectly suitable for representing the various features of flow organisation. Shear vorticity is steadily injected in the shear layer by incoming boundary layer. Shear layer travelling waves break onto the trailing edge, hence, producing vortices and injecting vorticity along the downstream wall of the cavity. In time, mass fluxes are cyclically exchanging fluid between the inside and outside flows, due to shear layer oscillations.

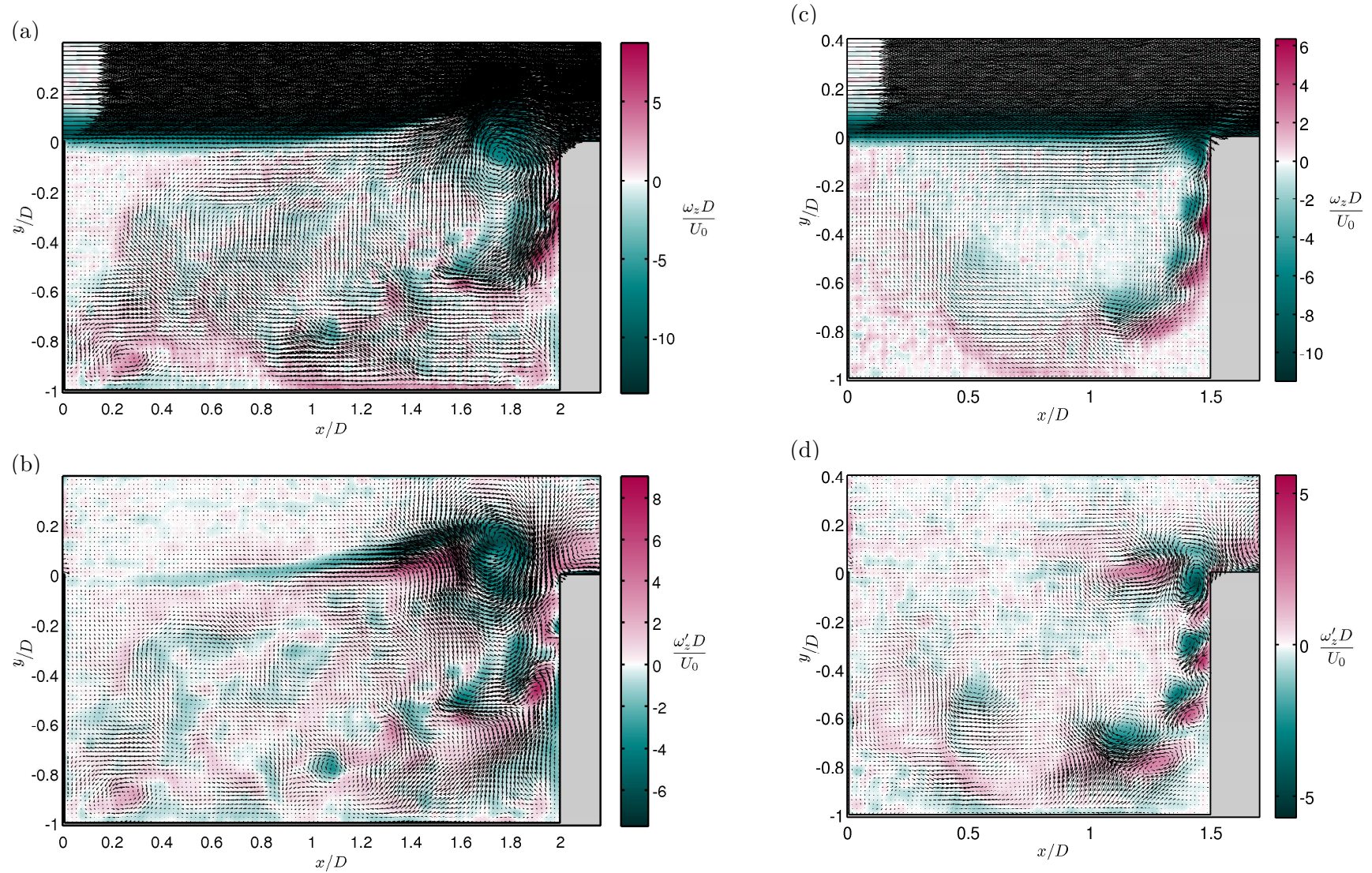


Figure 4.2: Snapshots extracted from TR-PIV data, in the cross-stream plane ($x, y, z/D = 0.4$), for two cases, (a,b) $L/D = 2.0$, $L/\theta_0 = 96$, $\text{Re}_L = 12670$, ($U_0 = 1.89$ m/s); and (c,d), $L/D = 1.5$, $L/\theta_0 = 76$, $\text{Re}_L = 10240$, ($U_0 = 2.10$ m/s). At the top (a,c), colours scale dimensionless vorticity $(\bar{\omega}_z + \omega_z')D/U_0$ and vectors represent total velocity $\bar{u} + u'$ and $\bar{v} + v'$. At the bottom, (b,d) depict fluctuating field only: colours scale dimensionless vorticity fluctuations $\omega_z'D/U_0$ and vectors represent velocity fluctuations u' and v' .

4.1.2 Inflow characteristics

When studying an impinging shear flow such as the shear layer developing above a rectangular cavity, one must logically characterise the flow conditions at separation. Incoming velocity profile impacts shear layer oscillations primarily and inner-flow for a lower part. In the incompressible regime in particular, shear layer frequencies have been demonstrated as depending strongly on incoming boundary layer (Rockwell, 1977; Rockwell and Naudascher, 1978, 1979; Knisely and Rockwell, 1982). More specifically, the incoming boundary layer profile injects vorticity which initiates the shear layer, as seen in Figure 4.2.(a,c). As described in Section 1.1.1, Monkewitz and Huerre (1982) demonstrated that in the ideal case of inviscid free shear layers, initial vorticity thickness δ_{ω_0} , depends on the momentum thickness at separation θ_0 . Section 4.1.5 focuses on shear layer local stability in regards to Kelvin-Helmholtz modes. More insight thus will be provided regarding the evolution of the vorticity thickness from separation to impingement.

Streamwise velocity profile at separation was measured out of the mean flow for different flow conditions and cavity shape ratio. In order to characterise the incoming boundary layer, of crucial importance in shear layer stability, Blasius model can be considered. In theory, assuming a Blasius profile at separation in our case is a strong assumption since the main stream is in fact a channel flow and perturbations from the cavity flow can propagate back upstream. Let us discuss the validity of such a model.

Dealing with a channel flow instead of an open flow induces changes mainly on the external part of the boundary layer, in other words, the determination of the main stream velocity U_0 . Concerning the laminar assumption, the investigated cases exhibit RMS levels between 1 and 2% at separation, which is already reasonably low. Moreover, smoke visualisations presented in previous section (Figure 4.1) have confirmed that a parallel flow is generated upstream of the cavity. Indeed, parallel streaklines from honey comb pattern can be observed. Furthermore, note that those RMS values integrate PIV noise as well. With the aim of quantifying wind-tunnel intrinsic turbulence rate only, further velocity measurements were performed in the main stream using Laser Doppler velocimetry (LDV) to reduce measurement noise. Normalised RMS was measured below 1% for velocities higher than 0.7 m/s. As often for experimental facilities, turbulence rate increases at low regime. As seen in Table 4.1, the present work focuses on velocities higher than 1 m/s.

First, let us consider raw experimental data. Figures 4.3.(a,b) provide experimental velocity profiles at separation for various cases, normalised by external velocity U_0 , directly estimated from measured velocity profile. Basically, the shape seems quite close to a laminar profile except for the external region where profiles show some variations. Those fluctuations, where mean velocity profile should rather be flat, are likely caused by PIV computation errors. Indeed, here are used raw velocity fields, before outliers have been searched. It so happens that the free stream above the leading edge corresponds to the extreme upstream corner of the field, where computation divergence occurs more often (see Section 2.3 for details). In order to bypass this issue, an estimation of U_0 is obtained by averaging over the entire external region.

On the other hand, the non-zero value at the wall, for all cases, constitutes another concern. This could be related to a systematic error on wall position ($y = 0$). Furthermore, a slight

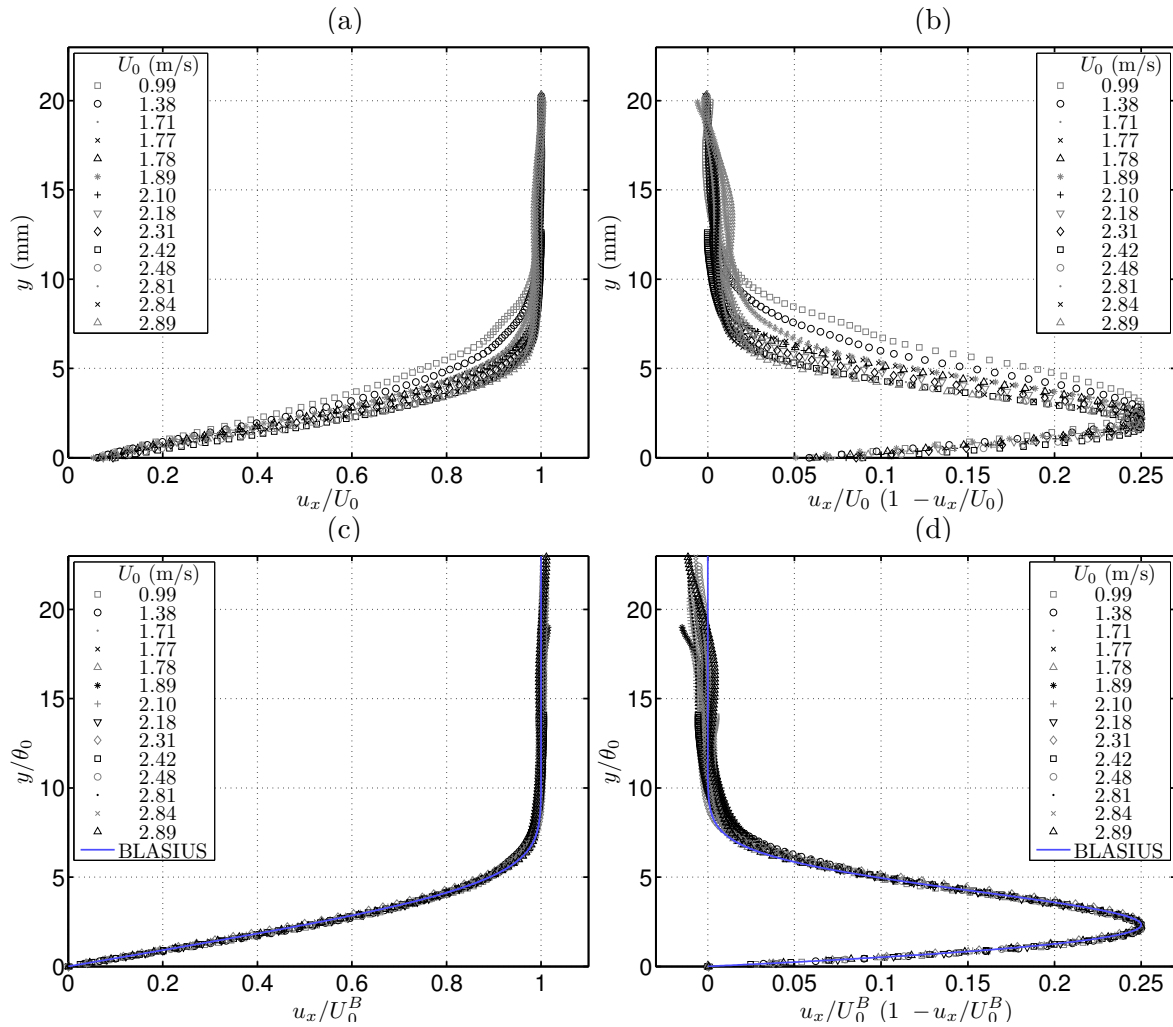


Figure 4.3: Incoming boundary layer profiles for various cases; (top), raw data, (bottom) revised profiles collapsed by normalising by momentum thickness θ_0 , as described in text. Blasius profile is given in plain line as a reference.

inflection point is observed around 1 mm from the wall, likely due to light reflexions inducing computation errors. Since both issues are clearly due to non-physical causes, velocity profiles are revised prior to any boundary layer thicknesses estimation or Blasius fitting. By considering the highest velocity gradient, typically at the 6th pixel of the profiles, as equal to wall gradient, corrections consisted in padding the profile accordingly until it reaches zero velocity. From that comes a new wall position $y = 0$ and the estimated error around $\epsilon_y = -0.3$ mm (2 pixels). Profiles have been only slightly modified so as to satisfy the boundary conditions.

Blasius fit is performed on each case using least mean square optimisation varying the external velocity U_0^B . Establishment length, from the elliptical edge, is already known, $l_x = 0.300$ m. Associated momentum thickness θ_0 is obtained through Blasius fit such that

$$\theta_0 = 0.4696 \sqrt{\frac{2\nu l_x}{U_0^B}}, \quad (4.4)$$

By normalising velocity measurements with U_0^B and momentum thickness θ_0 , profiles collapse almost perfectly onto Blasius model, as seen in Figures 4.3(c,d). Non negligible gap remains confined outside of the boundary layer. Difference between experimental data and Blasius model can be quantified by the standard deviation as follow.

$$\Delta fit = \frac{\sum_i \sqrt{(u_i^B - u_i)^2}}{\sum_i \sqrt{((u_i^B + u_i)/2)^2}}, \quad (4.5)$$

where u_i is the experimental profile and u_i^B the Blasius fit. In fact, Δfit can be considered as quantifying the degree of turbulence of the incoming flow. Δfit is often lower than 1%, 1.3% at the most. All characteristics of the incoming flow are provided in Table 4.1, for the cases investigated in the forthcoming analysis. Except for the case $L/D = 1.0$, for which the *rms* rate rises up to 6.4%[†], other configurations show less than 2% of *rms*. The dimensionless numbers are also given. In particular, the dimensionless cavity length L/θ_0 , already pointed out in Section 1.1, constitutes a control parameter for self-sustained oscillations of the shear layer, as in any impinging flow.

Table 4.1: Characteristics of the wall bounded laminar inflow at the leading edge.

L (mm)	ν (mm ² /s)	U_0 (m/s)	* <i>rms</i> (%)	** Δfit (%)	δ_0^{99} (mm)	θ_0 (mm)	Re_L	Re_{θ_0}	L/D	L/θ_0
50	15.6	2.42	6.4 [†]	0.6	6.86	0.92	7700	143	1.00	54
75	15.1	1.77	1.1	0.6	7.99	1.07	8800	126	1.50	70
75	15.4	2.10	1.3	0.9	7.37	0.99	10200	135	1.50	76
75	15.4	2.31	1.3	0.9	7.04	0.94	11200	141	1.50	79
75	14.9	2.81	1.6	1.3	6.38	0.86	14100	161	1.50	88
75	14.9	2.89	1.6	0.5	6.28	0.84	14600	164	1.50	89
88	15.4	2.48	1.0	0.7	6.77	0.91	14100	146	1.75	96
100	15.1	1.38	1.9	1.3	9.08	1.22	9100	111	2.00	82
100	14.9	1.71	1.8	0.9	8.17	1.10	11500	126	2.00	91
100	14.9	1.89	1.9	1.2	7.78	1.04	12700	132	2.00	96
100	15.0	2.18	2.0	0.9	7.22	0.97	14500	141	2.00	103

* *rms* corresponds to standard deviation of velocity measurements, averaged over crosswise position y and normalised by external velocity U_0 .

** Δfit characterises the statistic difference between experimental mean profile and Blasius fit, such as described in Equation 4.5.

[†] The higher *rms* rate for the case $L/D = 1.0$, $L/\theta_0 = 54$ is due to PIV errors more than flow turbulence. In fact, the PIV time delay was too large to handle the important velocity gradients. This case was only aimed to be used as subsidiary data and for inner-flow analysis (Section 4.5), so that this noise does little damage.

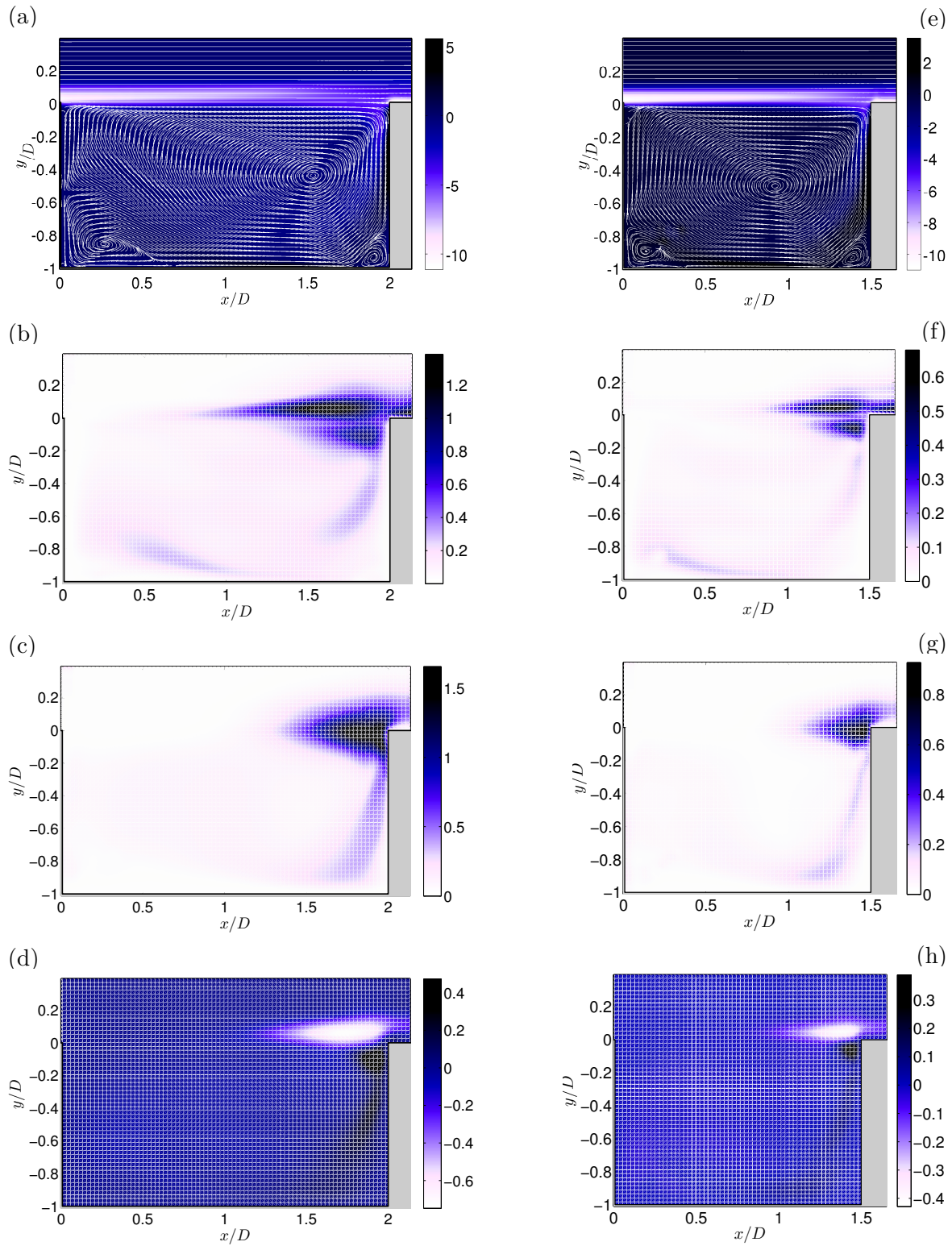


Figure 4.4: Statistical moments extracted in a cross-stream plane (x, y) for two examples: on the left-hand side, $L/D = 2.0$, $L/\theta_0 = 91$; on the right side, $L/D = 1.5$, $L/\theta_0 = 79$. (a,e) Mean flow with mean vorticity $\bar{\omega}_z$ in colour scales and streamlines; (b,f) streamwise Reynolds stress $\overline{u'u'}/U_0^2$ (%); (c,g) crosswise Reynolds stress $\overline{v'v'}/U_0^2$ (%); (d,h) Reynolds cross-component $\overline{u'v'}/U_0^2$ (%).

4.1.3 Statistical moments

In this section, the mean flow and normalised Reynolds stresses are presented and briefly discussed. Figures 4.4.(a,e) depict the mean flow for two geometries. Again, parallel incoming flow is confirmed by streamlines above the cavity. The main vortex inside the cavity is almost centred in the $L/D = 1.5$ case, whereas it is much more confined in the downstream half of the cavity when $L/D = 2$. Streamlines indicate secondary steady vortices nested in bottom corners of the cavity.

Now considering the fluctuations, they are statistically characterised by Reynolds stress tensor components $\overline{\rho u'_i u'_j}$, computed from time-resolved PIV datasets and hereafter normalised by ρU_0^2 (given in %). If one considers independently time-series of 4096 field realisations each, statistical convergence is already within 2% for the mean flow and within 10% for Reynolds tensor components. Furthermore, convergence is improved by averaging over 15 different recordings. Both geometries presented in Figures 4.4.(b-d,f-h) show a similar signature. As expected, the Reynolds tensor components, $\overline{u'u'}$, $\overline{v'v'}$, $\overline{u'v'}$, clearly show that most of the fluctuating energy is concentrated in the impinging shear layer, near the cavity trailing edge. Indeed, the shear layer flapping motion is the most energetic phenomenon of the fluctuating flow. In addition, intensity distribution of velocity fluctuations is not equivalent for x and y components. In particular, $\overline{u'u'}$ – in Figure 4.4.(b,f) – exhibits a structure in two lobes distributed on both sides of the cavity top plane ($y = 0$), while $\overline{v'v'}$ – Figure 4.4.(c,g) – has a gaussian-like shape centred on $y = 0$. Similar distribution was observed by Williams and Hama (1980); Kuo and Huang (2001); Forestier et al. (2003). The structure in $\overline{u'v'}$ shows that u' and v' are, in average, of opposite signs atop, and of the same sign below, the cavity top-plane. By making the connexion with instantaneous snapshots seen earlier (Figures 4.1 & 4.2), this probably indicates a segregation of travelling vortices at the impingement. More precisely, impinging vortices such with $\omega_z < 0$ – thus corresponding to $u'(y > 0) > 0$ and $u'(y < 0) < 0$ – dive into the cavity, inducing a higher inflow velocity along the wall, that is $v' < 0$. On the other hand, positive vortices ($\omega_z > 0$) – in other words $u'(y > 0) < 0$ and $u'(y < 0) > 0$ – are “pushed upwards” at the trailing edge, to be advected downstream in the wake. Henceforth, one may infer that flapping motion is responsible for a fluid exchange between inner-flow and outflow at the impingement. Negative vortices gathering vorticity from the incoming boundary layer carry some outflow into the cavity, while positive vortices, yielding a lack of vorticity in the shear layer, can catch some fluid from the main recirculation and bring it up out.

Some fluctuations of secondary order are also observed inside the cavity, likely corresponding to vortices advected from the impingement back upstream *via* the main recirculation. Note that similar results were obtained for the case $L/D = 2.0$, $L/\theta_0 = 96$, in Basley et al. (2011).

4.1.4 Spectral signature

The most distinctive property of impinging flows is their coherence, resulting in a sparse spectral signature. Self-sustained oscillations convey a few enhanced frequencies scaling approximately on U_0/L due to pressure feedback, instantaneous in the incompressible regime (see Sections 1.1.2 & 1.1.3 for details). This is verified by spectra shown in Figure 4.5, which all exhibit a distribution of well-defined peaks, around $St = f_n L / U_0 = n/2$, with $n = 1, 2, 3, \dots$. In the cases under study, the dominant peak is often located near $St = 1$ and produces harmonics. Details regarding the computation of power spectral densities can be found in Sections 3.1.1-3.1.2.

Spectra have been ordered with increasing dimensionless cavity length L/θ_0 . This corresponds either to higher velocities, through Expression 4.4 ($\frac{1}{\theta_0} \propto \sqrt{U_0}$) or to larger cavity length. Note that energy globally exhibited by spectra is correlated with L/θ_0 . When L/θ_0 increases, the energy distribution evolves from low to high Strouhal numbers. All peaks experience a slow but regular drift towards higher frequencies. More particularly, the stage of dominant peaks around $St \simeq n/2$ rises with the parameter L/θ_0 : ($n = 1, 2$) at low L/θ_0 and then $n = 3$ appears for high values of L/θ_0 .

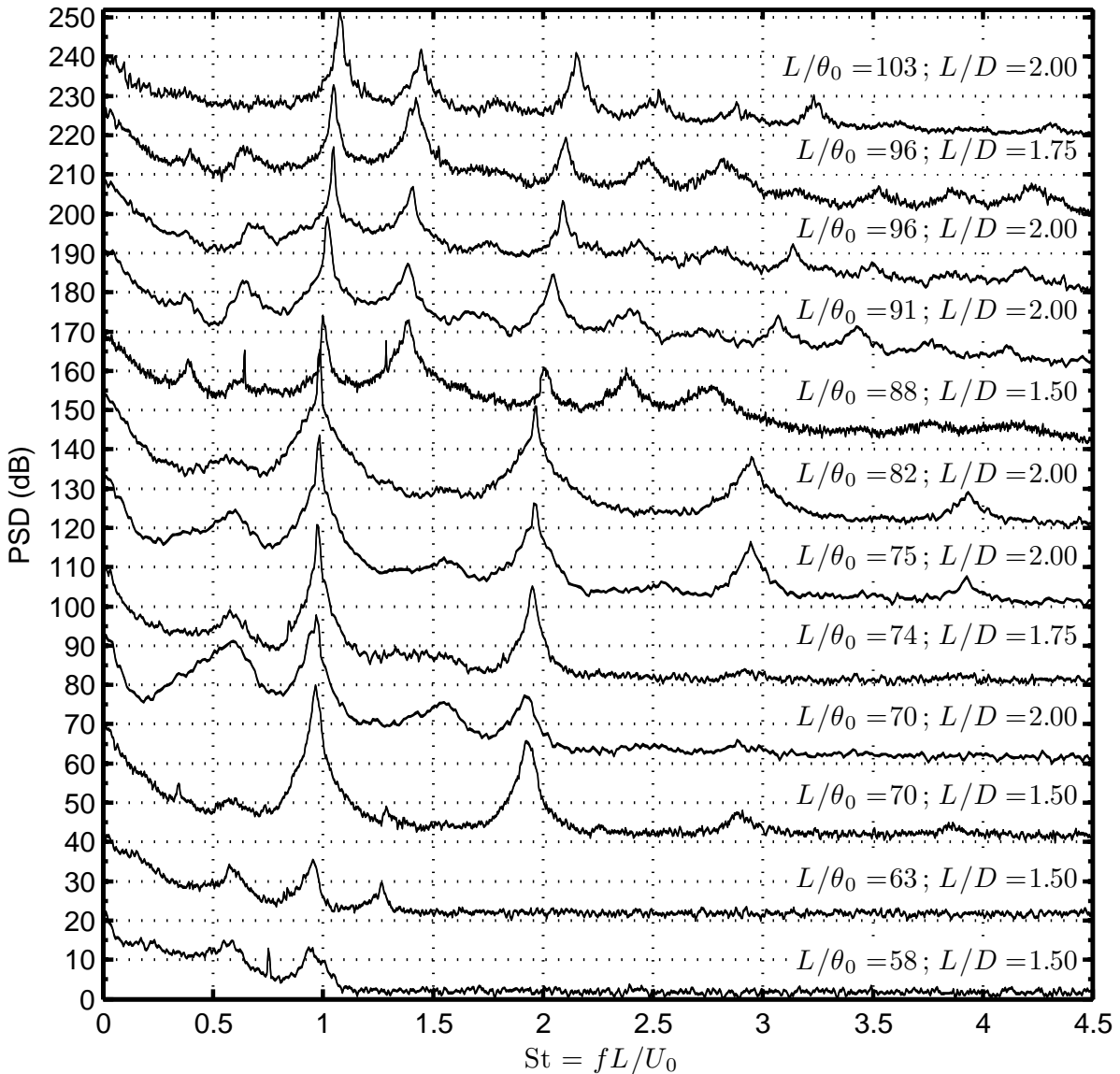


Figure 4.5: Power spectral densities (streamwise velocity component) at ($x = L - 5$ mm, $y = 5$ mm) for various cases. This yields the evolution of spectral signature with increasing dimensionless cavity length L/θ_0 , as a function of Strouhal number based on cavity length. For the sake of clarity, each spectrum is incremented by 20 dB. Curve thickness corresponds to 95%-confidence interval.

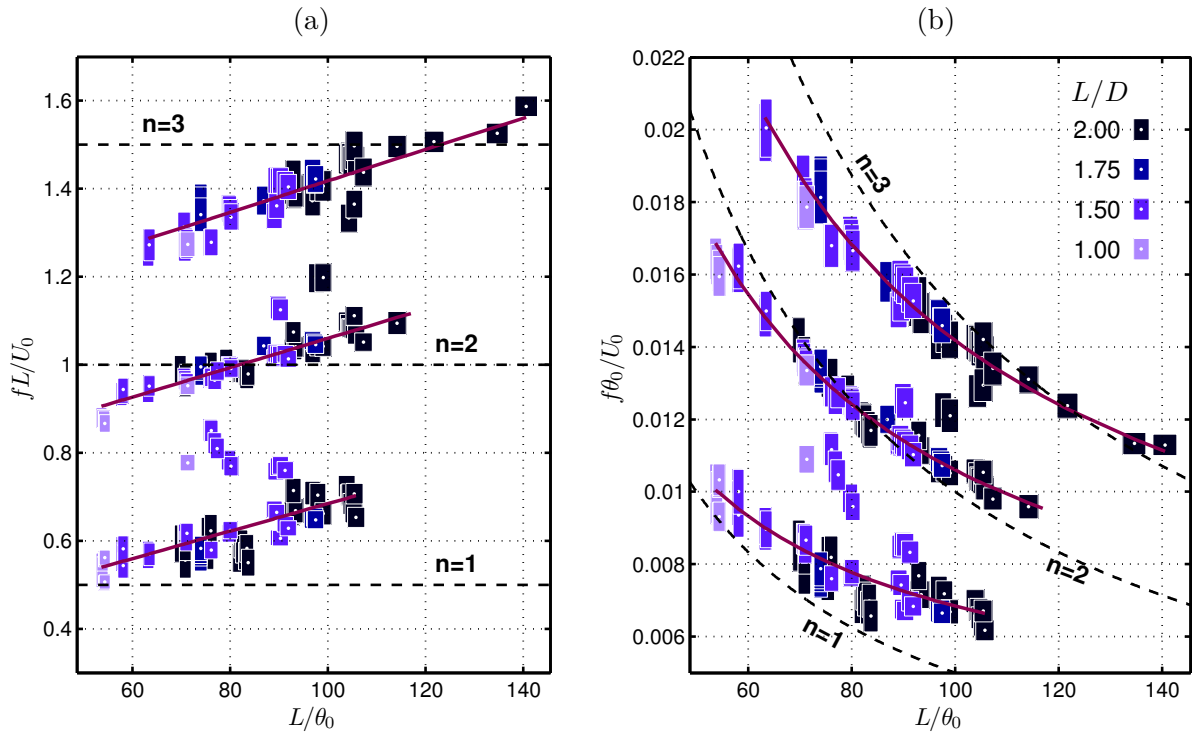


Figure 4.6: Parametric evolution of shear layer frequencies as functions of the dimensionless cavity length L/θ_0 . Data are extracted from LDV spectra, for numerous cases investigated during the past few years. (a) Frequencies normalised as Strouhal numbers based on cavity length L . Linear fits for the three locked-on modes, each one around a stage $n/2$ with $n = \{1, 2, 3\}$. Corresponding expressions are given in Equation 4.6. (b) The same data divided by L/θ_0 , resulting in Strouhal numbers based on momentum thickness at separation θ_0 . Colours indicate L/D configurations and rectangle dimensions represent uncertainties.

In order to depict the evolution of the shear layer flapping motion in the parametric space, the focus is now on the most energetic peaks in power spectra out of the shear layer region. Using both LDV and TR-PIV measurements, frequencies associated with shear layer oscillations have been collected in Figure 4.6.(a,b), with respect to dimensionless cavity length L/θ_0 . The same data are displayed in both diagrams with different Strouhal normalisations: (a) $St_L = fL/U_0$ and (b) $St_{\theta_0} = f\theta_0/U_0$.

Results are in very good agreement with experimental data obtained by Sarohia (1977) and insightful studies by Rockwell and co-authors (Rockwell, 1977; Rockwell and Naudascher, 1978, 1979; Rockwell and Knisely, 1980b), or more recently, Kuo and Huang (2001); Kuo and Jeng (2003); Delprat (2010). In particular, Figure 4.6.b matches perfectly data presented in Rockwell and Knisely (1980b)–*Figure 1*, or Rockwell and Naudascher (1979)–*Figures 8b&9*. Similarities are also found with various impinging shear flows, as in Knisely and Rockwell (1982)–*Figure 4* in the case of a backward-facing step followed by a thick edge.

Most of L -based Strouhal numbers (Figure 4.6.a), obtained for various configurations L/D and incoming velocities U_0 , collapse onto three different stages, close to $n/2$ with $n = 1, 2, 3$. They are often referred to as *locked-on* frequencies. As described in the literature review in Sections 1.1.2 & 1.1.3, such a spectral signature driven by dimensionless cavity length, L/θ_0 , and evolving regardless of cavity shape-ratio L/D , depicts the dual interplay of both pressure-based feedback and shear layer instability. The parameter n can be seen as the number

of cycles within the cavity length: the phase difference between leading and trailing edges is constant around $2\pi n$ (Knisely and Rockwell, 1982). Locked-on modes (n) are selected or not, according to their amplification by the shear layer. When two regimes are equally amplified, mode switching occurs, as mentioned in Section 1.1.4 (Pastur et al., 2008; Lusseyran et al., 2008).

Shear layer frequencies do not align strictly with the simplistic model in which L -based Strouhal numbers are equal to $n/2$ (Equation 1.10). Many factors left aside in this simple model are likely to change the idealised feedback loop. The underlying Kelvin-Helmholtz instability is only taken into account through velocity profile at separation (U_0 and θ_0), whereas shear layer characteristics evolves along x from leading to trailing edge of the cavity. The influence of the inner-cavity flow has also been neglected. The corrective term γ from Equation 1.9, often seen as the signature of a phase delay due to corner interaction, can be reintroduced and determined empirically from the present dataset (Figure 4.6.a). Using the linear fits expressed as

$$\frac{f_n L}{U_0} = \frac{n}{2} + \frac{L/\theta_0 - 41n}{20(17-n)} \approx \frac{3n}{8} + \frac{L/\theta_0}{340}, \quad (4.6)$$

the coefficient γ writes as an affine function of L/θ_0 with n as a parameter:

$$\frac{f_n L}{U_0} = \frac{n - \gamma_n}{2} \quad \text{with} \quad \gamma_n(L/\theta_0) = \frac{41n - L/\theta_0}{10(17-n)}. \quad (4.7)$$

Note that $\gamma_n = 0$ when control parameter $L/\theta_0 = 41n$. Physically, one can assert that those values of L/θ_0 correspond to regimes in which both shear layer intrinsic instability and phase-locking are in perfect resonance.

Finally, one may notice a few points which depart from the “locked-on” scheme. Those frequencies are investigated in detail in a paper under revision and will be discussed further in Sections 4.3 & 4.5.

4.1.5 Local stability in the shear layer

To discuss more thoroughly the mechanism leading to self-sustained oscillations, it is tempting to apply local linear stability analysis of free shear layers to our system. It is however very important to remember that characteristics of the shear layer are here obtained from a saturated state instead of the actual base-flow. Although the mean flow – Figures 4.4.(a,e) – seems quite similar in shape to the base flow obtained using numerical simulations for linear stability analyses, such as in Brès and Colonius (2008); Barbagallo et al. (2009); de Vicente (2010), both fields are not equivalent in nature. The basic flow represents the stationary solution, generally unstable in working conditions, while the mean flow is, by definition, the arithmetic mean of the flow *after saturation has occurred*. Furthermore, local stability studies theoretically apply to free shear layers, considered as two-dimensional parallel inviscid flows (Michalke, 1964; Monkewitz and Huerre, 1982; Huerre and Monkewitz, 1985; Amram, 1995; Huerre and Rossi, 1998). Such an assumption is intrinsically ruled out by the impingement at the trailing corner and the inner-cavity flow, responsible for the emergence of global stability properties. As a result, the following analysis based on a self-similar model and a critical frequency directly related to vorticity thickness must be interpreted with caution.

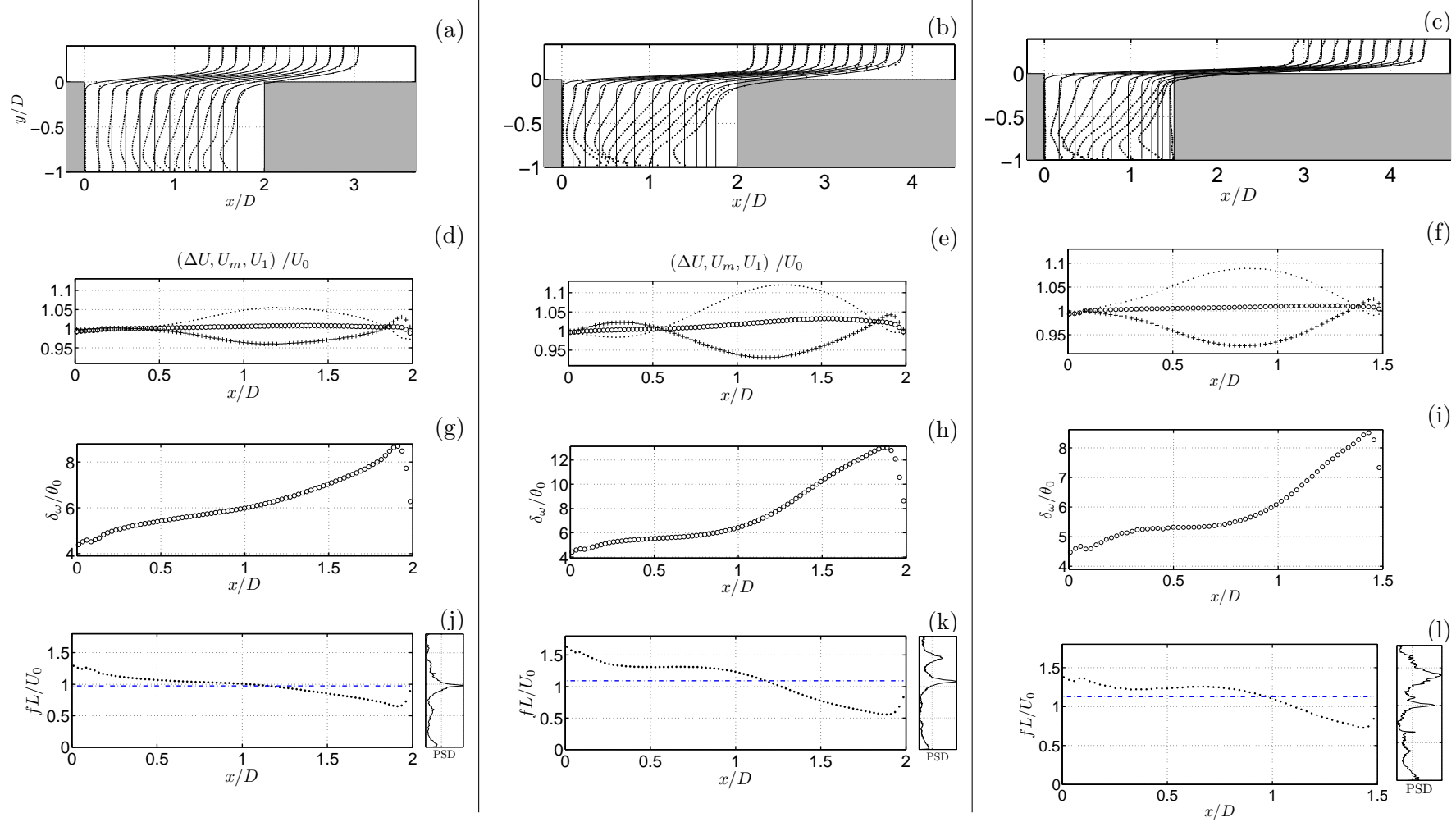


Figure 4.7: Shear-layer local features along streamwise coordinate x/D : (a,b,c) cross-stream profiles fitted by a hyperbolic-tangent law; (d,e,f) twice the mean velocity $2U_m(\cdot)$, shear strength ΔU (+) and $U_1 = \bar{U}_x(y \rightarrow +\infty)$ (\circ); (g,h,i) normalised vorticity thickness δ_ω/θ_0 ; (j,k,l) the most destabilising Strouhal number based on L (\cdot), estimated as in a free shear layer, the wave celerity being given by $c = U_m(x)$, together with its average (---) and measured power spectral density. Three cases are presented: (left) $L/D = 2.0$, $U_0 = 1.38$ m/s, $L/\theta_0 = 82$; (middle) $L/D = 2.0$, $U_0 = 2.18$ m/s, $L/\theta_0 = 103$; (right) $L/D = 1.5$, $U_0 = 2.89$ m/s, $L/\theta_0 = 89$.

To begin with, cross-stream velocity profiles $\bar{U}_x(y)$, extracted from mean flow at different abscissas x , are fitted with an hyperbolic-tangent profile of the form:

$$\bar{U}(y) = U_m + \frac{\Delta U}{2} \tanh\left(\frac{2(y - y_c)}{\delta_\omega}\right) \quad (4.8)$$

where ΔU is the shear strength and U_m the mean velocity at the inflexion point $y = y_c$. Shear-layer vorticity thickness δ_ω is defined as:

$$\delta_\omega = \frac{\Delta U}{\left(\frac{\partial U}{\partial y}\right)_{\max}}, \quad (4.9)$$

The fit is performed by minimising its \mathcal{L}_2 -norm difference with the mean cross-stream profile, for which the shear layer region only is considered ($-0.4 \leq y/H \leq 0.4$). Examples of fitted profiles are provided in Figures 4.7.(a,b,c). The inflexion point is such that the gradient $(\partial \bar{U}_x / \partial y)$ is maximum, by definition. In addition, $\bar{U}_x(y_c)$ corresponds to the mean velocity $U_m = (U_1 + U_2)/2$. The extrema velocities are defined as $U_1 = \bar{U}(y \rightarrow +\infty)$ and $U_2 = \bar{U}(y \rightarrow -\infty)$, respectively. The shear strength is then given as $\Delta U = U_1 - U_2$. In Figures 4.7.(d,e,f), U_m and ΔU exhibit a variation along the shear layer, due to the evolution of $U_2(x)$ implied by the recirculating flow. More complexity is observed when L/θ_0 increases (mixing strengthens). In particular, for the higher $L/\theta_0 = 103$ case – Figure 4.7.(middle) – U_2 first decreases for $x/D < 0.5$, indicating a counter flow due to secondary vortex, then it rises with the main recirculation. In Figures 4.7.(g,h,i), vorticity thickness at the leading edge is $\delta_{\omega 0} \simeq 4\theta_0$ (Equation 1.3), which satisfies the theoretical properties of Blasius-profile mixing layers, as defined by Monkewitz and Huerre (1982). Then, δ_ω shows a fairly monotonic increase along the shear layer, until very close to the impingement, where it abruptly decreases.

That evolution is coherent with the results found in literature, from pioneer experiments by Sarohia (1977) to TR-PIV results in Haigermoser et al. (2008) or two-dimensional numerical simulations in Rowley et al. (2002). The inflexion point, y_c , estimated from hyperbolic tangent fits, remains roughly unchanged along x/L . In Figure 4.8.a is provided the parametric evolution of shear layer vorticity thickness $\delta_\omega(x/D)$ normalised by θ_0 . The unique value $\delta_\omega(0)/\theta_0 \simeq 4$ at separation confirms the validity of Equation 1.3 for all our cases. All curves fairly collapse until $x/D = 0.8$, where vorticity thickness becomes dependent of the dimensionless cavity length: the slope $\frac{\partial \delta_\omega}{\partial x}$ along the shear layer strengthens with L/θ_0 .

Once such characteristics have been obtained, the most amplified frequency associated with each hyperbolic-tangent profile $\bar{U}(y)$ can be estimated. Following Michalke (1964); Monkewitz and Huerre (1982); Amram (1995); Huerre and Rossi (1998), the critical frequency f_c in a free shear layer satisfies $f_c = 0.142U_m/\delta_\omega$ (see Section 1.1.1); and the neutral mode (zero growth-rate) is given by $f_m = 0.32U_m/\delta_\omega$. As well as both $U_m(x)$ and $\delta_\omega(x)$, f_c is expected to be a function of streamwise position x/D . It actually shows a decrease along the shear layer in Figures 4.7.(j,k,l).

Critical Strouhal number based on momentum thickness at separation $f_c(x/D)\theta_0/U_0$ is plotted in Figure 4.8.b for different L/θ_0 . Its behaviour mainly depends on that of vorticity thickness, mean velocity U_m varying only by about 10% at the most. In Section 1.1.1, Equations 1.3 & 1.2 were merged to estimate the critical θ_0 -based Strouhal number just after separation, $f_{c0}\theta_0/U_0 \approx 0.018$ (see Equation 1.4). In the present study, the critical Strouhal number at separation is around 0.015 for all L/θ_0 cases. Then it stabilises around 0.013 and starts to decrease drastically from $x/D = 1$ to a close vicinity of the impingement.

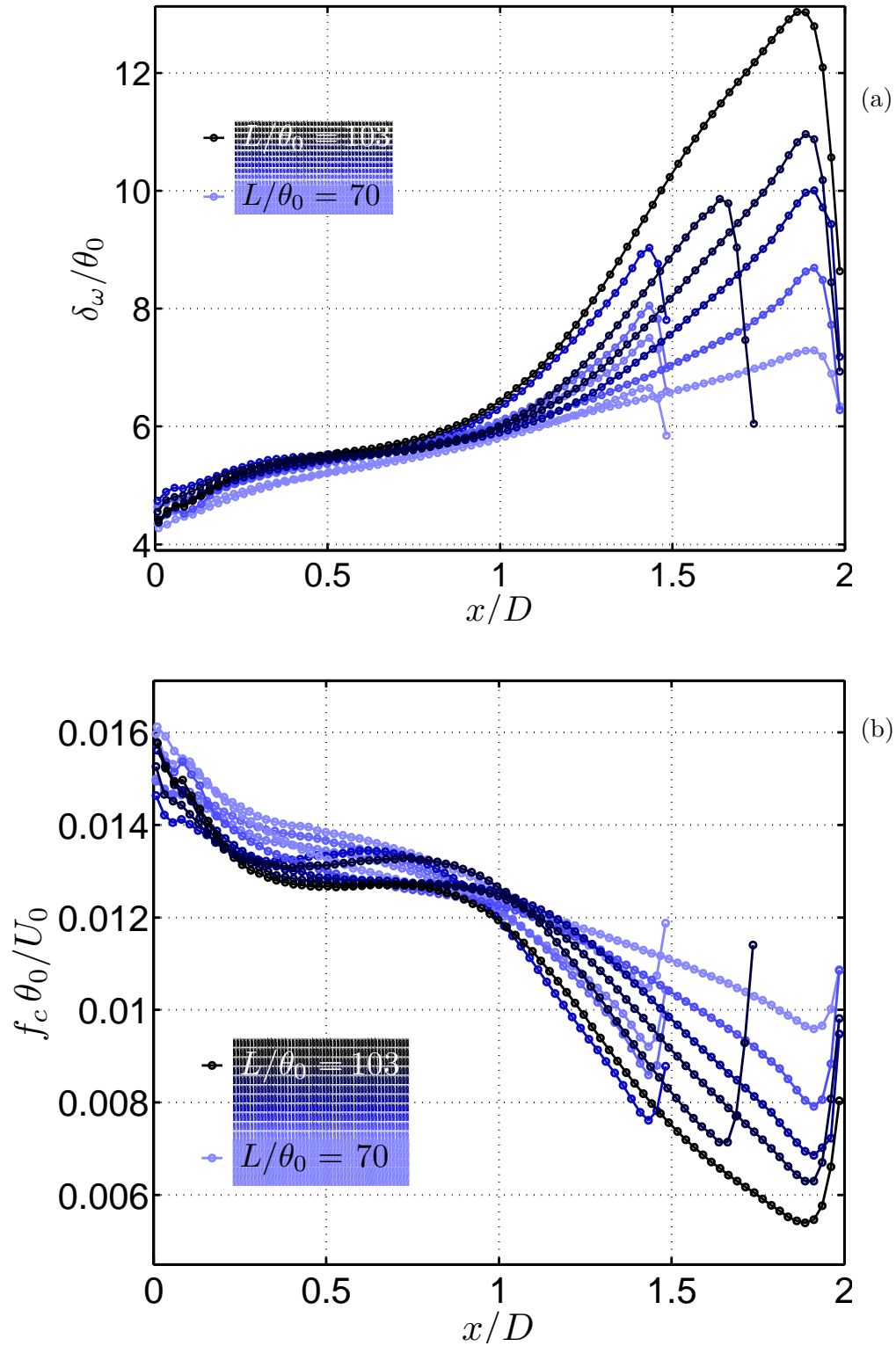


Figure 4.8: Streamwise evolution of the shear layer for all investigated cases: (a) vorticity thickness δ_ω normalised by momentum thickness at separation θ_0 , (b) most destabilising Strouhal number based on θ_0 . Colours scale the dimensionless cavity length L/θ_0 .

It has been already pointed out that the critical frequency estimated through a local hyperbolic-tangent law stability analysis cannot be fully reliable since the system under study is known to be globally unstable, firstly due to the impingement and to a lower part, to the inner-flow. Shear layer frequencies remain constant across the entire flow contrarily to what is assumed with local stability analysis.

Nevertheless, estimations of critical frequency f_c are consistent with regards to the actual frequencies of self-sustained oscillations (peaks emerging in spectra). In every case, the dominant frequency f_a and other energetic peaks arise within the range explored by $f_c(x)$. Averaging f_c over the cavity length even matches the single peak $f_a L/U_0 = 1.0$ in the first case, see Figure 4.7.j. Concerning the second and third cases, in Figures 4.7.(k,l), pressure feedback imposes two different frequencies of self-sustained oscillations of stages $n = 2$ and $n = 3$, close to critical frequency f_c : $St = 1.4$ and $St = 1$ for $L/\theta_0 = 89$; $St = 1.1$ and $St = 1.5$ for $L/\theta_0 = 103$. Ultimately, Kelvin-Helmholtz instability represents the intrinsic mechanism underlying the shear layer flapping motion, despite the global organisation of the flow. Cavity length resonance enhances one or two locked-on modes – satisfying phase relation between cavity edges – from the range of unstable frequencies, depending on their relative position to critical frequency f_c .

4.1.6 Nonlinear dynamics of the self-sustained oscillations

The rest of this chapter aims to provide more insight regarding the space-time dynamics of the shear layer travelling waves in the permanent regime. In particular, the nonlinear interactions at play in the different regimes of self-sustained oscillations are investigated by making great use of the time-resolved space-extended data out of the TR-PIV campaign. Four aspects can be highlighted:

- saturation of the self-sustained oscillations (Section 4.2)
- multiple shear layer modes and amplitude modulation (Section 4.3)
- Mode switching and overmodulation (Section 4.4)
- Inner-flow frequencies (Section 4.5)

4.2 Self-sustained oscillations and harmonic families

In this section, space-time coherent structures corresponding to self-sustained oscillations of the shear layer are investigated in depth by making use of time-resolved space-extended data. In order to study the self-sustaining mechanism only, we focus on cases with harmonic spectral signature, that is exhibiting a single harmonic family: $L/D = 2.0$, $L/\theta_0 = 82$. A power spectral density of such a flow is provided in Figure 4.9. Note that power spectra performed on TR-PIV data have been validated by comparison with LDV data in Basley et al. (2011).

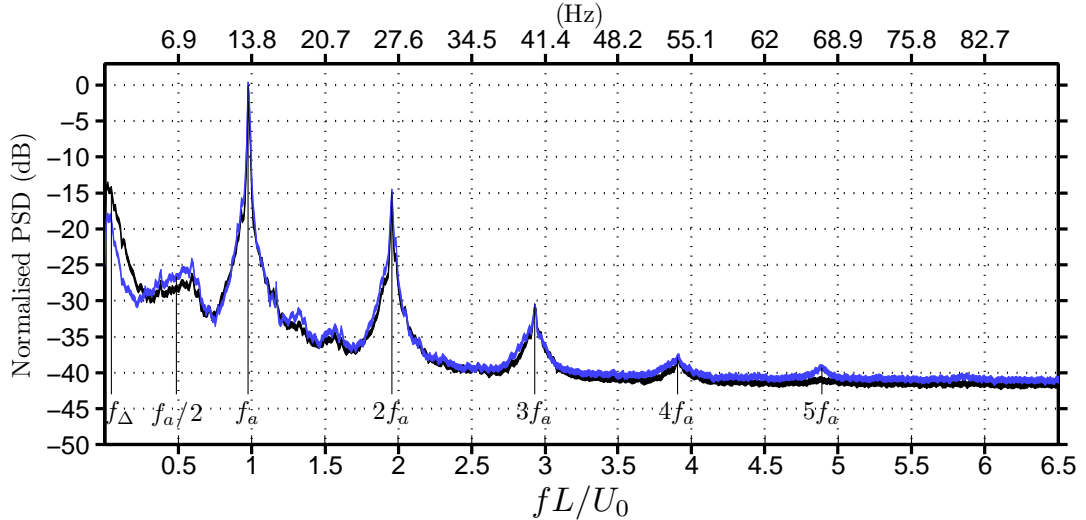


Figure 4.9: Normalised power spectral distribution of u' (black) and v' (blue) fluctuations for case $L/D = 2.0$, $L/\theta_0 = 82$; out of the PIV time series and space-averaged over the impingement vicinity ($1.6 \leq x/D \leq 2.0$ and $-0.25 \leq y/D \leq 0.25$). Line heaviness corresponds to 95%-confidence interval.

Spectrum exhibits a dominant frequency, $f_a = 13.5$ Hz, corresponding to a Strouhal number $f_a L/U_0 = 0.98$. Not less than four harmonics emerge from noise level, $h f_a$ with $h = 2, 3, 4, 5$. This monochromatic signature indicates a strong nonlinear saturation of a single locked-on mode concentrating most of the energy. In other words, a highly coherent flow with periodic dynamics. Note nonetheless the existence of a low energy peak at sub-harmonic $f_a/2$, which recalls first regime in Rockwell and Knisely (1980b). In addition, energy levels rise for low frequencies, around $f_\Delta L/U_0 = 0.05$ ($f_\Delta = 0.7$ Hz), that is one order of magnitude below the dominant modes, corresponding to slow motions of the flow.

4.2.1 Space-time structures of self-sustained oscillations

In order to describe self-sustained oscillations of the shear layer, various space-time representations are employed. The observed sample is a close-up in time, extracted from one of the fifteen 16 s-long recordings available for case $L/\theta_0 = 82$, $L/D = 2.0$. The excerpt lasts over 2.5 s, *ie.* $21 < t \frac{U_0}{L} < 55$ in dimensionless time units.

As a visual and qualitative approach, a (x, y, t) -volume is depicted in Figures 4.10 & 4.11 in which iso-surfaces of spanwise vorticity fluctuations $\omega'_z D/U_0$ are displayed. Negative and positive vorticity structures are coloured in blue and yellow, respectively. Such a 3D representation uses t -axis as a third (*spanwise*) dimension. Two-dimensional eddies, existing in an xy -plane,

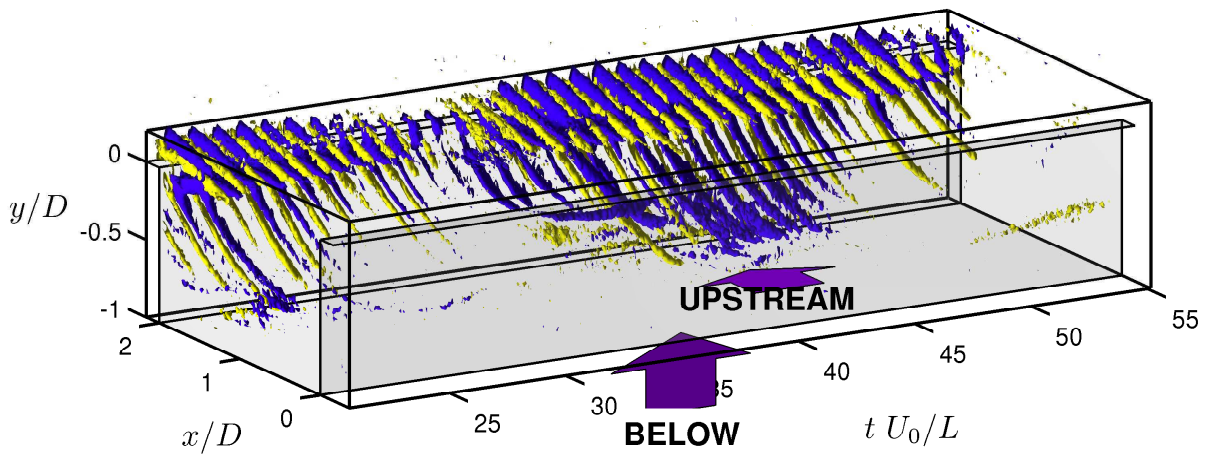


Figure 4.10: Iso-surfaces of vorticity fluctuations, $\omega'_z D/U_0 = 1.8$ (yellow) and $\omega'_z L/U_0 = -1.8$ (blue), in the space-time volume (x, y, t) , issued from time-resolved PIV data for configuration $L/\theta_0 = 82$. Only an excerpt of the entire set, such as $21 < t \frac{U_0}{L} < 55$, is displayed.

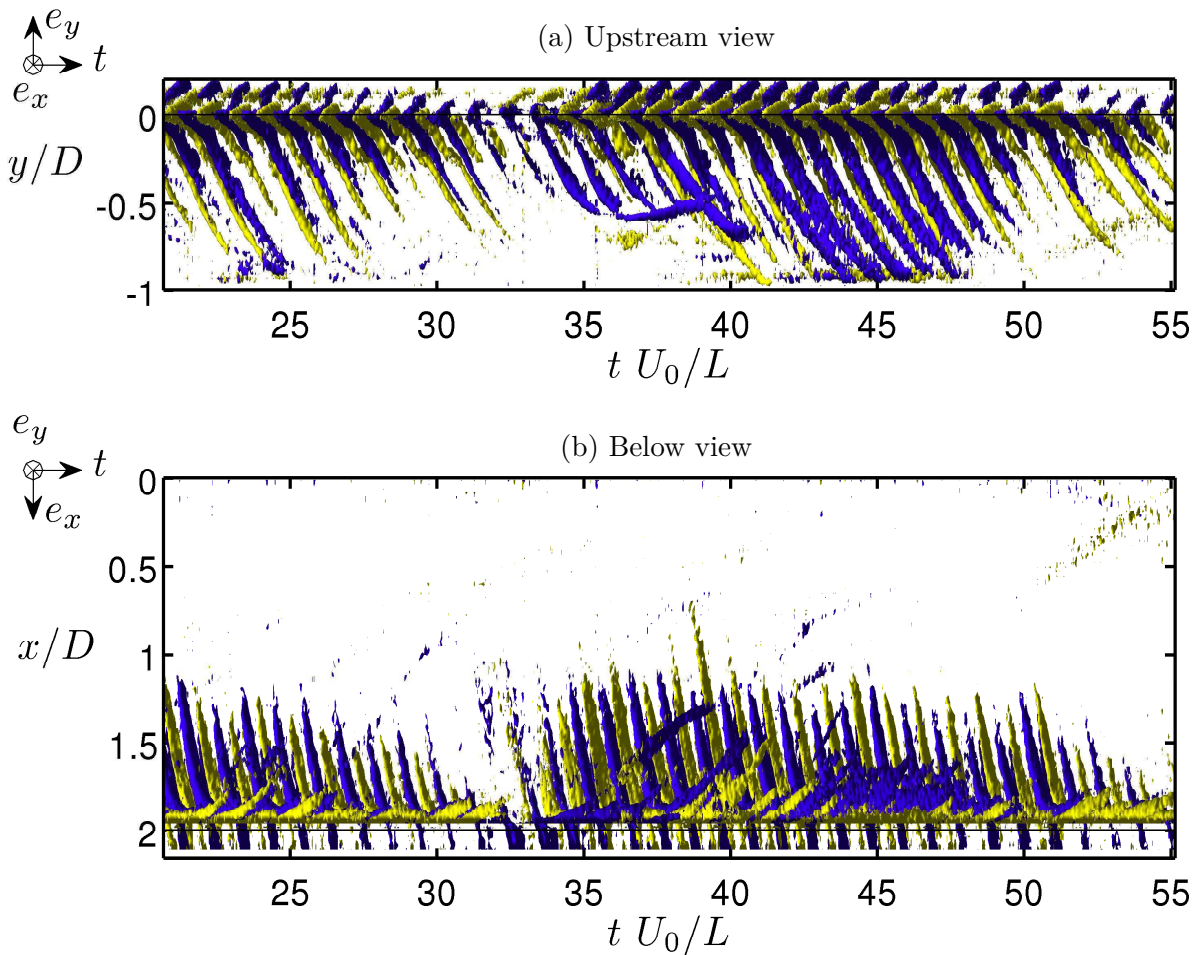


Figure 4.11: Same space-time domain as Figure 4.10, shown from upstream (a) and below (b).

therefore appear as *3D-tubes*. The *upstream* and *below* views, in Figure 4.11.(a,b), constitute projections of the space-time volume (x, y, t) upon planes (t, y) and (t, x) , respectively.

Self-sustained oscillations of the shear layer are observed around the impingement, at frequency f_a , Figure 4.10. Shear layer vortices travelling and impinging onto the downstream corner of the cavity produce periodic inflows injected along the forward-facing wall. These vortical structures are advected upstream around the main recirculation. Positive vorticity *tubes* seem to develop closer to the walls, likely enhanced by positive velocity-gradients inside the boundary layers. For similar reasons, negative vorticity structures remain at a smaller radius inside the main vortex.

For more quantitative aspects, Figure 4.12 consists of extracted *space-time planes* and times-series at key locations inside the cavity. Details regarding extraction points are given in Figure 4.12(f). Streamwise space-time diagrams are built at three different positions y/D in Figure 4.12.(a,b,c). They display contours of vorticity fluctuations. Vertical and horizontal axes represent dimensionless time $t \frac{U_0}{L}$ and streamwise coordinate x/L , respectively. Similarly, Figure 4.12.(d,e) represent two crosswise space-time diagrams, whose horizontal and vertical axes are dimensionless time $t \frac{U_0}{L}$ and crosswise coordinate y/H , respectively. Phase-velocities of the shear-layer waves can be estimated from slopes depicted by space-time structures. Streamwise component $u_\varphi = \Delta x / \Delta t$ from Figure 4.12.(a-c), and crosswise component $v_\varphi = \Delta y / \Delta t$ from Figure 4.12.(d,e). Local insight of the temporal behaviour is provided by time-series extracted from three intersections of the space-time planes (a) to (e). The first two time-series are picked up in the shear layer at the intersection of planes (a,d) and (b,d), respectively — see Figures 4.12.(a \cap d) and 4.12.(b \cap d). The time-series in Figure 4.12.(c \cap e), at the intersection of planes (c) and (e), characterises the temporal dynamics of the main recirculation. Both components of velocity fluctuations are plotted and normalised by U_0 .

Shear layer locked-on oscillations appear in Figure 4.12.(a) & (a \cap d). As expected, vortices of alternative sign travelling downstream along the shear layer constitute a *fast wave* whose associated phase velocity, C_a , is fairly constant in the streamwise direction. In Figure 4.12.(a), the slope gives $C_a \simeq 0.5 U_0$. In Figure 4.12.(a \cap d), both velocity components u' and v' exhibit strong f_a oscillations and are in phase opposition. Moreover, time-series in the top cavity plane ($y = 0$), plotted in Figure 4.12.(b \cap d), show less energy in streamwise fluctuations, while crosswise component experiences high amplitude oscillations. These results are consistent with statistics presented earlier in Figure 4.4.

Like the streamwise-travelling vortices of the shear layer, crosswise-travelling eddies along the forward-facing wall are indicated by stripes in Figure 4.12.(d). Corresponding to inflows induced by shear layer flapping motion at the trailing edge, they yield the same frequency $f_a L / U_0 \simeq 1$ but travel at a lower velocity $0.12 U_0$.

Space-time planes in Figures 4.12.(c,e), as well as time-series in Figure 4.12.(c \cap e), are mostly free of self-sustained oscillations. On the contrary, only large scales (frequencies an order of magnitude lower than shear layer locked-on mode) are visible in the inner-flow, along the main recirculation.

4.2.2 Wave properties

Shear layer locked-on oscillations have been globally observed inside the space-time domain (x, y, t) . They correspond to progressive waves along streamwise direction, as expected from Kelvin-Helmholtz instability based disturbances. The present section aims at estimating the

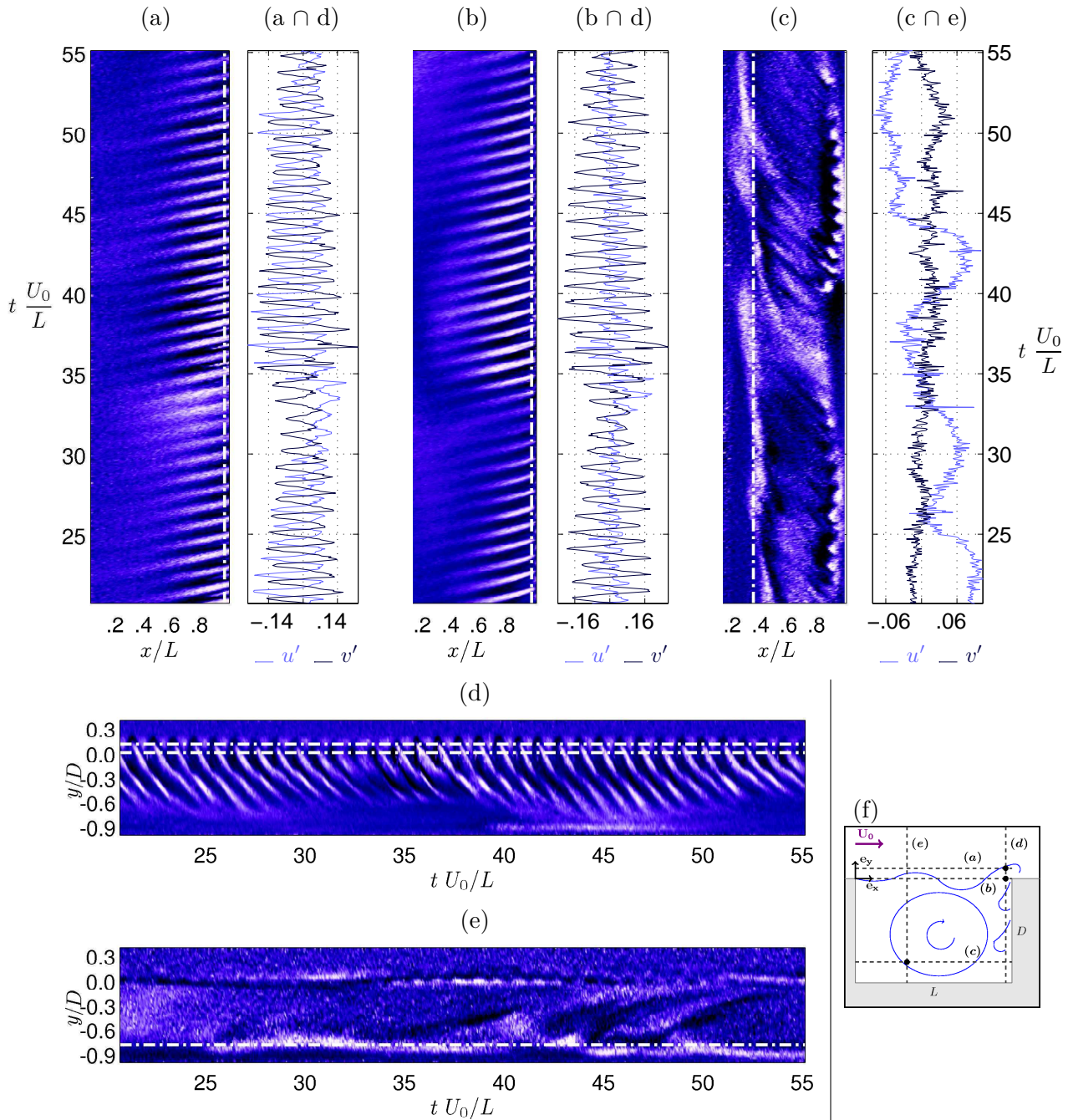


Figure 4.12: Space-time diagrams and time-series issued from time-resolved PIV data for configuration $L/\theta_0 = 82$, $L/D = 2.0$ with the same abstract in time as Figure 4.10 ($21 < t \frac{U_0}{L} < 55$). The space-time diagrams are obtained at (a) $y/D = 0.1$, (b) $y/D = 0$, (c) $y/D = -0.7$ (streamwise) and at (d) $x/L = 0.96$, (e) $x/L = 0.33$ (crosswise). Contour levels of vorticity fluctuations $\omega'_z D/U_0$ range from (a), -4.1 (dark) to 3.5 (light); (b), -10.7 to 5.5; (c), -3.2 to 3.5; (d), -7.4 to 5.7; (e), -2 to 2.1. Three characteristic time-series, for both streamwise and crosswise velocity fluctuations u'/U_0 and v'/U_0 , are extracted at intersections of these space-time planes: at the impingement, above the top-cavity plane (a ∩ d), on the top-cavity plane (b ∩ d); inside the main recirculation, (c ∩ e). Schematic (f) locates extraction regions.

travelling wave properties of each frequency related to locked-on mode, *ie.* the harmonic family $h f_a$. Indeed, since the velocity fields are both spatially and temporally resolved, it is possible to directly estimate the wavelength and phase-velocity associated with a given frequency, by using transfer functions between two locations within the shear-layer. The procedure is described in Section 3.1.3.

Transfer functions are estimated on crosswise component v' in the shear layer because it exhibits larger oscillations whose amplitude is more continuous in space than those of streamwise component u' , as seen Figures 4.4 & 4.12.(b & d). Estimate is performed for different x -values in the streamwise direction, at height $y/D = 0$, where turbulence intensity is maximum. Phases along x are referenced with respect to the signal at $x_0/L = 0.5$ (where $\phi = 0$) because the velocity fluctuations are too weak to provide a clean reference point at the cavity leading corner, $x/L = 0$. Similarly, at $x/L = 1$, boundary effects at the trailing corner may alter the phase. At mid-length, spectrum exhibits strong peaks, and the fluctuations are still exponentially increasing with space, indicating that linear instability approximation stands and non-linear effects do not play a significant role yet. Transfer functions are estimated at points distant by a multiple of $\delta x/L = 0.016$ from the reference point ($x_0/L = 0.5$). The plus/minus sign depends on whether the point under consideration is downstream or upstream, relatively to the reference point. The dominant frequency $f_a = 13.5$ Hz ($f_a L/U_0 = 0.98$), together with its first two harmonics

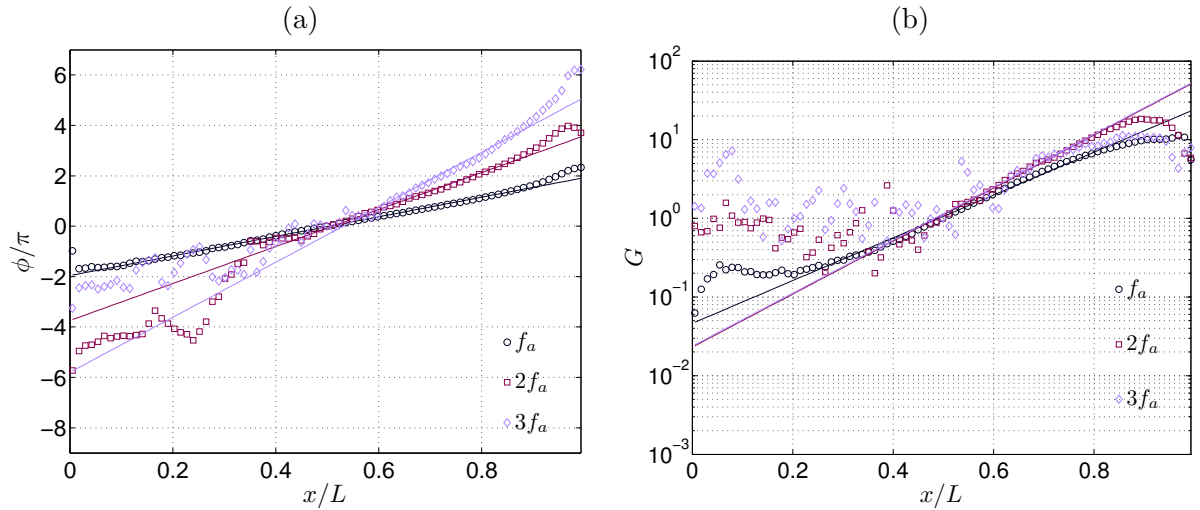


Figure 4.13: Streamwise evolution from trailing to leading corners of the unwrapped phase $\phi(x/L)/\pi$ (a) and amplitude $G(x/L)$ (b), for shear layer locked-on harmonic family $h f_a$, with $h = 1, 2, 3$, for the case $L/\theta_0 = 82$, $L/D = 2.0$.

$f_{a2} = 2f_a$ and $f_{a3} = 3f_a$ are investigated. In Figure 4.13.a, the unwrapped phase $\phi(x)$ is shown with respect to x/L for the main frequencies associated with self-sustained oscillations of the shear layer. The phase $\phi(\omega_a, x)$ varies quasi-linearly along the shear layer, as expected from progressive Kelvin-Helmholtz waves. Overall phase variation over L is close to 4π , indicating that the wavelength is of the order of $L/2$. More precisely, a linear regression on $\phi(x)$ for f_a , of the form:

$$\phi(\omega, x) = \alpha(\omega)x + \gamma(\omega), \quad (4.10)$$

Table 4.2: Wave characteristics for shear layer harmonic family $h f_a$ measured at $y/D = -0.05$.

(*)	f_*L/U_0	C_*/U_0	Λ_*/L	k_*L	ζ_*L
a	0.98	0.50	0.52	3.9π	6.3
$a2$	1.96	0.53	0.27	7.3π	7.8
$a3$	2.94	0.54	0.18	10.9π	7.8

is computed from $x/L = 0.1$ to $x/L = 0.9$, such as to avoid boundary effects. It gives an estimated mean dimensionless phase gradient (or normalised wavenumber) $k_aL = L(\partial\phi/\partial x)_{\text{mean}} = 3.9\pi$ for f_a . Equation 3.25 gives $\Lambda_a/L = 0.52 \simeq 1/2$. Corresponding phase velocity can be estimated at $C_a = 0.50U_0$, which matches the slope observed in space-time planes (Figures 4.12.(a,b)).

For the harmonics $2f_a$ and $3f_a$, the phase is not defined before $x/L \simeq 0.5$. Fitting $\phi(\omega_{a2}, x)$ from $x/L = 0.5$ to $x/L = 0.9$ gives the phase gradient $k_{a2}L = L(\partial\phi/\partial x)_{\text{mean}} = 7.3\pi$. The resulting wavelength is therefore $\Lambda_{a2}/L = 0.27$, which implies a phase velocity $C_{a2}/U_0 = 0.53$ m/s. Similarly, one obtains for the second harmonic $3f_a$, $k_{a3}L = 10.9\pi$ and $\Lambda_{a3}/L = 0.18$ and $C_{a3}/U_0 = 0.54$ m/s. As expected, phase velocities C_{ah} corresponding to every harmonic of the locked-on mode f_a are identical, which implies a non-dispersive medium with respect to the self-sustained oscillations of the shear layer. Indeed, $h f_a$ modes are not independent from one another. They all pertain to a single underlying Kelvin-Helmholtz wave. This wave is distorted by nonlinearities, thus it ends up decomposed into a harmonic family in Fourier space and yields the trivial linear dispersion relation:

$$C_a = \frac{2\pi f_{ah}}{k_{ah}} = \Lambda_{ah} f_{ah} \simeq \frac{U_0}{2} \quad \text{with } h = 1, 2, 3... \quad (4.11)$$

The growth rate ζ of shear layer travelling waves can be estimated from streamwise distributed transfer functions – see Equation 5.5. However, it is more sensitive to signal/noise ratio than phase. As a result, only the dominant frequency f_a has its amplitude defined across the cavity. A travelling wave is considered as linearly spatially unstable if ζ is constant along x , such that the amplitude of the mode grows exponentially as $e^{\zeta(x-x_0)}$. This is the case for ζ_a , constant from $x/L = 0.2$ to $x/L = 0.8$, that is before saturation and distortion nearby the trailing edge. Prior to linear growth, it must be noted that the dominant mode f_a is already enhanced just after the separation. This might be the signature of the feedback-loop responsible for the self-sustained oscillations of the shear layer.

On the contrary, growth rates corresponding to harmonics are obtained on a rather restricted region of the shear layer. In Figure 4.13.b, linear regressions on $(\partial \ln |G(\omega, x)|/\partial x)$ are performed such that $0.2 \leq x/L \leq 0.7$ for f_a , $0.5 \leq x/L \leq 0.8$ for $2f_a$ and such that $0.5 \leq x/L \leq 0.7$ for $3f_a$. Note that harmonics are likely to be only nonlinearly unstable, hence they are not expected to grow exponentially. Wave properties for $h f_a$ harmonics are collected in Table 4.2.2.

Transfer functions performed along the shear layer constitute the first step of a global space-time analysis, restricting only to two-point correlation along the shear layer. The next step consists in globally distributed time Fourier transforms, which yield the spatial structures associated with any temporal frequency of the spectrum.

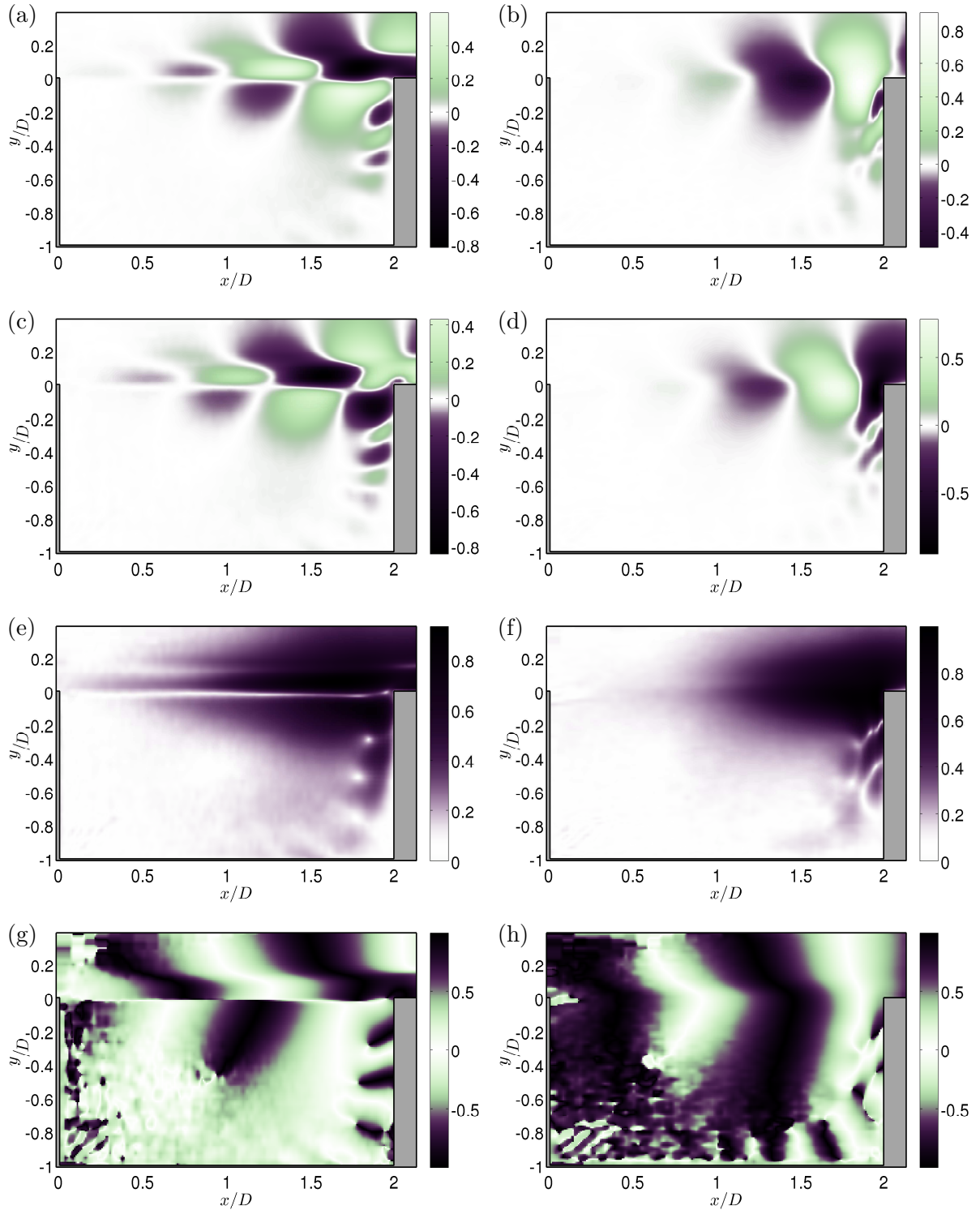


Figure 4.14: Global Fourier modes for frequency f_a in case $L/\theta_0 = 82$ & $L/D = 2.0$. *Top*: from streamwise u' (left) and crosswise v' (right) velocity fluctuations. Colours scale (a,b), real part; (c,d), imaginary part, (e,f) $\sqrt{\text{modulus}}$; (g,h) complex angle (in π units).

4.2.3 Spatial structure of the shear layer modes

The identification of the coherent structures constitutive of the flow can be achieved by applying *global* Fourier decomposition to time-resolved space-extended data issued from TR-PIV measurements. The procedure is described in Section 3.1.4 and in Basley et al. (2011). We refer to *global Fourier modes*, the spatial distribution of Discrete Fourier-transforms (DFT) in the entire field, associated with one temporal frequency. Considering the case $L/\theta_0 = 82$, $L/D = 2.0$, Fourier mode associated with locked-on frequency f_a is presented in Figure 4.14. For this first mode, many features are displayed for both components of velocity fluctuations u' and v' : real and imaginary parts, modulus and angle. The following remarks based on these figures can be generalised to other shear layer modes. For instance, similar results have been obtained in Basley et al. (2011) for a case $L/\theta_0 = 96$, $L/D = 2.0$.

As expected, growing oscillations are observed inside the shear layer, along the line $y = 0$ – see Figures 4.14.(a-d). Their wavelength is logically $\Lambda_a/L = 0.5$, the same as for transfer function in previous section. One remarks that real and imaginary parts are in phase quadrature. Coherently, the complex angle (or phase) shows a monotonic variation in the streamwise direction – Figure 4.14.(g,h) –, featuring a travelling wave.

Spatial structures differ from one component to another. While v' crosswise profiles are even functions, u' exhibits odd profiles along the shear layer. This is consistent with the literature, notably the results in Williams and Hama (1980). In other words, u' consists of two (roughly) anti-symmetrical domains on both sides of a streamwise line just below $y = 0$. This results in a zero-energy line in the intensity map displayed in Figure 4.14.e, and corresponds to a phase discontinuity in Figure 4.14.g. That distribution recalls of RMS components seen earlier in Figure 4.4. The shear layer mode associated with frequency f_a represents in fact most of the energy contained in the spectrum. Such a spatial distribution is the signature of an alley of eddies travelling downstream along the shear layer, in a cartesian reference frame (x, y) . That can be explained through a simplified model of purely azimuthal vortices, such that

$$\mathbf{v}_{eddy}(\mathbf{r}) = v_\theta(\mathbf{r}) \mathbf{e}_\theta. \quad (4.12)$$

It comes that induced fluctuations in the cartesian reference frame write as

$$u' \mathbf{e}_x + v' \mathbf{e}_y = v_\theta(\mathbf{r}) \sin \theta \mathbf{e}_x + v_\theta(\mathbf{r}) \cos \theta \mathbf{e}_y \quad (4.13)$$

Consequently, streamwise axis x is null on the line $\theta = 0, \pi$, carrying the centres of eddies. On the contrary, v' , projection on the crosswise direction, is maximal there.

Inflow vortices are visible along the forward facing step. Evolution of the angle seen in Figures 4.14.(g,h) shows eddies are advected downwards and then upstream close to the bottom of the cavity. Since those eddies yield by construction the same frequency as the self-sustained oscillations of the shear layer, primary and secondary travelling waves superimpose to produce an interference pattern depicted by slack water regions in intensity maps displayed in Figures 4.14.(e,f).

Finally, vorticity maps for both real and imaginary parts are given along with vector fields in Figure 4.15, in order to identify directly vortical structures. Vorticity distributions also exhibit a phase discontinuity or separation along the shear layer but it does not coincide with

the one observed for u' . Instead, it is located around the inflexion point. Similar results were briefly presented in Rowley et al. (2000). In spite of the impingement, the present results can be favourably compared to linearised stability theory of free shear layers. For instance, one can see the profiles of vorticity obtained in pioneer numerical work by Michalke in 1964 in the case of temporally growing waves: Figure 4.16 is directly printed from Michalke (1964). However, temporally amplified disturbances cannot predict the asymmetry and distortion exhibited by global Fourier mode at f_a . In order to take into account the non-periodical evolution of vorticity profiles along the shear layer, Michalke then proposed to consider spatially growing disturbances in Michalke (1965). *Figure 10* of the latter reference is provided in Figure 4.17.

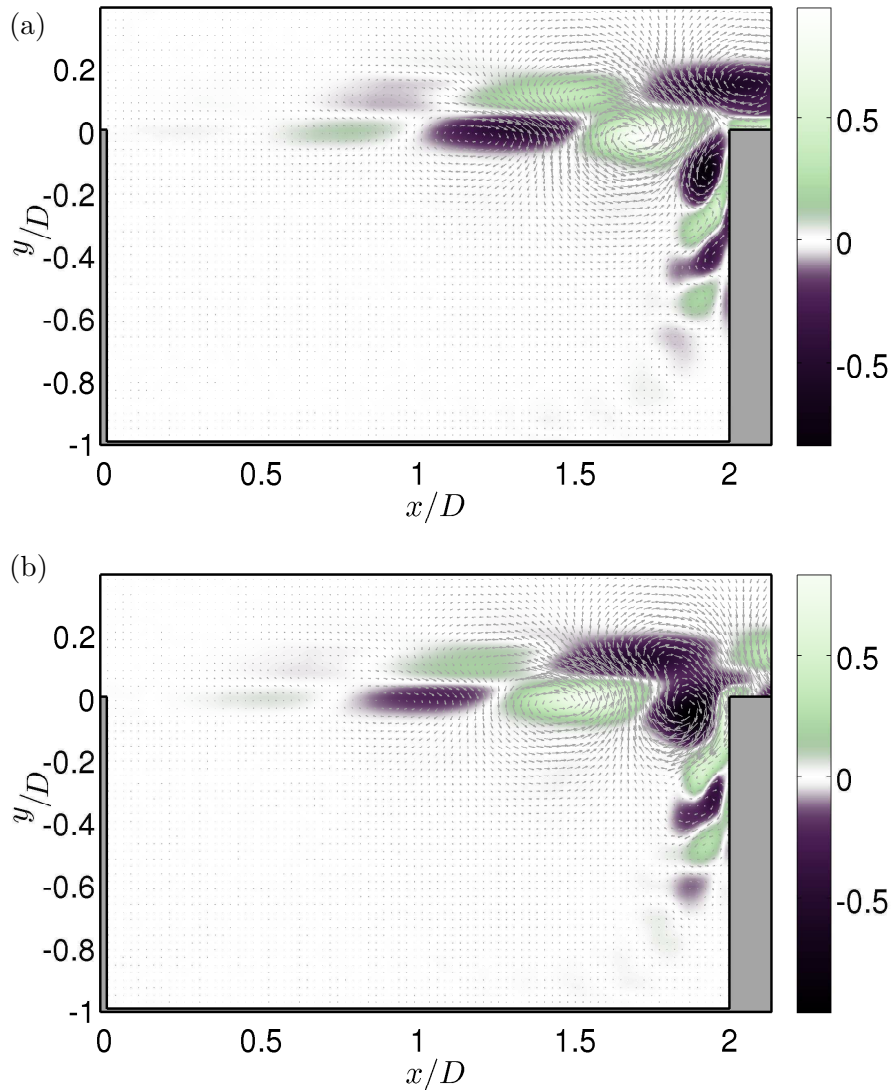


Figure 4.15: Global Fourier mode for frequency f_a in case $L/\theta_0 = 82$ & $L/D = 2.0$ (continued). Colours encode vorticity ω_z' , vector fields depict velocity, (a) real part, (b) imaginary part.

If one considers saturation which eventually occurs in a real flow, global Fourier modes associated with harmonics of the dominant frequency f_a yield the spatial structures corresponding to nonlinear distortion. Spatial structures associated with harmonics $2f_a$ and $3f_a$, in

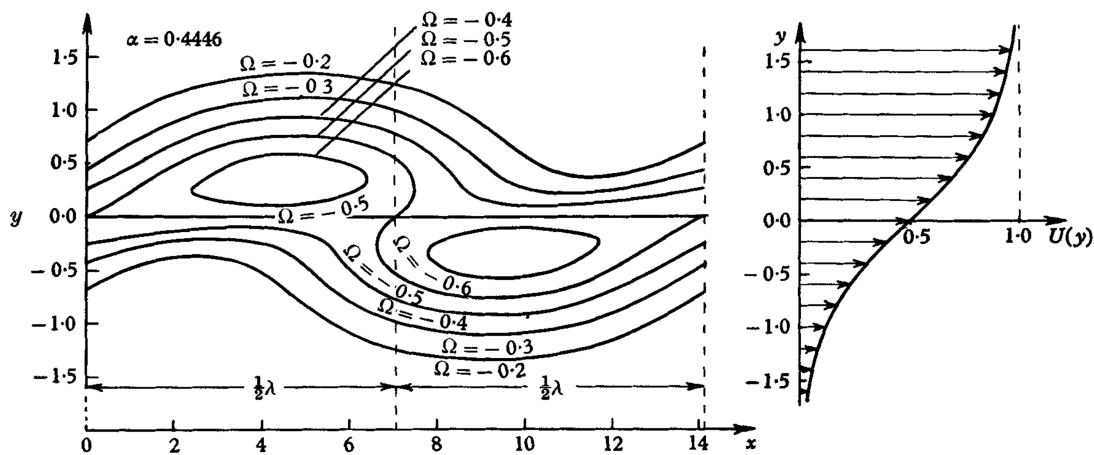


Figure 4.16: Lines of constant vorticity $\Omega = \bar{\Omega} + \omega'_z$ of the disturbed hyperbolic-tangent velocity profile for the wavenumber $\alpha = 0.4446$ of maximum amplification at the time $t = 0$ and a disturbance amplitude $\epsilon = 0.2$ (from Figure 10 in Michalke (1964)).

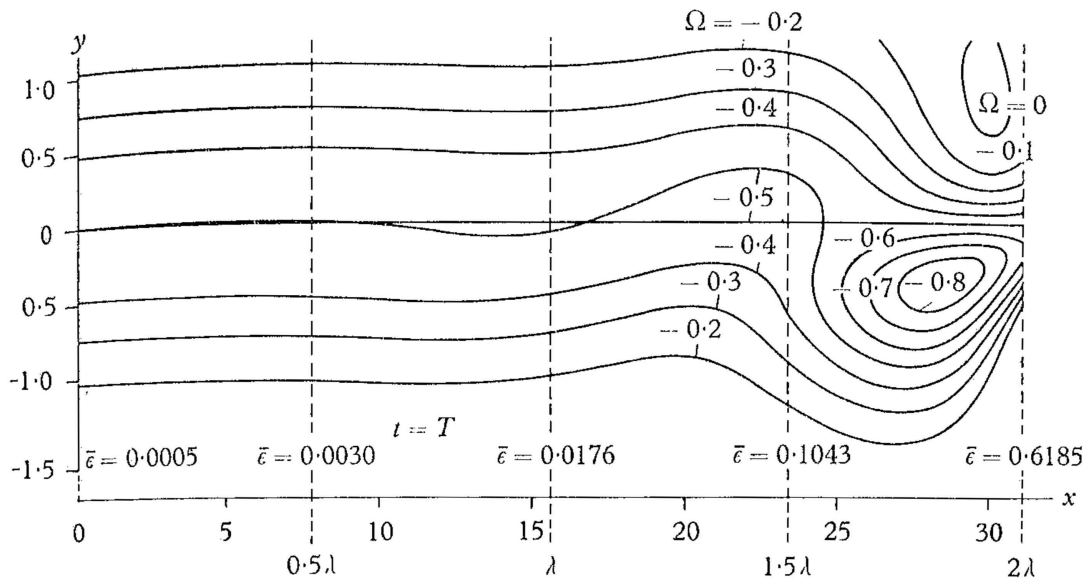


Figure 4.17: Lines of constant vorticity $\Omega = \bar{\Omega} + \omega'_z$ of the disturbed hyperbolic-tangent velocity profile in the spacewise case for the frequency 0.2067 of maximum amplification with a disturbance amplitude $\epsilon = 0.0005$ (from Figure 10 in Michalke (1965)).

Figures 4.18 & 4.19, respectively, concentrate in the vicinity of the impingement, that is where the self-sustained oscillations of the shear layer are of high amplitude. Depicted wavelengths get smaller when h is raised, as implied by the dispersion relation (Equation 4.11). Furthermore, oscillations are also visible along the cross-stream profiles. The resulting distribution organises as a *draughtboard* pattern of alternative vortical structures. Since crosswise space scales decrease the same way as streamwise ones (wavelengths) when h increases, higher harmonics correspond to finer structures, as observed in Sipp and Lebedev (2007); Ehrenstein and Gallaire (2008); Gloerfelt (2008)

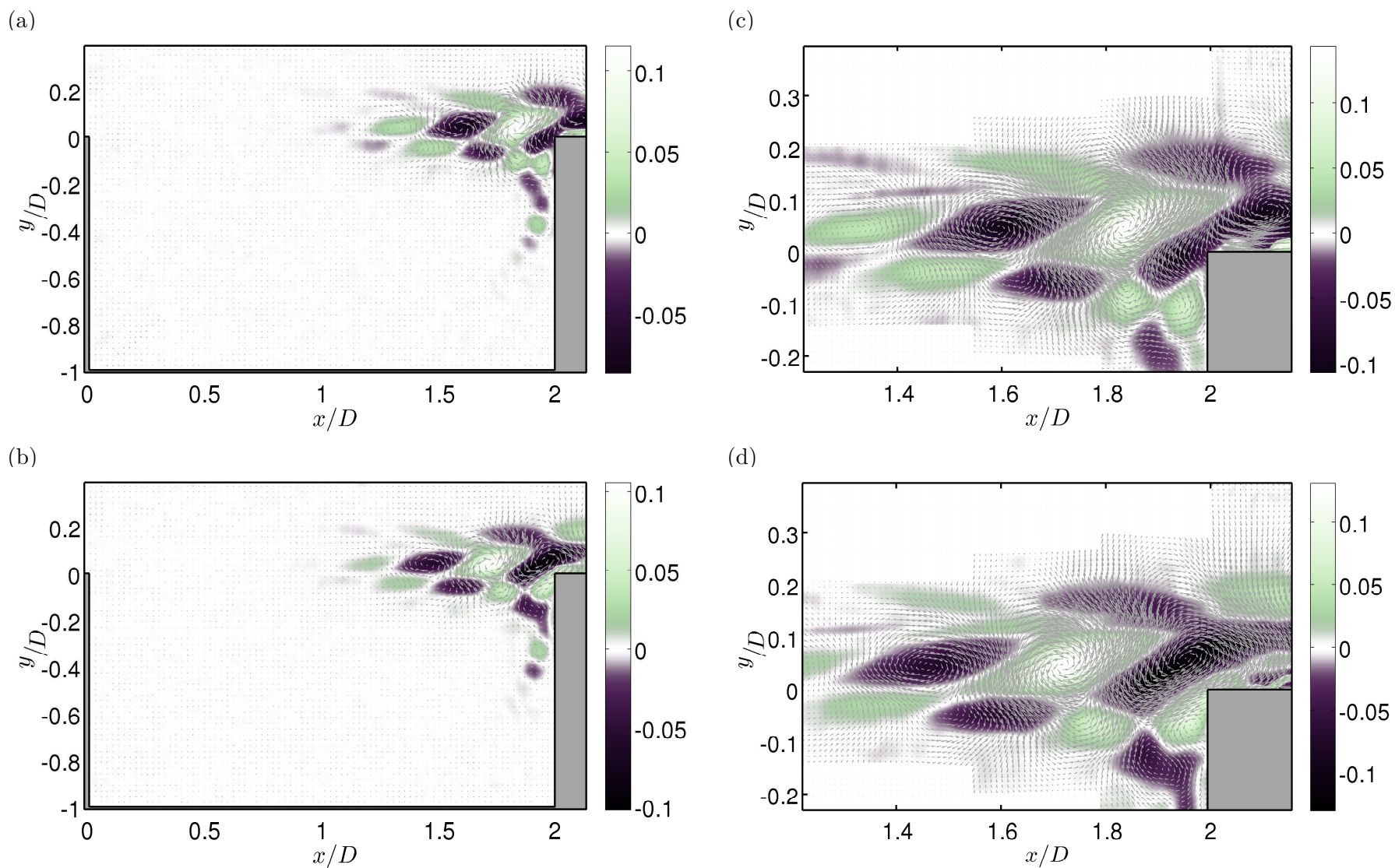


Figure 4.18: Global Fourier mode for first harmonic $2f_a$ ($St = 1.96$) in case $L/\theta_0 = 82$ & $L/D = 2.0$. Real part (top) and imaginary part (bottom) are displayed both in overview and close-up at the impingement. Colours encode vorticity and vector fields represent velocity.

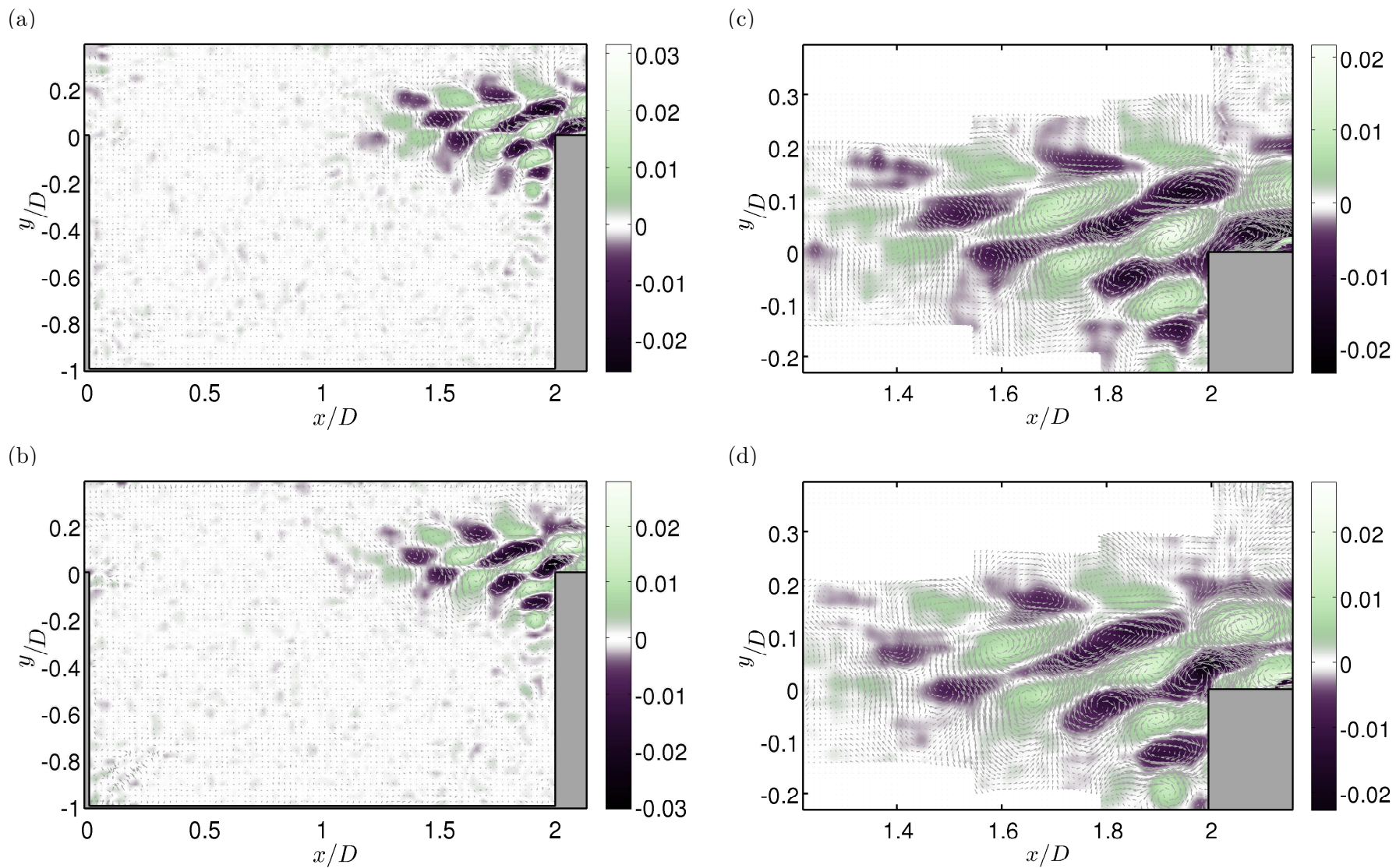


Figure 4.19: Global Fourier mode for second harmonic $3f_a$ ($St = 2.94$) in case $L/\theta_0 = 82$ & $L/D = 2.0$. Real part (top) and imaginary part (bottom) are displayed both in overview and close-up at the impingement. Colours encode vorticity and vector fields represent velocity.

4.3 Amplitude modulation

In general, dynamics of impinging shear layers do not restrict to a single harmonic series. As displayed earlier in Figure 4.5, spectra often exhibit secondary peaks, which do not necessary pertain to a harmonic family. Instead, these peaks have been identified as products of an *amplitude modulation* of the self-sustained oscillations at the impingement. They are named *side-band peaks* in the following.

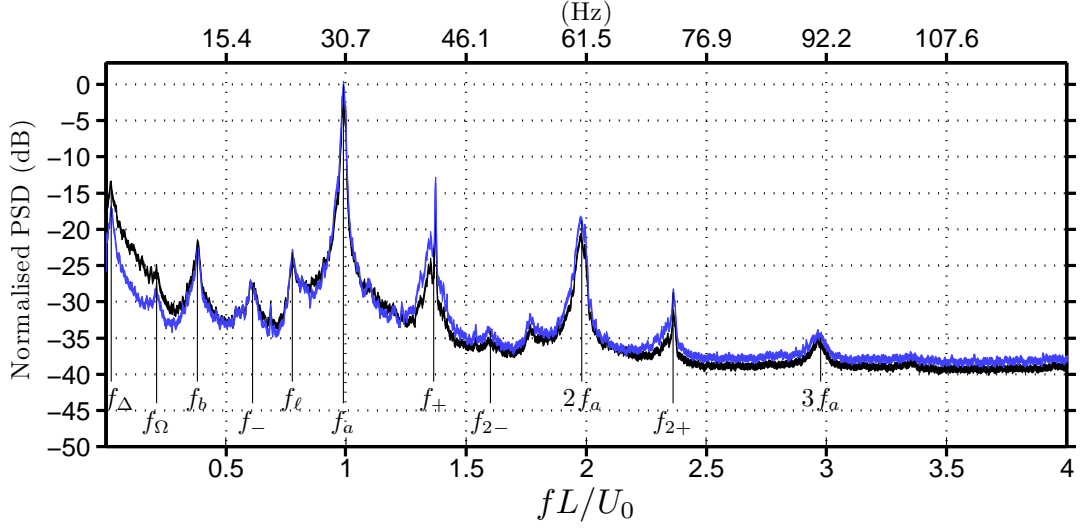


Figure 4.20: Normalised power spectral distribution of u' (black) and v' (blue) fluctuations for the case $L/D = 1.5$, $L/\theta_0 = 79$; out of the PIV time series and space-averaged over the impingement vicinity ($1.3 \leq x/D \leq 1.5$ and $-0.25 \leq y/D \leq 0.25$). Line heaviness corresponds to 95%-confidence interval.

4.3.1 Side-band peaks and low frequencies

An example of spectrum exhibiting such side-band peaks is given in Figure 4.20, for the case $L/D = 1.5$, $L/\theta_0 = 79$. The self-sustained oscillations of the shear layer are represented by the predominant harmonic family $f_{ah} = hf_a = [30.5 \text{ Hz}, 61 \text{ Hz}, 91.5 \text{ Hz}]$, corresponding to L -based Strouhal numbers $f_{ah}L/U_0 = [0.99, 1.98, 2.96]$. Then, the main side-band peaks belong to a triadic interaction involving hf_a harmonics and the low frequency $f_b = 11.7 \text{ Hz}$ ($St = 0.38$), the associated frequencies writing as

$$f_{h+} = hf_a + f_b \quad \text{and} \quad f_{h-} = hf_a - f_b \quad (4.14)$$

for right and left side-band peaks, respectively, located around the harmonic hf_a . For instance, the side-band frequencies associated with the dominant frequency f_a are $f_+ = f_a + f_b = 42.2 \text{ Hz}$ ($St = 1.37$) and $f_- = f_a - f_b = 18.8 \text{ Hz}$ ($St = 0.61$). Such a spectral signature is distinctive of saturated oscillations yielding the *carrier* frequency f_a modulated in amplitude by the *modulating* frequency f_b . In addition, note that two other low frequencies are observed: *i*) the very low frequency f_Δ appears again (here equal to 0.7 Hz, *ie.* $f_\Delta L/U_0 = 0.023$); *ii*) the modulating frequency $f_\Omega = 6.5 \text{ Hz}$ ($f_\Omega L/U_0 = 0.21$). The latter interacts with f_a and $2f_a$ to produce further side-band peaks $f_\ell = f_a - f_\Omega$ and $f_{2\ell} = 2f_a - f_\Omega$, respectively. Frequencies f_Δ and f_Ω are discussed in detail in Section 4.5.

Spectra only give a statistical information on flow features. To go one step further, Fig-

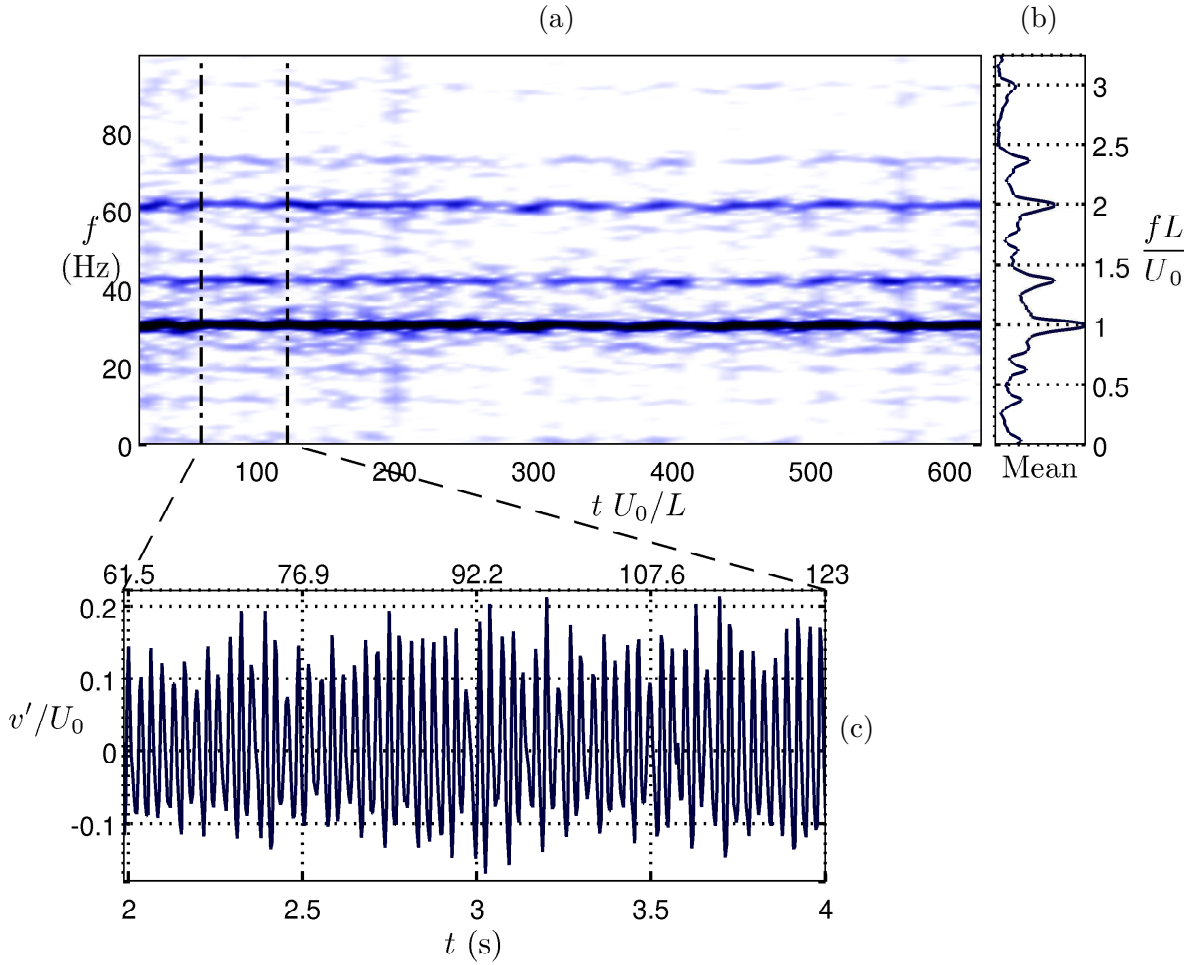


Figure 4.21: Temporal evolution of velocity fluctuations $v'(x_p, y_p, t)$ at point ($x_p/D = 1.35, y_p = 0$), out of TR-PIV data for the case $L/D = 1.5, L/\theta_0 = 79$. (a) Time-frequency diagram for the entire recording (21 s), colours encoding spectral density; (b) corresponding mean spectrum (in log scale); (c) time excerpt of the investigated time-series $v'(x_p, y_p, t)/U_0$, such that $61 \leq t U_0/L \leq 123$ in dimensionless time units ($2 \text{ s} \leq t \leq 4 \text{ s}$).

ure 4.21.a consists of a time-frequency diagram of velocity fluctuations v'/U_0 , extracted at the point ($x/L = 0.9, y/D = 0$) out of the TR-PIV velocity fields. This point is located in the core of the shear layer, just upstream of the impinging corner. The spectrogram is obtained by the mean of short-time Fourier transforms, using sliding windows of width $T_{wdw} = 1 \text{ s}$ ($T_{wdw} U_0/L = 30$) with 80%-overlap. The corresponding averaged spectrum is plotted in Figure 4.21.b.

The time-frequency diagram indicates the regime is permanent, exhibiting the dominant peak at f_a at all time, which confirms the case of a unique (constant) carrier frequency. The right side-band peak at $f_+L/U_0 = 1.37$ is always less energetic than carrier f_a . Coherently, the same applies to the right side-band peak at $f_{2+}L/U_0 = 2.36$. As for the left side-band peak at $f_-L/U_0 = 0.61$ and modulating frequency $f_bL/U_0 = 0.38$, they are both barely discernible in this time-series. They mostly appear in conjunction with f_+ , indicating periods of stronger amplitude modulation. Such a period is observed in the excerpt of velocity fluctuations time-

series $v'(t)/U_0$ plotted in Figure 4.21.c. Note that both the left side-band peak $f_\ell L/U_0 = 0.78$ and the right side-band peak $f_r L/U_0 = 1.20$ are also sporadically present, without respect to the primary modulation by f_b .

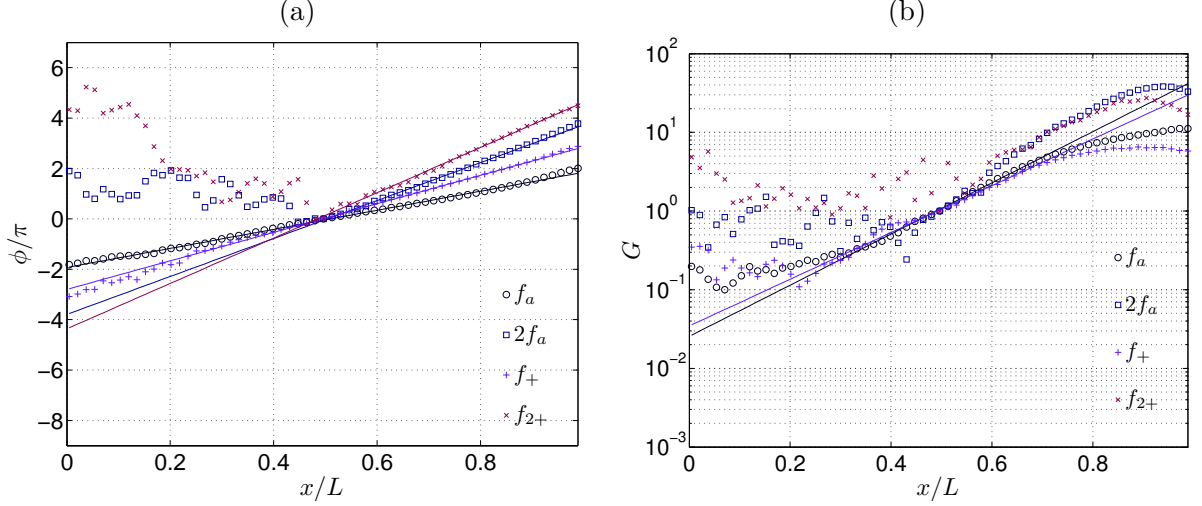


Figure 4.22: Streamwise evolution from trailing to leading corners of the unwrapped phase $\phi(x/L)/\pi$ (a) and amplitude $G(x/L)$ (b), for the shear layer modes f_a , $2f_a$, f_+ , and f_{2+} , for the case $L/\theta_0 = 79$, $L/D = 1.5$.

4.3.2 Wave properties of the side-band peaks

Investigating the wave properties of the side-band peaks relative to carrier frequency may be of interest. Do the side-band peaks pertain to the same wave family as hf_a harmonics? How does their amplitude grow along the shear layer?

Transfer functions give access to local phase and amplitude as functions of x/L for every selected spectral component. Results are plotted in Figure 4.22. Wave characteristics deduced from those plots can be found in Table 4.3.2. According to the amplitude evolution plotted in Figure 4.22.b, the considered shear layer modes are properly defined at least in the second half of the shear layer ($x/L \gtrsim 0.5$). There associated growth rates estimated from the slopes displayed in Figure 4.22.b are of the same order. Note that both $2f_a$ and f_{2+} are expected to be only nonlinearly unstable, produced through saturation and amplitude modulation, respectively. Consequently, constant growth rates seem irrelevant and in any case could only be estimated from a small portion of the plot.

The phase exhibits a linear increase for all considered frequencies, carrier ($f_a, 2f_a$) and side-band (f_+, f_{2+}) alike, indicating progressive waves. Remark notably that both amplitude and phase related to frequency f_+ point out a very coherent wave, defined as clearly as the dominant (carrier) wave at f_a . Furthermore, the phase velocities related to side-band frequencies are equal to those of carrier modes:

$$C_+ \simeq C_{2+} \simeq C_a \simeq 0.5U_0. \quad (4.15)$$

Therefore, carrier and side-band modes all pertain to the same non dispersive wave family. One may notice the phase-gap between leading and trailing edges $k_+L = 6\pi$, of the side-band peak

Table 4.3: Wave characteristics for the amplitude modulated regime (f_a and f_+ components) measured at $y/D = 0.05$

(*)	f_*L/U_0	C_*/U_0	Λ_*/L	k_*L	ζ_*L
a	0.99	0.53	0.53	3.8π	7.5
$+$	1.37	0.49	0.35	6.0π	6.8
$a2$	1.98	0.53	0.27	7.5π	-
$2+$	2.36	0.53	0.22	9.0π	-

f_+ , fulfils the phase relationship between leading and trailing edges ($\Delta\phi = 2n\pi$), which implies the right side-band peak f_+ is a locked-on mode at stage $n = 3$.

The second side-band peak f_{2+} on the other hand, do not satisfy such a relation, which suggests this mode has no connection with the pressure feedback loop. It is only a spectral signature of the amplitude modulation.

4.3.3 Modulating and side-band frequencies in the parameter space

More generally, amplitude modulation of the self-sustained oscillations is encountered in most of the cases investigated in the present study. In Figure 4.23, parametric diagrams depicting the evolution of locked-on Strouhal numbers against the dimensionless cavity length L/θ_0 (given in Section 4.1.4) are completed with low frequencies f_b and f_Ω . Most of the low frequencies are noted f_b and satisfy

$$0.3 \leq f_b L/U_0 \leq 0.45. \quad (4.16)$$

Frequencies f_b exist for various geometries and are independent of L/D . Recall that the locked-on frequencies collapse around $n = 1, 2, 3$ stages and more precisely, satisfy the feedback equation 4.7. Many of them can now be identified as side-band peaks associated with low frequencies f_b , which precisely correspond to the gap between two locked-on modes. Then, a question naturally arises: What does this amplitude modulation physically represent?

In other words, does the low frequency predates side-band frequencies? Or the other way around, does the side-band peaks come first and produce the low frequency by nonlinear interaction at the impingement?

Following Rockwell and Knisely (1980b); Knisely and Rockwell (1982), low frequency generation and amplitude modulation are indeed related to vortex-edge interaction at the impingement (see Section 1.1.5 for more references). However, there is no details regarding the selection of the particular frequency f_b . In particular, vortex-edge interaction exists in every case without respect to amplitude modulation occurrence. Therefore, it cannot explain alone the appearance of an amplitude modulated regime.

On the other hand, side-band frequencies f_\pm align continuously and equally with carrier frequencies f_a in the parametric space. This suggests a mechanism relying on cavity length resonance. Incidentally, linear stability analyses performed in highly unstable impinging shear layers, *ie.* $L/\theta_0 \gg 1$, have exhibited linearly growing modes whose frequencies are equidistant in the spectral space but not in an harmonic ratio. Such a spectral organisation designates all locked-on modes as linearly unstable, contrary to low frequencies f_b . Hence, f_b would only come up in the permanent regime, resulting from a nonlinear coupling between two co-existing locked-on global modes.

Nevertheless, time-frequency diagram as well as time-series (Figure 4.21) have shown that a single carrier frequency f_a is observed. The side-band peaks, the highest being at f_+ , only appear through amplitude modulation. One can assert that the energy carried by frequency f_+ is too small compared to that of the dominant frequency f_a to be observed as another mode of self-sustained oscillations. For instance, the spectrum in Figure 4.20 averaged over the region of impingement has shown a 12dB-gap between the peaks at f_a and f_+ .

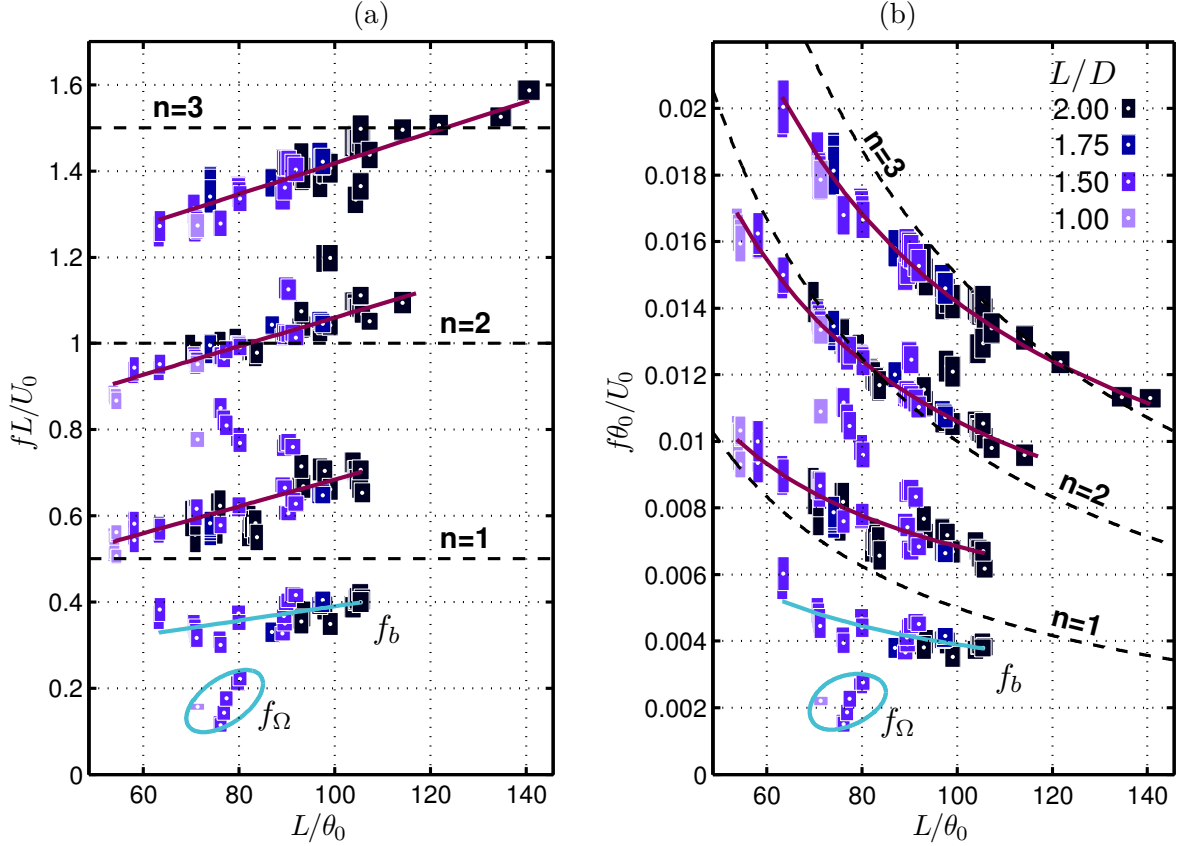


Figure 4.23: Parametric evolution of both shear layer and low frequencies as functions of the dimensionless cavity length L/θ_0 . Data are extracted from LDV spectra, for numerous cases investigated during the past few years. (a) Frequencies normalised as Strouhal numbers based on cavity length L . Linear fits (purple lines) correspond to the empirical locked-on condition (Equation 4.7). (b) The same data, divided by L/θ_0 , resulting in Strouhal numbers based on momentum thickness at separation θ_0 . Colours indicate different L/D configurations and rectangle dimensions represent uncertainties.

Ultimately, it can be inferred that the amplitude modulation of the self-sustained oscillations can be initially caused by the superposition of multiple (two) unstable locked-on modes, rather than the interaction with the low frequency f_b . The locked-on mode of highest amplitude saturates and produces harmonics, while the other, barely visible, only appears through the interference process. The low frequency f_b present in the spectrum would come out later *via* nonlinear interactions. Space-time analysis in the next section will bring more insight into the connection between side-band f_\pm and low frequencies f_b .

A few low frequencies have been designated as f_Ω peaks because they deviate from the above-described organisation. They cluster as

$$0.1 \leq f_\Omega L/U_0 \leq 0.22$$

and their associated side-band peaks ($f_a - f_\Omega$) do not satisfy the locked-on relation (Equation 4.7). Moreover, they seem to restrict to a narrow range of the parameter space (L/θ_0). Thus, this is likely the signature of another mechanism.

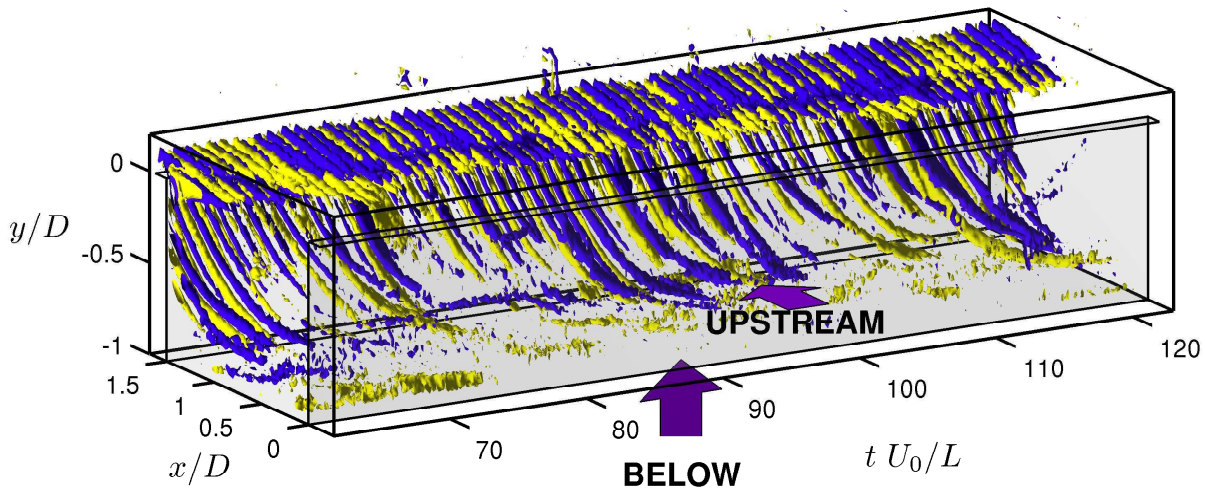


Figure 4.24: Iso-surfaces of vorticity fluctuations, $\omega'_z D/U_0 = 1.1$ (yellow) and $\omega'_z D/U_0 = -1.1$ (blue), in the space-time volume (x, y, t) , issued from time-resolved PIV data for configuration $L/\theta_0 = 79$. Only an excerpt of the entire set, such as $61 < t \frac{U_0}{L} < 123$, is displayed.

4.3.4 Space-time dynamics

Amplitude modulation mechanism and modulating frequency f_b are studied throughout their space-time dynamics, the same way as the self-sustained oscillations of the shear layer in Section 4.2. Figures 4.24 & 4.25 provide iso-vorticity surfaces in a 3D-representation of the space-time domain.

Similarly to the harmonic case in Section 4.2, one observes self-sustained oscillations of the shear layer inducing periodic inflows inside the cavity along the forward-facing step. The resulting stream downwards the cavity now fluctuates depending on amplitude variations of the flapping shear layer: larger oscillations at the impingement correspond to stronger inflows. In Figure 4.25, when one follows the inflows down along the forward-facing step, oscillations at the shear layer frequency f_a are overwhelmed by fewer and stronger vortical structures. These vortices are advected further upstream along the main recirculation. Remark that they seem to be periodically generated at a time scale about 2 to 3 times larger than the one of the self-sustained oscillations. This would be consistent with the low frequency $f_b L/U_0 = 0.38$ (11.7 Hz), relatively to dominant frequency $f_a L/U_0 = 0.99$ (30.5 Hz).

The correlation between strong vortical structures along the forward-facing step and f_b

frequency component is well-confirmed by the space-time slice in Figure 4.26.d. Oscillations at frequency f_b are even dominant in the time-series in Figure 4.26.(b \cap d). These oscillations correspond to modulations of the envelope of the self-sustained oscillations depicted in Figures 4.26.(a & a \cap d). In the following, the modulating frequency f_b will be known as *edge frequency*.

The travelling eddies observed in the (x, y, t) -volume near the bottom of the cavity (Figures 4.24,4.25) can here be identified as large scale fluctuations and followed across the space-time slice in Figure 4.26.c.

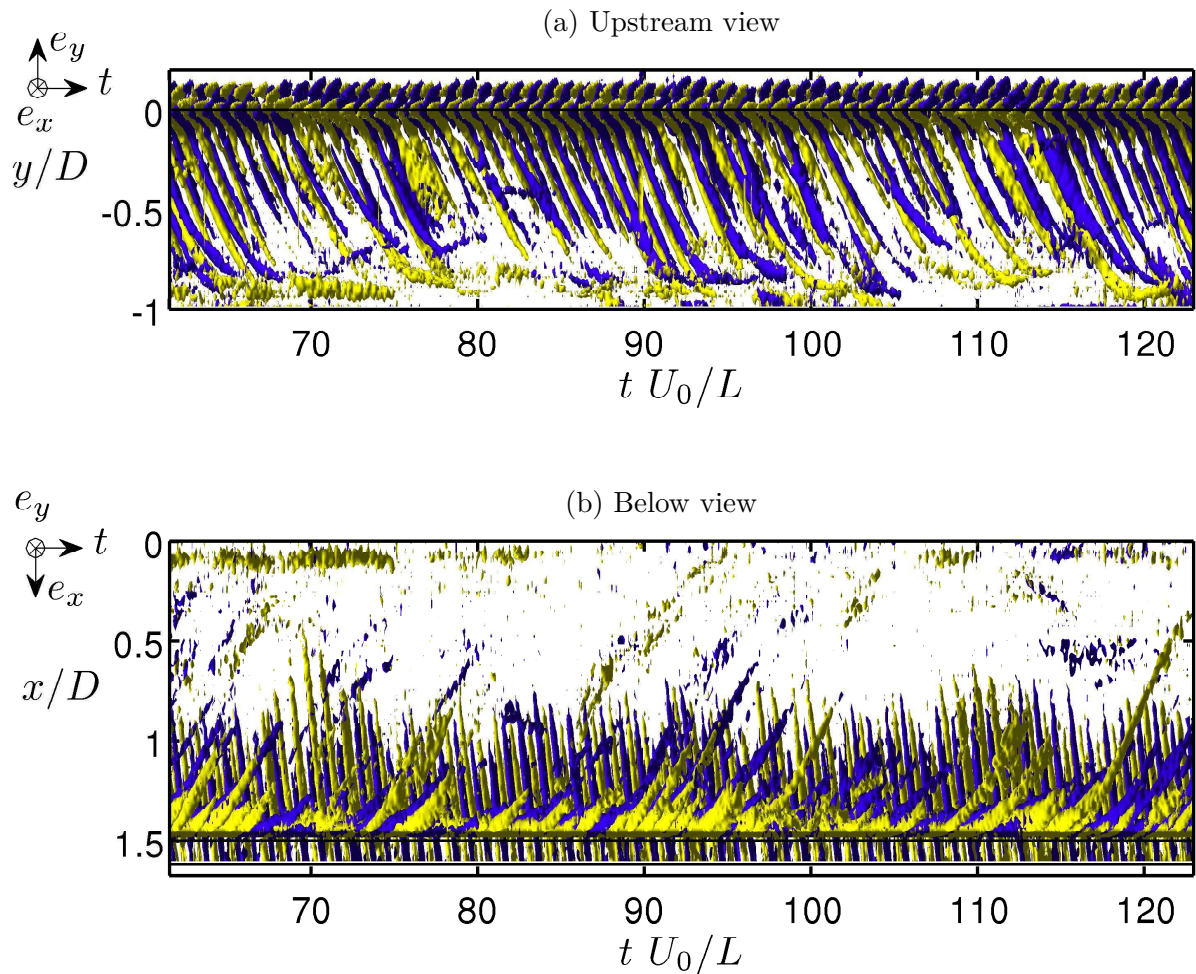


Figure 4.25: Same space-time domain as Figure 4.24, shown from upstream (a) and below (b).

Finally, even lower frequencies are observed when reaching the upstream half of the cavity – see Figures 4.26.(e & c \cap e).

To conclude, observations in the space-time domain have confirmed that the amplitude modulation occurs at the impingement and generates the *edge frequency* f_b through pulsating inflows. Broad-banded low frequency disturbances travel downwards the forward-facing step and then are advected back upstream *via* the main vortex. This mechanism might imply a

secondary delayed feedback for the flow, on top of the pressure-loop.

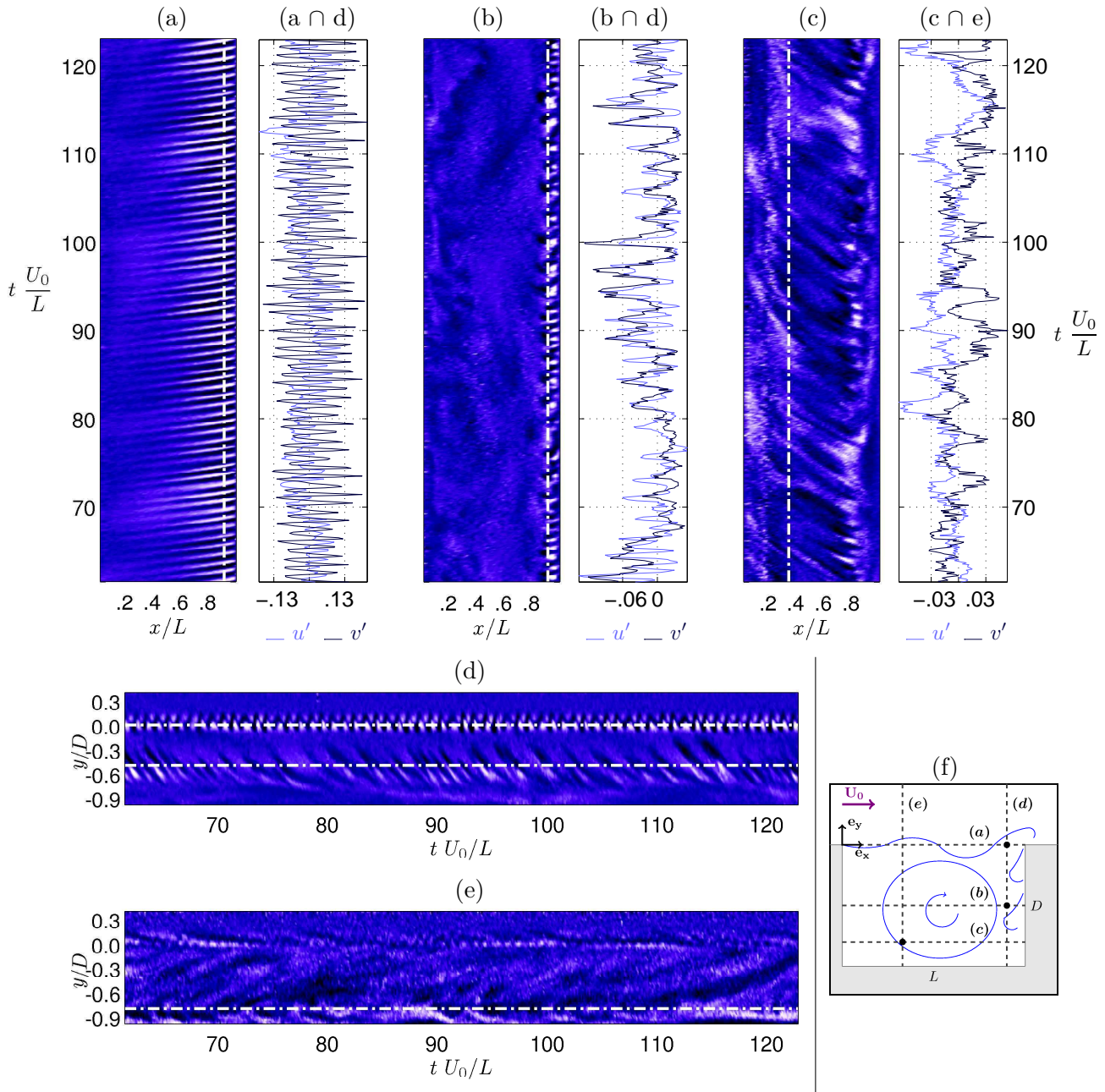


Figure 4.26: Space-time diagrams and time-series issued from time-resolved PIV data for configuration $L/\theta_0 = 79$, $L/D = 1.5$, with the same excerpt in time as Figure 4.24 ($61 < t \frac{U_0}{L} < 123$). The space-time diagrams are obtained at (a) $y/D = 0$, (b) $y/D = -0.5$, (c) $y/D = -0.8$ (streamwise) and at (d) $x/L = 0.9$, (e) $x/L = 0.33$ (crosswise). Contour levels of vorticity fluctuations $\omega'_z D/U_0$ range from (a), -7.0 (dark) to 5.5 (light); (b), -4.2 to 5.6; (c), -2.5 to 3.4; (d), -7.3 to 5.5; (e), -2.0 to 1.9. Three relevant time-series, for both streamwise and crosswise velocity fluctuations u'/U_0 and v'/U_0 , are extracted at intersections of these space-time planes: at the impingement, on the top-cavity plane ($a \cap d$); along the forward-facing wall of the cavity ($b \cap d$); upstream inside the main recirculation, ($c \cap e$). Schematic (f) locates extraction regions.

4.3.5 Spatial structure of the amplitude modulated shear layer

The dynamics of the amplitude modulated shear layer at the impingement has been observed as a whole. Global Fourier decomposition enables identifying the spatial structure associated with each characteristic time-scale (see Section 3.1.4 regarding the method). Presently, the global Fourier modes associated with the locked-on frequencies, namely the dominant (carrier) frequency $f_a L/U_0 = 0.99$ and its right side-band frequency $f_+ L/U_0 = 1.37$ are shown in Figures 4.27.(a,b) & 4.27.(c,d), respectively.

One observes that both spatial modes are very much alike that of dominant mode $f_a = 13.5 \text{ Hz}$ of the harmonic case in the previous Section (4.2). Those shear layer modes are composed of an alley of eddies of alternative vorticity, travelling downstream along the shear layer as indicated by the phase shift between imaginary and real parts. More precisely, the dominant mode exhibits two wavelengths along the cavity length as expected from a locked-on mode at stage $n = 2$. Regarding the mode associated with the right side-band frequency f_+ , it is very similar except it fits three wavelengths along the shear layer, so it rather corresponds to a locked-on mode at stage $n = 3$. This confirms the intrinsic instability of the spectral component f_+ , existing without respect to the amplitude modulation of the carrier wave f_a by the modulating frequency f_b .

In Figure 4.28 are given the global modes associated with the first harmonic of the carrier mode $2f_a$ and its corresponding right side-band frequency $f_{2+} = 2.36$. As expected, they pertain to the same non-dispersive wave packet: the associated space-scales decrease proportionally with the increasing frequencies, so as to travel at the same phase velocity.

More interesting is the global Fourier mode associated with the edge frequency $f_b = 11.7 \text{ Hz}$ ($St = f_b L/U_0 = 0.38$) in Figure 4.29.(a,b). It shows a travelling mode, as indicated by the shift between real and imaginary parts. It arises just before the impingement and then describes a travelling wave along the forward-facing step of the cavity. One observes an alley of counter-rotating vortex pairs travelling downwards. This constitutes the by-product of the amplitude modulation of the self-sustained oscillations in the shear layer. Indeed, larger oscillations at the impingement imply greater inflows into the cavity. These inflows are then advected away from the impingement, together with induced counter-rotating eddies, *via* the main recirculation.

The global Fourier mode associated with the left side-band frequency $f_- = f_a - f_b = 18.8 \text{ Hz}$ ($f_- L/U_0 = 0.61$), in Figure 4.29.(c,d), exhibits shear layer oscillations of wavelength $\lambda_- \approx L$ – that is a locked-on mode at stage $n = 1$ – but energy levels are too low to see any coherent vortical structure arising along the shear layer. Like other shear layer-related modes, the oscillations induce inflows into the cavity at the impingement. However in that case, the alley of alternative vorticity cells travelling along the forward-facing step are particularly energetic relatively to self-sustained oscillations. The spatial signature of this frequency f_- appears quite similar to the one of edge frequency f_b . This might indicate that f_- component is rather due to the by-product of amplitude modulation (nonlinearly induced by f_b) than to a linear unstable mode like the right side-band peak at f_+ .

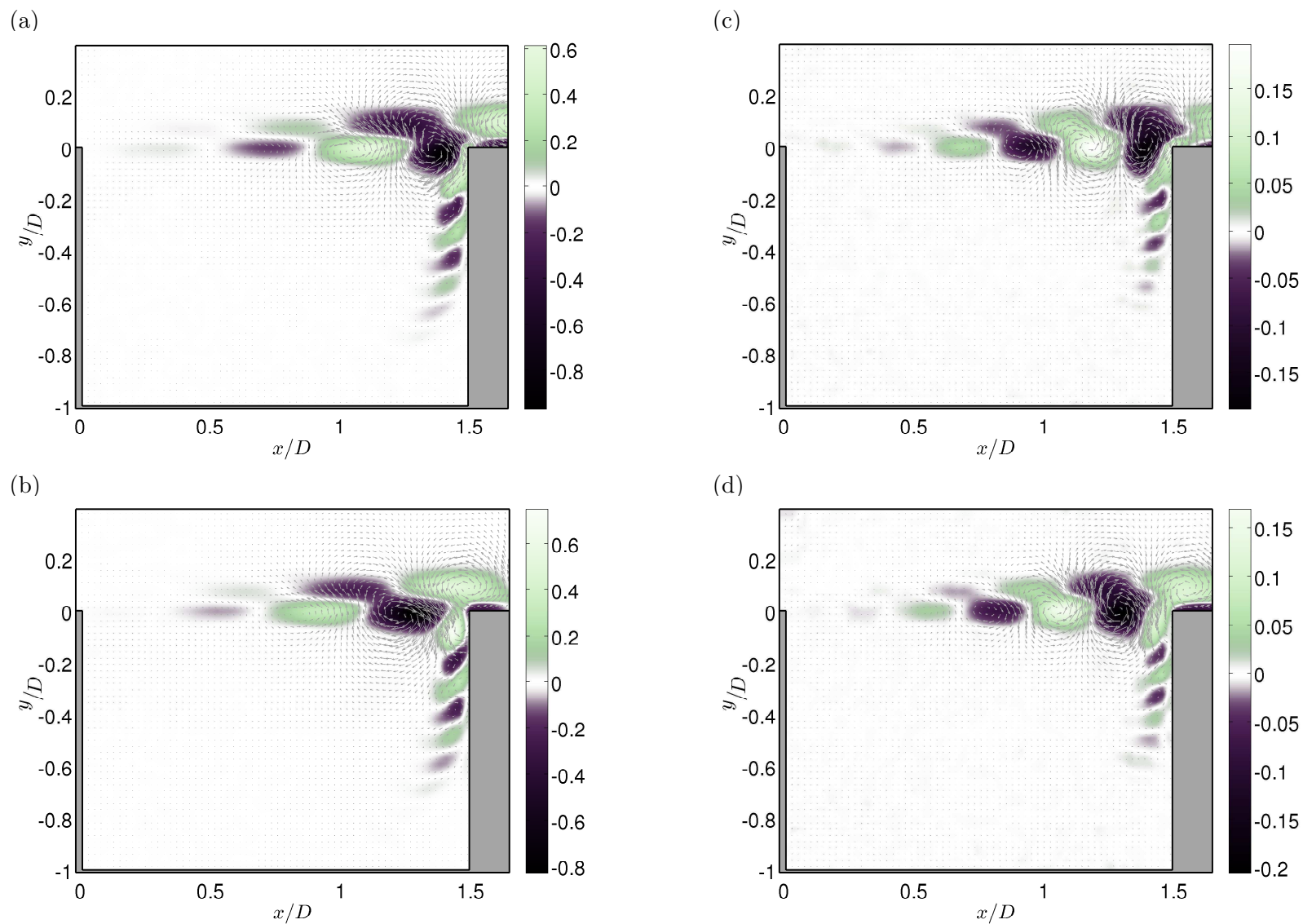


Figure 4.27: Global Fourier modes for the predominant locked-on frequencies, (a,b), carrier mode f_a ; (c,d), right side-band frequency f_+ in case $L/\theta_0 = 79$ & $L/D = 1.5$. Real part (top) and imaginary part (bottom) are displayed with colours encoding vorticity and vector fields representing velocity.

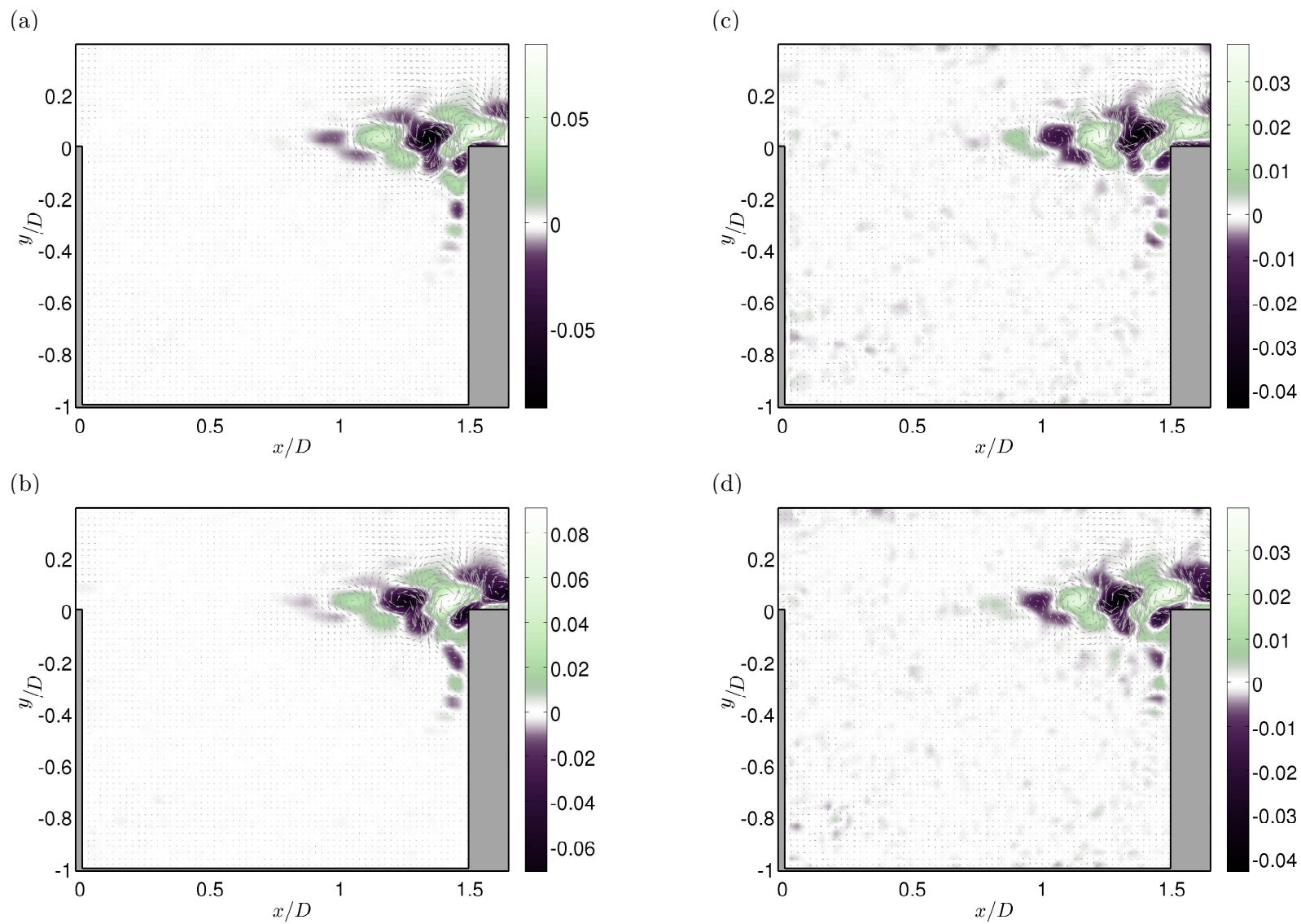


Figure 4.28: Global Fourier modes for (a,b), the first harmonic $2f_a$; (c,d), the second-rank side-band frequency f_{2+} , in case $L/\theta_0 = 79$ & $L/D = 1.5$. Real part (top) and imaginary part (bottom) are displayed with colours encoding vorticity and vector fields representing velocity.

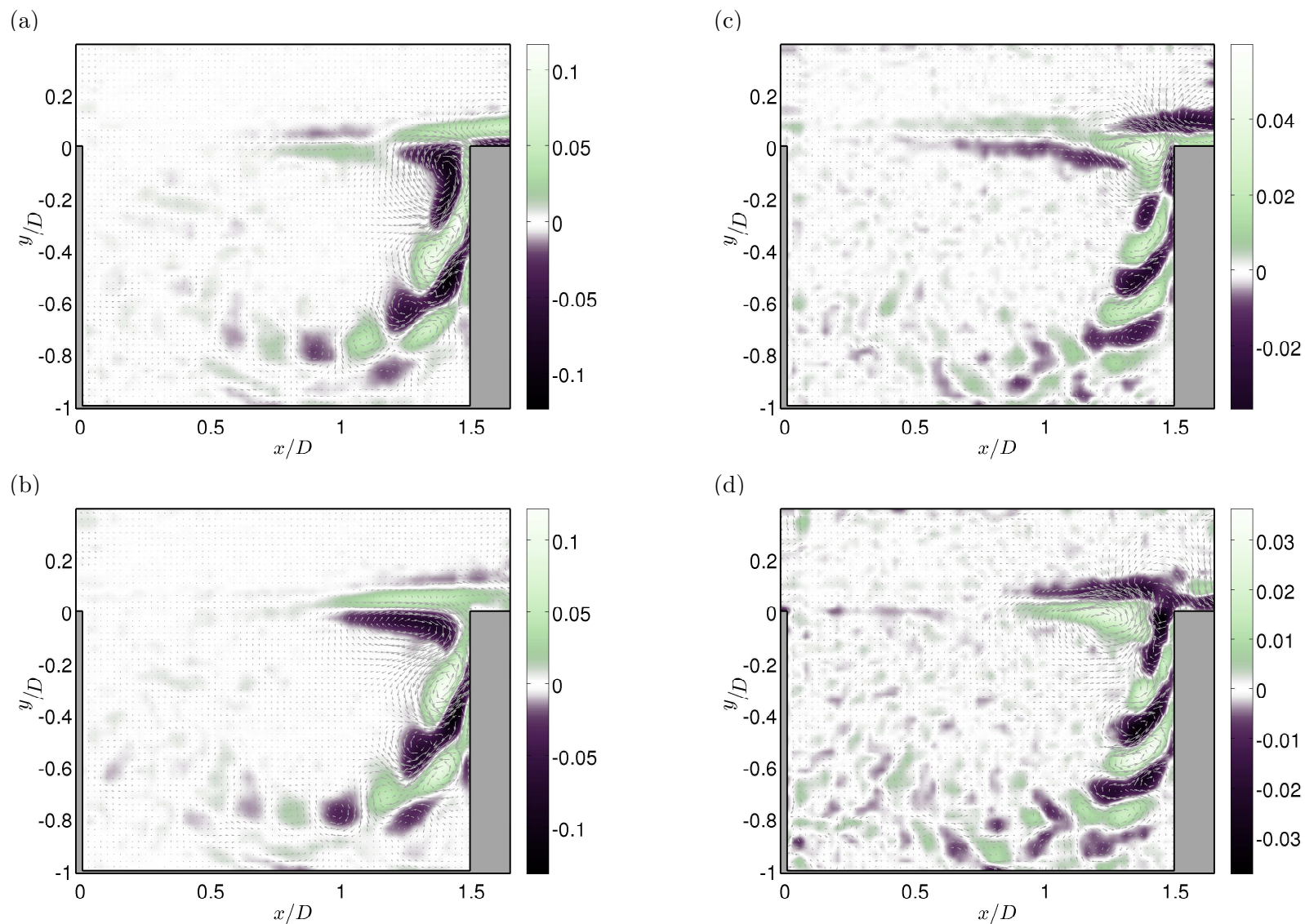


Figure 4.29: Global Fourier modes for (a,b), the edge frequency $f_b = 11.7$ Hz; (c,d), the left side-band frequency $f_- = 18.8$ Hz, in case $L/\theta_0 = 79$ & $L/D = 1.5$. Real part (top) and imaginary part (bottom) are displayed with colours encoding vorticity and vector fields representing velocity.

Note that the relative contributions of the two side-band peaks f_{\pm} vary with the dimensionless cavity length L/θ_0 . Configurations other than ($L/D = 1.5$, $L/\theta_0 = 79$) can exhibit a more energetic left side-band peak. For instance, the LDV spectra plotted for cases ($L/D = 2.0$, $L/\theta_0 = 70$) and ($L/D = 2.0$, $L/\theta_0 = 75$) in Figure 4.5 present only left side-band peaks. Located around $St = f L/U_0 \simeq 0.5$, these spectral components correspond to locked-on modes at stage $n = 1$.

Another instance is found for the case studied in Section 4.2. If one recalls the frequency detected as the sub-harmonic $f_a/2$ in Figure 4.9, one can remark that the broad-band peak is actually the conjunction of both modulating frequency $f_b L/U_0 \simeq 0.4$ and left side-band frequency $f_- = f_a - f_b \simeq 0.6$. The amplitude of these peaks indicates the self-sustained oscillations are indeed only slightly amplitude modulated.

4.3.6 Main remarks on the amplitude modulated regime

In this section, the interest was on the amplitude modulation of the self-sustained oscillations in the impinging shear layer. One could realise that amplitude modulation generally involves several locked-on modes – satisfying the phase-locking condition between separation and impingement $\Delta\phi = 2n\pi$ – and a low (modulating) frequency f_b .

(i) One locked-on mode is selected and enhanced and produces harmonics: it corresponds to the carrier family $h f_a$ (with $h = 1, 2, 3, \dots$).

(ii) The other locked-on modes may become side-band peaks $f_{\pm} = f_a \pm f_b$. Nonlinear effects produce side-band peaks around the carrier harmonics, *ie.* $f_{h\pm} = h f_a \pm f_b$.

(iii) The edge frequency f_b corresponding to oscillations of the envelop is initially generated by the interaction of the locked-on modes at the impingement. Then the global organisation of the flow induces a feedback in bringing the disturbances at frequency f_b back downstream into the shear layer, reinforcing the amplitude modulation.

Every shear layer mode pertains to the same non-dispersive wave packet travelling at the same phase velocity $C_a \simeq U_0/2$ (Kelvin-Helmholtz waves). In other words, each frequency-wavenumber pair corresponding to a locked-on mode is proportionally related, such that

$$4\pi \{St_{ah,h\pm}\} \simeq \{k_{ah,h\pm}\} L \quad \forall h \in [1, 2, 3, \dots] \quad (4.17)$$

Also, both carrier and side-band frequencies verify the feedback relation (Equation 4.7) proposed in Section 4.1.4 for self-sustained oscillations frequencies. Finally, remember that the selection of locked-on modes is governed by the control parameter L/θ_0 . The amplitude of the locked-on modes, carrier and side-band alike, varies continuously across the parameter space depending on L/θ_0 . Most of the cases under study organise around a stage $n = 2$ carrier, nonetheless f_a actually goes from one stage n to another when L/θ_0 is modified. In the next section, the investigation focuses on the transitions from one stage n to another $n \pm 1$.

4.4 Mode switching and overmodulation

The previous section has shown that the amplitude modulation of the self-sustained oscillations near the impingement is primarily due to the superposition of multiple locked-on modes, existing simultaneously in the shear layer. For the previously investigated case, the spectrum was organising around a carrier f_a and side-band peaks f_{\pm} at least an order of magnitude below.

What happens when the system exhibits a regime in which two locked-on modes are evenly unstable?

4.4.1 Time-frequency dynamics

In Figure 4.30 is depicted the time evolution of the crosswise velocity fluctuations v' extracted out of TR-PIV data inside the impinging shear layer for the control parameters $L/D = 1.75$, $L/\theta_0 = 96$. The time-series is extracted in the core of the impinging shear layer ($x_p/D = 1.35$, $y_p/D = 0$). A time-frequency diagram in Figure 4.30.a is processed the same way as in previous section. It shows that dominant frequencies seen in the averaged spectrum (Figure 4.30.b) are not persistent anymore. Naming the two locked-on frequencies at play: f_a ($St_a = f_a L/U_0 = 1.03$) corresponding to the most energetic peak, and the right side-band frequency f_+ ($St_+ = f_+ L/U_0 = 1.39$), one observes a competition between those two modes. There are time periods during which f_a is dominant ($130 \leq tU_0/L \leq 280$), time periods with both frequencies co-existing simultaneously ($0 \leq tU_0/L \leq 120$), and time periods when f_+ drastically overcomes f_a ($280 \leq tU_0/L \leq 380$).

This is the signature of a system experiencing *mode switching* or *intermittency*. That versatile and non periodic phenomenon was discussed in the literature review (Section 1.1.4). Mode switching is often considered as implying “jumps” from one regime of oscillation to another. The transitions appear as discontinuities in the spectrum. The *transitions* between different regimes are indeed rather abrupt but not within one cycle of oscillation. It is interesting to study the mode switching process in the frame of signal processing: that is with regards to temporal evolutions of both amplitude and carrier of the signal under consideration. Close-ups in time are realised and corresponding time-series are plotted in Figures 4.30.(c,d) in order to probe directly the time-fluctuations.

- ($1s \leq t \leq 3.9s$) The first sequence under investigation is a period of co-existence of the two modes, recalling what was observed for the amplitude modulated case in Section 4.3. Levels of energy are rather even in the present case (see Figure 4.30.a). The close-up time-series plotted in Figure 4.30.c exhibits tremendous amplitude modulations at almost any given time of the excerpt. This is completely consistent with the co-existence of two modes. Superimposing waves of equivalent amplitude indeed induces *overmodulation*. As in the previous section, the envelope oscillates at the difference frequency $f_+ - f_a = f_b$, but with far higher amplitudes leading to drastic distortion of the signal (null or even negative envelope). Regarding the carrier frequency, as the second component f_+ grows closer to dominant component f_a , the carrier is no more approximately equal to f_a but in the range between the two frequencies. It does not show up in the spectrum but physically, it corresponds to the small time-scales of the signal and evolves continuously depending on the relative amplitude of the two peaks.

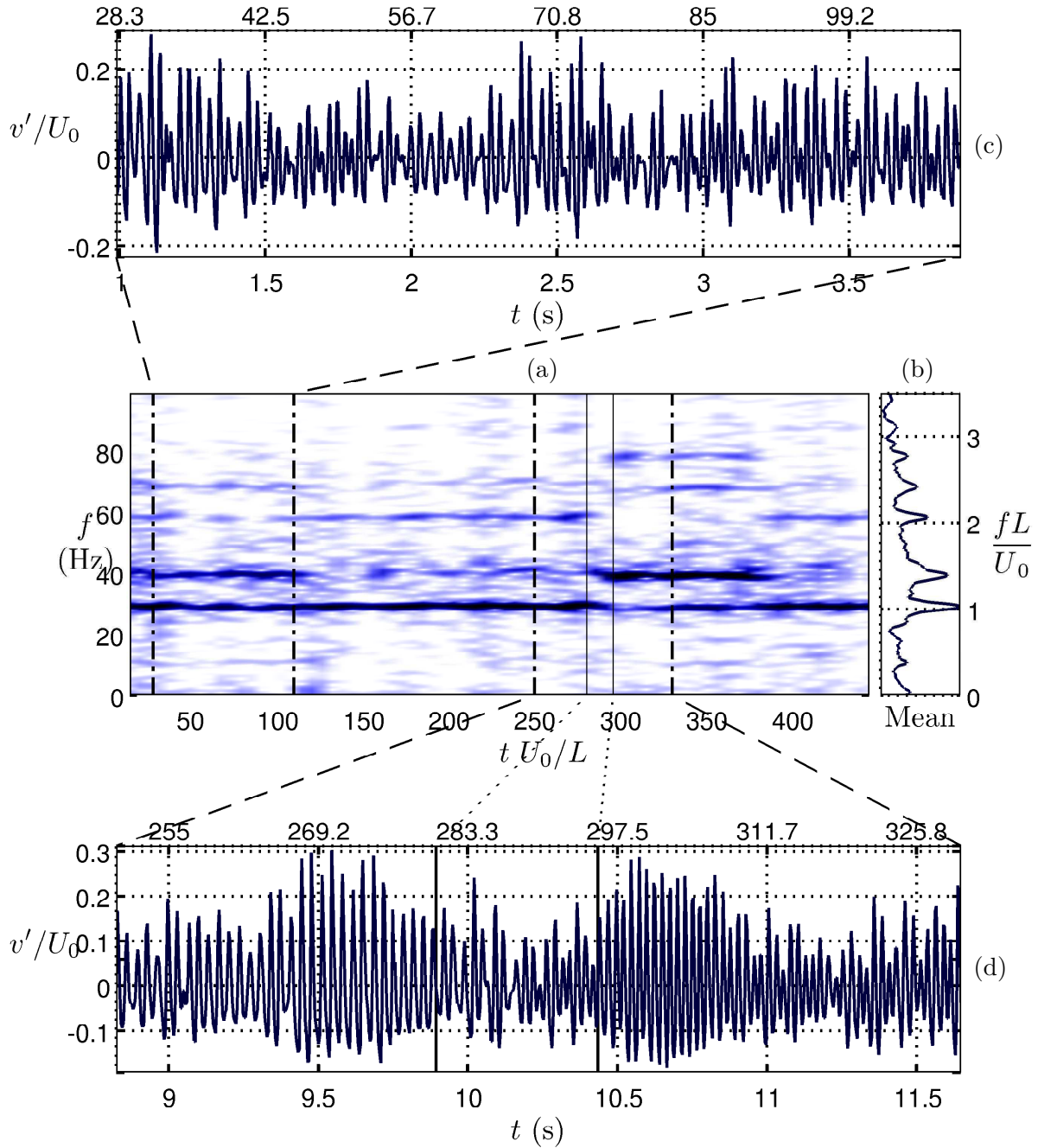


Figure 4.30: Temporal evolution of velocity fluctuations $v'(x_p, y_p, t)$ at the extraction point $(x_p/D = 1.35, y_p = 0)$, out of TR-PIV data for the case $L/D = 1.75, L/\theta_0 = 96$. (a) Time-frequency diagram for the entire recording (16 s), colours encoding spectral density; (b) corresponding mean spectrum (in log scale); Two time excerpts of the investigated time-series $v'(x_p, y_p, t)/U_0$ are displayed such that (c), $28 \leq t U_0/L \leq 110$ in dimensionless time units ($1 \text{ s} \leq t \leq 3.9 \text{ s}$); (d), $250 \leq t U_0/L \leq 330$ ($8.8 \text{ s} \leq t \leq 11.6 \text{ s}$)

The nonlinear interactions are modified by such a regime. There can be almost no energy detected for any harmonic of either frequencies f_a or f_+ , whereas an harmonic $2f_a$ is clearly visible when f_a is on its own (for $130 \leq tU_0/L \leq 280$). This likely implies that the energy of f_a is drained out by the presence of another dominant mode f_+ . Instead, energy levels are quite high for the second right side-band peak $f_{2+} = f_a + f_+ = 68.3$ (St= 2.41). Such an energy spike at that frequency is produced nonlinearly by the two locked-on modes f_a and f_+ .

•(8.8s $\leq t \leq 11.6$ s) The second closeup in Figure 4.30 consists of four successive periods: one first observes oscillations at f_a , then a transition towards the mode f_+ occurs, leading to a period with f_+ alone, and finally the oscillating regime at f_+ undergoes interferences of the mode f_a , rising again. It can be seen that the co-existence of the two modes implies again an overmodulation of the signal. Each time the amplitude of the oscillations is forced to zero due to that overmodulation, the frequency is no more defined. As a result, the system can lock on one or the other available modes.

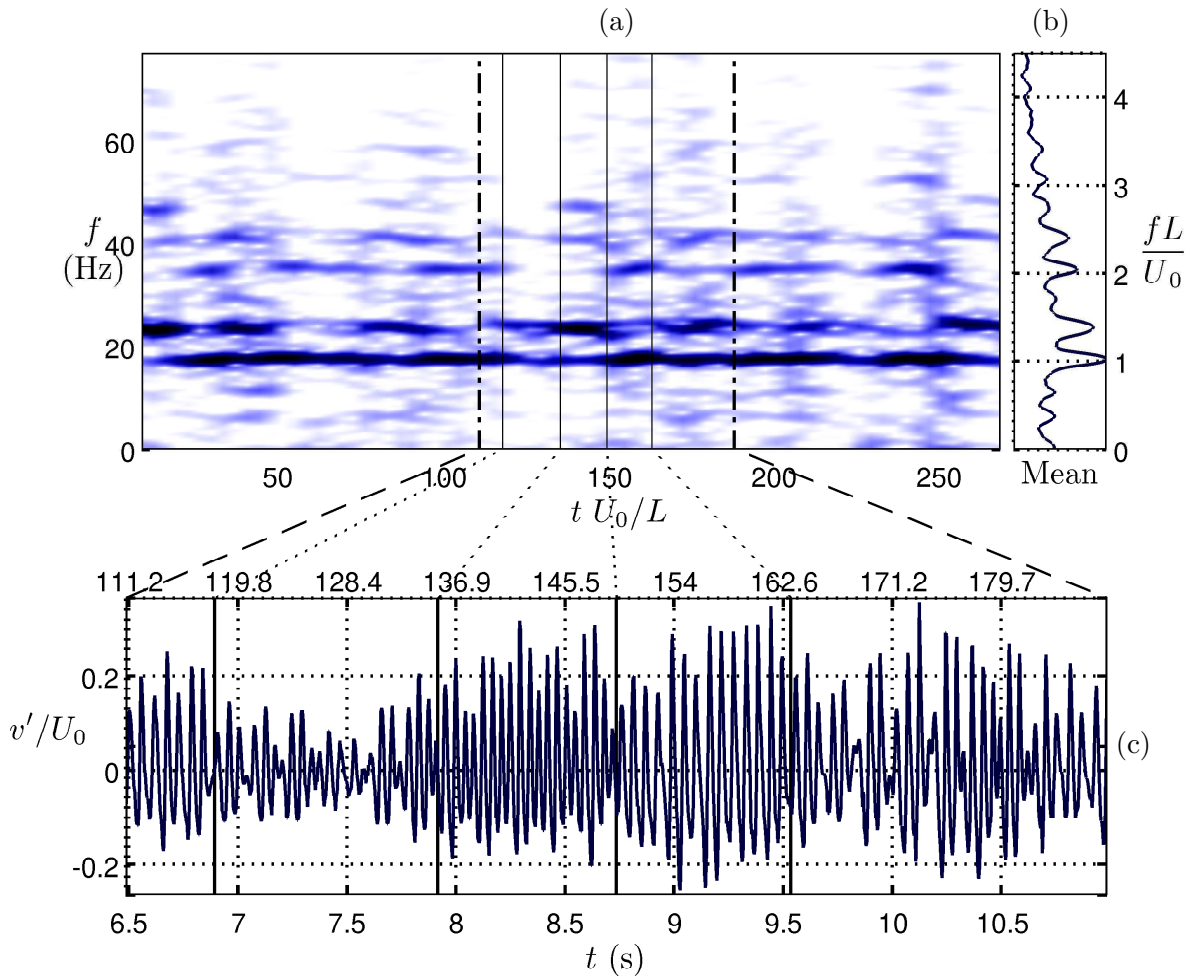


Figure 4.31: Temporal evolution of velocity fluctuations $v'(x_p, y_p, t)$ at the extraction point ($x_p/D = 1.70, y_p = 0$), out of TR-PIV data for the case $L/D = 2.0, L/\theta_0 = 91$. (a) Time-frequency diagram for the entire recording (16 s), colours encoding spectral density; (b) corresponding mean spectrum (in log scale); (c) time excerpt of the investigated time-series $v'(x_p, y_p, t)/U_0$, such that $111 \leq tU_0/L \leq 188$ in dimensionless time units ($6.5 \text{ s} \leq t \leq 11.0 \text{ s}$).

Another case is presented in Figure 4.31. Obtained for a different geometry $L/D = 2.0$ and control parameter $L/\theta_0 = 96$, it presents nonetheless a similar spectral organisation (Figure 4.31.b). The time-frequency dynamics shows numerous transitions between the two locked-on modes (Figure 4.31.a). In particular, a very abrupt transition from f_+ to f_a at $t \simeq 8.7$ s. This configuration presents a constant overmodulated state since the two locked-on modes are almost always present with variable intensities. This is indicated by the coupling frequency $f_{2+} = f_a + f_+$.

4.4.2 Saturation of the second locked-on mode: two harmonic families

One of the major changes in the intermittent regimes is the rising of second harmonic family $h f_+$ in competition with the (initially) dominant family $h f_a$. The spectral signature is no more organised around a unique carrier harmonic family with side-band peaks. One of the side-band peaks is energetic enough to saturate and thus produce harmonics of its own. This is illustrated by the spectrum in Figure 4.32. A peak at $2 f_+$ now rises on top of other side-band peaks. Of course, this can already be observed in the time-frequency diagrams during the periods when f_+ overcomes f_a and becomes the carrier of the self-sustained oscillations. This is the case for instance, in Figure 4.31 for $7.9 \text{ s} \leq t \leq 8.7 \text{ s}$.

Remark that noting f_a the peak at 29.2 Hz and f_+ the right side-band peak at 39.4 Hz is an arbitrary choice because f_a is more present than f_+ and therefore has a higher energy level in the spectrum. An evolution of the presence ratio between those two modes could lead to consider the lower frequency as a left side-band frequency ($f_a \rightarrow f_-$) of the dominant mode ($f_+ \rightarrow f_a$). That is why the parametric evolution of the self-sustained oscillation frequencies is often referred to as ‘‘jumps’’ from one stage to another by considering only the dominant (or most present) shear layer mode.

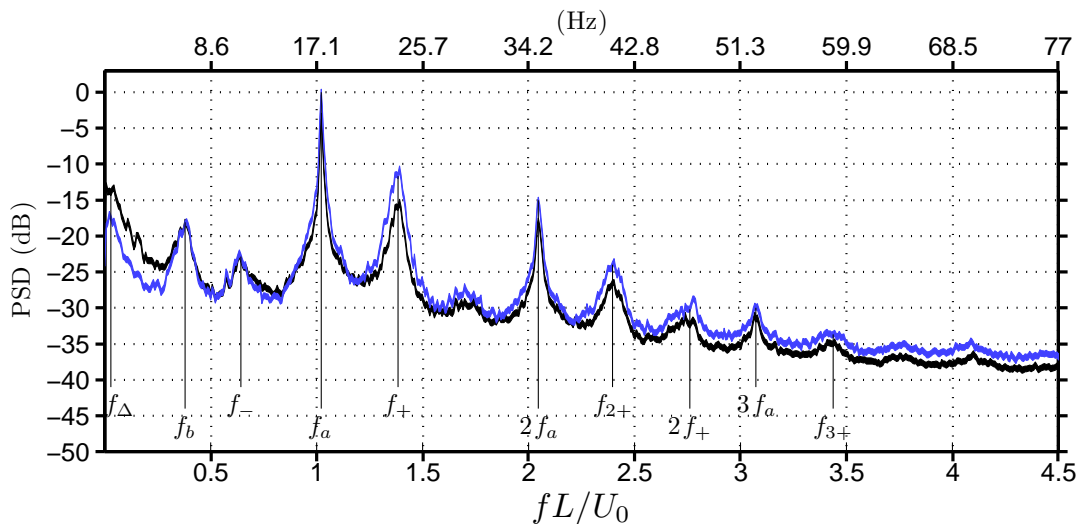


Figure 4.32: Normalised power spectral distribution of u' (black) and v' (blue) fluctuations for the case $L/D = 2.0$, $L/\theta_0 = 91$; out of the PIV time series and space-averaged over the impingement vicinity ($1.6 \leq x/D \leq 2.0$ and $-0.25 \leq y/D \leq 0.25$). Line heaviness corresponds to 95%-confidence interval.

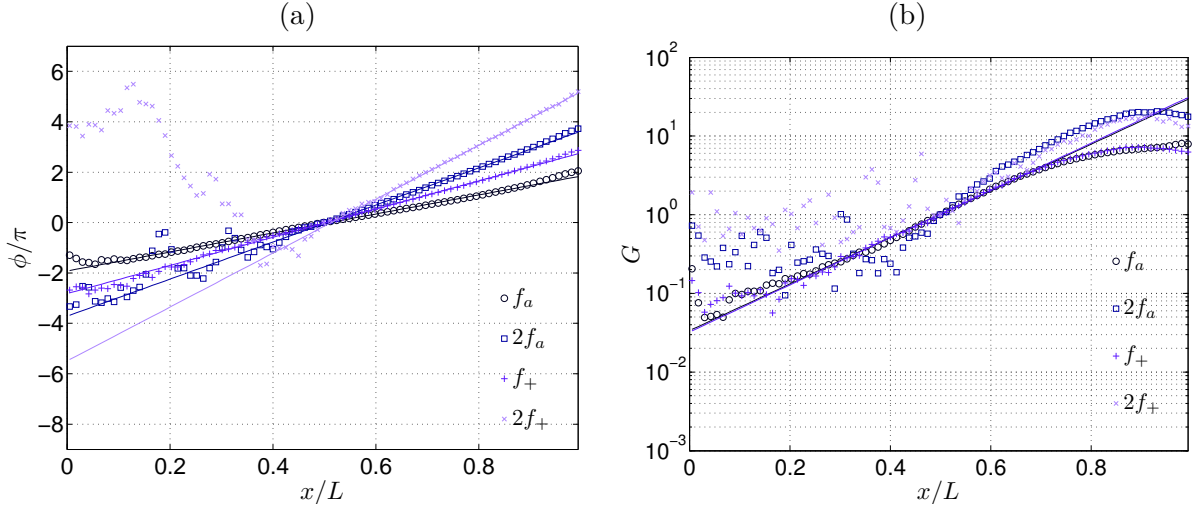


Figure 4.33: Streamwise evolution from trailing to leading corners of the unwrapped phase $\phi(x/L)/\pi$ (a) and amplitude $G(x/L)$ (b), for the two locked-on modes, f_a and f_+ , and their first harmonics $2f_a$ and $2f_+$, for the case $L/\theta_0 = 91$, $L/D = 2.0$.

Table 4.4: Wave characteristics for an intermittent regime (two families f_a and f_+). Estimated at $y/D = 0.05$ for the case $L/D = 2.0$, $L/\theta_0 = 91$.

(*)	f_*L/U_0	C_*/U_0	Λ_*/L	k_*L	ζ_*L
a	1.02	0.54	0.53	3.8π	6.8
$+$	1.38	0.49	0.36	5.6π	6.9
$a2$	2.05	0.56	0.27	7.4π	-
$+2$	2.76	0.52	0.19	10.7π	-

4.4.3 Wave properties of the two competing families

The wave properties of family hf_+ can be estimated the same way as hf_a to compare the two waves. Transfer functions have been computed (Section 3.1.3 for method) for the parameters $L/D = 2.0$, $L/\theta_0 = 91$ along the shear layer at $y/D = 0.05$. The resulting gain and phase of the waves associated with frequencies f_a , f_+ , $2f_a$, $2f_+$ are plotted in Figure 4.33. Wave properties deduced from these plots are provided in Table 4.4.2.

Both waves at fundamental frequencies f_a and f_+ carry enough energy to be well defined across the entire cavity length. Harmonics $2f_a$ and $2f_+$ are properly defined only in the second half of the shear layer. By definition, harmonic components require the larger scales to be energetic enough before the nonlinear saturation may occur. The phase of the four modes increases regularly, which indicates constant phase velocities. In Table 4.4.2, the estimated average phase velocities are roughly equal to $0.5U_0$, as expected from Kelvin-Helmholtz waves.

The gain profiles along the shear layer for both locked-on frequencies f_a and f_+ are almost identical. Hence they yield the same growth rate, which is estimated from the fit between 0.3 and $0.7L$ (linear growth region). As for the harmonics $2f_a$ and $2f_+$, they present

also a similar profile along the shear layer. In brief, there are two Kelvin-Helmholtz waves, propagating along the shear layer and saturating before the impingement but pertaining to different stages of self-sustained oscillations: ($n = 2$ for $h f_a$ and $n = 3$ for $h f_+$).

4.4.4 Spatial structures of the two harmonic families

Global Fourier decomposition is performed on case $L/D = 1.75$, $L/\theta_0 = 96$ with the aim of confirming the spatial structure of frequency $2f_+$, expected to correspond to the spatial harmonic of that of the right side-band peak f_+ . The two harmonic families ($f_a, 2f_a$) and ($f_+, 2f_+$) are associated with shear layer locked-on modes, in Figures 4.34 & 4.35, respectively. The rise of f_+ first harmonic is confirmed by the vortices advected along the impinging shear layer, twice smaller than the structures exhibited by f_+ spatial structure.

The saturation of the second locked-on mode, occurring when it is actually selected as a carrier frequency, can be used as a simple criterion for distinguishing persistent regimes of oscillation from intermittent regimes. Based on the spectrum measured near the impingement where the saturation occurs, the existence of two distinct harmonic families indicates mode switching dynamics.

4.4.5 Critical stability region for self-sustained oscillations

The carrier frequency of the self-sustained oscillations can be distinguished from a side-band peak through the existence of associated harmonics. The parametric diagram depicting the evolution of the locked-on frequencies as functions of the dimensionless cavity length L/θ_0 – presented in Section 4.3 – can be edited by separating the carrier from side-band frequencies. The resulting plot is shown in Figure 4.36.

Such a separation is actually quite insightful because it highlights a *critical region* in which most of the frequencies are enhanced so that they become carrier frequencies. This region is defined *a posteriori* for L -based Strouhal numbers as

$$\text{St} = 0.014 (L/\theta_0 - 11) \pm 1/3 = \frac{f_* L}{U_0} \pm 1/3 \quad (4.18)$$

The centreline corresponds to f_* , which can be seen as a critical frequency of the impinging shear layer. It passes through the stages $n = 1, 2, 3$ where the experimental fits actually satisfy the simplified model (Equation 1.10), that is the feedback equation without correction term ($\gamma_n = 0$). A critical frequency defined *a posteriori* should take into account the global stability of the system. However, it is most interesting to note that $f_*\theta_0/U_0 \simeq 0.012$ (for the range of parameters under study) is very close to preliminary results from local linear stability analysis obtained in Section 4.1.5 (see Figure 4.8.b).

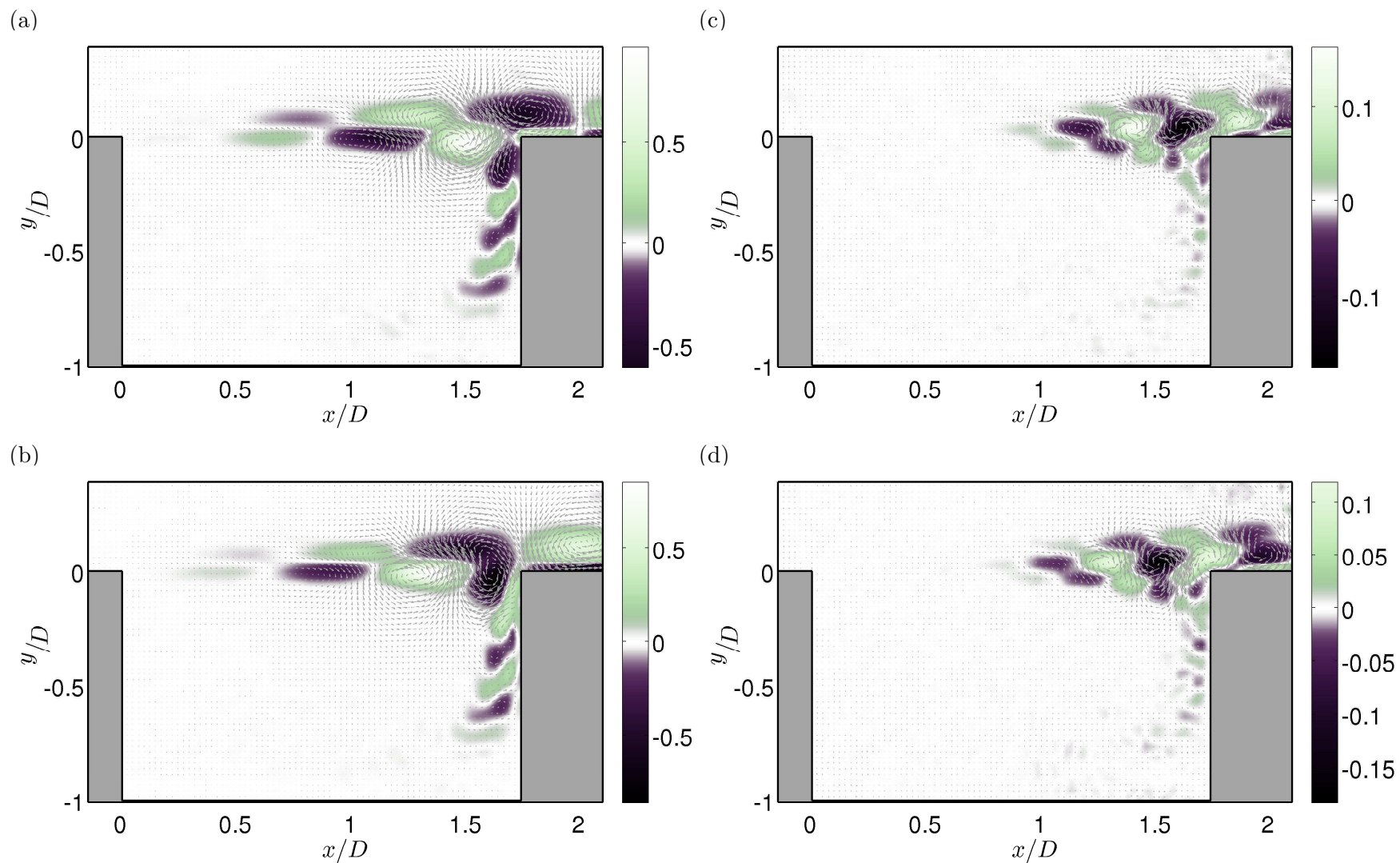


Figure 4.34: Global Fourier modes for (a,b), the dominant mode f_a ; (c,d), its first harmonic $2f_a$, in case $L/\theta_0 = 96$ & $L/D = 1.75$. Real part (top) and imaginary part (bottom) are displayed with colours encoding vorticity and vector fields representing velocity.

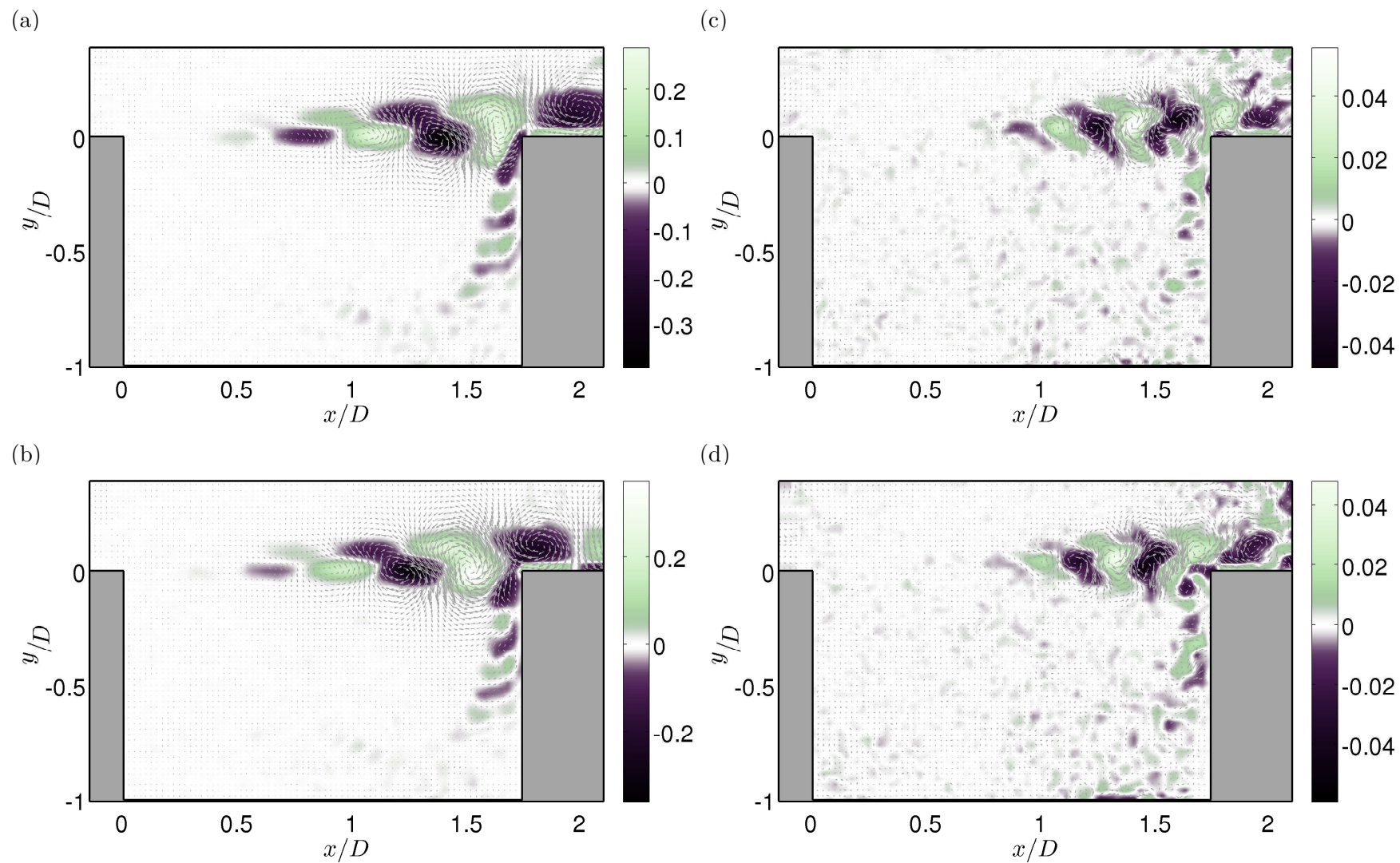


Figure 4.35: Global Fourier modes for (a,b), the second mode f_+ ; (c,d), its first harmonic $2f_+$, in case $L/\theta_0 = 96$ & $L/D = 1.75$. Real part (top) and imaginary part (bottom) are displayed with colours encoding vorticity and vector fields representing velocity.

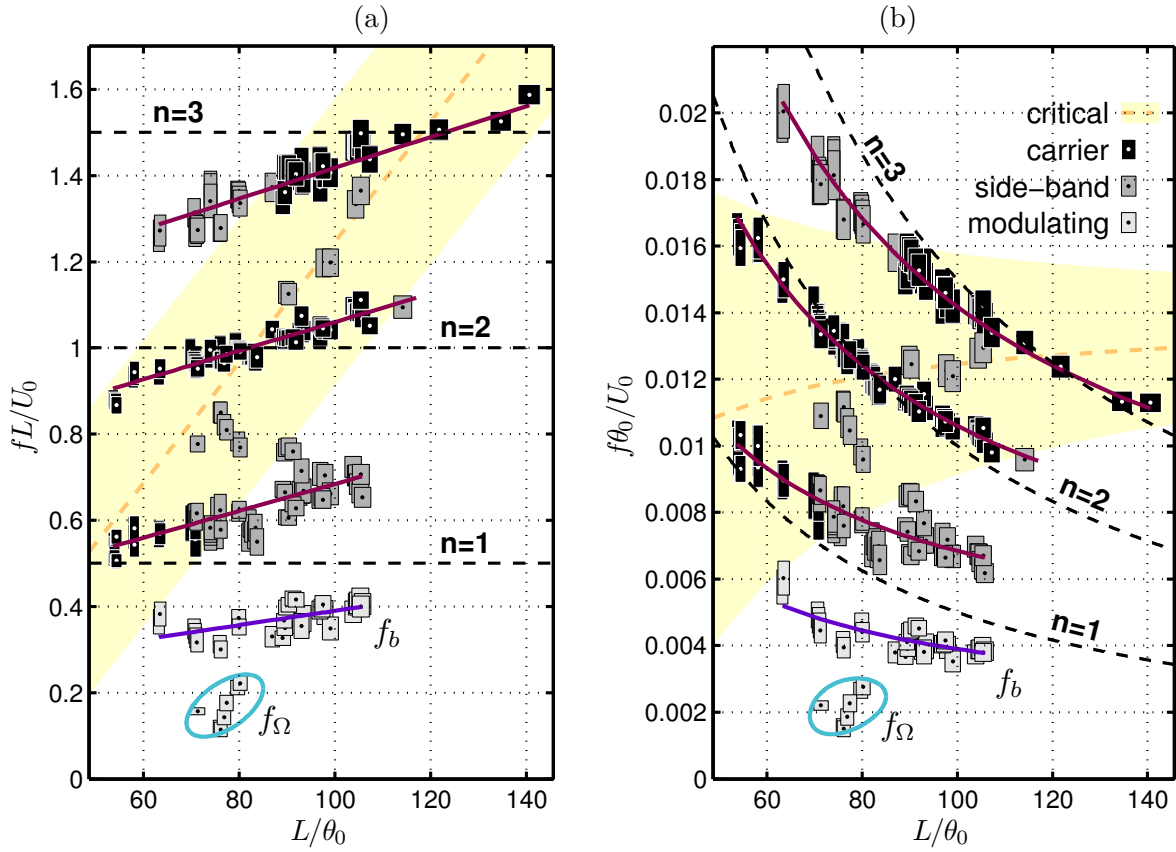


Figure 4.36: Parametric evolution of both shear layer and low frequencies as functions of the dimensionless cavity length L/θ_0 . Same data as Figure 4.23. (a) Strouhal numbers based on cavity length L . Linear fits (purple lines) correspond to the empirical locked-on condition (Equation 4.7). (b) Strouhal numbers based on momentum thickness at separation θ_0 . Carrier frequencies, producing harmonics, are displayed in black and side-band frequencies in grey. Rectangle dimensions define estimated uncertainties. The shaded region is drawn *a posteriori* such as to distinguish carrier from side-band locked-on frequencies. It is delimited by an affine law $St^L = 0.014 (L/\theta_0 - 11) \pm 1/3 = St_*^L \pm 1/3$, where the middle line St_*^L can hence be defined as a critical Strouhal number.

4.5 Inner flow and very low frequencies

The self-sustained oscillations of the shear layer are the most salient mechanism in open cavity flows. That is why the nonlinear dynamics of the shear layer modes has concentrated most of our attention up to now. However, the flow organisation does not restrict to that only aspect. As reviewed in Section 1.1.6, frequencies one to two orders of magnitude lower than shear layer frequencies are generally also at play and correspond to coherent structures arising inside the cavity. Some of these “very low” frequencies are expected to be due to three-dimensional instabilities (f_Δ), as discussed in Brès and Colonius (2008). Others are observed more sporadically (f_Ω) and might be concerned with a secondary feedback inside the cavity driven by the shear layer.

4.5.1 Secondary feedback

On top of the locked-on modes and edge frequencies f_b , the spectral signature of the flow may exhibit other shear layer frequencies departing from the generic scheme. Those peculiar configurations are apparently restricted to a narrow region of the parameter space (f_Ω and corresponding side-band peaks in Figure 4.23). A similar organisation could already be observed for equivalent parameters in Rockwell (1977); Rockwell and Naudascher (1978). This is illustrated by two parametric plots extracted from Rockwell (1977) (*Figures 6,7*), provided in Figure 1.2 of Section 1.1.3. While most of the peaks corresponded to locked-on frequencies aligning with the three stages $n = 1, 2, 3$, a few shear-layer frequencies were located between two n -stages for $1 \leq L/D \leq 2$: they did not satisfy the feedback relation (Equation 1.9). That discrepancy was not highlighted at the time. However, these results along with other similar low frequencies for compressible cases (Gloerfelt, 2006; Delprat, 2010), suggest that a secondary mechanism could be at play for certain configurations, on top of edge modulation f_b .

In this context, two unusual spectral distributions can be seen in *Figure 5. (b,c)* of Basley et al. (2011). One of them is the configuration $L/D = 1.5$, $L/\theta_0 = 79$, which has been investigated in Section 4.3. Low frequencies, noted f_Ω , are part of an amplitude modulation process in which they interact with the dominant locked-on mode (carrier frequency f_a and its harmonic $2f_a$), to induce side-band peaks

$$f_\ell = f_a - f_\Omega \quad \text{and} \quad f_{2\ell} = 2f_a - f_\Omega. \quad (4.19)$$

Yet, they do not match the spectral organisation expected from modulating frequencies related to locked-on mode selection, such as f_b . Instead, f_Ω frequencies are such that

$$0.1 \leq f_\Omega L/U_0 \leq 0.22. \quad (4.20)$$

Consequently, one can assume that frequencies f_Ω are not due to nonlinear interactions between locked-on modes. With the aim of answering that question, spatial structures associated with frequency $f_\Omega = 6.5$ Hz ($St = 0.21$) and its corresponding left side-band peak $f_\ell = 24.0$ Hz ($St = 0.78$) are displayed in Figure 4.37.(a,b) and Figure 4.37.(c,d), respectively.

The global Fourier mode associated with f_Ω exhibits vortical structures of alternative sign all along the main recirculation. The shift between imaginary and real parts denotes the propagation of those eddies. The whole structure revolves in the inner-flow, filling the entire cavity in the xy plane.

Such a spatial signature could probably imply a hydrodynamic feedback, on top of the pressure-feedback due to impingement.

As for the left side-band peak, the associated spatial structure depicts a shear layer mode. One observes oscillations of growing amplitude when closing in the impingement and splitting up at the trailing edge of the cavity to produce inflow vortices travelling downwards, along the forward-facing step of the cavity. Note that the inflow vortices are as intense as the shear layer oscillations. This is consistent with the other left side-band peak at f_- observed in Figure 4.29.(c,d). It is unambiguously produced through nonlinear interactions between dominant and low frequencies f_a and f_Ω .

This matter would require more attention in order to settle the precise nature of the underlying mechanism responsible for the apparition of frequency f_Ω .

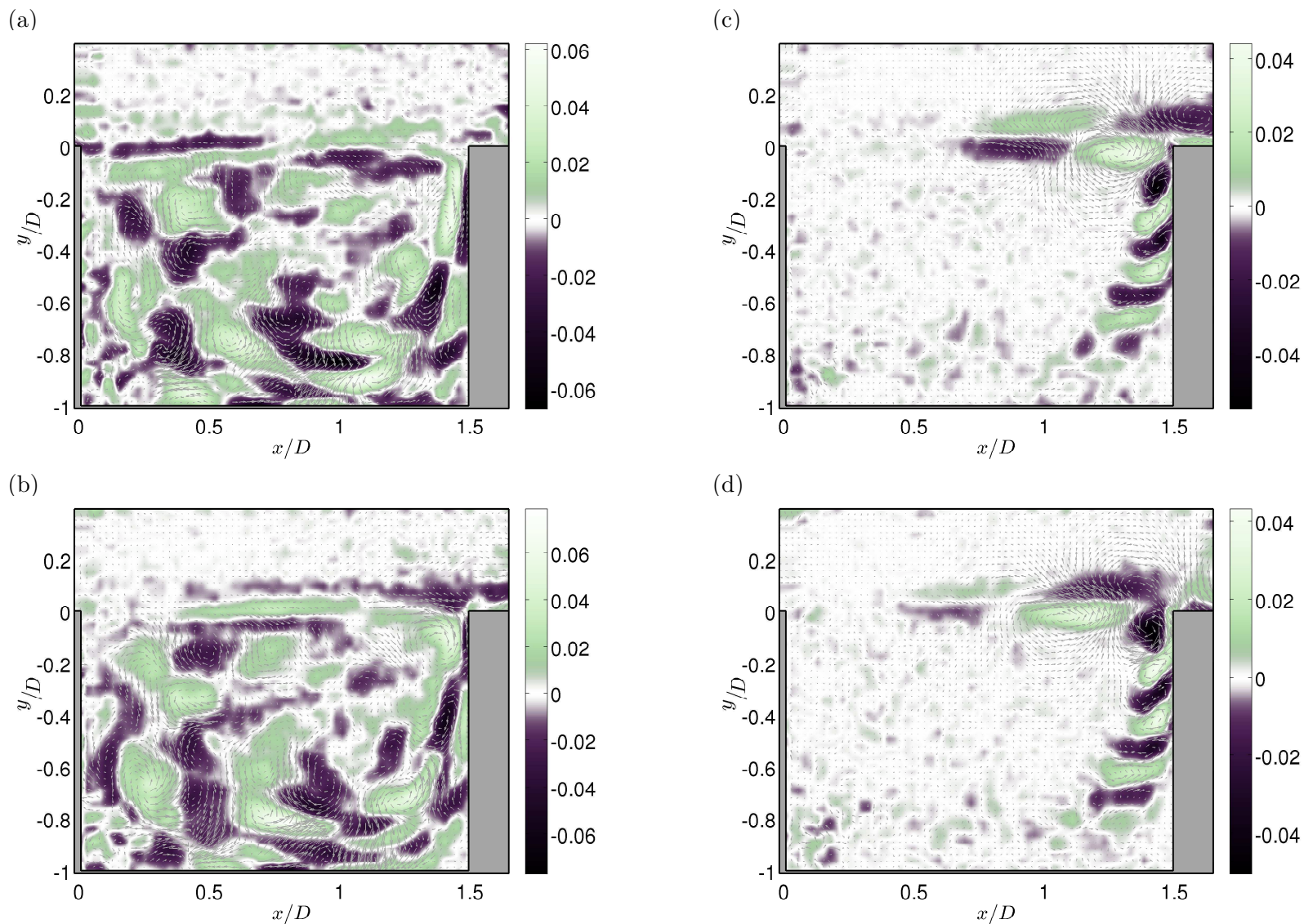


Figure 4.37: Global Fourier modes for (a,b), the low frequency f_{Ω} ; (c,d), the left side-band frequency f_{ℓ} , in case $L/\theta_0 = 79$ & $L/D = 1.5$. Real part (top) and imaginary part (bottom) are displayed with colours encoding vorticity and vector fields representing velocity.

4.5.2 Three-dimensional structures in the inner-flow

Almost the entire range of the spectrum has been investigated and the characteristic spectral components have all been identified and discussed apart from the *very low* frequencies, denoted as f_Δ in Sections 4.2 and 4.3. Streamwise fluctuations u' out of experiments all consistently show high levels of energy for frequencies below $St < 0.2$. Such low frequencies have often been overlooked as they are considered as physically irrelevant, believed to be caused by experimental defects, despite the consistency of their presence in the measurements. Studying frequencies of such a low order of magnitude relatively to salient time scales of the shear layer is indeed challenging at best.

However, a few investigations highlighted the importance of such scales in the open cavity flows, notably Rockwell and Knisely (1980b); Neary and Stephanoff (1987); Delprat (2010) (see Section 1.1.6 for the detailed review). They usually pointed to a three-dimensional organisation of the inner-flow responsible for those frequencies.

Lately, global linear stability analysis, commonly used for confined flows in lid-driven cavities (Ramanan and Homsy, 1994; Poliashenko and Aidun, 1995; Albensoeder et al., 2001; Blackburn and Lopez, 2003; Theofilis et al., 2004; Chicheportiche et al., 2008), has been applied to open cavities, notably by Brès and Colonius (2008); de Vicente (2010), with the aim of demonstrating the existence of linearly growing modes in the spanwise direction. They showed that such modes actually exist for low Reynolds numbers and low dimensionless cavity lengths ($L/\theta_0 < 60$) yield very low frequencies compared to shear layer dynamics ($f D/U_0 \simeq 0.02$). Using direct numerical simulations, Brès and Colonius (2008) have shown that these modes may interact with the latter.

4.5.3 Another drastic amplitude modulation

In Figure 4.38, time-series of crosswise v' and streamwise u' velocity fluctuations and associated spectra are plotted for two points picked up in the shear layer and in the cavity, respectively. They depict the difference of the dynamics between the inner-flow and the shear layer self-sustained oscillations. In particular, the dominant frequency f_a investigated in Section 4.2 is absent of the spectrum extracted near the bottom of the cavity. On the contrary, time-scales about 30 times larger than shear layer oscillations are encountered inside the cavity rather than in the shear layer – especially regarding the crosswise component.

In fact, such low frequencies correspond to amplitude modulations of the self-sustained oscillations. As seen in Figure 4.38.a, the energy of the shear layer flapping motion can actually decrease dramatically because of these very low frequency modulations. Note that these large time scales are not strictly a periodic phenomenon, which suggests a broad-band range of low frequencies. Nonetheless, the tip of that broad-band peak, already named f_Δ in previous sections, is clearly recovered both on its own and in terms of side-band peaks,

$$f_a \pm f_\Delta \quad \text{with} \quad f_\Delta D/U_0 \simeq 0.02, \quad (4.21)$$

visible around the dominant frequency f_a in the spectrum (Figure 4.38.b).

This amplitude modulation is particularly robust since the tip of the broad-band peak at f_Δ is encountered in all investigated cases for values such that

$$0.010 \leq f_\Delta D/U_0 \leq 0.027. \quad (4.22)$$

Those values strikingly recall the results from the literature, regarding the spanwise organisation of the inner-flow, notably the recent numerical studies on open cavity flows at low Reynolds numbers by Brès and Colonius (2008); de Vicente (2010). See Section 1.1.6 for more detail. Such a match suggests that centrifugal instabilities yielding three-dimensional structures govern the inner-flow, in spite of the strong disturbances implied by shear layer inflows.

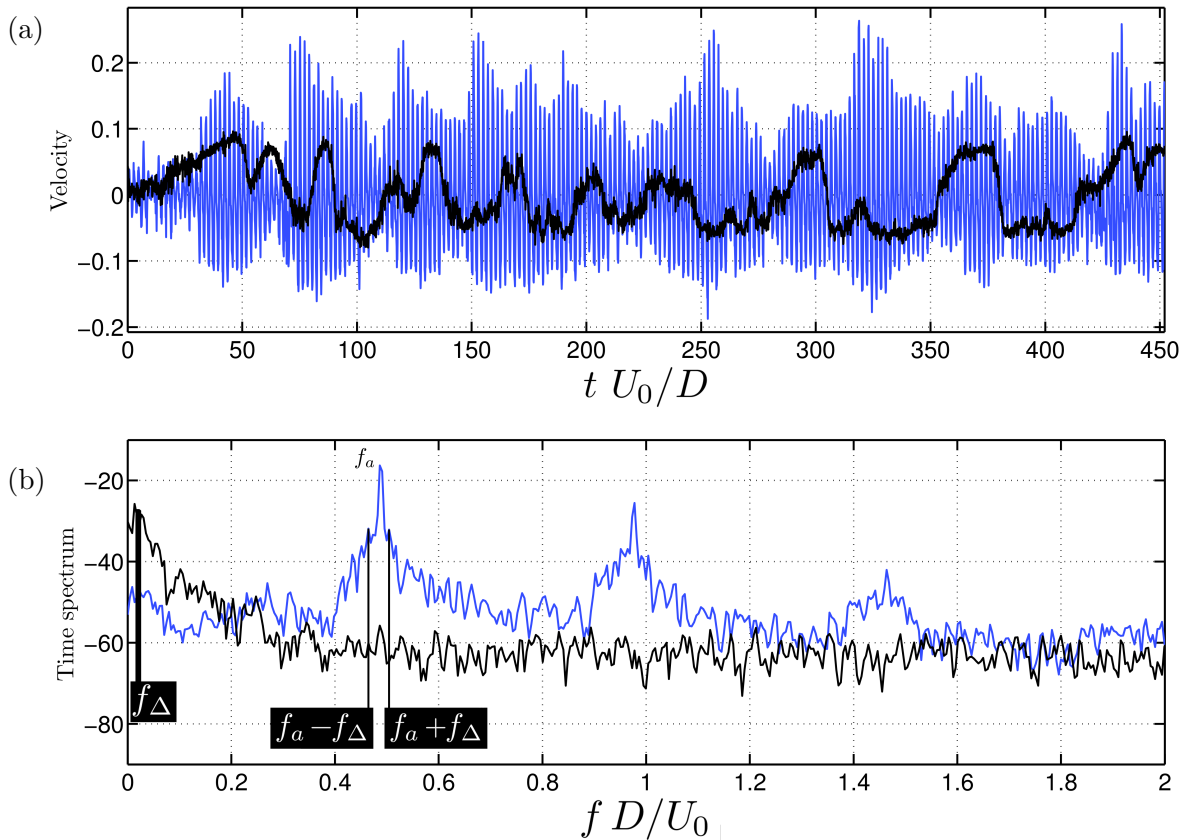


Figure 4.38: Velocity fluctuations extracted from TR-PIV datasets for $L/D = 2.0$, $L/\theta_0 = 82$: (light blue) crosswise fluctuations v'/U_0 extracted inside the shear layer ($x_p/D = 1.70$, $y_p = 0$); (black) streamwise fluctuations u'/U_0 extracted inside the cavity ($x_p/D = 1.0$, $y_p/D = -0.75$). (a) Time-series and (b) corresponding time spectrum (window averaged).

4.5.4 Spatial structures associated with very low frequencies

Low frequencies around f_Δ have been identified as likely due to centrifugal instabilities and their nonlinear interaction with the shear layer modes has been revealed. Hence, the underlying spatial organisation inside the cavity would be insightful. Examples of global Fourier modes associated with f_Δ frequencies for various control parameters are provided in Figures 4.39-4.41. Though the spatial structures differ from one configuration to another, several common features appear without ambiguity:

- These low frequencies yield high energy levels, even when compared to shear layer modes.
- the structures organise themselves in various branches winding on the main recirculation.

- there is no salient indication of travelling waves inside the xy -plane (no clear shift between real and imaginary parts).
- outflow is visible at the impingement, confirming once more the impact of those inner-flow large-scales upon the flapping motion of the impinging shear layer.

Case $L/D = 1.0$ in Figures 4.39.(a,b) is of particular interest for comparison purposes with numerical data performed by Yann Fraigneau and presented in Section 6.2.

More generally, various L/D geometries have been studied numerically for lower Reynolds numbers Re_D , that is closer to the threshold. Most notably, the global Fourier modes obtained in the present study are very similar to xy -cuts of three-dimensional eigen modes issued of linear stability analyses (Brès and Colonius, 2008; de Vicente, 2010; Meseguer-Garrido et al., 2011). The coherent structures observed in the experiments likely correspond to the saturated state of spanwise waves covering the entire cavity along the span. That is why the second part of our investigation will focus on spanwise dynamics.

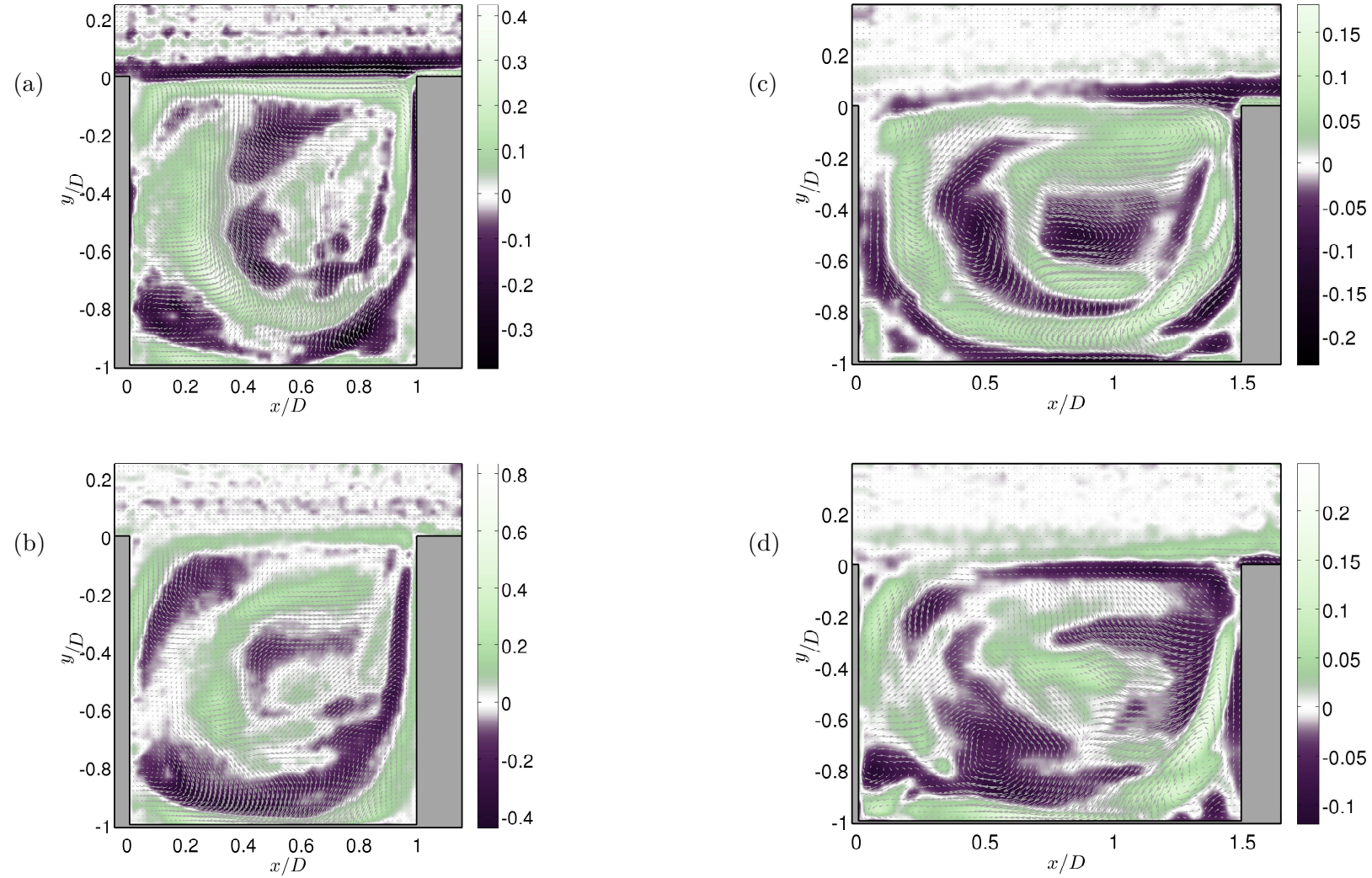


Figure 4.39: Global Fourier modes associated with low frequency f_Δ for (a,b), $L/\theta_0 = 54$, $L/D = 1.0$, $\text{Re}_D = 7700$, $f_\Delta D/U_0 = 0.017$. (c,d), $L/\theta_0 = 79$, $L/D = 1.5$, $\text{Re}_D = 7470$, $f_\Delta D/U_0 = 0.019$. Real part (top) and imaginary part (bottom) are displayed with colours encoding vorticity and vector fields representing velocity.

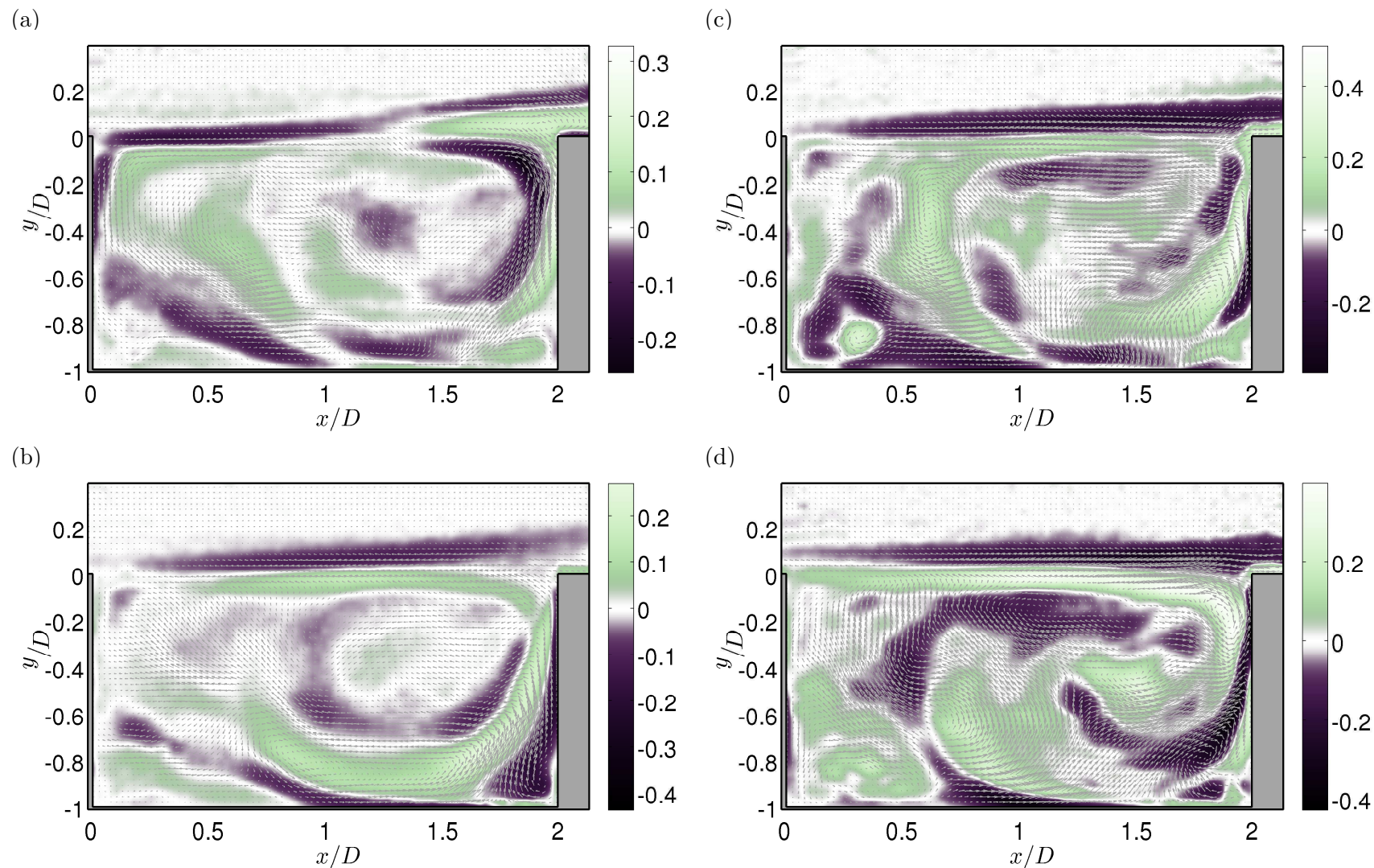


Figure 4.40: Global Fourier modes associated with low frequency f_Δ for (a,b), $L/\theta_0 = 82$, $L/D = 2.0$, $\text{Re}_D = 4550$, $f_\Delta D/U_0 = 0.026$. (c,d), $L/\theta_0 = 91$, $L/D = 2.0$, $\text{Re}_D = 5750$, $f_\Delta D/U_0 = 0.025$. Real part (top) and imaginary part (bottom) are displayed with colours encoding vorticity and vector fields representing velocity.

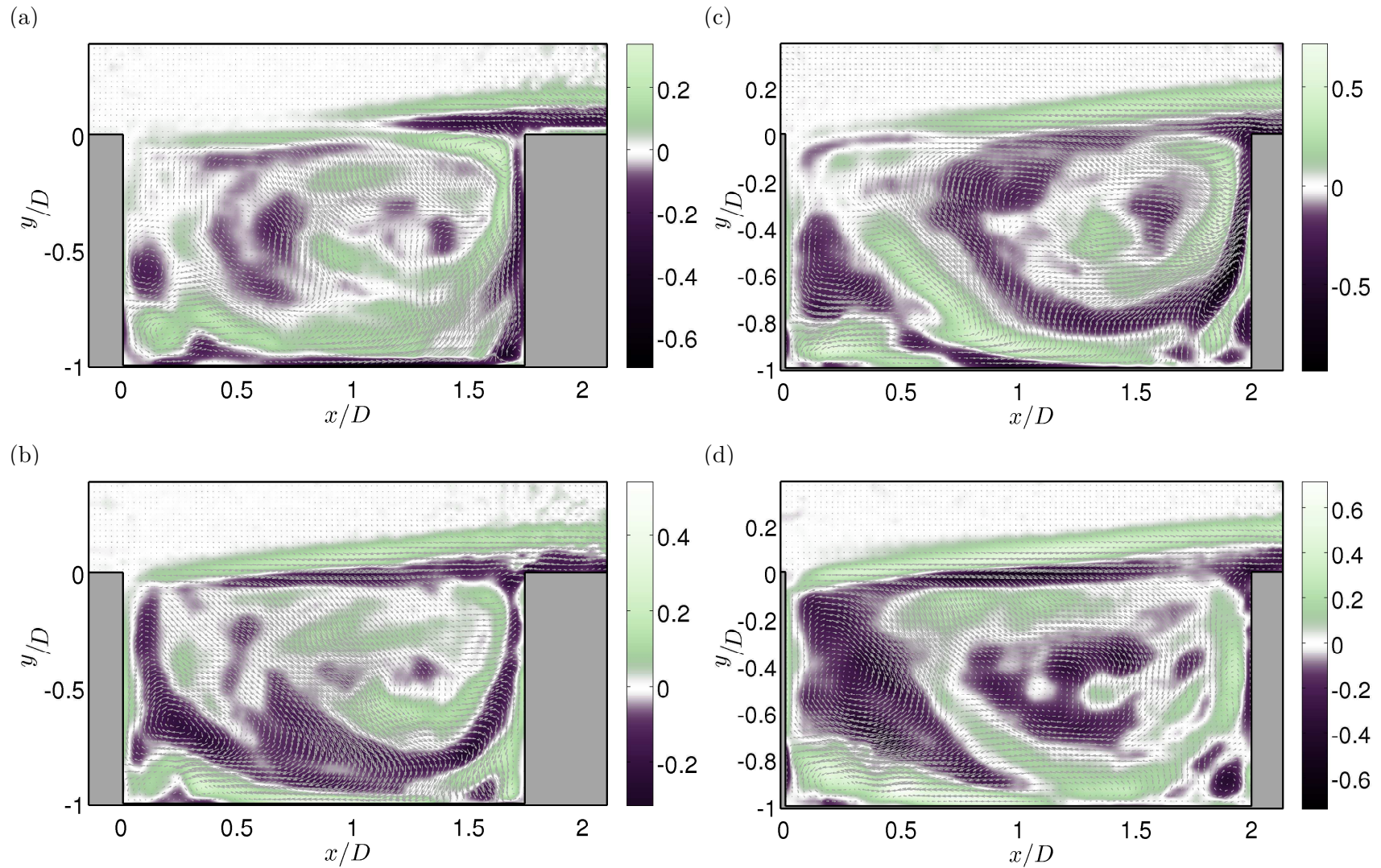


Figure 4.41: Global Fourier modes associated with low frequency f_{Δ} for (a,b), $L/\theta_0 = 96$, $L/D = 1.75$, $\text{Re}_D = 8060$, $f_{\Delta} D/U_0 = 0.021$. (c,d), $L/\theta_0 = 96$, $L/D = 2.0$, $\text{Re}_D = 6340$, $f_{\Delta} D/U_0 = 0.016$. Real part (top) and imaginary part (bottom) are displayed with colours encoding vorticity and vector fields representing velocity.

Spanwise dynamics

Until now, the analysis has focused on the main features of the open cavity flow, namely the impinging shear layer, usually exhibiting intense self-sustained oscillations, and its nonlinear interactions with the inner-flow. To that aim, the investigation dealt with a cross-stream (xy) plane containing the main directions of the flow. A common feature to all configurations under study was the dramatic modulations of the shear layer dynamics by modulating frequencies one to two orders of magnitude below the locked-on frequencies of the self-sustained oscillations. These “very low” frequencies formed a broad-band peak, whose tip was noted f_Δ in the previous chapter. The dynamics associated with such large time scales were identified as slow moving structures in the inner-flow, overriding the flapping motion of the shear layer, deep inside the cavity. More specifically, the fluctuations associated with f_Δ concentrated onto the main recirculation and inside the boundary layers induced alongside the cavity walls. Such space and time scales suggest an underlying three-dimensional organisation.

As a matter of fact, though cavity flows have often been modelled as invariant in the spanwise direction (z), the main recirculation inside the cavity can give rise to three-dimensional structures. As introduced in the literature review (Section 1.1.6), existence of spanwise waves resulting from centrifugal instabilities has been shown both using experimental observations (Djenidi et al., 1999; Albensoeder et al., 2001; Faure et al., 2007, 2009) and linear stability analyses (Brès and Colonius, 2008; de Vicente, 2010). The study now concerns the space-time dynamics in a zx -plane inside the cavity to characterise such instabilities.

5.1 Preliminary remarks

5.1.1 PIV datasets

Experimental data have been generated from PIV images acquired in the spanwise zx -plane located at $y_{piv} = -0.1D$, just below the shear layer, with $D = 50$ mm the cavity depth. The two-dimensional two-component velocity fields (2D-2C) write

$$\frac{\mathbf{U}_{zx}(z, x, y_{piv})}{U_0} = \frac{w(z, x, y_{piv})}{U_0} \mathbf{e}_z + \frac{u(z, x, y_{piv})}{U_0} \mathbf{e}_x, \quad (5.1)$$

here normalised by U_0 , the outflow velocity at separation (above the leading edge of the cavity). Set-up and PIV computations have been discussed in Chapter 2, where the three investigated cases are described (Table 2.1).

The shear layer may be unstable or not, depending on the dimensionless cavity length L/θ_0 (Rockwell and Naudascher, 1978, 1979). Laser-sheet location $y_{piv} = -0.1D$ was chosen with the aim of identifying the three-dimensional structures of the cavity inner-flow where they can impact directly the impinging shear layer. Another interest of such a plane is its tangency to the rotating main recirculation: out-of-plane velocity $v(z, x, y_{piv})$ is far smaller than in-plane velocity \mathbf{U}_{zx} except for the outer regions of the main recirculation, nearby the leading and

trailing edges of the cavity.

Examples of instantaneous velocity (and vorticity) fields are presented in Figures 5.1 and 5.2. The region of interest comprises the entire cavity span $S = 10D$. Dimensionless velocity components extracted from PIV datasets split up into mean flow (time-averaged field) and fluctuations as follow:

$$\frac{\mathbf{U}_{zx}}{U_0} = \frac{\bar{w} + w'}{U_0} \mathbf{e}_z + \frac{\bar{u} + u'}{U_0} \mathbf{e}_x. \quad (5.2)$$

As for the corresponding vorticity, it comes

$$\frac{\omega_y D}{U_0} = \frac{\partial u / U_0}{\partial z / D} - \frac{\partial w / U_0}{\partial x / D} = \frac{(\bar{\omega}_y + \omega_y') D}{U_0}. \quad (5.3)$$

As expected for such Reynolds numbers, the cavity flow is three-dimensional: highly coherent spanwise-oscillating structures can be observed. No visible trace of two-dimensional streamwise-travelling wave from the shear layer is found in levels of crosswise vorticity component ω_y . Indeed, shear layer modes remain mainly confined in xy -plane, hence generating only spanwise vorticity component ω_z .

The first two configurations (*A*: $\text{Re}_D = 1500$, $D/\theta_0 = 23.2$) and (*B*: $\text{Re}_D = 2400$, $D/\theta_0 = 29.4$), respectively in Figures 5.2.(a-b), exhibit large scale structures with phase-frontlines all along the cavity length. The entire section, from upstream to downstream cavity walls, experiences a spanwise oscillation. Spanwise-oscillating vortical structures appear to be closely entangled to the base flow: *ie.* the main and secondary recirculations. For both cases, phase evolves continuously in the spanwise direction but experiences discontinuities around $x/D \simeq 0.7$ and $x/D \simeq 1.8$ with fluctuations nearby the leading and trailing edges of the cavity out of phase relatively to the main recirculation. Such phase discontinuities are consistent with qualitative results by Migeon (2002); Migeon et al. (2003). These demarcation borders are also pointed out by converging (resp. diverging) streamlines which, in a slice of a three-dimensional flow, mark off the position of a sink (resp. source). Although they are generated with fluctuations of velocity, streamlines are still pulled in and stretched by an out-of-plane velocity, resulting in strong concentrations of vorticity. These features indicate that centrifugal instability waves travel along the main xy -recirculation cell. As for the characteristic length of the centrifugal instabilities, preliminary observations lead to a dominant wavelength of $\lambda \simeq D$, as expected for a $L = 2D$ -length-cavity (Faure et al., 2007; Brès and Colonius, 2008; Faure et al., 2009; de Vicente, 2010).

Contrarily to low D/θ_0 ratios, case *C* ($\text{Re}_D = 5550$, $D/\theta_0 = 46.6$) in Figure 5.1.c has lost most of its spanwise organisation. It shows numerous vortical structures at small scale, erratically distributed, in particular near the downstream edge of the cavity. That evolution throughout parameter θ_0 can be explained by a mutation of the three-dimensional flow. Being at first dominant for low D/θ_0 cases, centrifugal instabilities generate well-organised spanwise waves in the inner cavity flow. Their associated vorticity is mainly carried by the xy -plane ($\boldsymbol{\omega}_{ci}' = \omega_{ci_x}' \mathbf{e}_x + \omega_{ci_y}' \mathbf{e}_y$). Then in case *C*, centrifugal instabilities dynamics is disturbed by the unstable shear layer. Indeed, intense spanwise vorticity ω_z' comes from the self-sustained oscillations whose amplitude grows with parameter L/θ_0 (Rockwell and Naudascher, 1979; Knisely and Rockwell, 1982). An increase of the complexity with the dimensionless cavity depth D/θ_0 is in accordance with previous works (Albensoeder and Kuhlmann, 2006; Brès and Colonius, 2007, 2008; Faure et al., 2009; de Vicente, 2010).

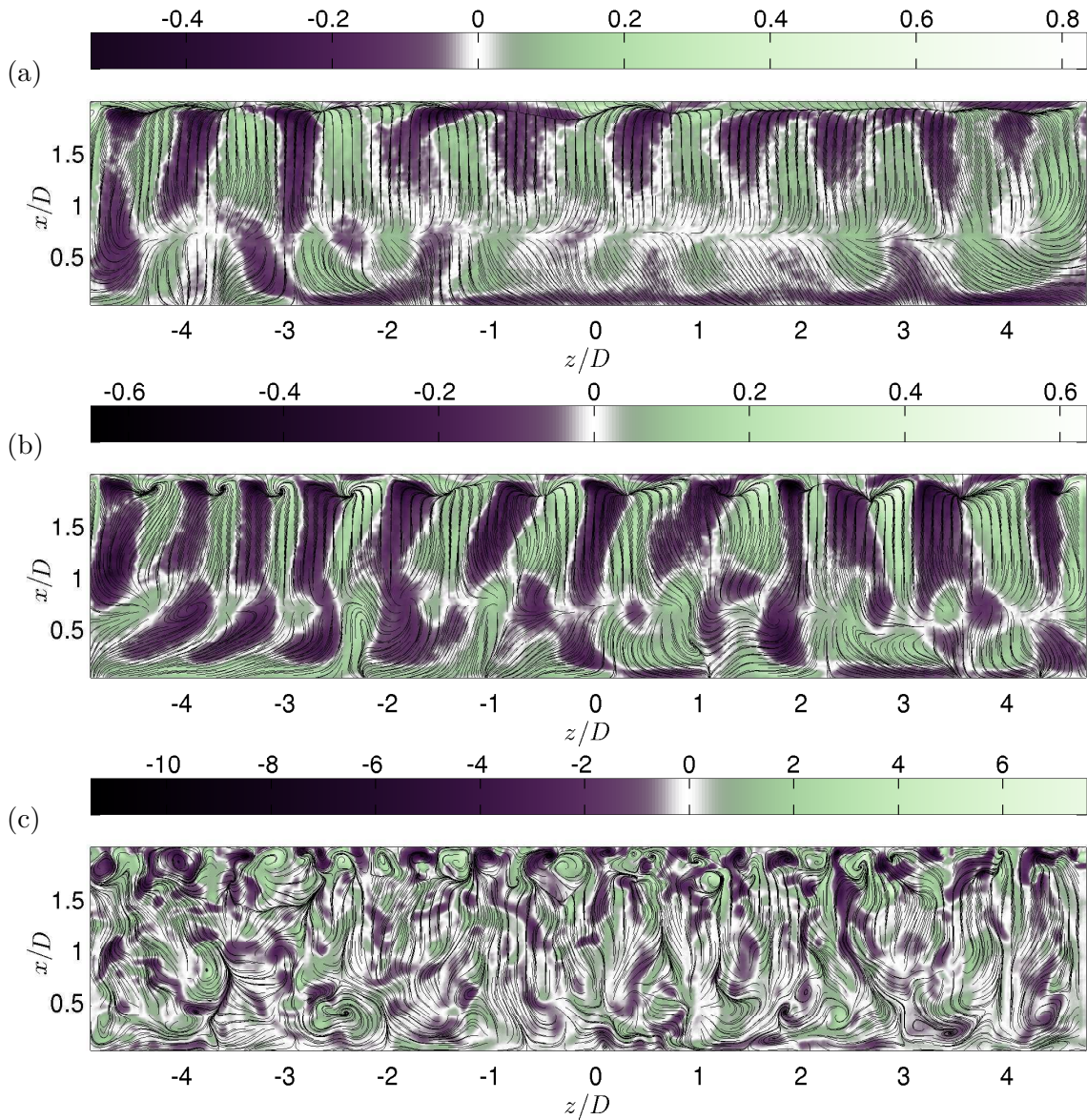


Figure 5.1: Examples of instantaneous fields in plane $(x, y = -0.1D, z)$ for the three configurations $Re_D = 1500$, $D/\theta_0 = 23.2$, (a); $Re_D = 2400$, $D/\theta_0 = 29.4$, (b); $Re_D = 5550$, $D/\theta_0 = 46.6$, (c). Dimensionless vorticity $\omega_y D/U_0$ is displayed in colour scales along with streamlines.

5.1.2 Spanwise boundary conditions

It must be noted that in opposition to numerical simulations which often use periodic spanwise conditions, an experimental facility implies the cavity span to be limited by no-slip boundary conditions. In the present case, cavity endwalls are the floor and ceiling of the water-tunnel.

$$\mathbf{U}(x, y, z = \pm S/2) = \mathbf{0} \quad \text{with } S = 10D \quad (5.4)$$

Instead of a 2D-base flow like those used in linear stability analysis (Brès and Colonius, 2008; de Vicente, 2010; Theofilis, 2011; Meseguer-Garrido et al., 2011), such boundary conditions lead to the creation of Bödewadt (Ekman-like) layers of opposite sign near both endwalls. They form slow-rotating centripetal disks making the junction between the main recirculation and rigid

boundaries. Albensoeder et al. (2001); Albensoeder and Kuhlmann (2006) have investigated the case of a square lid-driven cavity $S/D = 6.5$. The endwall regions therein expand as far as a quarter of the span, restricting vortical cells to the central region only (see Figure 1.5). The present results are closer to those obtained by Faure et al. (2007, 2009), who observed spanwise oscillations until a close vicinity of the endwalls.

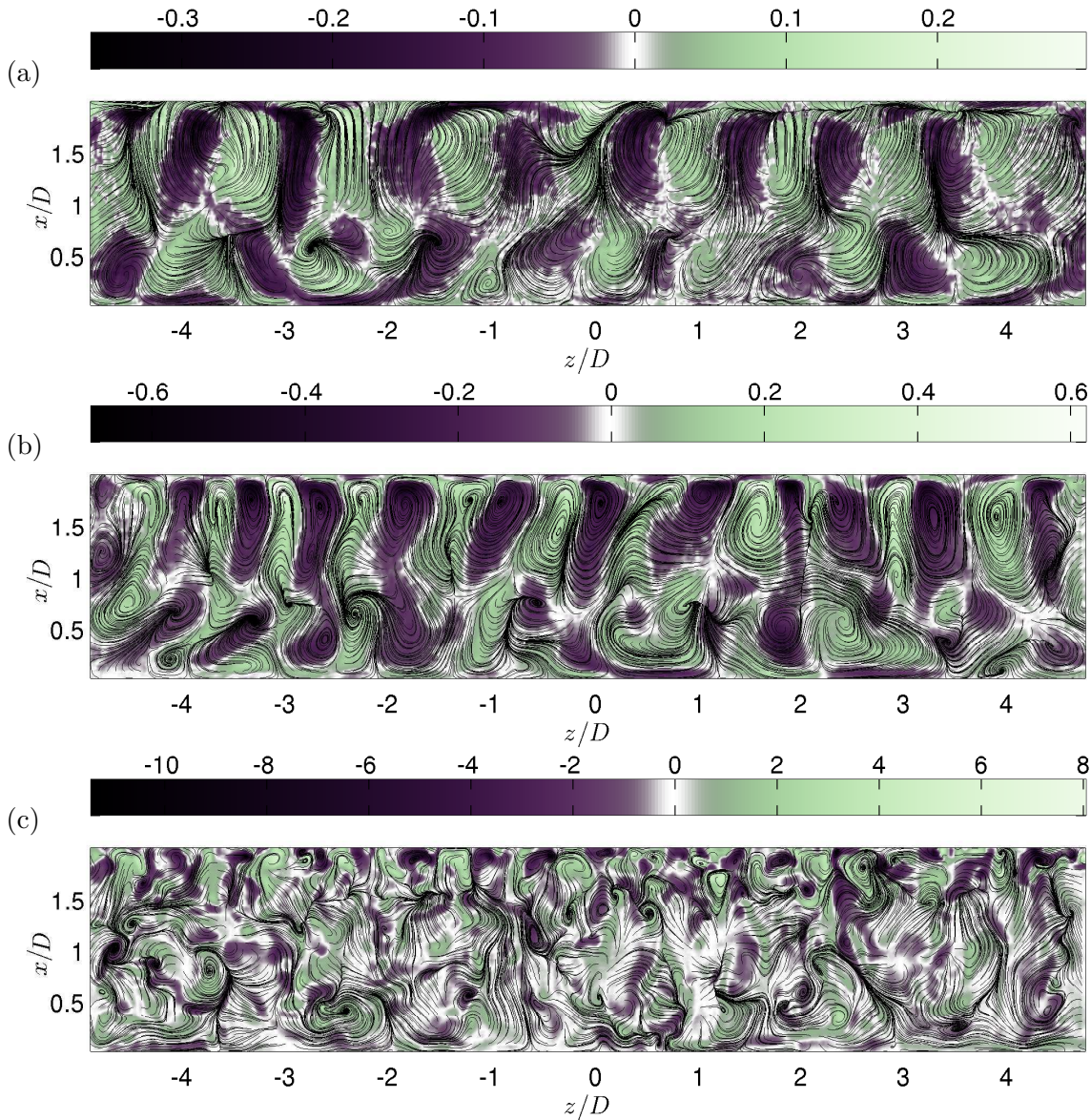


Figure 5.2: The same instantaneous fields as Figure 5.1 with the mean flow subtracted. Dimensionless vorticity fluctuations $\omega_y' D/U_0$ are displayed in colour scales along with streamlines generated from fluctuations only.

Furthermore, both numerical and experimental flows in lid-driven cavities Guermond et al. (2002); Migeon (2002); Migeon et al. (2003) as well as open cavities Faure et al. (2007, 2009) have shown that Bödewadt layers draw the outer edge of the internal cavity flow from the mid-span region and then reinject the fluid back through the centreline of the main recirculation. That steady secondary flow may induce an *additional spanwise drift* to the centrifugal instability

vortices twining around the main recirculation.

On the other hand, the solid boundary conditions imposed by endwalls are also known to have a *braking* effect on the main recirculation of the inner-flow (Shankar and Deshpande, 2000). This suggests that coiling perturbations, growing due to centrifugal instabilities, would propagate at a slower pace in the three-dimensional base-flow than in a two-dimensional base-flow.

5.2 Spanwise wavelengths analysis

5.2.1 Space Fourier transform

In order to determine spanwise wavelengths at play in the cavity inner-flow, a space Fourier analysis can be undertaken along the direction z . Spanwise wavenumbers are defined as

$$\beta = \frac{2\pi D}{\lambda} \quad (5.5)$$

where λ is the corresponding spanwise wavelength. The principal issue with space Fourier Transform applied to that system is the lack of precision in the wavenumbers identification. Relying on spanwise array length, here $S = 10D$, wavenumber resolution is basically $2\pi/10 = 0.63$. That is problematic since wavenumbers to be resolved are of the order of 2π , that is only 10 wavelengths in the whole span. Length of spanwise arrays is increased by padding them with zeros before Fourier Transform computation. The spectral resolution of space Fourier spectra is thus improved in spite of induced noise: dimensionless wavenumber step is decreased to $\delta\beta = 0.32$. Statistics are then performed on spectra $|\mathcal{F}^z(\omega_y')|$ to obtain a mean spectrum $\langle |\mathcal{F}^z(\omega_y')| \rangle$: averaged over various x positions (one out of 4 rows, that is about 40 spanwise arrays) and the whole set of velocity fields (more than 2000 samples for each configuration). Spectra samples used for averaging are not fully independent. Nonetheless, having about 80000 spanwise arrays of different phase is large enough to get sufficient convergence in terms of Fourier transform intrinsic noise, hence a reduced confidence interval (see Section 3.1.2). Statistical convergence regarding the flow dynamics cannot be settled since we deal with a system exhibiting a high sensitivity to initial conditions and involving extremely large time-scales.

The mean Fourier spectrum is displayed against dimensionless wavenumbers β in Figure 5.3 for the three cases. When the entire span is studied (dashed lines), the spectrum embraces side effects caused by Bödewadt boundary layers and evolution of centrifugal instability wavelengths along z . On the other hand, such boundary conditions also skew the assumption of periodic series and hence induce noise and globally scale down energy in spectrum. To reduce boundary effects, vorticity fields have been multiplied by a Hamming window (Equation 5.6) prior to Fourier computation (plain lines in Figure 5.3).

$$\Omega(z) = 0.54 + 0.46 \cos\left(\frac{2\pi z}{S}\right) = 0.54 + 0.46 \cos\left(\frac{2\pi z/D}{10}\right) \quad (5.6)$$

The range and amplitude of active wavelengths grow wider and larger when going from cases A to C . This yields an increase of energy and complexity. Case C even shows a continuous spectrum, indicating a reduction of flow coherence. All cases exhibit maximal energy around $\beta_{\max} \simeq 2\pi$ (that is $\lambda \simeq D = 50$ mm). More particularly, the highest peak is located at $\beta_{\max}(A) = 6.3$, $\beta_{\max}(B) = 5.8$ and $\beta_{\max}(C) = 6.8 (\pm 0.16)$, respectively. These results are coherent with those found in literature (Brès and Colonius, 2008; Faure et al., 2009). Secondary peaks appear also for case B around $\beta \simeq 7.5$ and $\beta \simeq 10$.

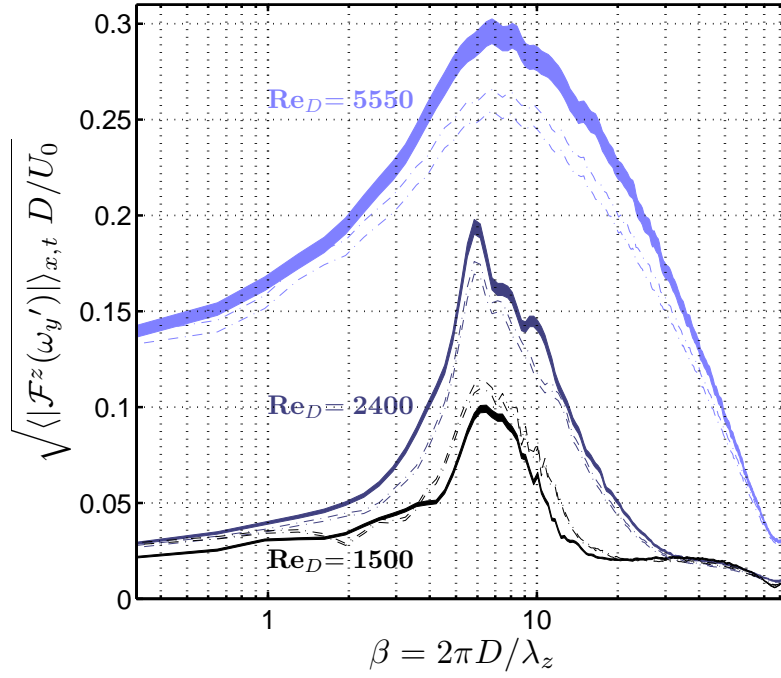


Figure 5.3: Space Fourier spectrum as a function of dimensionless wavenumbers β , for the three cases A : $\text{Re}_D = 1500$, $D/\theta_0 = 23.2$; B : $\text{Re}_D = 2400$, $D/\theta_0 = 29.4$; C : $\text{Re}_D = 5550$, $D/\theta_0 = 46.6$. Fourier transform is performed on vorticity fluctuations ω_y' , non-dimensionalised by U_0/D . Prior to Fourier computation is applied either a square window (dashed) or a Hamming window (plain). Integrated along x/D and snapshots for greater statistics, curve thickness corresponds to the 95%-confidence interval of Fourier calculation.

5.2.2 Space Hilbert-Huang transform

On top of a poor resolution, space Fourier spectra only provide an averaged energy, integrated along the entire span series. If the signal under study is strongly modulated, either in amplitude or in frequency (wavenumber in the present case), projecting on Fourier modes removes local information. On the other hand, Hilbert-Huang transform (HHT) gives access locally to amplitude and wavenumber associated with each *empirical* mode. The description of the methodology (*Empirical Mode Decomposition* followed by *Hilbert transform*) in Section 3.2 constitutes a prerequisite to the forthcoming analysis.

Applied to the same datasets as space FFT, spanwise HHT can be used to build intensity distributions $HH^z(z, \beta)$, which yield the wavenumber contents and evolutions along the spanwise direction z . In practice, obtaining such distributions is not straightforward. The procedure is pictured in Figure 5.4. In brief,

- 1) From any snapshot, vorticity fluctuation $\omega_y'(z, x)$ field is considered as a set of spanwise arrays (one out of 4 rows).
- 2) These spanwise arrays are processed with Empirical Mode decomposition (1D), resulting in *Intrinsic Mode Functions* (IMF).
- 3) Then, Hilbert transforms are computed on the IMFs to give access to spanwise functions of local amplitude $\mathcal{A}(z)$ and local wavenumber $\beta(z)$ for each IMF at every considered position x of any snapshot in the TR-PIV dataset.
- 4) Re-ordering by descending averaged amplitude, the first IMF usually contains most of the

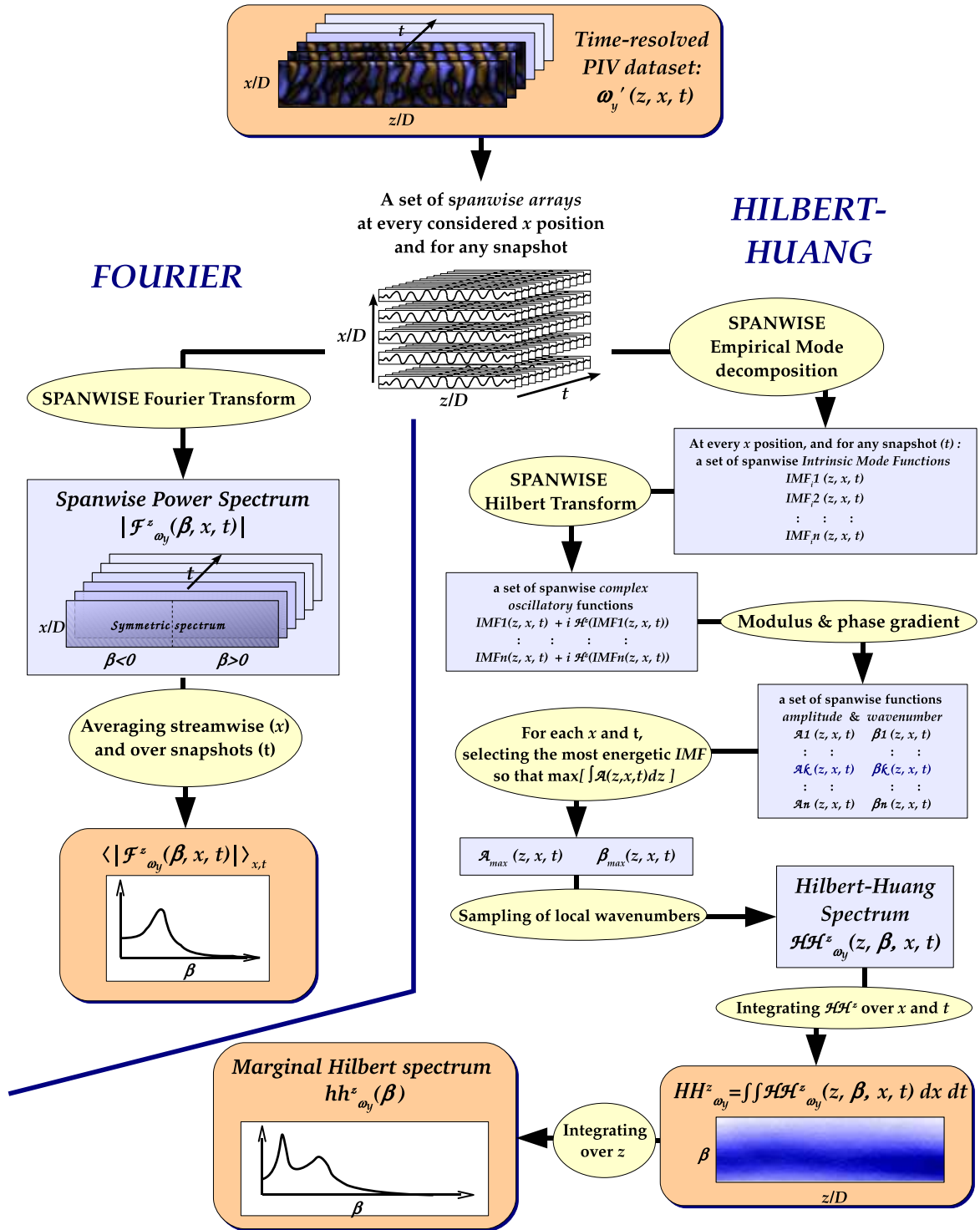


Figure 5.4: Schematic outline of the space decomposition methodology using both Fourier and Hilbert-Huang transforms performed on dimensionless vorticity fluctuations ω_y' non-dimensionalised by U_0/D

energy already. In consequence, contributions of the other IMFs are neglected.

5) Noting t the snapshot index, one gets two 3D-matrices $\mathcal{A}(z, x, t)$ and $\beta(z, x, t)$.

6) Local wavenumbers $\beta(z, x, s)$ are equally sampled, such that

$$\hat{\beta} = i \delta\beta \quad \text{with } i \in \mathbb{N}^+ \quad \text{and } \delta\beta = 0.1 \quad (5.7)$$

and weighted by corresponding local amplitudes in order to construct the amplitude distribution map $\mathcal{H}\mathcal{H}^z(z, \beta, x, t)$, so-called *Hilbert spectrum* in Huang et al. (1999).

$$\mathcal{H}\mathcal{H}^z(z, \hat{\beta}, x, t) = \mathcal{A}(z, x, t) \quad \text{if } \hat{\beta} - \delta\beta/2 < \beta \leq \hat{\beta} + \delta\beta/2 \quad (5.8)$$

7) Integrating over streamwise position and snapshots, it comes (Figure 5.5)

$$HH^z(z, \beta) = \int \int \mathcal{H}\mathcal{H}^z(z, \beta, x, t) dx dt. \quad (5.9)$$

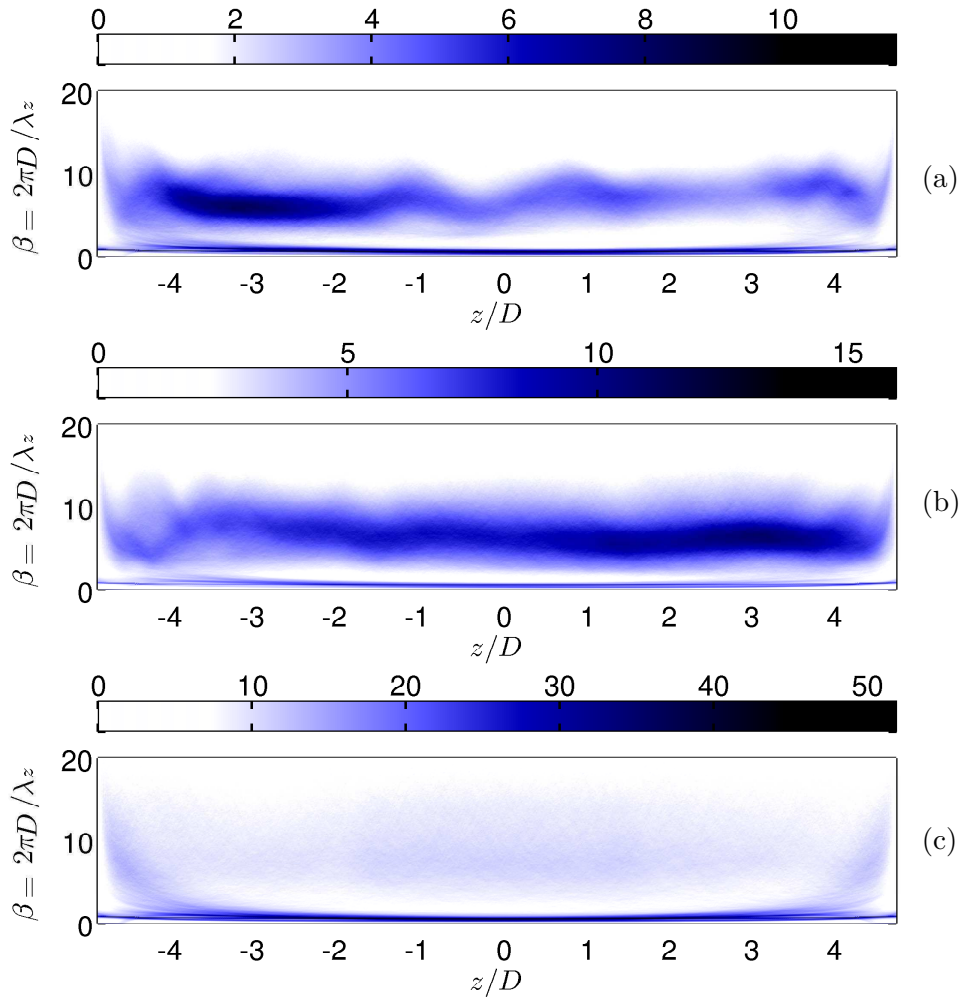


Figure 5.5: Hilbert-Huang spectral analysis performed on dimensionless vorticity fluctuations $\omega_y' D/U_0$, for the three cases *A*: $\text{Re}_D = 1500$, $D/\theta_0 = 23.2$; *B*: $\text{Re}_D = 2400$, $D/\theta_0 = 29.4$; *C*: $\text{Re}_D = 5550$, $D/\theta_0 = 46.6$. Colours encode HH^z distribution in a $(z/D, \beta)$ -space.

Figures 5.5.(a-c) confirm that dynamics mainly scales on wavenumber $\beta = 2\pi$ – corresponding to a wavelength $\lambda/D = 1$. Indeed, both low Reynolds number configuration *A* and *B* show a concentration of high amplitudes for $5 \leq \beta \leq 10$. As expected from Fourier spectrum, case

C exhibits a rather sparse distribution of wavenumbers. A common feature to all cases is the continuum of low wavenumbers $2\pi/10 \leq \beta \leq 1$ present along the entire span. They correspond to the largest space scales of the flow since the cavity spans over $S/D = 10$. An increase is observed only when approaching the strict vicinity of lateral walls: larger gradients must be induced inside the Bödewadt layers as a consequence a solid spanwise conditions. That feature is particularly visible in Figure 5.5.c. It is remarkable that such space scales, corresponding to spanwise boundary conditions, persist despite the removal of the mean flow.

The *marginal spectrum* (Huang et al., 1999) is obtained by integrating over z :

$$hh^z(\beta) = \int_z HH^z(z, \beta) dz \quad (5.10)$$

It is not equivalent to Fourier spectra. Instead of a power spectral density, a marginal Hilbert spectrum is rather a “probability” function of β , weighted by associated amplitudes \mathcal{A} . Marginal spectra hh^z are plotted in Figure 5.6 for the three cases. Part from the signature of the boundary conditions at $\beta = 2\pi/10$, the most “probable” wavenumbers are respectively $\beta(A) = 6.35$, $\beta(B) = 6.25$ and $\beta(C) = 7.2 (\pm 0.05)$.

Asymmetries are revealed, in case A : $\text{Re}_D = 1500$ especially, for which more energy is found on the left side of the cavity. For a lower part in case B : $\text{Re}_D = 2400$ where, on the other hand, higher amplitudes are observed towards the right wall. On the contrary, case C at higher Reynolds has become approximately homogeneous. Asymmetries will be discussed further in the following.

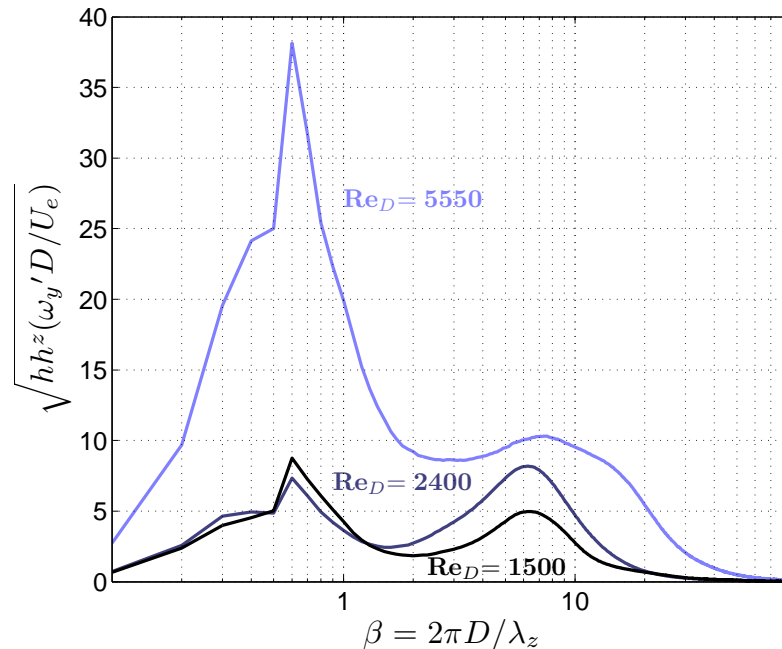


Figure 5.6: Hilbert-Huang marginal spectrum performed on dimensionless vorticity fluctuations $\omega_y' D / U_0$, for the three cases.

5.3 Space-Time structures in the inner flow

Until now, the study has been restricted to space scales only. Snapshots are used as samples to perform a statistic approach on spatial spectra. Though in a saturated regime, time evolution of centrifugal instabilities yet remains to be investigated. Spanwise structures could be time-modulated, travelling waves or steady phenomena, implying or not Strouhal numbers. In the following, the discussion focuses on temporal evolution of characteristic length-scales in the inner-flow.

5.3.1 Dataset coherence

Time scales are only available as long as successive snapshots remain dependent, at least in regards to frequencies at play in the inner-flow. PIV sampling rates for the three cases are $f_s(A) = 0.34$ Hz, $f_s(B) = 0.37$ Hz, $f_s(C) = 0.33$ Hz, corresponding to dimensionless frequencies $St(A) = f_s(A)D/U_0 = 0.57$, $St(B) = f_s(B)D/U_0 = 0.39$, $St(C) = f_s(C)D/U_0 = 0.15$, respectively. Those rates provide Nyquist Strouhal numbers far greater than frequencies expected to be involved in centrifugal instabilities. However, rising shear layer modes disturb spanwise fluctuations, which may lead to a swift loss of correlation in time.

A covariance matrix can help to highlight time-correlation in datasets. To that aim, a spanwise line is extracted at a given position $x_c/D = 0.5$ from velocity fields such as to form a matrix $V_i = [V_1(z, x_c) \ V_2(z, x_c) \ \dots \ V_N(z, x_c)]$ with N the number of snapshots considered. Then, the covariance cov_{ij} between two instants V_i and V_j is calculated such as

$$cov_{ij} = \sum_k \sum_l \left(V_i(z_k) - \bar{V}_i \right) \left(V_j(z_l) - \bar{V}_j \right), \quad (5.11)$$

where \bar{V}_i is the span-averaged value at instant V_i . One can normalise cov_{ij} to get correlation coefficients C_{ij} as below

$$C_{ij} = \frac{cov_{ij}}{\sqrt{cov_{ii} \ cov_{jj}}}. \quad (5.12)$$

One obtains a symmetric matrix, whose diagonal is identically equal to 1. Correlation maps are given for the three cases A, B, C in Figure 5.7. The correlation matrix associated with case A reveals a strongly periodic pattern of period $\tau_{corr}U_0/D \simeq 50$, properly resolved in PIV dataset. Note the *dominant* Strouhal number corresponding to correlation period is $St = (\tau_{corr}U_0/D)^{-1} = 0.02$. There is also a long-period modulation corresponding to $St \simeq 300^{-1} = 0.0033$. Regarding case B , correlation map reveals a rather complex organisation. Hypothesis of dataset coherence continues to be valid as shown by maximum time-correlation values still extending to several successive snapshots (around matrix diagonal). However, despite some diagonal patterns barely visible, coherence period is not as long as for case A , which indicates that the flow involves multiple modes of oscillations.

On the contrary, case C appears totally uncorrelated in time: high correlation coefficients are observed strictly on the diagonal. This was expected since the shear layer – greatly unstable for such parameters ($L/\theta_0 = 93.2$) – implies much mixing inside the cavity. It drastically disturbs at high frequency the inner-flow dynamics. The forthcoming part of this chapter will focus on low Reynolds cases A and B , for which space-time coherence is present.

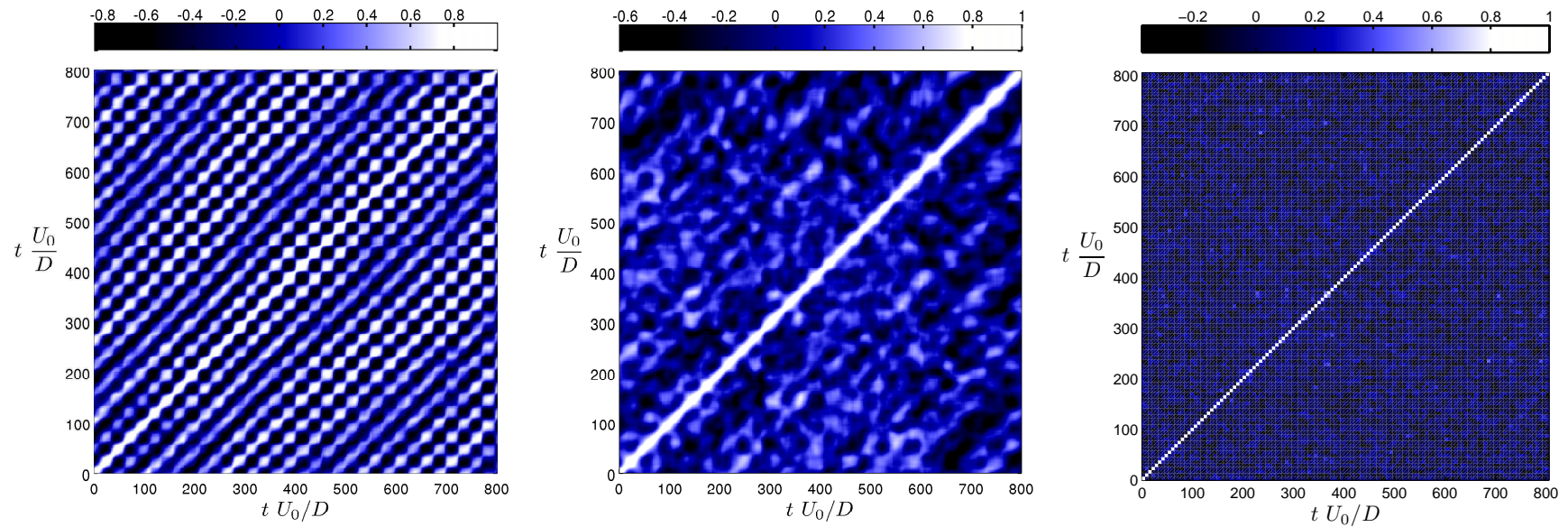


Figure 5.7: Time-correlation maps for cases A : $\text{Re}_D = 1500$, $D/\theta_0 = 23.2$ (left) and B : $\text{Re}_D = 2400$, $D/\theta_0 = 29.4$ (middle) and C : $\text{Re}_D = 5550$, $D/\theta_0 = 46.6$ (right). Colours encode correlation coefficients between two instants, as a function of dimensionless time $t \frac{U_0}{D}$. Statistics material is given by a spanwise line extracted at $x_c/D = 0.5$, $y_{piv}/D = -0.1$ for 800 time units.

5.3.2 Space-Time diagrams

Space-time planes are employed to investigate temporal evolution of vorticity fluctuations in the inner-flow for cases *A* in Figure 5.8.(a-f), and *B* in Figure 5.8.(g-i). Horizontal axes stand for spatial coordinates $z' = z/D$ and $x' = x/D$, successively, while vertical axis represents dimensionless time $t' = t \frac{U_0}{D}$. On the left hand side, diagrams display a spanwise slice (z', t') at a given position x' . On the right hand side, slices are streamwise (x', t') and extracted from two distinct z' positions. Black dashed lines mark the positions of extracted space-time planes. Note that two different segments of the dataset are presented for case *A* in Figures 5.8.(a-c) & 5.8.(d-f), respectively for $30 \leq t' \leq 390$ and $1775 \leq t' \leq 1905$. The dimensionless time unit $\frac{D}{U_0}$ is chosen for it was shown to be suitable to scale the frequencies involved in the inner-flow (Brès and Colonius, 2008). That time-scale corresponds to D -based Strouhal numbers, which will be used exclusively from now on ($St = f D/U_0$).

Spanwise space-scales are observed out of any horizontal line of (z, t) -planes, in Figures 5.8.(a,d,g). As expected from space Fourier spectra in Section 5.2, both cases exhibit strong spanwise oscillations, whose characteristic wavelength is mainly found around $\lambda = D$ ($\beta = 2\pi$). That wave-like signature corresponds to the centrifugal instabilities arising and rolling along the main recirculation. Three main scenarios are observed: *i*) left or right travelling waves represented by characteristic lines $z = w_\varphi t$, with w_φ the associated phase velocity; *ii*) interference effects when two counter-propagating waves superimpose; *iii*) steady structures nearby the endwalls.

i) Travelling waves

Phase velocities w_φ of travelling waves can be estimated from slopes depicted by space-time structures. Some are pointed out by white plain lines, and provided in Table 5.1. The dimensionless spanwise phase velocity $w_\varphi/U_0 = \Delta z'/\Delta t'$ is obtained out of Figures 5.8.(a,d,g).

For case *A*, the lines (1), (2), (3) and (7) follow the primary spanwise travelling waves. Left or right waves, they travel at various dimensionless phase velocities of modulus $|w_\varphi/U_0|$ from 0.006 and 0.022. These velocities link up the main spanwise wavelength $\lambda \simeq D$ (wavenumber $\beta \simeq 2\pi$) to a Strouhal number through the expression

$$St = \frac{w_\varphi \beta}{U_0 2\pi} = \frac{w_\varphi D}{U_0 \lambda} \approx \frac{|w_\varphi|}{U_0}. \quad (5.13)$$

The main time scales can be roughly estimated from streamwise diagrams (extracted streamwise lines), in Figures 5.8.(b-c,e-f,h-i). For example, one can guess from Figure 5.8.c the Strouhal numbers $St(2) \simeq 1/50 = 0.02 \approx w_\varphi(2)$ (for $t' \leq 180$) and $St(3) \simeq 1/150 = 0.007 \approx w_\varphi(3)$ (for $t' \geq 180$). Similarly, one gets $St(7) \simeq 1/50 = 0.02 \approx w_\varphi(7)$ from Figure 5.8.f.

Space-time diagrams displayed in Figures 5.8.(g,h,i) correspond to the dataset *B*: $Re_D = 2400$, $D/\theta_0 = 29.4$. In Figure 5.8.g, part from some space-time correlated features depicted by the slopes (8) and (9) on the right-hand side of the cavity span ($-2 \leq z/D \leq 5$), a localised structure is pulsating for $-4 \leq z/D \leq -2$.

ii) Interferences (beating)

For some regions, those counter-propagating waves overlay and induce interferences (or *beating*), seen as draughtboard patterns in (z, t) -planes. This can be modelled as follow

$$\psi(z', x', t') = A_\psi(x') [\sin(2\pi St_{\mathcal{L}} t' - \beta_{\mathcal{L}} z') + \sin(2\pi St_{\mathcal{R}} t' - \beta_{\mathcal{R}} z')] \quad (5.14)$$

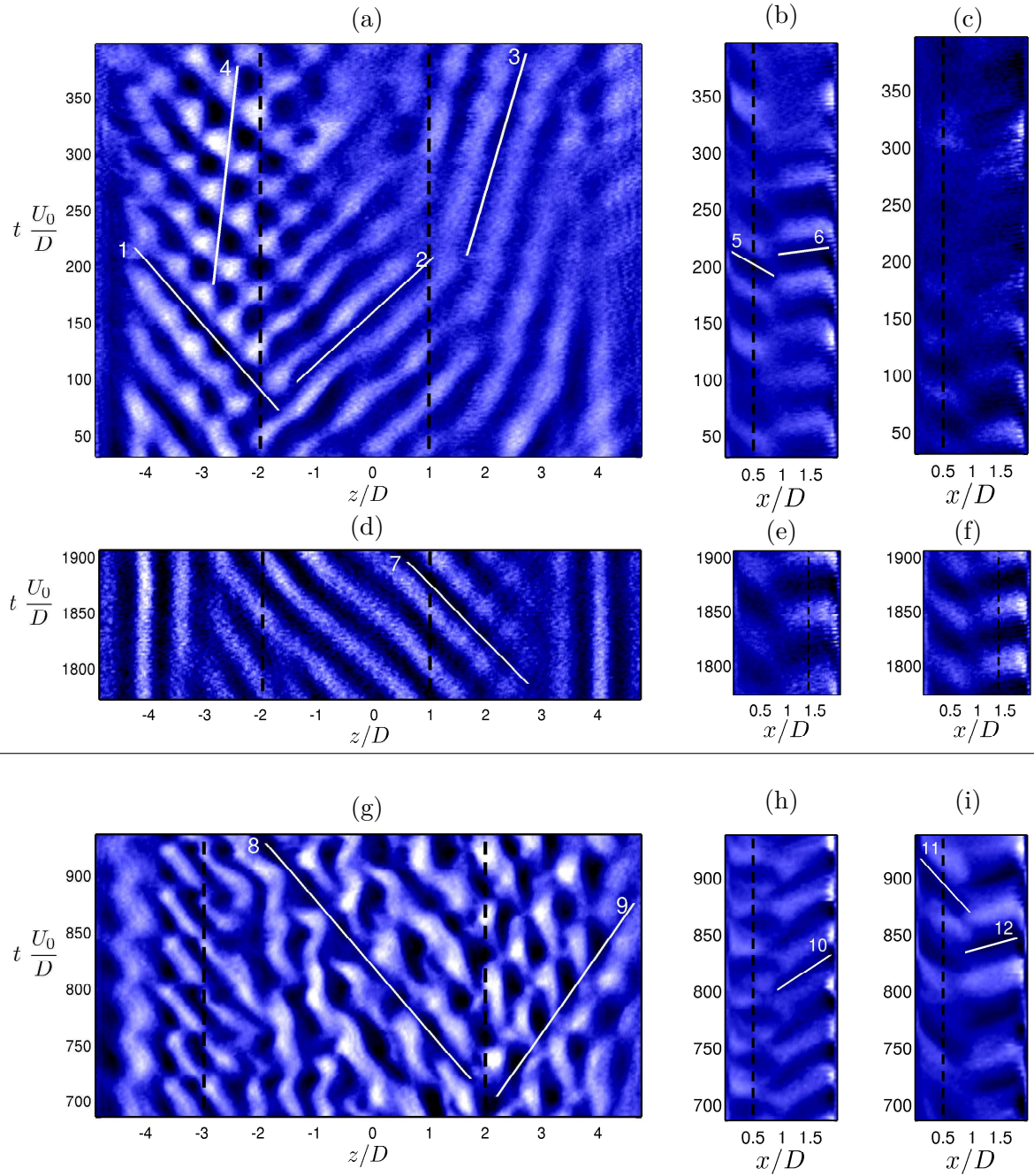


Figure 5.8: Space-time diagrams at $y/D = -0.1$ for cases *A*: $Re_D = 1500$, $D/\theta_0 = 23.2$ – two time-abstracts (a-c) & (d-f) – and *B*: $Re_D = 2400$, $D/\theta_0 = 29.4$ (g,h,i). Fluctuations of normal vorticity ω_y' (negative values are dark) are extracted from (left) spanwise lines, and (right) streamwise lines, providing parametric functions of dimensionless time $t \frac{U_0}{D}$ and dimensionless position, z/D and x/D , respectively. Spanwise diagrams are extracted at (a), $x/D = 0.5$; (d), $x/D = 1.5$; (g), $x/D = 0.5$; and streamwise diagrams are extracted at (b,e), $z/D = -2$; (c,f), $z/D = 1$; (h), $z/D = -3$; (i), $z/D = 2$. Dashed black lines represent intersections between streamwise and spanwise diagrams. Several slopes corresponding to travelling structures are also displayed (white plain lines).

where $\beta_{\mathcal{L}} \leq 0$ and $\beta_{\mathcal{R}} \geq 0$. This rewrites as the product of two waves

$$\psi(z', x', t') = 2 A_{\psi}(x') \cos(2\pi \text{St}^- t' - \beta^- z') \sin(2\pi \text{St}^+ t' - \beta^+ z'), \quad (5.15)$$

such that

$$\text{St}^{\pm} = \frac{\text{St}_{\mathcal{L}} \pm \text{St}_{\mathcal{R}}}{2} \quad \text{and} \quad \beta^{\pm} = \frac{\beta_{\mathcal{L}} \pm \beta_{\mathcal{R}}}{2}, \quad (5.16)$$

With this expression, one recognises a wave amplitude-modulating another wave. The phase velocities of the two resulting *interference waves* are given by

$$w_{\varphi}^{\pm} = 2\pi \frac{\text{St}^{\pm}}{\beta^{\pm}}. \quad (5.17)$$

The most salient example of such a pattern is given by the two counter-travelling waves depicted by slopes (1) and (2) in Figure 5.8.(a). In this case, the counter-propagating waves exhibit roughly equal wavelengths $\lambda \simeq D$,

$$\beta_{\mathcal{L}} = \beta(1) \simeq -2\pi \quad \text{and} \quad \beta_{\mathcal{R}} = \beta(2) \simeq 2\pi \quad (5.18)$$

therefore it comes

$$\beta^- \simeq -2\pi \quad \text{and} \quad \beta^+ \simeq 0 \quad (5.19)$$

As a consequence, the Strouhal numbers corresponding to the left and right waves (1) and (2) hence are approximatively equal to phase velocities (Equation 5.13):

$$\text{St}(1) \approx |w_{\varphi}(1)| = 0.018 \quad \text{and} \quad \text{St}(2) \approx |w_{\varphi}(2)| = 0.022, \quad (5.20)$$

which results in interference Strouhal numbers

$$\text{St}^- = \frac{\text{St}(1) - \text{St}(2)}{2} = -0.004 \quad \text{and} \quad \text{St}^+ = \frac{\text{St}(1) + \text{St}(2)}{2} = +0.020 \quad (5.21)$$

The value of St^+ is confirmed by observation of Figure 5.8.b. As for Strouhal number St^- , one can remember the correlation map previously presented in Figure 5.7.a, which showed an amplitude modulation of period 300 in dimensionless units, yielding the very same interference $\text{St}^- \approx 300^{-1}$. Finally, the phase velocities (given by Equation 5.17)

$$w_{\varphi}^- = +0.002 \quad \text{and} \quad w_{\varphi}^+ \rightarrow \infty \quad (5.22)$$

indicate that the beating pattern consists of a slow-travelling wave ($\text{St}^- = -0.004$, $\beta^- = -2\pi$, $w_{\varphi}^- = +0.002$), globally modulated in time at the dimensionless frequency $\text{St}^+ = 0.02$.

Another example of beating is barely visible in the other time-segment in Figure 5.8.d for which there is almost no right wave to be seen.

As for case *B*, a highly energetic draughtboard pattern is found in Figure 5.8.g. However, the underlying travelling waves are not clearly visible because the space-time structures are rather distorted by increased complexity of the dynamics ($\text{Re}_D \nearrow$, $D/\theta_0 \nearrow$). Nonetheless, two propagating features can be extracted by slopes (8) and (9) from Figure 5.8.g. In that case, remark that the left wave ($w_{\varphi}(8) = -0.017$) is faster than the right wave ($w_{\varphi}(9) = 0.014$). In Figure 5.8.i is observed a temporal oscillation of Strouhal number $\text{St} \simeq 1/65 = 0.015$. This could match an interference pattern composed of slopes (8) and (9) in Figure 5.8.g. If $\lambda/D = 1$,

Expression 5.13 is still valid, hence

$$\text{St}^+ = \frac{\text{St}(8) + \text{St}(9)}{2} \approx \frac{w_\varphi(8) + w_\varphi(9)}{2} \quad (5.23)$$

One can wonder why the counter-propagating wave patterns are not symmetrical ($|w_\varphi(1)| \neq |w_\varphi(2)|$ and $|w_\varphi(8)| \neq |w_\varphi(9)|$).

Could the setup imperfections be responsible for those symmetry breaking?

As in any experiments, experimental conditions are characterised within uncertainties. Imperfections that could lead to spanwise asymmetries are concerned with the cavity geometry (*a*) and/or the incoming velocity profile, which can be altered by either a systematic asymmetrical velocity profile caused by the water-tunnel design (*b*); an angular discrepancy between the cavity rig and the water-tunnel (*c*) (see Figure 2.3 for setup). No systematic bias is observed since asymmetry varies depending on series. Therefore, uncertainties on both cavity geometry (*a*) and water-tunnel design (*b*) are ruled out for they remained unchanging during the entire campaign.

On the other hand, the set-up had to be opened (roof removal) in order to clean regularly the test-section of settling particles. As a result, the position of the rig could vary by about ± 1 mm over the span $S = 500$ mm. Such an uncertainty (*c*) of $\pm 0.2\%$, corresponding to an angular error of $\pm 0.11^\circ$, cannot explain alone the symmetry breaking. Consequently, an intrinsic sensitivity of the dynamics should rather be considered, as it will be discussed in Chapter 6.

iii) (Quasi)-steady structures

For case *A*, the second segment presented in Figure 5.8.d shows steady structures near the lateral walls of the cavity (at $|z/D| \lesssim 0.5$). These structures may be related to Bödewadt layers.

Regarding the streamwise space-time planes, Figures 5.8.(b-c,e-f,h-i) indicate a phase discontinuity around $x/D = 0.8$, likely corresponding to the frontier between the two recirculations. This is consistent with phase velocities u_φ of opposite sign on each side of this position. When $x/D > 0.8$ phase velocities are positive ($u_\varphi(6), u_\varphi(10), u_\varphi(12) > 0$), while waves travel backwards for $x/D < 0.8$ ($u_\varphi(5), u_\varphi(11) < 0$).

Table 5.1: Phase velocities out of space-time diagrams.

Line	w_φ/U_0	u_φ/U_0
1	-0.018	–
2	0.022	–
3	0.006	–
4	0.002	–
5	–	-0.036
6	–	0.158
7	-0.020	–
8	-0.017	–
9	0.014	–
10	–	0.031
11	–	-0.018
12	–	0.074

5.4 Space-time modal decomposition

The space-time dynamics of the cavity inner-flow has been thoroughly characterised in the physical domain. More insight can be obtained through an investigation of the same patterns in the spectral domain. To that aim, a modal decomposition in time would give access to coherent structures associated with a given time-scale. Indeed, when samples are time-resolved, Fourier transform can be performed along time-series extracted from various points spatially distributed across the velocity fields, as shown in Section 3.1.4. If every point of the grid is selected, one ends up with a set of complex spatial modes of dimensions equal to those of velocity fields, each associated with a Strouhal number. Then, additional decomposition can help to identify the space scales yielded by each complex spatial modes under study.

5.4.1 Characteristic Strouhal numbers

Prior to investigation of coherent structures, a preliminary study consists in performing the power spectral density over time-series and integrating in space. Such *time spectra* are presented in Figure 5.9. Fourier transform uncertainty is reduced thanks to integration over the entire field and to window averaging: 95 %-confidence interval is about ± 0.12 dB. Windows of 650 samples correspond to about 1130 and 1680 dimensionless time units (tU_0/D) for cases *A* and *B*, respectively. Recall that time units are chosen accordingly to Strouhal numbers based on cavity depth D , a relevant scaling for frequencies induced by centrifugal instabilities (Brès and Colonius, 2008). Padding with zeros, Fourier transforms are computed over 1024 points, which results in spectral steps $\delta\text{St}(A) = 0.00056$ and $\delta\text{St}(B) = 0.00038$, respectively.

Both cases exhibit a spectrum culminating around $\text{St} = fD/U_0 = 0.02$, as expected from space-time diagrams and correlation maps. Other peaks are also observed but they could either represent independent modes or result from nonlinear interactions. They are classified in arbitrary spectral families $m = \{0 - 4\}$, which will be investigated in Section 5.4.4.

- $m = 0$ → Steady features
- $m = 1$ → Slow variations (large time-scales)
- $m = 2$ → Dominant time scales
- $m = 3$ → Secondary peaks
- $m = 4$ → Possibly the harmonics of the dominant peaks

Many well-defined spectral components are visible in case *A* : $\text{Re}_D = 1500$, $D/\theta_0 = 23.2$. For instance, the peaks rising at $\text{St} = \{0.038, 0.057\}$ in case *A* likely correspond to harmonics of the dominant Strouhal number since $0.038 = 2 \times 0.019$ and $0.057 = 3 \times 0.019$.

On the contrary, the spectrum of case *B* ($\text{Re}_D = 2400$, $D/\theta_0 = 29.4$) shows overall a higher background level, as expected from higher values of control parameters. Indeed, as the system goes further from threshold, more modes become unstable, leading to a wider range of active frequencies. Also, case *B* involves more energy than case *A* (see Figure 5.3), which can theoretically imply stronger nonlinear interactions. Settling the origin of these various peaks would be premature without an investigation of their associated spatial structure.

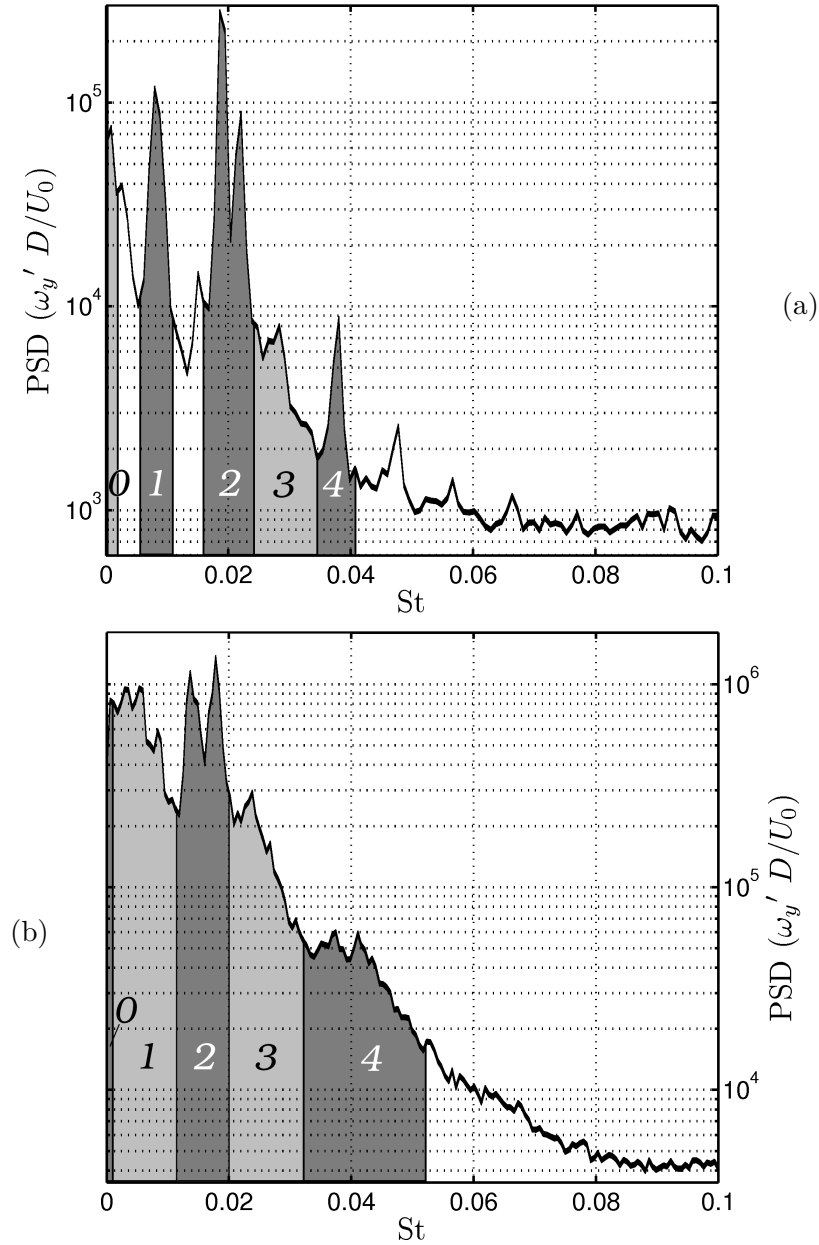


Figure 5.9: Time Fourier power spectral density performed on dimensionless cross-stream vorticity fluctuations $\omega_y' D/U_0$ for cases *A* (a) and *B* (b). Indices $m = [0, 1, 2, 3, 4]$ correspond to arbitrary spectral subdomains for the sake of clarity in the following.

5.4.2 Associated spatial modes

After the space-integrated power signature, spectral analysis can be developed through spatially extended (2D) time Fourier decomposition, as used in the previous chapter. The methodology is described in Section 3.1.4. Projecting the dataset on $\exp(2\pi i f_k t)$ functions, the resulting complex spatial modes (*global Fourier modes*) are available for any Strouhal St_k such that

$$St_k = k \frac{\delta f D}{U_0} = \frac{k}{N} \frac{D}{U_0 \delta t} \quad \text{with } k = -N/2, \dots, -1, 0, 1, 2, \dots, N/2 \quad (5.24)$$

where $\delta t U_0/D$ is the sampling step in dimensionless time units, and $N + 1$ the number of snapshots. Samples of $N + 1 = 430$ snapshots are used so that Strouhal steps are respectively

$$\frac{D/U_0}{N \delta t_{(A)}} = 13 \cdot 10^{-4} \quad \& \quad \frac{D/U_0}{N \delta t_{(B)}} = 8.9 \cdot 10^{-4} \quad (5.25)$$

Real and imaginary parts of global Fourier modes associated with relevant Strouhal numbers are depicted in Figures 5.11-5.27.(a,b).

5.4.3 Identifying space-scales

In order to identify space-scales associated with each relevant Strouhal number, both Hilbert-Huang and space Fourier transforms have been applied spanwise to (time) global Fourier modes, using the same methodology as in Section 5.2. The reader will find a schematic outline of the decomposition in Figure 5.10.

On the Hilbert-Huang transform (HHT), Empirical Mode Decomposition is performed successively on real and imaginary parts of each time Fourier mode. One out of two x -positions are used. Then considering only the first two most energetic Intrinsic Mode Functions (IMFs), Hilbert transform gives access to local (β, \mathcal{A}) couples throughout the field. For the sake of clarity and synthesis, the intensity maps of the picked IMFs are summed up resulting in Hilbert-Huang spectra $\mathcal{H}\mathcal{H}_{\omega_y}^z(z, \beta \geq 0, x, St_k)$. Integrating over the streamwise position x , one ends up with a Hilbert-Huang distribution $HH_{\omega_y}^z(z, \beta)$ for each Strouhal number St_k . Hereafter, Hilbert-Huang distributions will simply write HH^z for the sake of simplicity (HHT has only been applied to ω'_y fluctuations). Remark that both real and imaginary parts are considered independently from one another when HHT is applied. As a consequence, the information in phase contained in complex global Fourier modes is lost, which implies unsigned wavenumbers. HH_k^z maps are provided in Figures 5.11.b, 5.18.b and Figures 5.12.c to 5.27.c.

Regarding the spanwise Fourier analysis, it is carried out at every position x and provide $\mathcal{F}^{zt}(\beta, x, St_k)$ spectra in Figures 5.11.c, 5.18.c for the mean flow and in Figures 5.12.d to 5.27.d. Spanwise arrays are originally composed of 823 points (823 vectors spanwise in the velocity fields). To increase spectral resolution, they are padded with zeros to reach 1024 points (corresponding to a length of 1.25S). Despite that extension of spanwise arrays, spectral resolution of $\mathcal{F}^z(\beta, x, St_k)$ remains far lower than the one of HHT spectra. On the other hand, Fourier transform provides a spectrum of signed wavenumbers. Indeed, by taking into account the phase of the (complex) time Fourier modes, space Fourier transform preserves left or right-travelling waves. The Fourier spectrum is not integrated over x to provide a streamwise distribution of *energetic* wavenumbers, while the HHT spectrum gives access to their spanwise distribution.

5.4.4 Results

We aim to discuss the coherent structures revealed by time and space decompositions applied to our experimental results. For each considered time scale, space scales distribution can help to identify the underlying phenomenon. Note that it would be fastidious and pointless to discuss every frequency extracted from the spectrum. Instead, only a handful of global Fourier modes are presented here. Remark that results are obtained out of a limited number of events. In this sense, they yield characteristic features of the present dataset rather than an exhaustive

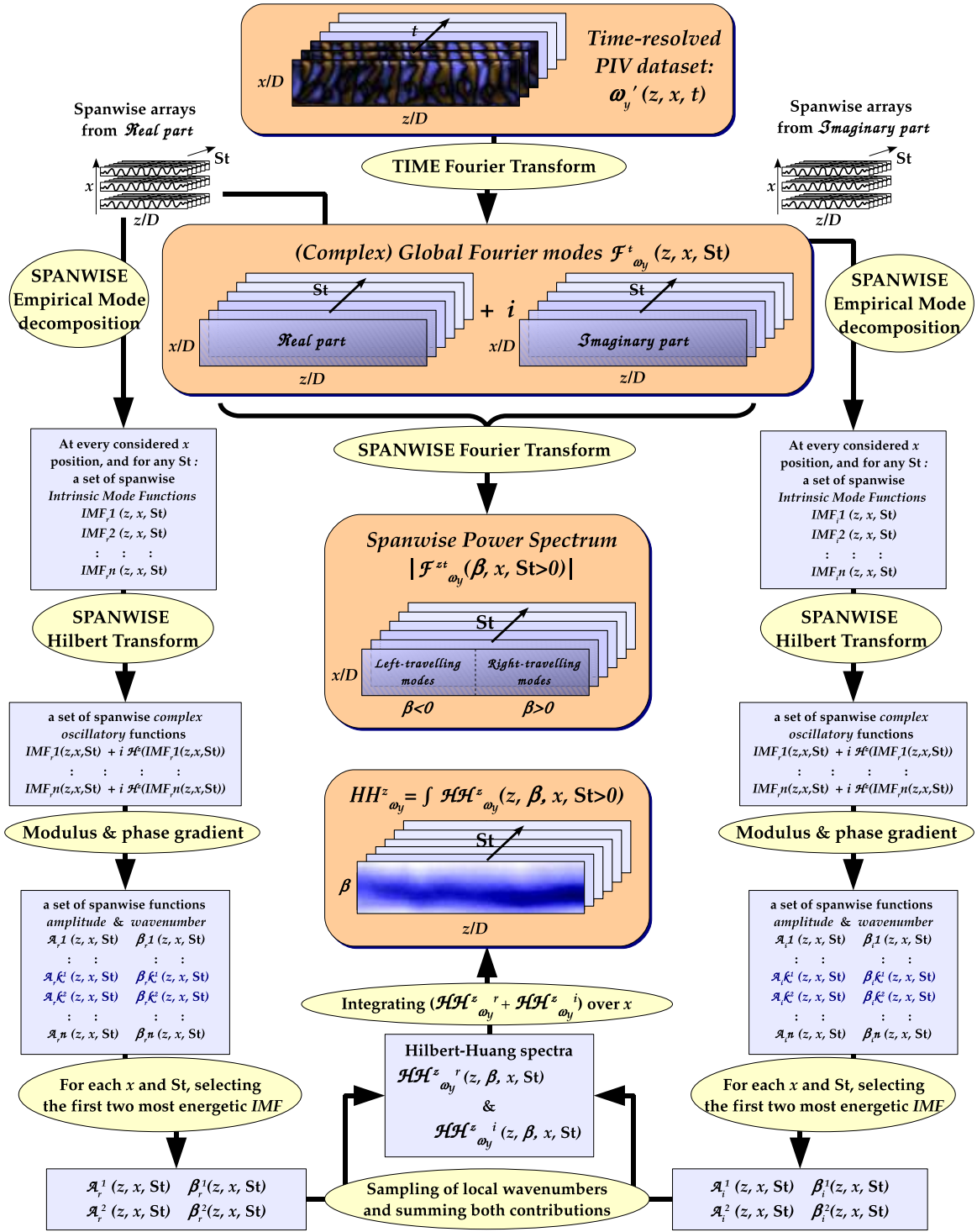


Figure 5.10: Schematic outline of the space-time decomposition methodology performed on vorticity fluctuations ω_y' non-dimensionalised by U_0/D

analysis of the inner flow, which would require more extensive statistics.

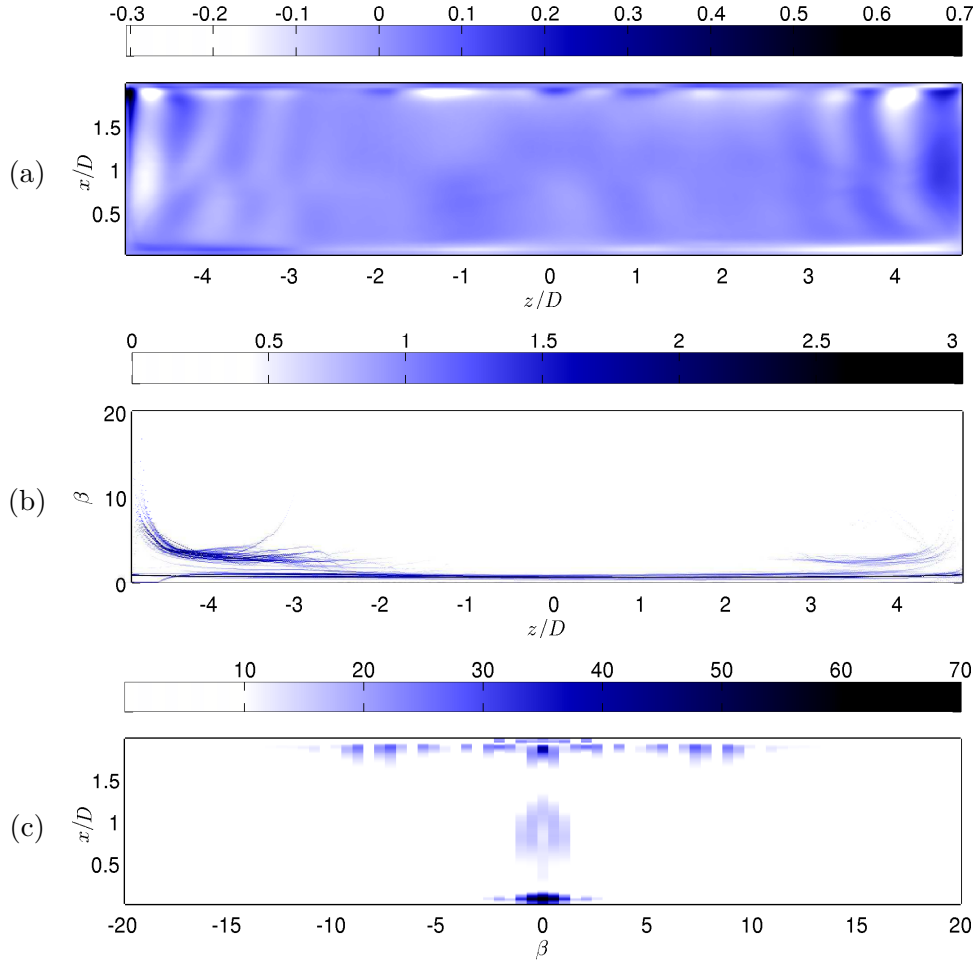


Figure 5.11: Mean flow ($St = 0$, $m = 0$) for case A : $Re_D = 1500$, $D/\theta_0 = 23.2$. (a) Colours encode fluctuations of dimensionless vorticity $\omega_y' D/U_0$; (b) $HH^z(z, \beta)$ map issued from Hilbert Huang Transform; (c) spanwise Fourier spectrum $\mathcal{F}^z(\beta, x)$ (in 10^{-3} units).

A. $Re_D = 1500$, $D/\theta_0 = 23.2$

• $m = 0$:

Prior to the study of characteristic Strouhal numbers of the dynamics, the first mode to be considered is the mean flow, which can be seen as the mode $St = 0$ (see Figure 5.11). Contrary to the forthcoming Fourier modes, the mean flow is obviously not complex since it yields no temporal behaviour by definition (the spanwise Fourier spectrum is thus symmetrical). Overall, it exhibits almost no spanwise oscillations so that $\beta \rightarrow 0$, indicating an organisation fairly two-dimensional (in terms of cross-stream vorticity ω_y). Note that $\beta = 0$ mode is available in space-Fourier spectrum whereas Hilbert-Huang transform deals only with oscillatory modes by definition (Intrinsic Mode Functions). As a result, for HHT spectra one gets $\min(\beta) = 2\pi/10$, which corresponds to the largest wavelength, that is the cavity span $S = 10D$.

Nevertheless, the endwall regions exhibit some energy with wavenumbers increasing to reach $\beta \simeq 10$ ($\lambda/D = 0.6$). This represents the (steady) signature of the spanwise solid boundary conditions. The spanwise space Fourier spectrum indicates the oscillations are of higher

amplitude near the downstream edge of the cavity (Figure 5.11.c).

As data acquisitions last for long periods (typically 20 min), experimental conditions can vary, implying slow motions in *theoretically* steady phenomena. Consequently, the lowest Strouhal numbers can be considered as completing the mean flow. For instance in Figure 5.12, the mode associated with $St = 0.001$ for case *A* involves slowly moving waves nearby the endwalls, at $\beta = \pm 10$, it is thus very similar to the mean flow.

• $m = 1$:

In the time-spectrum in Figure 5.9.a, a peak appears at $St_1 = 0.007$ for case *A*. Its spatial structure is displayed in Figure 5.13 and indicates a travelling mode (phase quadrature between real and imaginary parts). The unique positive wavenumber $\beta_1 = 8$ in the Fourier transform

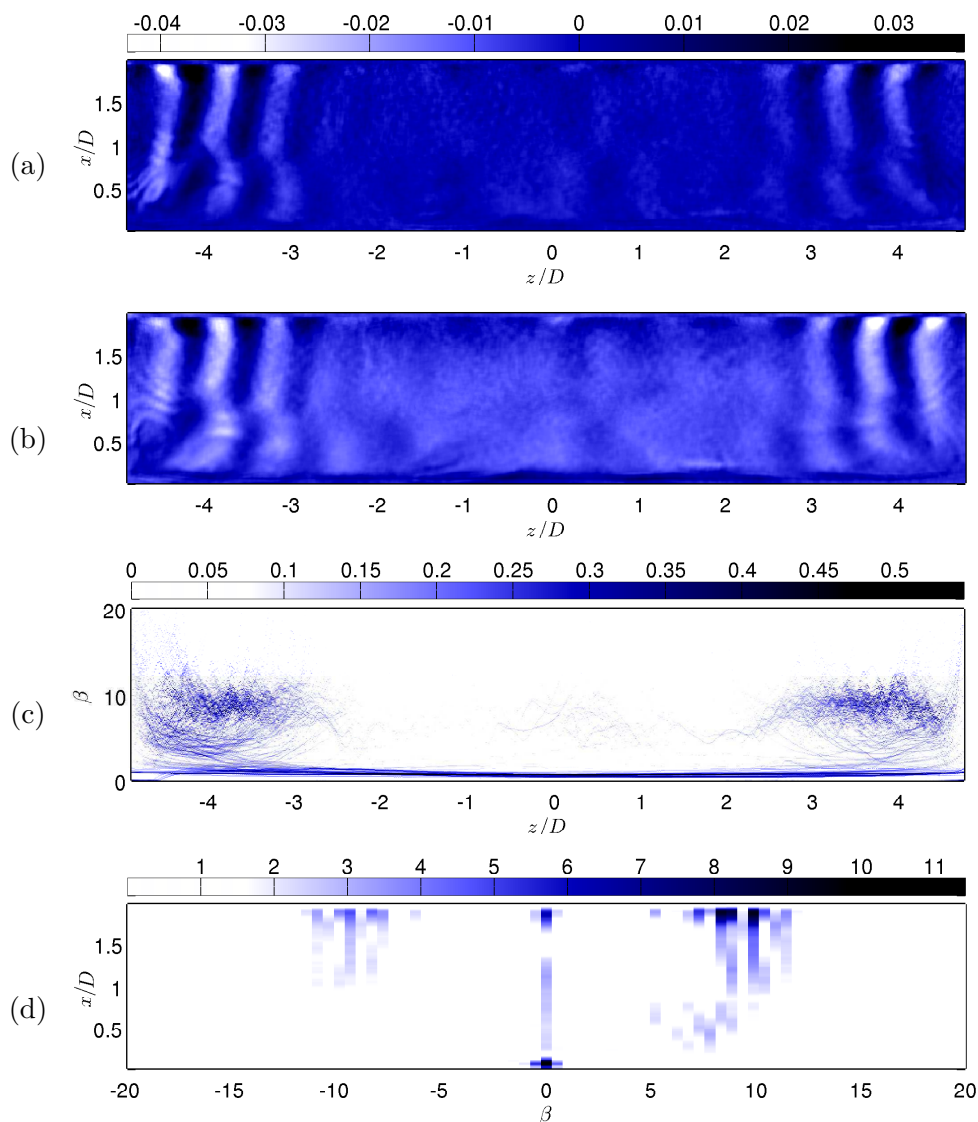


Figure 5.12: Spatial mode associated with $St = 0.001$ ($m = 0$) for case *A* : $Re_D = 1500$, $D/\theta_0 = 23.2$. (a,b) Real and imaginary parts of time Fourier mode, colours encode fluctuations of dimensionless vorticity $\omega_y' D/U_0$; (c) $HH^z(z, \beta)$ map issued from Hilbert Huang Transform; (d) spanwise Fourier spectrum $\mathcal{F}^z(\beta, x)$ (in 10^{-3} units).

implies a single right travelling wave $\psi_1(z, x, t)$ such as

$$\psi_1(z, x, t) = |\psi_1(z, x, t)| \exp[i(2\pi \text{St}_1 t' - \beta_1 x')] \quad (5.26)$$

with the dimensionless variables $x' = x/D$ and $t' = t U_0/D$. The associated phase velocity c_1 can be deduced through the relation

$$\frac{c_1}{U_0} = 2\pi \frac{\text{St}_1}{\beta_1} \simeq 0.0055 \quad (5.27)$$

The map $HH^z(z, \beta_1)$ locates most of the structure in the region $0.5 \leq z/D \leq 3.5$. It is worth making the connection between those global Fourier modes and the patterns observed earlier in space-time diagrams (Figure 5.8), as both displays are based on the same

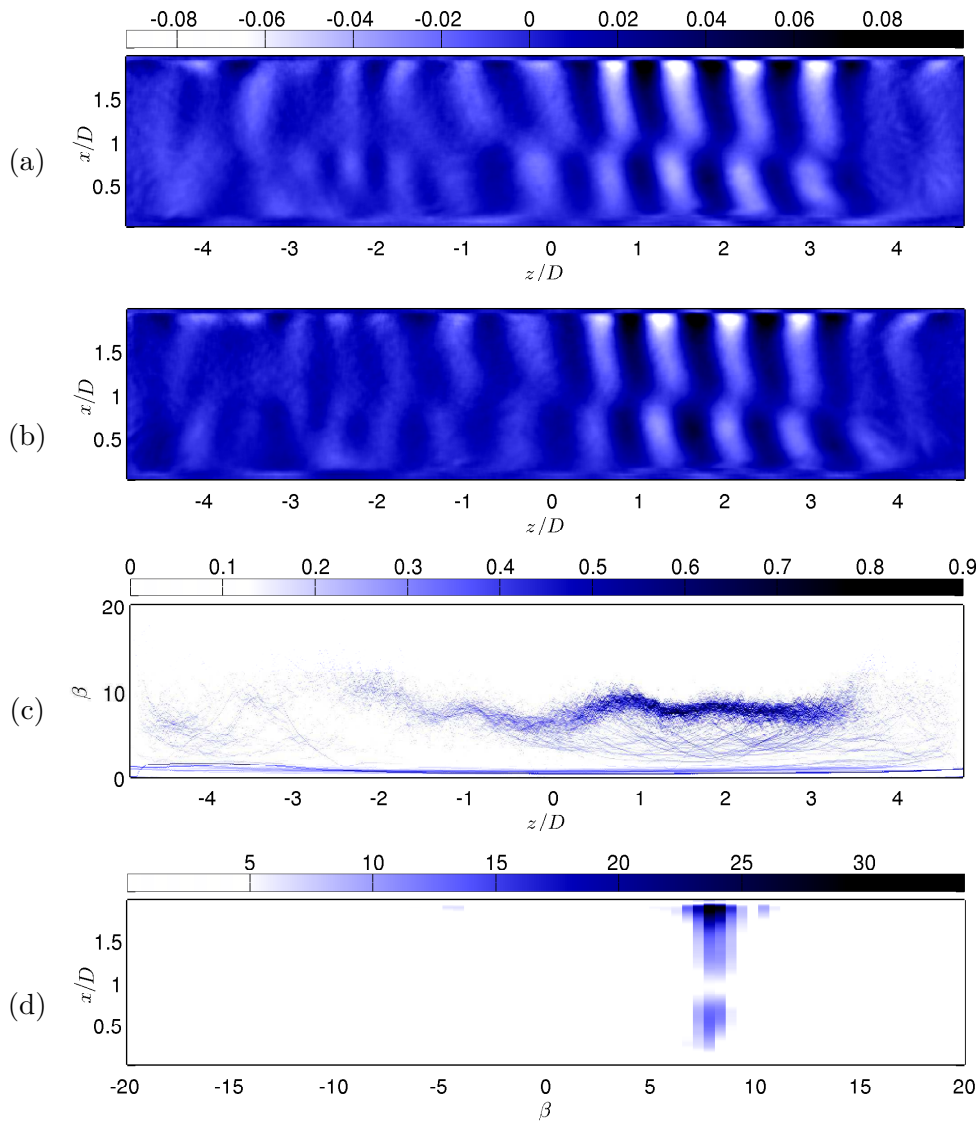


Figure 5.13: Spatial mode associated with $\text{St} = 0.007$ ($m = 1$) for case A : $\text{Re}_D = 1500$, $D/\theta_0 = 23.2$. (a,b) Real and imaginary parts, (c) Hilbert Huang Transform: $HH^z(z, \beta)$ map, (d) spanwise Fourier spectrum $\mathcal{F}^z(\beta, x)$ (in 10^{-3} units).

sample. For instance, the wave characteristics provided above match those already pointed out by slope β in the space-time diagram in Figure 5.8.a. This travelling mode stands alone, without any counter-propagating wave: locally, it yields most of the dynamics.

• $m = 2$:

The most energetic component of the time spectrum (Figure 5.9.a) is located around $St = 0.02$. An example of spatial mode associated with such a peak ($St_{2c} = 0.019$) is provided in Figure 5.14. It corresponds to a highly coherent left-travelling wave, observed for $z/D \leq -1$ and yielding a narrow distribution of wavenumbers around $\beta_{2c} = -2\pi$ ($\lambda_{2c}/D = 1$). The cells organise around the recirculation. Indeed, amplitude of oscillations is reduced with a discontinuity of phase at $x/D = 0.8$. Looking back at the space-time diagram in Figure 5.8.a, that left-travelling wave was already identified by slope 1 ($w_\varphi(1) = -0.018$), extracted at $x/D =$

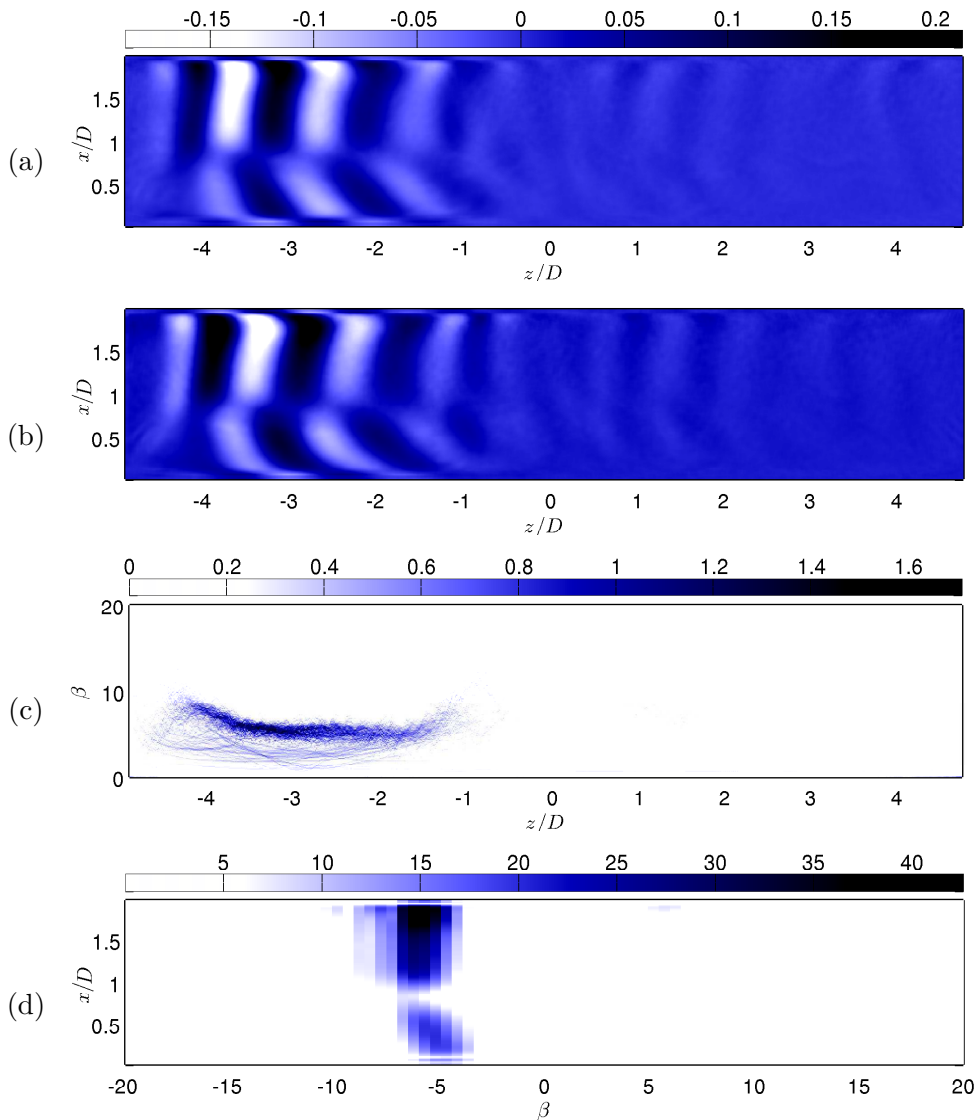


Figure 5.14: Spatial mode associated with $St = 0.019$ ($m = 2$) for case A : $Re_D = 1500$, $D/\theta_0 = 23.2$. (a,b) Real and imaginary parts, (c) Hilbert Huang Transform: $HH^z(z, \beta)$ map, (d) spanwise Fourier spectrum $\mathcal{F}^z(\beta, x)$ (in 10^{-3} units).

0.5. With the local wavenumber being about $\beta(x/D = 0.5) = -6$ according to Figure 5.14.d, both estimations fairly match

$$\frac{c_{2\mathcal{L}}}{U_0} = 2\pi \frac{\text{St}_{2\mathcal{L}}}{\beta_{2\mathcal{L}}} = -0.019 \approx w_\varphi(1). \quad (5.28)$$

Another peak at Strouhal number $\text{St}_{2\mathcal{R}} = 0.023$ also pertains to ($m = 2$) family. The associated spatial mode is roughly symmetric to the one associated with $\text{St}_{2\mathcal{L}} = 0.019$. In Figure 5.15, it consists of a right-travelling wave, yielding the same wavelength ($\beta_{2\mathcal{R}} \simeq 2\pi$) and corresponding to slope 2 in the corresponding space-diagram (Figure 5.8.a).

Both modes are centred on the left-hand side of the cavity. In fact, as suggested in Section 5.3.2, the draughtboard pattern observed in space-time diagram (Figure 5.8.a) actually

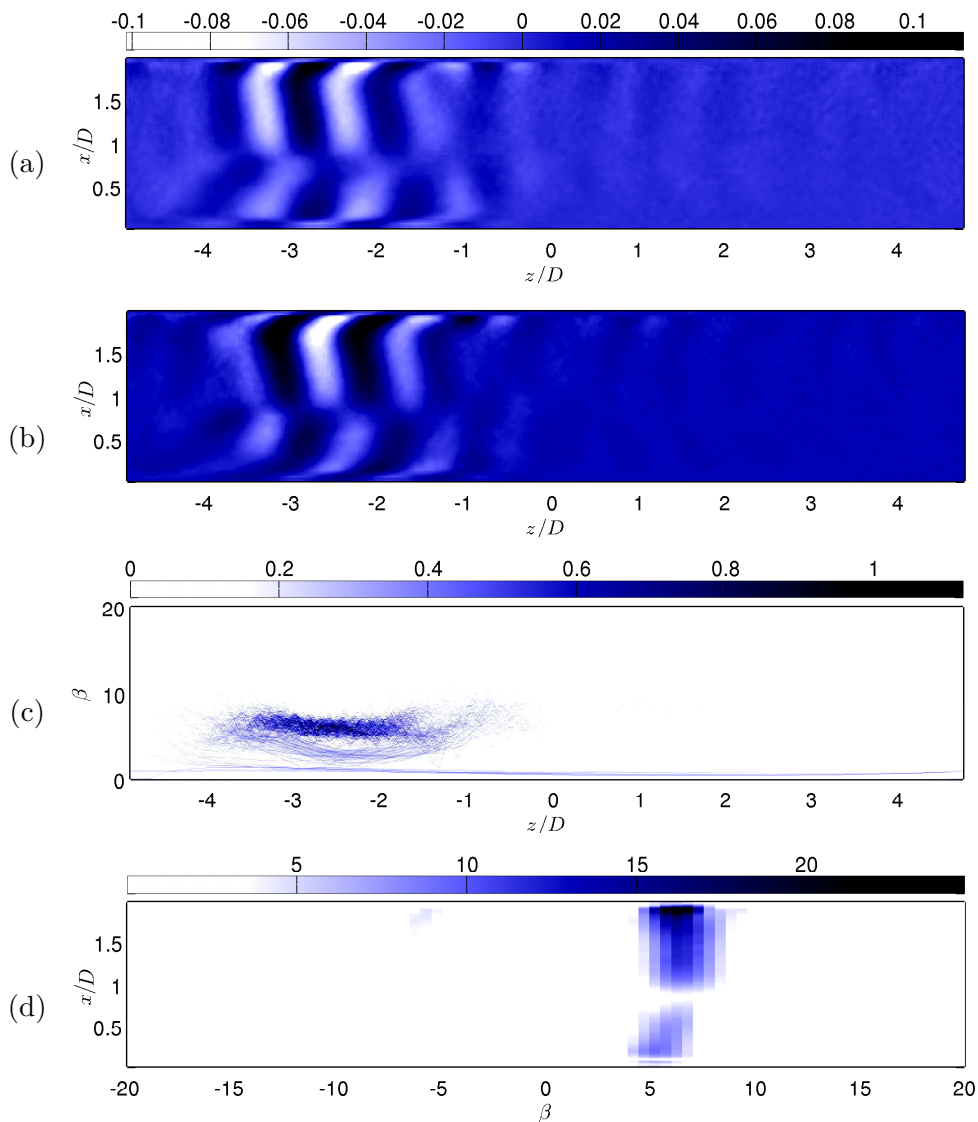


Figure 5.15: Spatial mode associated with $\text{St} = 0.023$ ($m = 2$) for case A : $\text{Re}_D = 1500$, $D/\theta_0 = 23.2$. (a,b) Real and imaginary parts, (c) Hilbert Huang Transform: $\text{HH}^z(z, \beta)$ map, (d) spanwise Fourier spectrum $\mathcal{F}^z(\beta, x)$ (in 10^{-3} units).

results from an interference of the two counter-propagating waves, that have been identified in Figures 5.14 & 5.15. Remark that if the counter-propagating waves ($2_{\mathcal{L}}$) and ($2_{\mathcal{R}}$) had been strictly symmetric, yielding identical Strouhal numbers ($St_{2_{\mathcal{L}}} = St_{2_{\mathcal{R}}}$) and opposite wavenumbers ($\beta_{2_{\mathcal{L}}} = -\beta_{2_{\mathcal{R}}}$), time Fourier decomposition would have collected both waves in the same global Fourier mode, which would have consisted of a *standing wave*.

• $m = 3$:

In the spectrum of Figure 5.9.a, a peak is found for Strouhal numbers such that $0.025 \leq St_3 \leq 0.030$, though energy level is far lower than the modes of family $m = 2$. An example of mode associated with $St_3 = 0.027$ is provided in Figure 5.16. Its spatial structure is particularly non-trivial. Spanwise space scales observed in both HH^z and \mathcal{F}^z are mainly clustered near both endwalls at wavenumbers such that $5 \leq \beta_3 \leq 10$. One also finds

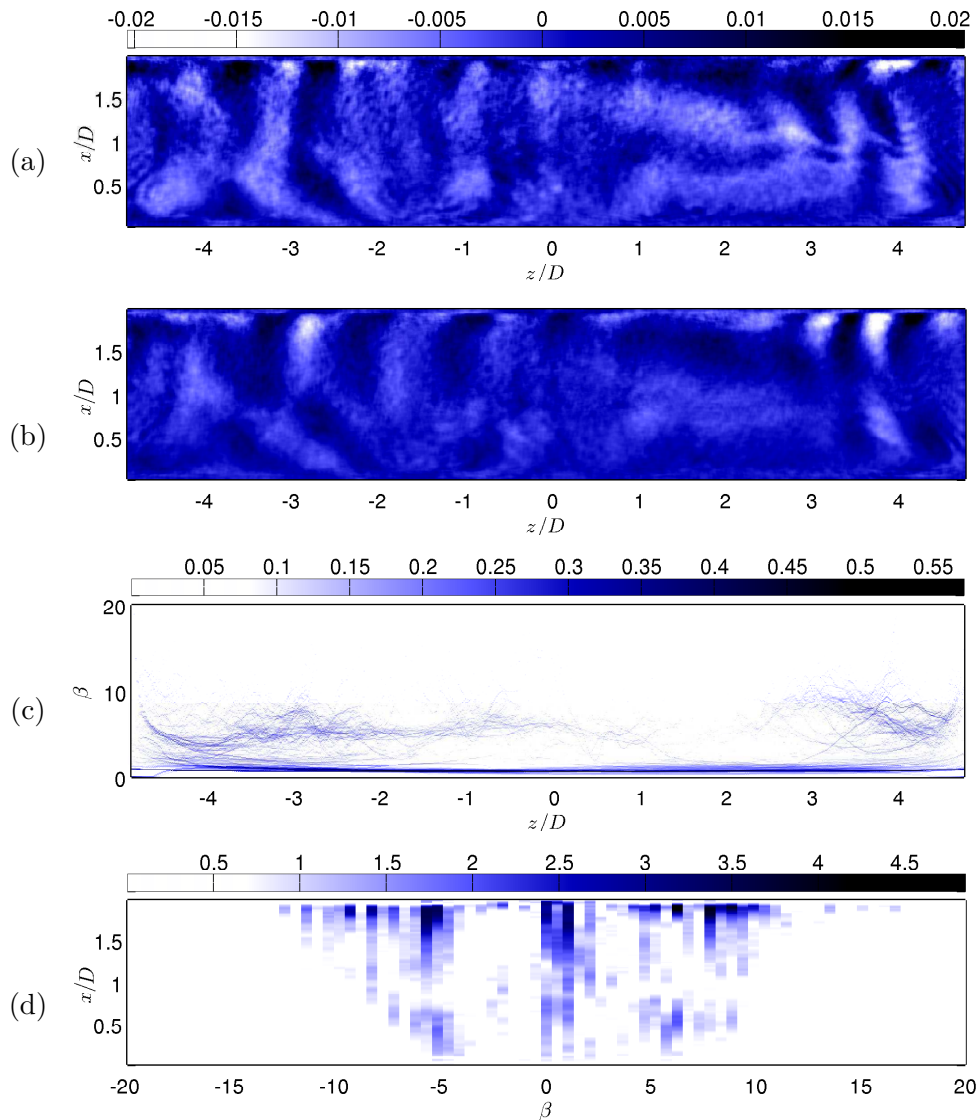


Figure 5.16: Spatial mode associated with $St = 0.027$ ($m = 3$) for case A : $Re_D = 1500$, $D/\theta_0 = 23.2$. (a,b) Real and imaginary parts, (c) Hilbert Huang Transform: $HH^z(z, \beta)$ map, (d) spanwise Fourier spectrum $\mathcal{F}^z(\beta, x)$ (in 10^{-3} units).

wavenumbers around $\beta = 0$, which correspond to quasi-streamwise oscillations according to Figures 5.16.(a,b).

• $m = 4$:

Extracted at $St_4 = 0.039$, the mode investigated in Figure 5.17 depicts a left-travelling wave of wavenumber roughly such that $10 \leq \beta \leq 13$. This mode unambiguously corresponds to the first harmonic of the dominant mode $2\mathcal{L}$, displayed in Figure 5.14. It doubles both Strouhal and wave numbers ($St_4 = 2St_{2\mathcal{L}}$ and $\beta_4 \simeq 2\beta_{2\mathcal{L}}$) and its spatial distribution – Figures 5.17.(a,b) – exhibits a similar shape, only changing in terms of wavelength. The presence of an harmonic indicates the dominant mode at $St_{2\mathcal{L}}$ experiences nonlinear saturation.

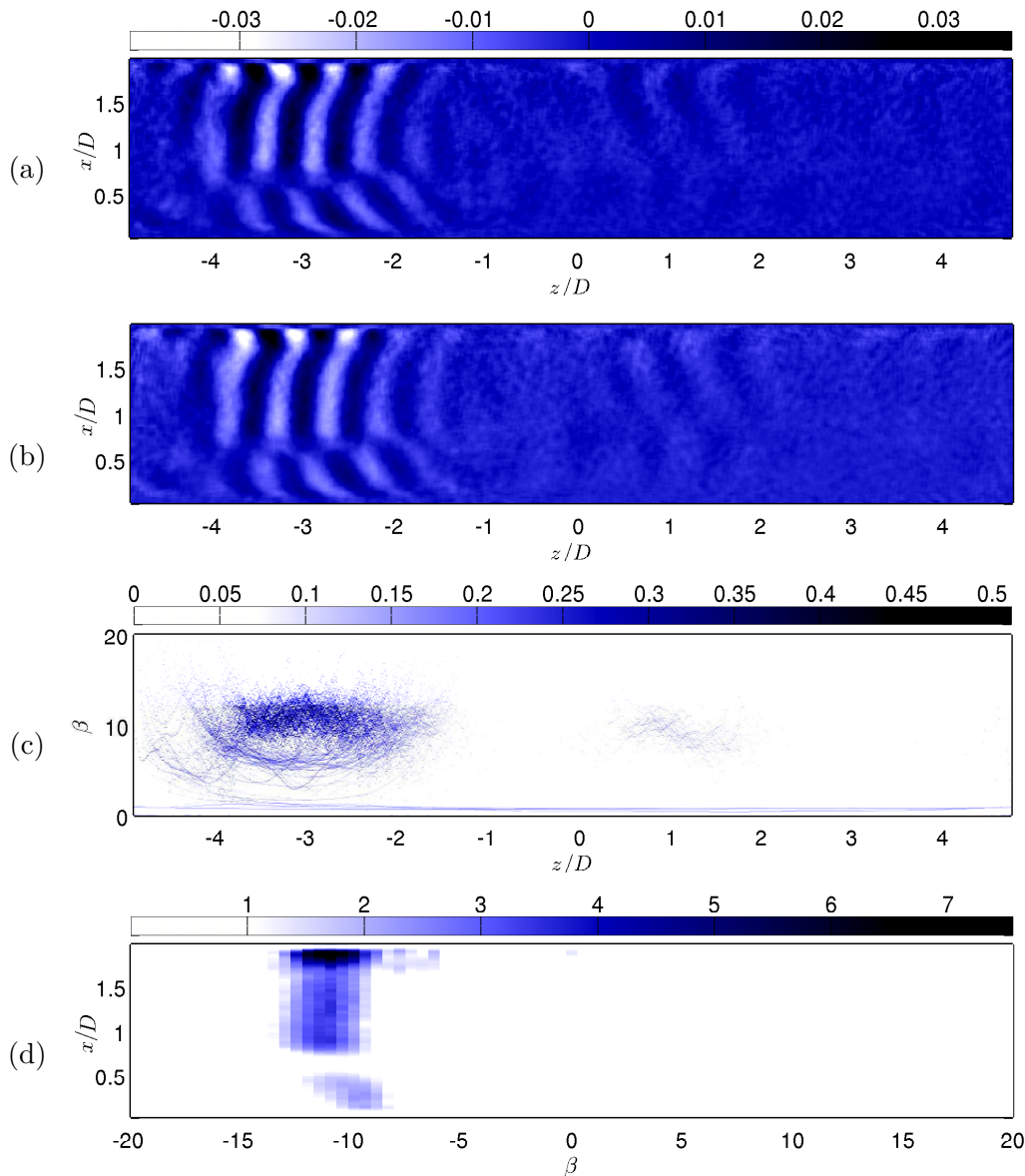


Figure 5.17: Spatial mode associated with $St = 0.039$ ($m = 4$) for case A : $Re_D = 1500$, $D/\theta_0 = 23.2$. (a,b) Real and imaginary parts, (c) Hilbert Huang Transform: $HH^z(z, \beta)$ map, (d) spanwise Fourier spectrum $\mathcal{F}^z(\beta, x)$ (in 10^{-3} units).

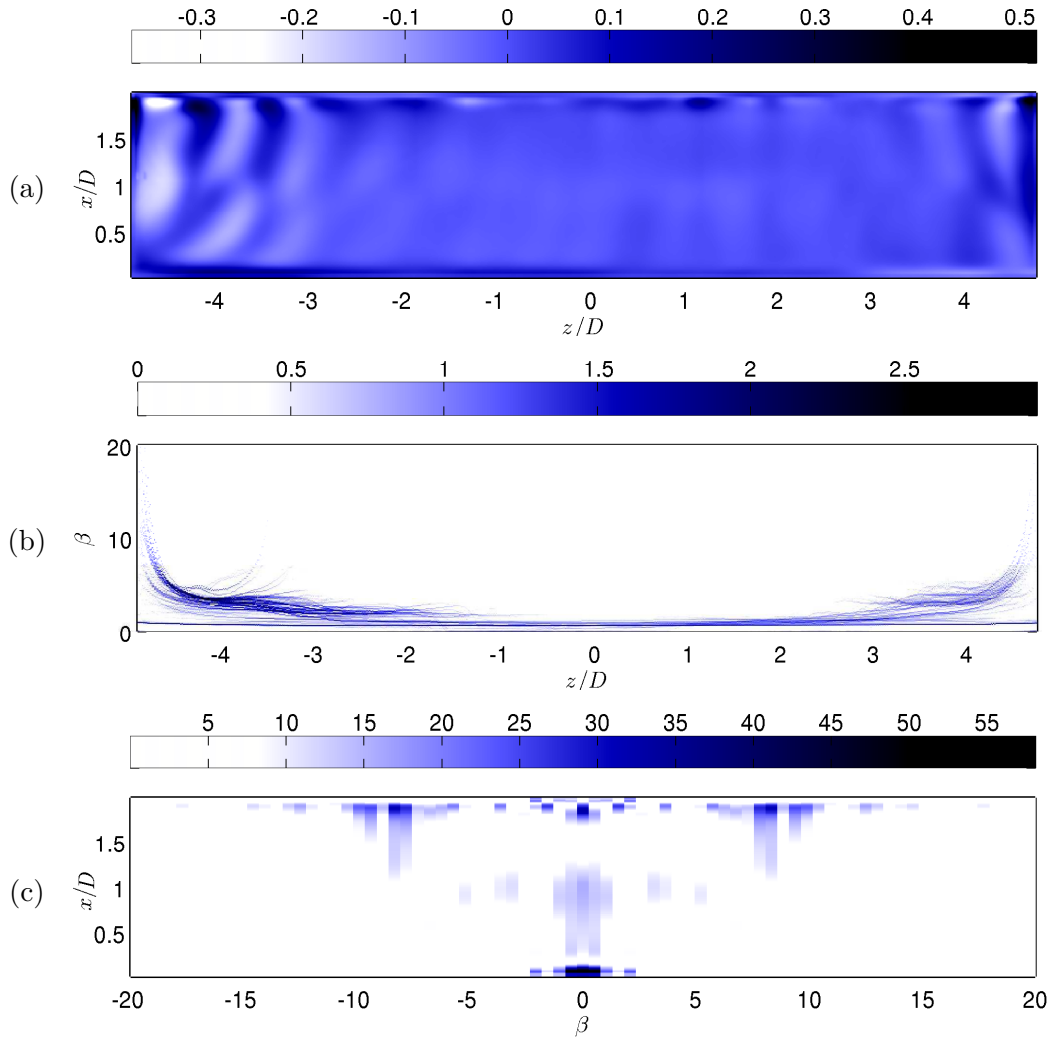


Figure 5.18: Mean flow ($St = 0$, $m = 0$) for case B : $Re_D = 2400$, $D/\theta_0 = 29.4$. (a) Colours encode fluctuations of dimensionless vorticity $\omega_y' D/U_0$; (b) $HH^z(z, \beta)$ map issued from Hilbert Huang Transform; (c) spanwise Fourier spectrum $\mathcal{F}^z(\beta, x)$ (in 10^{-3} units).

B . $Re_D = 2400$, $D/\theta_0 = 29.4$

The focus is now on case B for which the control parameters have been increased ($Re_D = 2400$ and $D/\theta_0 = 29.4$). The time spectrum in Figure 5.9.b has shown that temporal dynamics is richer than in case A . Characteristic global Fourier modes are presented and the associated spanwise space-scales are investigated the same way as before, using both Hilbert-Huang transform and space-Fourier transform.

• $m = 0$:

The meanflow in Figure 5.18 is similar to the one seen for case A . One primarily observes a strong two-dimensional signature ($\beta \simeq 0$) close to downstream and upstream cavity walls ($x/D \rightarrow 0$ and $x/D \rightarrow 2$). Low energy spanwise oscillations arise nonetheless nearby the endwalls.

The global Fourier modes associated with the lowest Strouhal numbers can be considered as steady structures within uncertainties and experimental defects. In this respect, they constitute an extension of the mean flow. The spatial structure presented in Figure 5.19 is associated with Strouhal number $St = 0.002$. Unlike case *A*, “quasi” steady spanwise oscillations are distributed over the entire span quite homogeneously (Figure 5.19.a-c) and broad-banded in the spectral space. Fluctuations yield both positive and negative wavenumbers ranging continuously over $7 \leq |\beta_0| \leq 13$ (that is $0.5 \leq \lambda/D \leq 0.9$). In addition, note that fluctuating energy corresponds essentially to spanwise fluctuations since the spectral range around zero ($\mathcal{F}^z(\beta \approx 0, x) \rightarrow 0$) is blank (Figure 5.19.d).

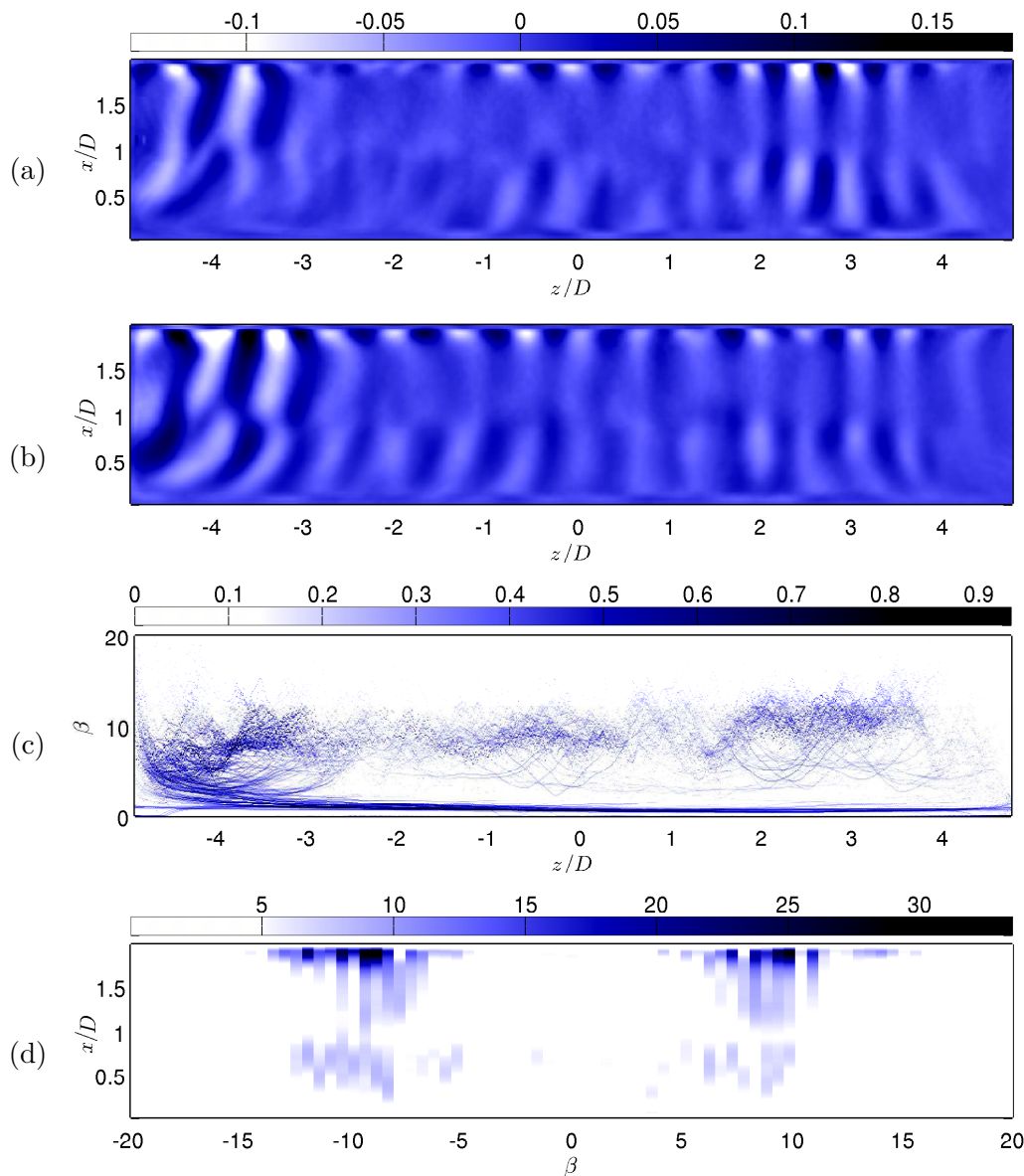


Figure 5.19: Spatial mode associated with $St = 0.002$ ($m = 0$) for case *B* : $Re_D = 2400$, $D/\theta_0 = 29.4$. (a,b) Real and imaginary parts, (c) Hilbert Huang Transform: $HH^z(z, \beta)$ map, (d) spanwise Fourier spectrum $\mathcal{F}^z(\beta, x)$ (in 10^{-3} units).

- $m = 1$:

Regarding “slow-moving structures” ($m = 1$), while case *A* exhibited a single mono-chromatic right-travelling wave, one observes in case *B* a continuum of modes for frequencies up to $St = 0.010$ (Figure 5.9.b). Associated spatial modes consist of left-travelling waves for which wavenumbers continuously decrease from $\beta \simeq 10$ to $\beta \simeq 4$. Examples of such modes are given in Figures 5.20 to 5.23.

Consider the Strouhal number $St = 0.003$ (Figure 5.20). The associated global mode consists of a single left-travelling wave entirely spanning the cavity and corresponding to wavenumbers around $-12 \leq \beta \leq -7$. One may also note in Figure 5.20.d that the amplitude of oscillations raises drastically when close to the downstream edge of the cavity (such that $x/D > 1.75$).

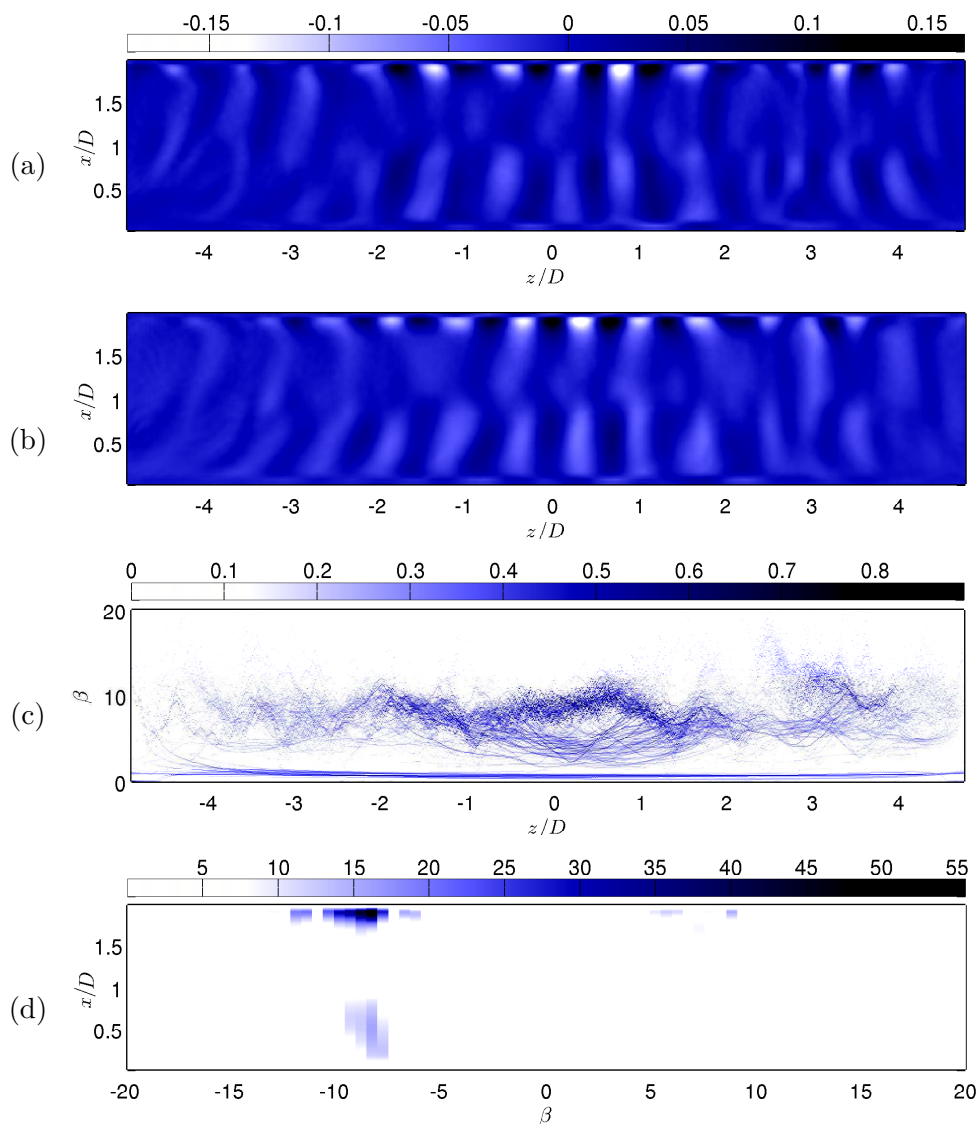


Figure 5.20: Spatial mode associated with $St = 0.003$ ($m = 1$) for case *B* : $Re_D = 2400$, $D/\theta_0 = 29.4$. (a,b) Real and imaginary parts, (c) Hilbert Huang Transform: $HH^z(z, \beta)$ map, (d) spanwise Fourier spectrum $\mathcal{F}^z(\beta, x)$ (in 10^{-3} units).

The main coherent structure associated with $St = 0.005$ (Figure 5.21) is also a left-travelling wave yielding a range of wavenumbers $-10 \leq \beta \leq -5$. From Figures 5.21.(a-c), one can assert that the wave is more confined ($-4 \leq x/D \leq -1.5$) than the one observed for $St = 0.003$. Other less energetic space scales are also observed in HH^z and \mathcal{F}^z maps, notably with wavenumbers $5 \leq \beta \leq 10$. Again, most of the energy is concentrated near the downstream wall (Figure 5.21.d).

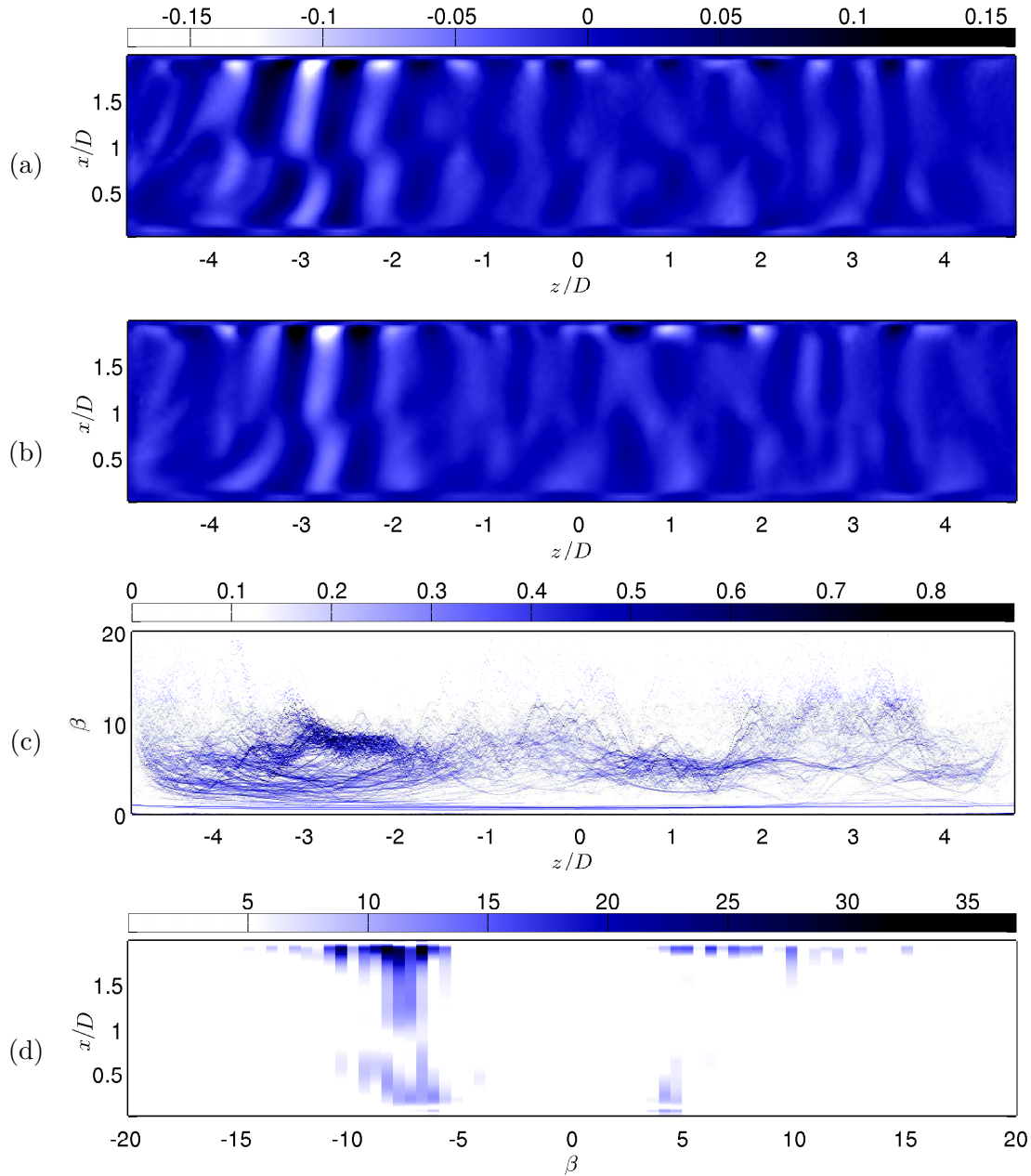


Figure 5.21: Spatial mode associated with $St = 0.005$ ($m = 1$) for case B : $Re_D = 2400$, $D/\theta_0 = 29.4$. (a,b) Real and imaginary parts, (c) Hilbert Huang Transform: $HH^z(z, \beta)$ map, (d) spanwise Fourier spectrum $\mathcal{F}^z(\beta, x)$ (in 10^{-3} units).

The global Fourier mode presented in Figure 5.22 shows another left-travelling wave whose wavenumbers range as $-7 \leq \beta \leq -4$. This wave is particularly interesting because it is tremendously modulated both in amplitude and wavenumber – see Figures 5.22.(a-c). In particular, one notices the parabolic evolution of the dominant wavenumbers in HH^z map.

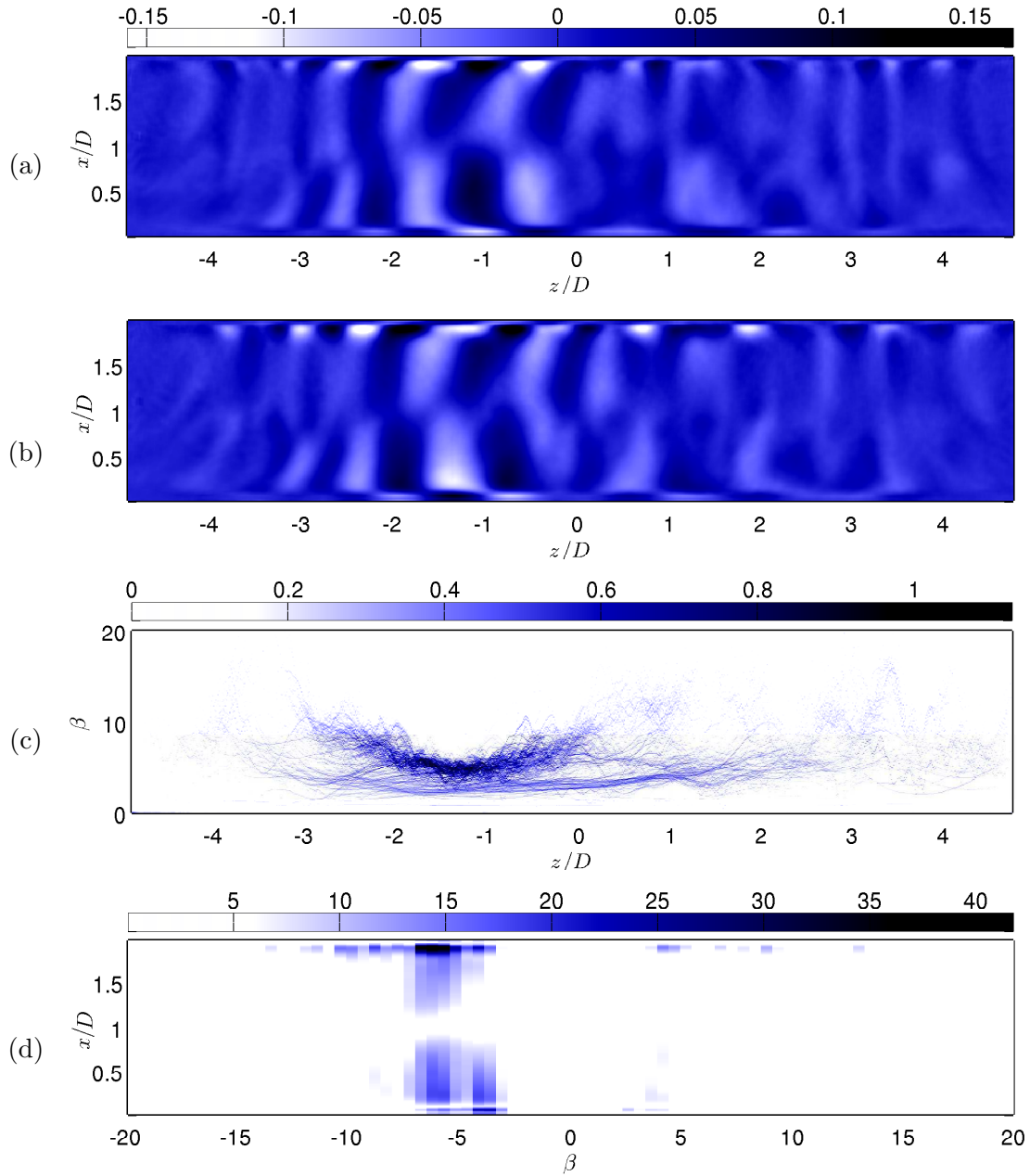


Figure 5.22: Spatial mode associated with $St = 0.008$ ($m = 1$) for case B : $Re_D = 2400$, $D/\theta_0 = 29.4$. (a,b) Real and imaginary parts, (c) Hilbert Huang Transform: $HH^z(z, \beta)$ map, (d) spanwise Fourier spectrum $\mathcal{F}^z(\beta, x)$ (in 10^{-3} units).

The global Fourier mode associated with Strouhal number $St = 0.009$ exhibits space scales such that $-7 \leq \beta \leq -2$ (Figure 5.23). Those large scale structures (typically $\lambda/D \approx 2\pi/4.5 = 1.4$) are carried by a left-travelling wave embracing the entire cavity.

In brief, as the Strouhal number raises, one observes a monotonic decrease of associated wavenumbers. As a result, these left-travelling modes pertaining to the family ($m = 1$) actually do not share the same phase velocity. Their phase velocities $c_1(\text{St}_1, \beta_1)$ indeed evolve quite continuously from -0.002 to -0.015 ,

$$\text{with } \text{St}_1 \nearrow, |\beta_1| \searrow \Rightarrow -0.002 \geq \frac{c_1}{U_0} = 2\pi \frac{\text{St}_1}{\beta_1} \geq -0.015. \quad (5.29)$$

This continuum of modes suggests an underlying multi-component wave, yielding a positive *group velocity*, that is opposite to the phase velocities of every wave components.

$$v_1 = 2\pi \frac{\partial \text{St}_1}{\partial \beta_1} \approx 0.01 \quad (5.30)$$

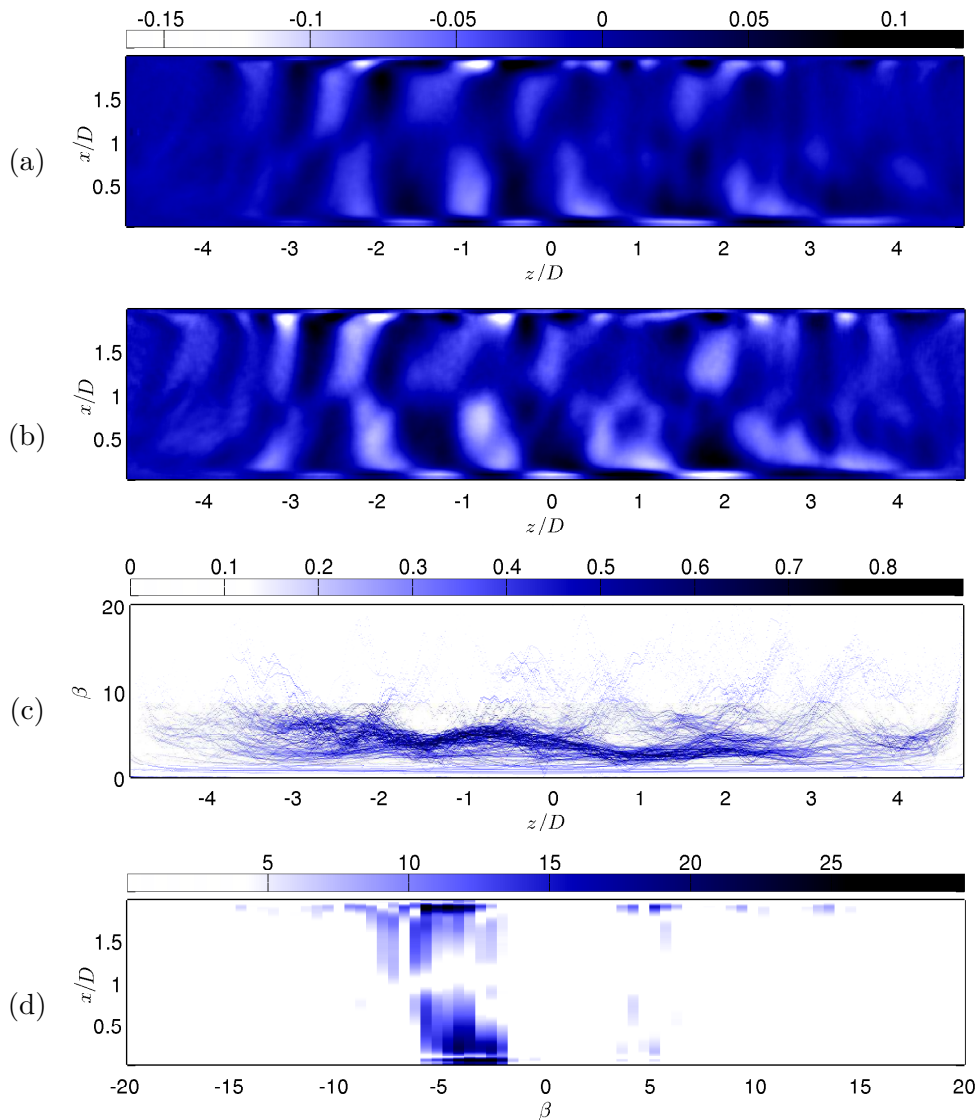


Figure 5.23: Spatial mode associated with $\text{St} = 0.009$ ($m = 1$) for case B : $\text{Re}_D = 2400$, $D/\theta_0 = 29.4$. (a,b) Real and imaginary parts, (c) Hilbert Huang Transform: $HH^z(z, \beta)$ map, (d) spanwise Fourier spectrum $\mathcal{F}^z(\beta, x)$ (in 10^{-3} units).

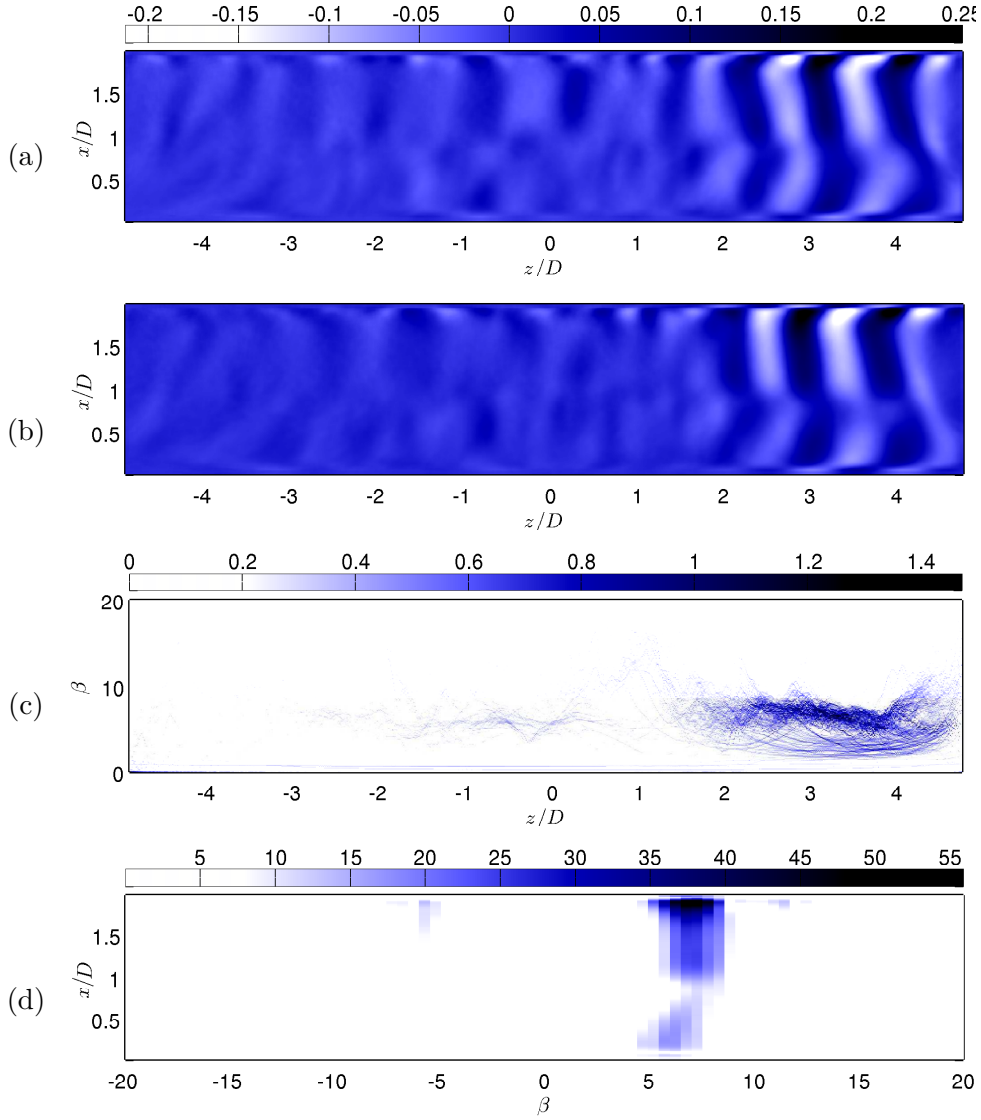


Figure 5.24: Spatial mode associated with $St = 0.013$ ($m = 2$) for case B : $Re_D = 2400$, $D/\theta_0 = 29.4$. (a,b) Real and imaginary parts, (c) Hilbert Huang Transform: $HH^z(z, \beta)$ map, (d) spanwise Fourier spectrum $\mathcal{F}^z(\beta, x)$ (in 10^{-3} units).

• $m = 2$:

Similarly to case A, the time spectrum for case B (Figure 5.9.b) shows a pair of dominant peaks corresponding to the dominant wavelength $\lambda/D \simeq 1$ ($\beta_2 = \pm 2\pi$). Those two peaks are found at $St = 0.013$ and $St = 0.018$, respectively.

The former is associated with the mode presented in Figure 5.24, consisting of a right travelling wave confined in the region $1.5 \leq z/D \leq 5$. Based on the same sample as the space-time diagram in Figure 5.8.g, the characteristics and the location of the present mode suggest a connection with the feature pointed out by slope 9. For that matter, there is a match between phase velocities (see Table 5.1)

$$\frac{c_{2R}}{U_0} = 2\pi \frac{St_{2R}}{\beta_{2R}} = 0.013 \approx w_\varphi(9) \quad (5.31)$$

The second mode ($St = 0.018$) is a counter-propagating wave (Figure 5.25), travelling from right to left and spreading from $z/D = 4$ to $z/D = -2.5$. This is the most energetic mode encountered and therefore corresponds to intense coherent structures (Figures 5.25.(a,b)), whose wavenumber $\beta_{2c} = -2\pi$ is fairly constant along the span and across the cavity length – see Figures 5.25.(c,d). This mode identifies the structures marked by slope δ in the space-time diagram (Figure 5.8.g),

$$\frac{c_{2c}}{U_0} = 2\pi \frac{St_{2c}}{\beta_{2c}} = -0.018 \approx w_\varphi(\delta). \quad (5.32)$$

Like case *A*, the pair of counter-propagating waves – labelled ($m = 2$) – yielding the dominant wavenumber $\beta_2 \simeq \pm 2\pi$, actually correspond to the two contributions to the interference pattern (draughtboard) observed earlier in the space-time diagram (Figure 5.8.g).

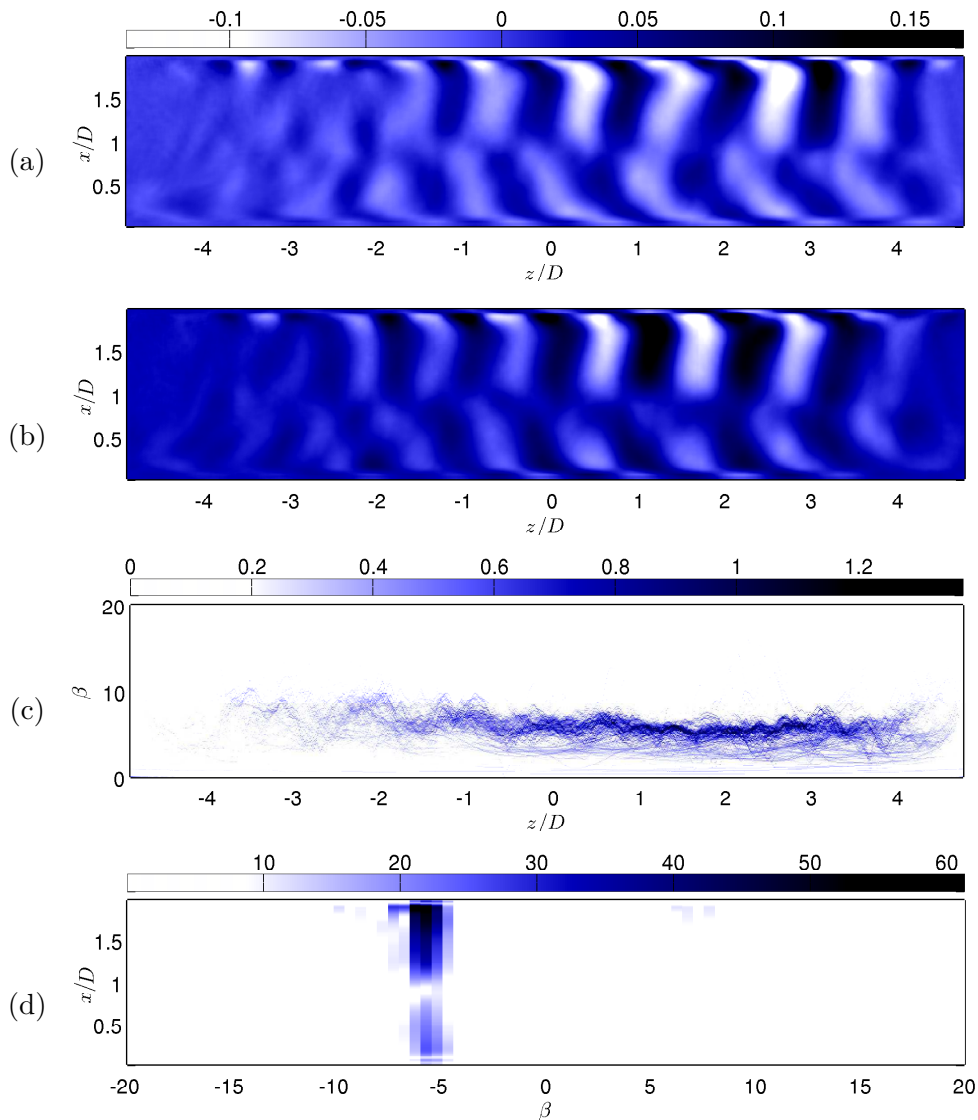


Figure 5.25: Spatial mode associated with $St = 0.018$ ($m = 2$) for case *B* : $Re_D = 2400$, $D/\theta_0 = 29.4$. (a,b) Real and imaginary parts, (c) Hilbert Huang Transform: $HH^z(z, \beta)$ map, (d) spanwise Fourier spectrum $\mathcal{F}^z(\beta, x)$ (in 10^{-3} units).

More generally, if one considers all travelling modes for both cases A and B , associated with the dominant wavenumber $\beta = \pm 2\pi$, one recognises a common characteristic shape, tilted with respect to the direction of propagation.

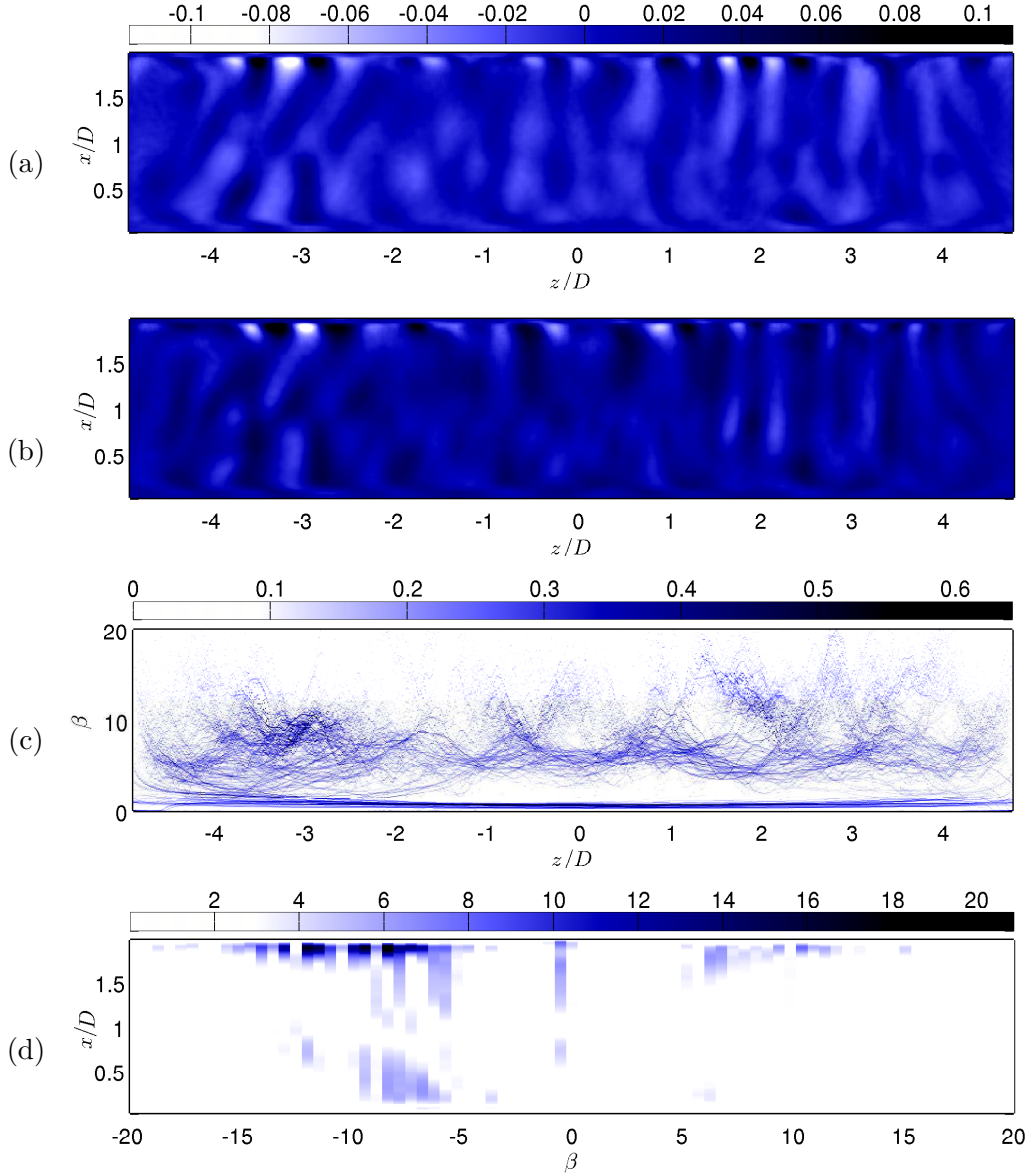


Figure 5.26: Spatial mode associated with $St = 0.024$ ($m = 3$) for case B : $Re_D = 2400$, $D/\theta_0 = 29.4$. (a,b) Real and imaginary parts, (c) Hilbert Huang Transform: $HH^z(z, \beta)$ map, (d) spanwise Fourier spectrum $\mathcal{F}^z(\beta, x)$ (in 10^{-3} units).

• $m = 3$:

Regarding the other peaks such that $0.02 \leq St_3 \leq 0.03$ for case B , Figure 5.26 shows a global Fourier mode associated with $St = 0.024$. It is more complicated than previous travelling waves. Multiple space scales are revealed: $5 \leq |\beta| \leq 15$ (Figure 5.26.d).

Spanwise fluctuations are distributed over the entire span and heavily modulated as shown by large variations of wavenumbers in the HH^z map (Figure 5.26.c).

- $m = 4$:

Finally, energy is found around $St_4 = 0.041$ in the time spectrum (Figure 5.9.b). Such a Strouhal number suggests an harmonic relationship with Strouhal number $St_{2\mathcal{R}}$. This mode could indeed correspond to the second harmonic of the right-travelling mode labelled $2\mathcal{R}$ ($\lambda_{2\mathcal{R}}/D = 1$), since

$$St_4 = 0.041 \simeq 3 \times St_{2\mathcal{R}} = 3 \times 0.0135. \quad (5.33)$$

Instead, Figure 5.27 reveals a left-travelling wave associated with space scales clearly larger than $\lambda = 1/3$, since $5 \leq \beta \leq 10$. In addition, this wave organises as "S"-shaped structures located around mid-span, a signature distinctive from any other Fourier mode extracted from the same sample. This rules out a nonlinearly produced structure and rather points to an independent origin: maybe another linearly unstable mode.

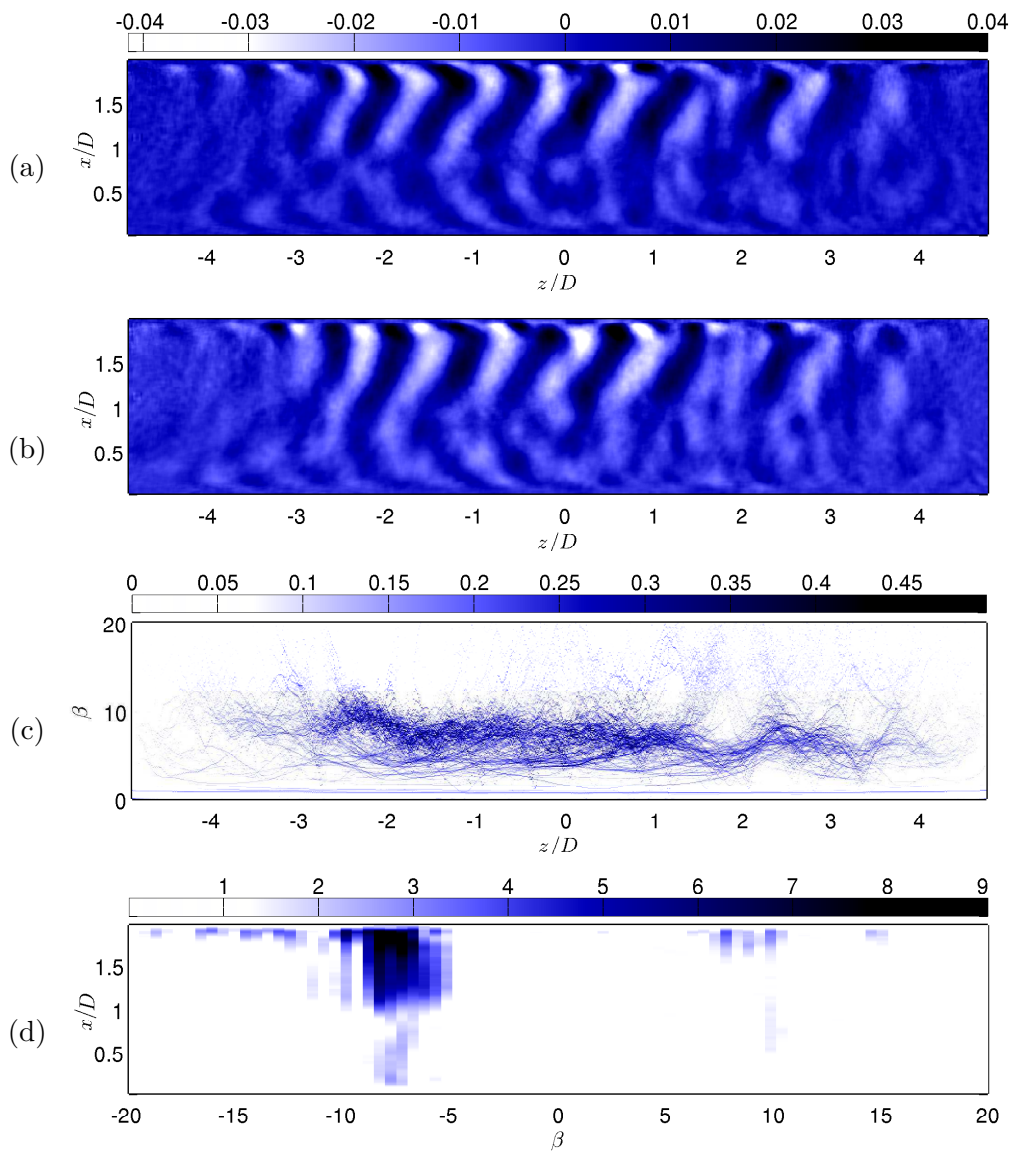


Figure 5.27: Spatial mode associated with $St = 0.041$ ($m = 4$) for case B : $Re_D = 2400$, $D/\theta_0 = 29.4$. (a,b) Real and imaginary parts, (c) Hilbert Huang Transform: $HH^z(z, \beta)$ map, (d) spanwise Fourier spectrum $\mathcal{F}^z(\beta, x)$ (in 10^{-3} units).

5.4.5 Synthesis

5.4.5.1 On the multiple modal decompositions

- Time Fourier modal decomposition provides very coherent modes, that identify unambiguously the different components of the flow, despite the fact that spanwise waves arising in the cavity inner-flow are not strictly periodic but rather strongly amplitude modulated.
- Also, modal identification using time Fourier transform is challenging when applied to dynamics exhibiting such a continuous spectrum. In that regard, the sample discussed here is not exhaustive but aims to provide an insightful picture of three-dimensional features encountered in the inner-flow, resulting from centrifugal instabilities in particular.
- Spanwise Fourier and Hilbert-Huang transforms have revealed themselves quite complementary. Results from both methods fairly match, thereby validating the identified space-scales. In addition, both methods complete each other as summarised in Table 5.2.

Table 5.2: Space modal decomposition diagnosis

Spanwise Hilbert-Huang Transform	Spanwise Fourier Transform
▷ Wavenumber high resolution/precision	▷ Left or right travelling waves
▷ Spanwise distribution	(signed wavenumbers)
▷ Fine information on both amplitude	▷ Streamwise distribution
and wavenumber modulations	▷ Spanwise integration
	(concise and statistic information)

5.4.5.2 On the identified dynamics

The main features of the dynamics observed in cases *A* and *B* are presented in Table 5.3. Both flows share several common characteristics in spite of different control parameters. The most important is the presence of highly coherent propagating waves such as described below.

Dominant counter-propagating waves

The dominant space-scale $\beta \simeq \pm 2\pi$ is associated with mono-chromatic travelling waves, corresponding to a single Strouhal number such that $St \in [0.013, 0.023]$. In fact, the dominant dynamics of the flow often involve pairs of counter-propagating waves, starting from a single source, not necessarily located at mid-span. When two travelling waves coexist, typically in the source region, they can therefore overlap to produce interferences (beating). However, standing waves are not likely since counter-propagating waves are generally not symmetrical.

Those dominant waves are consistently shaped as highly coherent structures covering the whole cavity length, with a phase discontinuity around $x/D = 0.8$. Because wavenumbers are roughly identical for all those waves, Strouhal number and phase velocity are directly connected.

Concerning the effect of lateral boundary conditions, travelling waves present smaller phase velocities nearby the endwalls. For instance, the source of the pair of counter-propagating waves shown in Figures 5.14 & 5.15 is located closer to the left-wall than to the right-wall. As a result, the right-travelling wave ($St = 0.023$) is faster than the left-travelling wave ($St = 0.019$).

The situation is inversed when considering the pair of counter-travelling waves shown in Figures 5.24 & 5.25. It can be inferred that wave properties of the flow depend on the source location, relatively to the endwalls: the propagation could be slowed down by solid boundary conditions (Shankar and Deshpande, 2000).

Broad-banded structures

Contrary to global stability analyses involving a two-dimensional basic flow and periodical boundary conditions, large scales are here imposed in the mean flow by the solid boundary conditions of the endwalls. This induces energy for wavenumbers $\beta \approx 2\pi/10$, corresponding to cavity span. On the other hand, modes associated with Strouhal numbers $St \rightarrow 0$ also contains (quasi) steady structures of smaller scales. They correspond to broadly distributed wavenumbers around $\beta_0 = \pm 10$. These steady structures are particularly broad-banded for case *B*.

Broad-banded structures can be unsteady as well: a continuous branch of wavenumbers ($5 \leq |\beta| \leq 15$) arises for Strouhal numbers around $St = 0.025$.

Continuum in case B

The time spectrum is more continuous in case *B*. The most characteristic feature of that richness consists of a continuum of modes for Strouhal numbers up to 0.01. These travelling waves whose wave and Strouhal numbers evolve continuously, range from slow-moving small-scale structures ($\beta \simeq -10$, $St \simeq 0.003$) to fast-moving large-scale structures ($\beta \simeq -4$, $St \simeq 0.01$). The modes shown in Figures 5.20-5.23 are extracted from a single sample and consist of left-travelling waves. Altogether, they form a wavepacket travelling at a positive group velocity, *ie.* opposite to all phase velocities. However, depending on the sample, right and left travelling waves are seen to arise indifferently, as long as their properties verify All the global Fourier modes presented above are left-travelling waves but it is not a necessary condition.

Table 5.3: Characteristics of global Fourier modes under study

m	$A : Re_D = 1500, D/\theta_0 = 23.2$		$B : Re_D = 2400, D/\theta_0 = 29.4$	
	St	β	St	β
0	0 ↓ 0.002	$ \beta_0 \approx 2\pi/10$ (BC*) & $ \beta_0 \simeq 10$	0 ↓ 0.002	$ \beta_0 \approx 2\pi/10$ (BC*) & $7 \leq \beta_0 \leq 13$
1	0.007	$\beta_1 = 8$ (right travelling wave)	0.003 ↓ 0.009	$-12 \leq \beta_1 \leq -7$ (left travelling waves) $-7 \leq \beta_1 \leq -2$
2	0.019 0.023	$\beta_{2L} \simeq -2\pi$ (left travelling wave) $\beta_{2R} \simeq 2\pi$ (right travelling wave)	0.013 0.018	$\beta_{2R} \simeq 2\pi$ (right travelling wave) $\beta_{2L} \simeq -2\pi$ (left travelling wave)
3	0.027	$\beta_3 \simeq 0$ & $5 \leq \beta_3 \leq 10$	0.024	$\beta_3 \simeq 0$ & $5 \leq \beta_3 \leq 15$
4	0.039	$\beta_{4L} \simeq -12$ (harmonic of left wave)	0.041	$-11 \leq \beta_4 \leq -5$ (left travelling wave)

(*) Signature of confinement (solid Boundary Conditions)

Discussion on centrifugal instabilities

The space-time analysis of the time-resolved zx -velocity fields has revealed different patterns resulting from the spanwise modulations of the cavity inner-flow. Direct observations of space-time diagrams extracted from the experimental datasets have been confirmed and quantified by the results issued of modal decomposition in the spectral domain. As the system was studied in the permanent regime, we have been dealing with saturated travelling waves arising in the inner-flow. In that regard, we expect that our observations be better-understood in the framework of amplitude equations.

6.1 Nonlinear regime

The previous chapter has shown that amplitudes of spanwise oscillations actually evolve over space and time, but at much larger scales than the characteristic wavelength and frequency of the underlying travelling waves. It is therefore reasonable to assume that scales are separated, hence, amplitude dynamics may be described by amplitude equations following an adiabatic reduction of the dynamics.

The form of the amplitude equations is imposed by the symmetries broken by the primary instability. In the present case, where the transition is fairly supercritical, let us consider the rising of two modes, counter-travelling waves of identical dimensionless frequencies, $\text{St}_{\mathcal{L}} = \text{St}_{\mathcal{R}}$, and opposite wavenumbers, $\beta_{\mathcal{L}} = -\beta_{\mathcal{R}}$, such that the state may be described as

$$\psi(z', t') = A_{\mathcal{L}}(z', t') e^{i(2\pi\text{St}_{\mathcal{L}}t' - \beta_{\mathcal{L}}z')} + A_{\mathcal{R}}(z', t') e^{i(2\pi\text{St}_{\mathcal{R}}t' - \beta_{\mathcal{R}}z')}. \quad (6.1)$$

with $z' = z/D$ and $t' = tU_0/D$ the dimensionless spanwise and time variables, respectively. In that case, the amplitude equations should reduce to cubic coupled complex Ginzburg-Landau equations (CCGLE) of the form

$$\begin{cases} \tau \left(\frac{\partial A_{\mathcal{L}}}{\partial t'} - v \frac{\partial A_{\mathcal{L}}}{\partial z'} \right) = \alpha A_{\mathcal{L}} - \xi |A_{\mathcal{L}}|^2 A_{\mathcal{L}} - \chi |A_{\mathcal{R}}|^2 A_{\mathcal{L}} + \eta \frac{\partial^2 A_{\mathcal{L}}}{\partial z'^2} \\ \tau \left(\frac{\partial A_{\mathcal{R}}}{\partial t'} + v \frac{\partial A_{\mathcal{R}}}{\partial z'} \right) = \alpha A_{\mathcal{R}} - \xi |A_{\mathcal{R}}|^2 A_{\mathcal{R}} - \chi |A_{\mathcal{L}}|^2 A_{\mathcal{R}} + \eta \frac{\partial^2 A_{\mathcal{R}}}{\partial z'^2} \end{cases} \quad (6.2)$$

where the coefficients are unknown but identical for both modes. Note that asymmetric modes would imply non-equal coefficients.

For each ‘‘carrier’’ mode (St_j, β_j) with $j = \{\mathcal{L}, \mathcal{R}\}$, the characteristic time-scale of the amplitude dynamics is given by τ . Physically, the real part of α/τ represents the linear temporal growth-rate of the underlying mode j , while the imaginary part of α/τ accounts for the angular frequency of the amplitude modulation, if it exists. Coefficients v and η are the group velocity and diffusion coefficient, respectively. Coefficients ξ and χ characterise the

contributions of the nonlinear terms. The real part of ξ is positive in order to counter-balance the (linear) growing of the mode. The imaginary part of ξ/τ accounts for the nonlinear frequency shift of the mode in the saturated regime and χ accounts for the coupling between both modes.

The evolution of these coefficients can be considered with respect to ϱ , the control parameter. If ε designates the distance to critical point ϱ_c in the parameter space

$$\varepsilon = \frac{\varrho - \varrho_c}{\varrho_c}, \quad (6.3)$$

then the coefficient α , which yields the temporal evolution, scales like ε . On the contrary, coefficients τ , v , η , ξ and χ are usually supposed to be, at the leading order, independent of the control parameter. On the other hand, since the present case deals with three-dimensional dynamics, diffusion and nonlinear coupling terms can logically depend on the 3D-distribution of the wave varying with respect to its wavenumber β . Consequently, CCGLE coefficients are likely functions of β . Moreover, note that in the present case, one expects a multi-dimension parameter space, yielding notably dimensionless cavity depth, Reynolds number or cavity aspect ratio. Control parameters hence actually write

$$\varrho = [\varrho_1, \varrho_2, \varrho_3, \dots] = [D/\theta_0, \text{Re}_D, L/D, \dots] \quad (6.4)$$

Embracing the inner-flow space-time dynamics would obviously require a much more complete system of coupled equations.

Nevertheless, even a single pair of counter-travelling waves actually suffices to explain the features encountered here. For instance, Riecke and Kramer (2000) used an equivalent system of two CCGLE to describe the interaction of two counter-propagating waves regarding the stability of standing waves with small group velocity, which recalls the patterns seen earlier in Sections 5.3.2 & 5.4. Indeed, the system under investigation in Riecke and Kramer (2000) was revealing space-time figures fairly similar to ours. In particular, one could find localised regions of the space-time domain where counter-travelling waves superimposed to create standing waves whereas the same travelling waves excluded each other in other regions of the space-time domain. The authors explained these dynamics using an amplitude stability analysis. This led to a stability condition of standing waves which can be reduced to the following criterion:

$$\begin{cases} \xi_r^2 > \chi_r^2 & \Rightarrow \text{Standing waves (superimposition)} \\ \xi_r^2 < \chi_r^2 & \Rightarrow \text{Stand - alone travelling waves (exclusion)} \end{cases} \quad (6.5)$$

where ξ_r and χ_r are the real parts of the coefficients ξ and χ , respectively. Such a condition compares the saturation effects (ξ_r) relatively to coupling between the two modes (χ_r). It seems reasonable that superimposition occurs only if the energy transfer between the two wave remains limited relatively to the wave enhancement.

More similarities can be found in numerous references making use of CCGLE. The systems under study, though generally of low dimension, already exhibit symmetry breakings and

dependence to initial conditions. For example in 1D-systems, sources and sinks due to two counter-travelling waves are investigated in van Hecke et al. (1999); Pastur et al. (2003a,b). In Malomed (1994), a separatrix of the space-time domain is identified as the collision of two travelling waves or a source or a sink.

To conclude, amplitude equations could provide an interesting prospect but obviously need further investigation. The scheme at hand is of course more complex than the one described by the idealised case of two rising symmetrical modes. Relying on (spanwise) linear stability analysis, the following discussion will show that several (continuous) branches of linearly growing modes are actually expected to arise in the inner-flow.

6.2 Linear regime

Until now, analysis of the flow dynamics focused on identifying and characterising the inner-flow in the permanent regime. The system under study was thus observed after saturation had occurred and in a three-dimensional geometry (solid spanwise conditions). While such a study is essential regarding the nonlinear interactions at play, it makes it difficult to settle the origin of the instabilities.

Investigation of the mechanism underlying the onset of instabilities consists in studying the *linear stability* of the system around a steady solution, the *base flow* \mathbf{U}_B . These days, it is commonly achieved through numerical simulations, as detailed in the literature review (Section 1.1.6).

In the case of three-dimensional instabilities in the cavity inner-flow, one generally uses a two-dimensional base-flow \mathbf{U}_B^{2D} to which spanwise wave disturbances are applied using *spanwise periodic conditions*. The rise or decay of these disturbances characterise the stability of the system against the considered space scale. The growth rate σ is obtained as a function of the wavelength λ/D (or wavenumber β).

Such a linear stability analysis was conducted by Yann Fraigneau at LIMSI, in the frame of this work (Pastur et al., 2012), along with three-dimensional direct numerical simulations of an incompressible open square cavity flow ($L/D = 1$). The direct numerical simulations (DNS) are briefly presented below but details on the OLORIN code and other technical informations can be found in Pastur et al. (2012).

6.2.1 Direct numerical simulations in an open square cavity

The numerical study addresses an incompressible and isothermal flow whose governing equation can be described by the non-dimensional Navier-Stokes equations:

$$\begin{cases} \frac{\partial \mathbf{U}}{\partial t} + (\mathbf{U} \cdot \nabla) \mathbf{U} &= -\nabla p + \frac{1}{\text{Re}_D} \Delta \mathbf{U} \\ \nabla \cdot \mathbf{U} &= 0 \end{cases} \quad (6.6)$$

where \mathbf{U} is the velocity field and p the pressure field. The geometric setup consists in an open cavity capped with a parallelepipedic duct in which is generated the channel flow driving the inner cavity flow. A cartesian coordinate system (x, y, z) , for streamwise, crosswise and spanwise directions, respectively, is set midspan at the top of the upstream cavity wall. The cavity dimensions are $L = 50$ mm, $L/D = 1$, $S/D = 6$, similar to experimental conditions at

LIMSI. Upstream and downstream lengths of the duct are respectively $L_u/L = 1$ and $L_d/L = 3$ and its height is $D_v/D = 3$. The Reynolds number is set to $\text{Re}_D = 3850$ (external velocity $U_0 = 1.2$ m/s), and the boundary layer momentum thickness is such that $D/\theta_0 = 38.5$. Data from the DNS are used further in this section as a reference for linear stability results.

6.2.2 Linear stability analysis

The linear stability analysis characterises the time-evolution of infinitesimal three-dimensional perturbations, \mathbf{u}' , with respect to an unstable steady base flow \mathbf{U}_B , by means of linearised Navier-Stokes equations. The method is described in Mamum and Tuckerman (2009). One rewrites the system as

$$\frac{\partial \mathbf{u}'}{\partial t'} = \mathcal{N}\mathbf{u}' + \Delta \mathbf{u}' \equiv \mathcal{A}\mathbf{u}', \quad (6.7)$$

where \mathcal{N} is the linearised operator of evolution around the base-flow \mathbf{U}_B , associated with the Eulerian part of the Navier-Stokes equations and Δ is the linear operator associated with viscous terms. The main instability features are depicted by the leading eigenpairs of the linear evolution operator, \mathcal{A} , namely eigenpairs with the greatest real part. Leading eigenpairs are determined by the Arnoldi method (Pastur et al., 2012).

In practice, the use of a full three-dimensional base flow is still out of reach. On the other hand, two-dimensionalised base flows \mathbf{U}_B^{2D} are now widely used, for instance in Albensoeder et al. (2001); Theofilis (2003); Theofilis and Colonius (2003); Ehrenstein and Gallaire (2005); Sipp and Lebedev (2007); Ehrenstein and Gallaire (2008); Brès and Colonius (2008); Barbagallo et al. (2009); de Vicente (2010); Theofilis (2011); Meseguer-Garrido et al. (2011). In order to get the two-dimensionalised base flow \mathbf{U}_B^{2D} , a preliminary *two-dimensional* numerical simulation is performed in the cross-stream plane (xy), for the same Reynolds number $\text{Re}_D = 3850$. Note that using spanwise periodic boundary conditions is indeed a simplification of the system. The base flow \mathbf{U}_B^{2D} is shown in Figure 6.1.

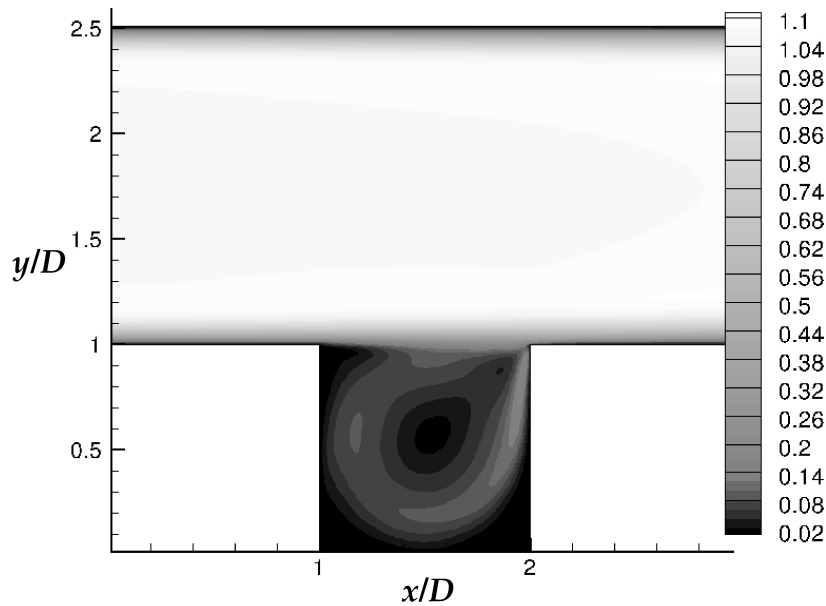


Figure 6.1: Two-dimensional steady base-flow for $\text{Re}_D = 3850$ and $L/D = 1$.

This square cavity configuration constitutes a canonic case providing a particularly straightforward analysis. Indeed, in spite of the relatively high Reynolds number, this two-dimensional geometry exhibits a *stable steady-state* (no shear layer oscillation). Using a $L/D = 2$ -cavity instead would have implied a larger dimensionless cavity length ($L/\theta_0 = 77$), the control parameter of the impinging shear layer. This would have led to an unstable two-dimensional flow and therefore would have required dedicated methods to converge to a steady base-flow. Hereinbelow are reported the salient results of the linear stability analysis, whose full extent is presented in Pastur et al. (2012).

A two-dimensionally stable flow implies that the instability of the complete three-dimensional base-flow \mathbf{U}_B must occur with respect to spanwise modes. Therefore, the initial conditions superimposed upon the two-dimensional base-flow \mathbf{U}_B^{2D} are of the form:

$$\mathbf{u}'(x, y, z) = \mathbf{u}_0(x, y) \cos\left(\frac{2\pi}{\lambda_m} z\right) \exp(\mu_m t), \quad (6.8)$$

that is, a mode of wavelength $\lambda_m = D/m$, $m \in \mathbb{N}^*$, in the spanwise direction, and (complex) growth-rate $\mu_m = \sigma_m + i\omega_m$, with σ_m the temporal growth-rate and the angular frequency

$$\omega_m = 2\pi \frac{\text{St}_m}{D/U_0}. \quad (6.9)$$

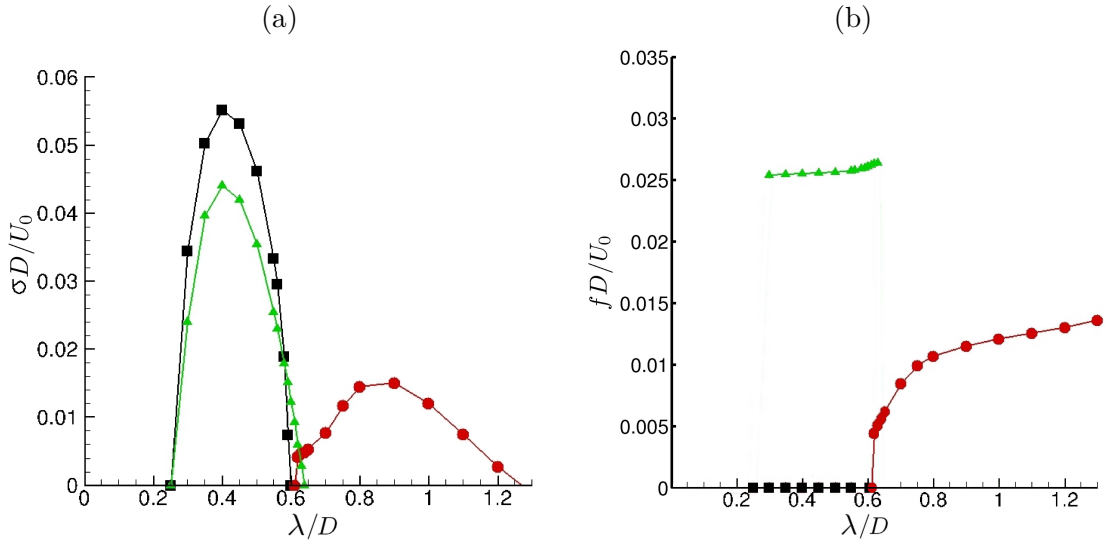


Figure 6.2: Dimensionless growth-rate (a) and frequency (b) with respect to dimensionless spanwise wavelength λ/D . Three families are found: *i*) steady growing modes (black squares), *ii*) oscillatory growing modes, with a constant frequency, $\text{St} = fD/U_0 \simeq 0.025$, and small wavelength, $0.24 \leq \lambda/D \leq 0.62$ (green triangles), *iii*) oscillatory growing modes of larger wavelength, with a frequency increasing with wavelength (red circles). The faster-growing mode belongs to family *i*) with a dimensionless wavelength $\lambda/D \simeq 0.4$.

Only stationary wave-like modes are considered because no spanwise drift is observed in the permanent flow (DNS). The base flow is unstable with respect to the modes such that $\sigma > 0$, resulting in three branches of linearly growing modes. The associated temporal growth-rates σ

and Strouhal numbers St are provided in Figure 6.2, as functions of λ/D . No unstable mode is found for wavelengths $\lambda/D > 1.32$, which confirms the base-flow stability with respect to streamwise perturbations ($\sigma < 0$ when $\lambda \rightarrow \infty$).

One branch (black squares in Figure 6.2) is associated with a steady structure ($St = 0$), for wavelengths $\lambda/D \in [0.24, 0.62]$. The largest growth-rate on this branch is found at $\lambda/D = 0.40$. We will refer to this mode as mode (i) . A spatial representation of mode (i) is shown in Figure 6.3.a, along with the most energetic spanwise Fourier mode in DNS velocity field, extracted at $\lambda/D \simeq 0.42$ in Figure 6.3.b. One observes that both wavelengths and associated spatial structures are almost identical.

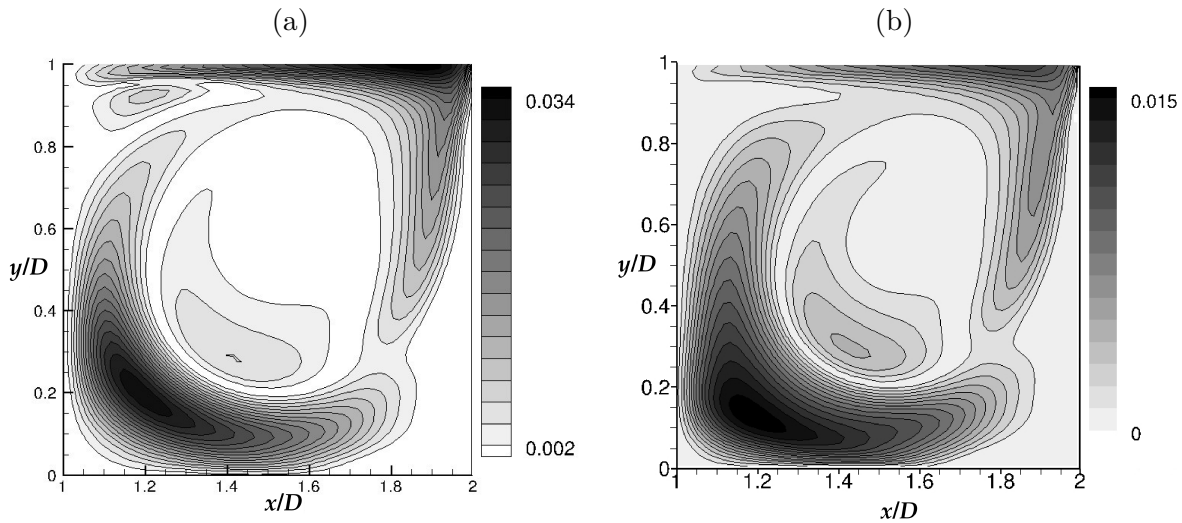


Figure 6.3: Cross-stream structure of (a) the spanwise eigenfunction with the largest growth rate in family (i) ($St = 0$), grey levels encode u' modulus; (b) the most energetic spanwise Fourier mode, $\lambda/D = 0.4$ ($\beta = 15.7$), grey levels encode power spectral density of u' , in units of U_0 .

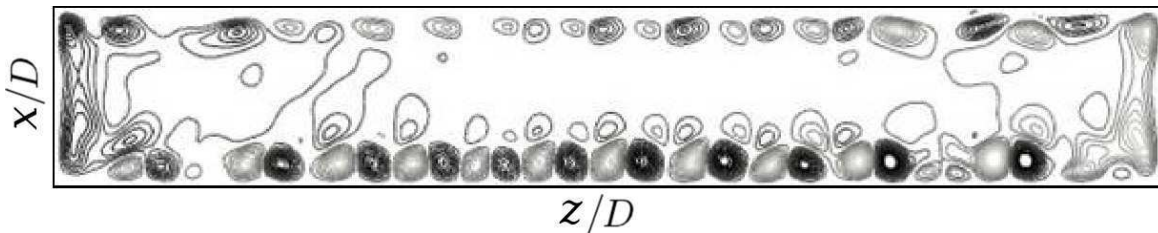


Figure 6.4: Vorticity contours from DNS data with *rigid boundary conditions*. Topview of zx -plane at $y/D = -0.3$.

Regarding the spanwise boundary conditions, the no-slip conditions implied by endwalls in the experiments could have an additional effect on the onset and the development of the linearly unstable mode. A DNS run has been performed in the very same conditions part from the spanwise *rigid boundary conditions*. The top view of an instantaneous field is displayed in Figure 6.4. It shows that no-slip conditions actually have a limited effect on the periodicity of

the structures: the non-invariance mostly restricting to the direct vicinity of the endwalls. The wavelength is otherwise equal to the one predicted by linear stability analysis ($\lambda/D \simeq 0.4$). However, one observes a drift of the vortical rolls from the mid-span region towards the endwalls, as expected from the experiments in the spanwise plane in the present chapter, as well as in the literature Faure et al. (2007, 2009).

Furthermore, one may recall the global Fourier modes obtained from experimental results in an xy -plane in previous chapter (Section 4.5). In particular, Figures 4.39.(a,b), displayed spatial structures associated with the tip of a broad-band peak at frequency $f_{\Delta} D/U_0 = 0.017$ in a similar geometry ($L/D = 1.0$), but for a much higher Reynolds number $Re_D = 7700$. The control parameter $L/\theta_0 = 54$ was such that shear layer oscillations were of particularly low amplitude. These structures fairly look like those of Figure 6.3 – mode (i) – but are unsteady. This is likely due to the same endwall-induced drift.

In Figure 6.2 is also found another branch of modes (green triangles), referred to as (ii), with similar space scales (over the same range of wavelengths $\lambda/D \in [0.24, 0.64]$) but oscillating in time. They exhibit Strouhal numbers roughly constant at $St_{ii} = 0.0255$. Again, the highest growth-rate corresponds to wavelength $\lambda/D \simeq 0.4$ ($\beta = 15, 7$). The complex spatial mode associated with the highest growth rate is given in Figure 6.5. The structure resembles that of the steady mode (i) but it indicates a swaying motion represented by the phase shift between the real and imaginary parts. Indeed, real and imaginary parts are neither phase opposed (as a standing wave) nor in quadrature of phase (as a travelling wave).

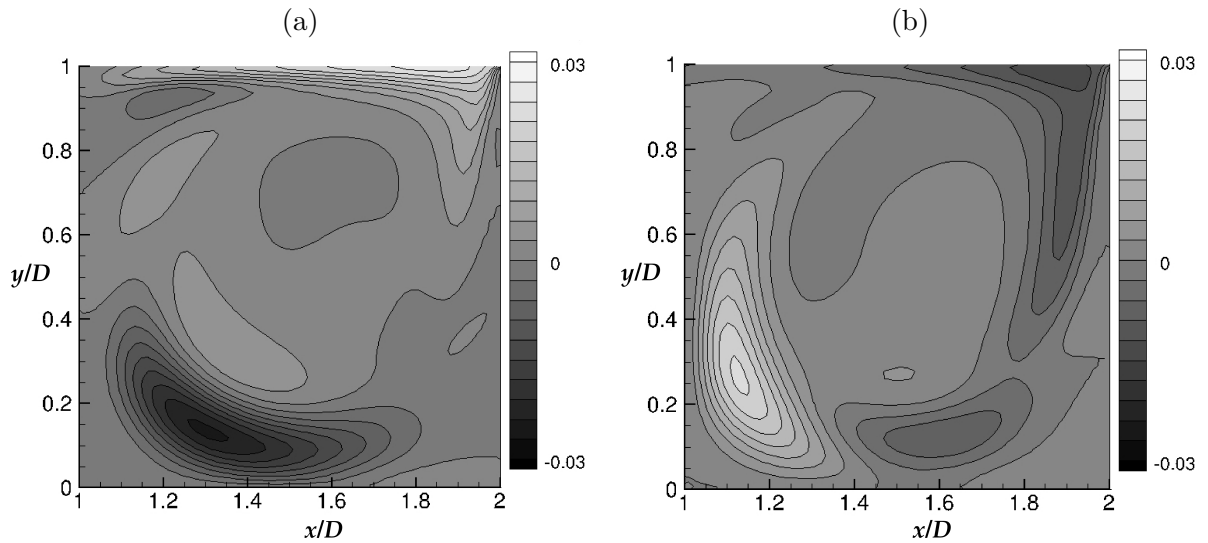


Figure 6.5: Cross-stream structure of the spanwise eigenfunction with largest growth-rate of the second family ($St_{ii} = 0.025$), referred to as mode (ii): real part (a), imaginary part (b). Grey levels encode streamwise component u' , in units of U_0 .

This family (ii) of oscillating modes yields smaller growth rates than the steady modes seen earlier. One can wonder if they actually influence the permanent regime. To that aim, a local measurement has been extracted from the saturated flow in the three-dimensional DNS. The power spectral density out of this time-series is plotted in Figure 6.6. The frequency of the fastest-growing mode of family (ii) is present at $St = f D/U_0 \simeq 0.026$, but the dominant peak rises at half this frequency, $St = f D/U_0 \simeq 0.013$. Those modes seem to modulate in time the underlying structures of the first family (i). Moreover, the dynamics associated with

$fD/U_0 = 0.026$ are similar to the eigenfunctions of family (ii) (see Pastur et al. (2012) for details). This suggests that both families (i) & (ii) appear in the flow in the permanent regime. In other words, the saturated flow is influenced by not only the most linearly unstable mode but rather a selection of several unstable eigenmodes.

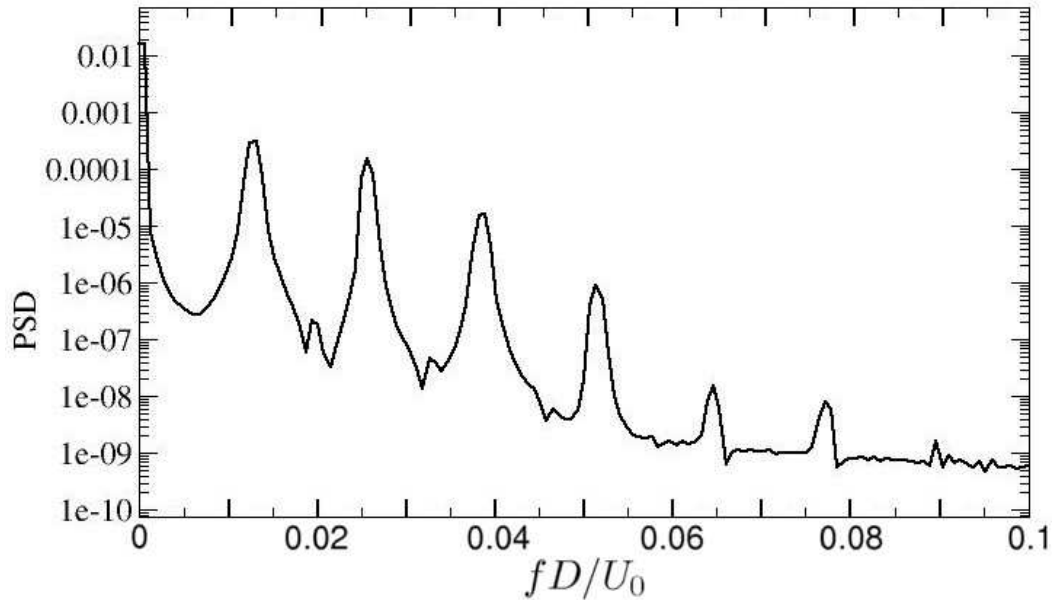


Figure 6.6: Power spectral density computed from velocity time-recording at a probe inside the cavity (DNS data with periodic lateral conditions).

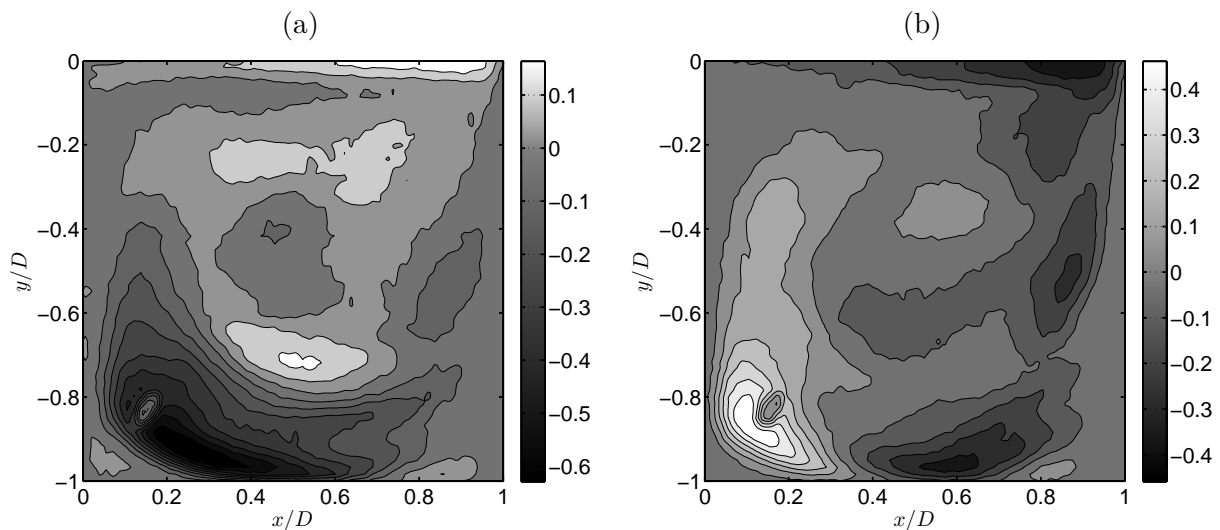


Figure 6.7: Global Fourier mode associated with Strouhal number $St = fD/U_0 = 0.027$, issued of a TR-PIV dataset in xy -plane (LIMSI campaign) for the case $L/D = 1.0$, $Re_D = 7700$, $L/\theta_0 = 54$: real part (a), imaginary part (b). Grey levels encode streamwise component u' , normalised as in Equation 3.17.

Once again, these spatial structures are insightful with regards to the global Fourier modes obtained from experimental results in an xy -plane. For the sake of comparison, Figure 6.7 presents the spatial structures of streamwise velocity component u' associated with Strouhal number $St = 0.027$, in the very same geometry $L/D = 1.0$ and for a higher Reynolds number $Re_D = 7700$. Except for the logically higher noise level in the experiment, both real and imaginary parts of the global Fourier mode in Figure 6.7 look very similar to those of the spanwise eigenfunction in Figure 6.5. They could coherently correspond to the saturated state of the linear mode (ii).

Finally, a third branch of linearly unstable modes is observed (red circles) in Figure 6.2. Denoted (iii), those modes are associated with larger wavelengths, starting from the point where the stationary branch becomes stable at $\lambda/D = 0.62$ until $\lambda/D = 1.32$. Corresponding Strouhal numbers increase from 0 to about $St = 0.0146$. The largest growth-rate is found for $\lambda_{iii}/D \simeq 0.82$ with $St_{iii} \simeq 0.012$. Note that the eigenfunctions of branch (iii) actually exhibit wave characteristics similar to those of the continuum of travelling waves pointed out in the experiments for case B .

To conclude, linear modes are recovered in the permanent regime without significant distortion, despite the nonlinear effects. Remark that such an assertion should not be trivially generalised to any configuration for the stability properties of the flow logically depend on the geometry. In fact, Brès and Colonius (2008); de Vicente (2010) have demonstrated that the square $L/D = 1$ cavities actually presents some peculiar features. For instance, the most linearly unstable mode corresponds to a wavelength of $\lambda/D = 0.4$ where larger aspect ratio typically show a wavelength of higher growth rate around $\lambda/D \simeq 1$. Linear stability studies have demonstrated that the mode family here-called (iii) becomes more unstable when L/D increases. Furthermore, wider cavities are generally also two-dimensionally unstable, against Kelvin-Helmholtz modes of the shear layer.

Nevertheless, eigenfunctions generally share similar characteristics with saturated dynamics observed in the experiments, regardless of the geometry. These salient features are summarised hereinafter:

- The existence of continua of modes over a large range of wavenumbers (wavelengths) is typical. It explains why multiscale patterns have been identified with the space-time analysis of the permanent regime, even without strong nonlinear couplings.
- Associated frequencies are scaled as similar D -based Strouhal numbers ($St \leq 0.03$).
- Eigenfunctions are fairly consistent with the global Fourier modes obtained from experiments.

Promising results are about to be published in the frame of an ongoing collaboration with Javier de Vicente and Fernando Meseguer from Universidad Politecnica de Madrid. They have performed an extensive parametric study of the global eigenfunctions in the open cavity flow. In particular, some of their configurations match the two cases experimentally investigated in this thesis ($L/D = 2$ and $Re_D = \{1500, 2400\}$).

6.3 Concluding remarks

- The two experimental campaigns, performed in both xy - and zx -planes, have confirmed the existence of a broad-banded dynamics within the inner-flow, associated with low frequencies such that $f D/U_0 \approx 0.02$. The spatial structures observed in both planes correspond to the very same three-dimensional dynamics, which consists of spanwise-distributed vortical structures coiling onto the main recirculation.
- The spanwise waves observed experimentally correspond to the saturated state of centrifugal instabilities, which are onset around the main recirculation alongside the cavity walls. The linear stability of a 2D base-flow with respect to (periodic) spanwise waves shows that entire wavepackets can arise naturally. The fluctuations due to centrifugal instabilities scale on the cavity depth D . In particular, spanwise wavelengths λ are typically such that $0.4 \leq \lambda/D \leq 1.6$.
- In the permanent regime, localised or global features can occur and endure, depending on the initial conditions or/and a slight uncertainty on flow conditions. The most salient phenomena are pairs of counter-travelling waves of wavelength $\lambda/D \simeq 1$ ($\beta \simeq 2\pi$), associated with frequencies such that $0.013 \leq St = f D/U_0 \leq 0.023$. That range of Strouhal numbers is in good agreement with the results from direct numerical simulations in the compressible regime by Brès and Colonius (2008) ($0.015 \leq St = f D/U_0 \leq 0.026$). Interference effects are observed between travelling waves. This results in a beating which induces an overall time modulation of the flow.
- The influence of solid walls as opposed to periodic boundary conditions is visible in the experiments. First, the closer to the endwalls travelling waves are, the slower they are. This might suggest that infinite distance from the endwalls (equivalent to periodic conditions) would result in dominant frequencies closer to those of linear stability analyses, that is around $St = 0.025$ (Brès and Colonius, 2008; de Vicente, 2010; Pastur et al., 2012). Second, steady (or slow moving) structures are more likely to be observed nearby the endwalls. These structures typically yield larger wavenumbers around $\beta = 10$.

Conclusions

Context

Open cavity flows have been long studied, along with other impinging flows, for their astonishing properties regarding the self-sustained oscillations of the shear layer. Extensive research has been carried out regarding the locked-on flapping motion of the shear layer, responsible for intense noise generation and fluid-structure interactions.

An exhaustive understanding of the global organisation of the cavity flow yet remains out of reach. In particular, secondary aspects have often been neglected. Side-band peaks resulting from nonlinear interactions induce a discrepancy between shear layer spectra from experiments and predictions of empirical simplified models. Through space-time analysis in the permanent regime, new insight about the saturated state of the self-sustained oscillations could be gained. In addition, both lid- and shear-driven cavities have become interesting objects in regards to three-dimensional dynamics at play around the main recirculation induced by either the lid or the outflow. The rise of centrifugal instabilities has been observed both experimentally and numerically, and confirmed by linear stability analysis.

When dealing with open cavities, shear layer dynamics inject fluctuations of spanwise vorticity, which interact with centrifugal instabilities to induce more complexity. Few observations have imputed low frequency amplitude modulations of the shear layer waves to spanwise oscillations in the inner-flow. Numerically, similar nonlinear interactions between centrifugal instability waves and Rossiter modes have been highlighted in the compressible regime for low Reynolds numbers (typically $Re_D = 1500$). However, experimental investigations were still needed to focus on the spanwise waves of the inner-flow in the permanent regime.

Means

We have focused this work on the space-time dynamics of an incompressible three-dimensional open cavity flow in the permanent regime. To that aim, experimental investigations using time-resolved PIV measurements have been realised. Giving access to time-resolved snapshots is particularly useful since it enables the modal decomposition in time of space-extended information. Hence, it helps in identifying spatial structures associated with any given time-scale. Coherent structures such as travelling waves, interference patterns or amplitude modulations can be revealed and characterised, bringing insightful information about the nonlinear effects at play in the saturated state.

The permanent regime allows us to use time Fourier transform for most of the analysis (no transient dynamics). Global Fourier modes were hence obtained through time Fourier decomposition applied to time-resolved velocity fields. On the other hand, the space scales of the spatially modulated spanwise waves observed in the inner-flow called for a more advanced identification. In particular, (complex) global Fourier modes issued of time-Fourier decomposition were investigated through spanwise modal decompositions: both Fourier and Hilbert-Huang transforms were used. The analysis took benefit of Hilbert-Huang transform for a precise and local esti-

mation of the amplitude and wavenumbers along the span through Hilbert-Huang transform. Statistic information and direction of the waves (sign of wavenumbers) were obtained by Fourier decomposition.

In order to study the shear layer nonlinear dynamics on one hand and the spanwise waves in the inner-flow on the other hand, two distinct experimental campaigns were undertaken in the salient plane of each aspect.

i) A cross-stream plane (xy) was chosen to focus on the locked-on Kelvin-Helmholtz waves propagating along the shear layer. High frame rate PIV acquisitions were performed in the wind-tunnel at LIMSI (Orsay) in the incompressible regime, for Reynolds numbers based on cavity length $8000 \leq \text{Re}_L \leq 15000$. A range of cavity lengths L and incoming velocities U_0 was investigated, so as to modify the control parameters L/θ_0 and L/D governing the impinging shear layer and the main recirculation. The time-resolved space-extended datasets enabled a time-Fourier analysis of time-scales over about three orders of magnitude ($10^{-1} \lesssim f \lesssim 10^2$ Hz).

ii) The study of centrifugal instabilities arising in the inside-flow was based on velocity fields acquired in a spanwise wall-parallel plane (zx), extracted at $y/D = -0.1$ inside a cavity such that $L/D = 2$. The experimental campaign was carried out in a large water-tunnel at LTRAC (Melbourne). With the aim of optimising the PIV processing of such low amplitude three-dimensional structures, three large-array-cameras had to be placed alongside and synchronised, so as to ensure high spatial resolution datasets, while covering the entire span. Despite the far lower data rate than in the high-speed PIV campaign at LIMSI, time-resolution was achieved nonetheless because the equivalent time scales at stake were drastically lowered by water viscosity. Furthermore, frequencies associated with the inner-flow dynamics are one to two orders of magnitude smaller than the shear layer locked-on modes. The focus was mostly on two low Reynolds configurations ($\text{Re}_D = 1500$, $D/\theta_0 = 23.2$) and ($\text{Re}_D = 2400$, $D/\theta_0 = 29.4$) exhibiting a highly coherent organisation across the entire cavity span ($S = 10D$).

By coupling these two approaches, the nonlinearly saturated coherent structures of the flow have been identified at every time and space scales.

Results

To begin with, shear layer dynamics has been investigated in the frame of a parametric study over ranges of cavity aspect ratios L/D and dimensionless cavity lengths L/θ_0 . The evolution of the spectral signature of the self-sustained oscillations has been revealed with respect to L/θ_0 . An empirical experimentally-based model was deduced from the parametric study. Using the phase relationship between separation and impingement $\phi(x=L) - \phi(x=0) = 2n\pi - \gamma$ with n the number of cycles within the cavity length – and the correction term γ as a function of L/θ_0 and parameter n , most locked-on frequencies observed in spectra can now be predicted. Selection of dominant frequencies among the unstable locked-on modes depends on a critical frequency evolving with L/θ_0 relatively to lock-on stages $n = 1, 2, 3$.

The space-time analysis of the various regimes of oscillation has notably revealed *a posteriori* a critical zone in the $(\text{St}, L/\theta_0)$ space. Inside that critical region, shear layer modes correspond to carrier frequencies. In other words, they are sufficiently enhanced to saturate and produce harmonics. On the other hand, locked-on frequencies outside this critical region do not produce harmonics, though they are still associated with growing modes. They become side-band peaks overlaying with the carrier to induce amplitude modulation. Their nonlinear interactions with the carrier generate more side-band peaks (non harmonic series). Furthermore, nonlinear interactions between locked-on modes produce a low frequency (edge frequency), issued of the

amplitude modulated self-sustained oscillations at the impingement.

In addition, mode switching process was also observed in many configurations under investigation. Intermittency is usually studied without regards to amplitude modulation mechanism. In the present work, mode switching has gained new insight using a signal processing approach. A connection exists between amplitude modulated regimes and intermittent regimes. When evolving across the parameter space, the system passes continuously from one stage of oscillation n to another $n \pm 1$. As a result, for some control parameters, two locked-on modes are actually in the critical region: both are thus largely enhanced. In that case, the interference between the two modes becomes predominant (overmodulation), which leads to dramatic drops of the envelope and enables competition to occur.

In the second part of the analysis the spanwise waves due to centrifugal instabilities in the inner-flow have been identified and characterised. Spanwise Fourier and Hilbert-Huang transforms performed directly on the experimental datasets have confirmed centrifugal structures exhibit wavelengths scaling on D and that the dominant spanwise wavelength for the control parameters under study is $\lambda/D \simeq 1$.

Then, space-time diagrams have shown the strongest structures in the inner-flow are spanwise travelling waves with wavelengths such that $0.3 \leq \lambda/D \leq 1.6$. The phase velocities strongly vary in space and from sample to another, implying a continuum of frequencies such that $f D/U_0 \leq 0.04$. Generally occurring by pairs of counter-propagating waves, coherent structures partially overlay to induce interference patterns, which cause a global amplitude modulation in time.

The spatial structure of the spanwise waves do not change drastically from the linear regime to their saturated state, as indicated by the good match between eigenfunctions and global Fourier modes in xy -planes. Nevertheless, not all linearly growing modes are observed everywhere and at any time in the experiments. Nonlinear mechanisms are likely responsible for the selection of different states in non-symmetrically separated regions. Consequently, the permanent regime of centrifugal instabilities could be perceived through coupled amplitude equations.

Perspectives

Further works remain to be accomplished in collaboration with the researchers J. de Vicente and F. Meseguer Garrido (Madrid) and obviously Professor J. Soria in Melbourne. Current studies concern the evolution of the spanwise waves in the inner-flow, from the onset of centrifugal instabilities (linear stability analyses performed in Madrid) to the permanent regime (experimental data from LTRAC).

Though far less coherent, the investigation of the spanwise dynamics of the inner-flow when the control parameters increase ($Re_D \nearrow$, $D/\theta_0 \nearrow \dots$) could be of interest. Using modal decomposition methods based on statistics rather than time-resolved data, such as proper orthogonal decomposition, would probably bring more insight into the distorted state of centrifugal instabilities far from the threshold.

In addition, this investigation has provided a precise identification of the spatial structures associated with the characteristic time scales of the flow ranging over at least two orders of magnitude. This knowledge will be most insightful for the application of close-loop control strategies to the very same experimental facility.

Résumé en Français

Étude Expérimentale des Ondes et Structures Cohérentes dans un Écoulement Tridimensionnel de Cavité Ouverte

Un écoulement de cavité ouverte tridimensionnel saturé non-linéairement est étudié par une approche spatio-temporelle utilisant des données expérimentales résolues à la fois en temps et en espace. Ces données ont été acquises dans deux plans longitudinaux, respectivement perpendiculaire et parallèle au fond de la cavité, dans le régime incompressible, en air ou en eau. À l'aide de multiples méthodes de décompositions globales en temps et en espace, les ondes et les structures cohérentes constituant la dynamique dans le régime permanent et pouvant être produites par des mécanismes d'instabilités différents sont identifiées et caractérisées.

Tout d'abord, on approfondit la compréhension de l'effet des non-linéarités sur les oscillations auto-entretenues de la couche cisailée impactante et leurs interactions avec l'écoulement intracavitaire. En particulier, l'analyse spectrale d'une portion de l'espace des paramètres permet de mettre en évidence un lien entre l'accrochage des modes d'oscillations auto-entretenues, la modulation d'amplitude au niveau du coin impactant et l'intermittence de ces modes. De plus, l'observation des basses fréquences interagissant fortement avec les oscillations auto-entretenues démontre l'existence d'une dynamique tridimensionnelle intrinsèque à l'intérieur de la cavité indépendamment des perturbations causées par la couche cisailée instable.

Les analyses de stabilité linéaire ont montré que des instabilités centrifuges peuvent résulter de la courbure induite par la recirculation. L'étude de la dynamique après saturation révèle de nombreuses structures cohérentes dont les propriétés sont quantifiées et classées en s'appuyant sur la forme des instabilités sous-jacentes: des ondes transverses progressives ou stationnaires. Enfin, certains comportements des structures saturées suggèrent que les mécanismes non-linéaires gouvernant le développement de l'écoulement une fois sorti du régime linéaire pourraient être étudiés dans le cadre des équations d'amplitude.

Mots-clés: cavité ouverte, dynamique spatio-temporelle, écoulement tridimensionnel, PIV résolue en temps, analyse spectrale, transformée de Fourier, transformée de Hilbert-Huang, couche cisailée impactante, accrochage de modes, instabilité de Kelvin-Helmholtz, modulation d'amplitude, intermittence, instabilités centrifuges, tourbillons de Taylor-Görtler, ondes progressives, interférences

Synthèse détaillée en Français

Ce mémoire de thèse porte sur une étude expérimentale des ondes et structures cohérentes dans un écoulement de cavité ouverte tridimensionnel. Le manuscrit est rédigé en anglais dans le cadre de la co-tutelle de thèse entre l'Université Paris-Sud à Orsay (Laboratoire LIMSI/CNRS) et l'Université de Monash à Melbourne (Laboratoire LTRAC).

B.1 Introduction

Le premier chapitre introduit la problématique générale du sujet de thèse. L'écoulement au-dessus d'une cavité est une configuration fondamentale et générique que l'on retrouve aussi dans de nombreuses applications. C'est à ce double titre qu'il a fait l'objet de nombreuses études. Schématiquement, l'écoulement de cavité présente deux caractéristiques dynamiques principales : *i*) l'instabilité intrinsèque de la couche cisailée se développant au-dessus de la cavité et le potentiel de rétroaction associé à l'impact de l'écoulement (et des structures tourbillonnaires éventuelles) sur la paroi avale de la cavité; *ii*) la recirculation générée à l'intérieur de la cavité. Le couplage entre ces différents éléments conduit à l'émergence d'oscillations auto-entretenues de la couche cisailée, dont la dynamique non-linéaire a révélé une richesse qui laisse de nombreuses questions ouvertes. On met ainsi en évidence la prédiction et la compréhension des modes auto-entretenus, la compétition entre ces modes et l'intermittence qui en découle, la modulation en amplitude des battements de la couche cisailée et l'organisation tridimensionnelle de l'écoulement en cavité d'envergure finie. Il a en effet été observé que des structures tridimensionnelles peuvent émerger de l'écoulement de recirculation intra-cavitaire. Vraisemblablement issues d'instabilités centrifuges dues à la courbure des lignes de courant dans la cavité, la transformation de cette dynamique transverse dans le régime permanent reste encore peu étudiée. Dans ce travail, on s'intéressera donc

- au mécanisme de sélection des modes d'oscillations auto-entretenues, concernant en particulier le lien entre la modulation d'amplitude au coin impactant et l'intermittence se produisant pour certains domaines de l'espace des paramètres;
- aux interactions non-linéaires entre les modes de couche cisailée et l'écoulement intra-cavitaire, notamment avec les très basses fréquences dominant l'écoulement à l'intérieur de la cavité.

Cela nous amènera ensuite

- à caractériser les structures cohérentes tridimensionnelles qui apparaissent dans l'écoulement intra-cavitaire dans le régime permanent;
- à étudier ces structures au regard des instabilités centrifuges émergeant le long de la recirculation principale, comme démontré par les analyses de stabilité linéaire.

Outils et Méthodes

B.2 Sur les données expérimentales

Ce travail vise à aborder ces questions ouvertes par le biais de mesures expérimentales, en particulier de champs de vitesse résolus en temps. Cette résolution temporelle de données spatialement étendues permet la mise en œuvre de méthodologies apportant une analyse fine des échelles spatio-temporelles de l'écoulement.

Dans un premier temps, les dispositifs expérimentaux utilisés au LIMSIS à Orsay et au LTRAC à Melbourne sont décrits et les choix expérimentaux sont discutés en fonctions des objectifs. D'abord, la soufflerie du LIMSIS est brièvement décrite (Figure B.1). L'équipement et les paramètres d'acquisition de la technique de vélocimétrie par images de particules (PIV) à haute fréquence sont ensuite détaillés. Ce premier banc expérimental est dédié à l'étude de l'écoulement de cavité dans un plan xy parallèle à l'écoulement et normal au fond de la cavité. La dynamique de l'écoulement dans ce plan, présentant une très large gamme de fréquences, impose d'importantes contraintes sur les mesures de champs de vitesse. Celles-ci sont rendues possibles par l'utilisation de PIV haute fréquence. Le deuxième banc expérimental, situé au LTRAC en Australie, est lui plus spécifiquement dédié à l'analyse de la structure spatiale tridimensionnelle de l'écoulement en se focalisant sur les champs de vitesse dans un plan zx perpendiculaire au plan de mesure choisi au LIMSIS, permettant d'analyser les structures spatio-temporelles dans toute la largeur de la cavité. La résolution spatiale nécessaire à l'analyse est obtenue par l'utilisation de trois caméras haute résolution (Figure B.1).

Dans un second temps, on s'intéresse aux algorithmes PIV utilisés pour traiter les données issues de ces campagnes. L'algorithme d'inter-corrélation (MCCDPIV) (Soria, 1996, 1998) est utilisé au LTRAC et un algorithme basé sur la minimisation des différences d'intensité optique et la programmation dynamique (OPFLOW) (Quénot, 1992; Quénot et al., 1998) est utilisé au LIMSIS. Ces deux méthodes sont décrites et comparées avec un code de référence du DLR (PIVview), ce qui permet de les valider et d'en faire une brève analyse critique.

B.3 Décomposer la dynamique saturée d'un écoulement réel

Les outils d'analyse utilisés dans la suite sont conçus pour tirer partie de la double définition en espace et en temps des mesures expérimentales. La première série d'outils est basée sur la transformée de Fourier, qui permet notamment de remonter à la densité spectrale et aux modes de Fourier globaux¹ de l'écoulement dans le plan de mesure. Par un processus similaire, le calcul de fonctions de transfert entre deux points distincts de l'écoulement rend aussi possible l'estimation des propriétés des ondes (longueur d'onde, vitesse de phase, taux de croissance spatial). Enfin, la transformée de Fourier est aussi utilisée spatialement, suivant l'envergure (direction z), afin d'obtenir les nombres d'onde des structures tridimensionnelles observées dans un plan zx .

Le second type de décomposition modale utilisée dans ces travaux fait intervenir la transformée de Hilbert-Huang, qui consiste en une décomposition en modes empiriques (Empirical Mode Decomposition, EMD), suivie d'une transformée de Hilbert. Appliquée à une onde spatiale 1D, cette technique permet de remonter aux caractéristiques locales de l'onde et en particulier le

¹ modes spatiaux complexes associés à une fréquence unique (Rowley et al., 2002; Basley et al., 2011). Ces structures spatiales sont obtenues en appliquant la transformée de Fourier en temps sur les séries temporelles extraites en tout point du champ (de vorticités par exemple)

spectre local en nombres d'onde. La transformée de Hilbert-Huang s'avérera particulièrement utile pour compléter les résultats de la transformée de Fourier dans l'étude des ondes le long de l'envergure. En effet, elle pallie aux limitations de la transformée de Fourier, en apportant une précision accrue et une information locale. L'utilisation conjointe des deux méthodes permet donc une analyse plus poussée et complète des échelles spatiales de l'écoulement intra-cavitaire.

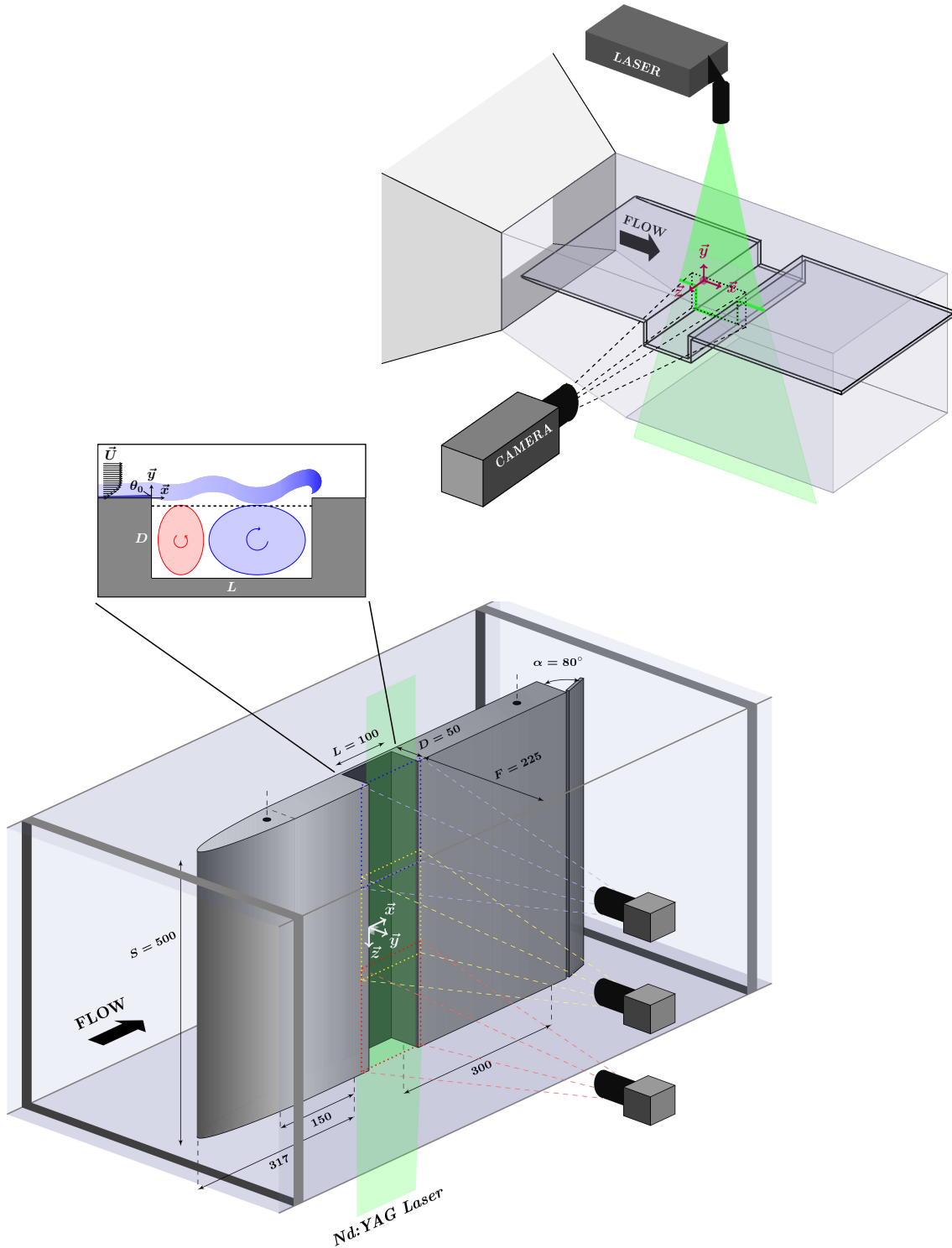


Figure B.1: Dispositifs expérimentaux utilisés pour les mesures PIV, (haut) LIMSI, (bas) LTRAC.

Analyse de l'Écoulement en Temps et en Espace

B.4 Les interactions non-linéaires dans la dynamique principale

L'analyse débute avec une étude dans un plan xy parallèle à l'écoulement et normal au fond de la cavité. Pour une cavité de largeur suffisante dans la troisième direction z , la dynamique quasi 2D de l'écoulement dans ce plan est en effet représentative au premier ordre de la dynamique globale de l'écoulement. L'écoulement en amont de la cavité est un écoulement de couche limite, bien représenté par un profil de Blasius, et dont l'épaisseur de quantité de mouvement θ_0 à l'entrée de la cavité constitue un paramètre physique important. En effet, il conditionne l'épaisseur de la couche cisailée au-dessus de la cavité et donc les caractéristiques des ondes d'instabilité de *Kelvin-Helmholtz* qui s'y développent. Les fréquences des oscillations auto-entretenues sont

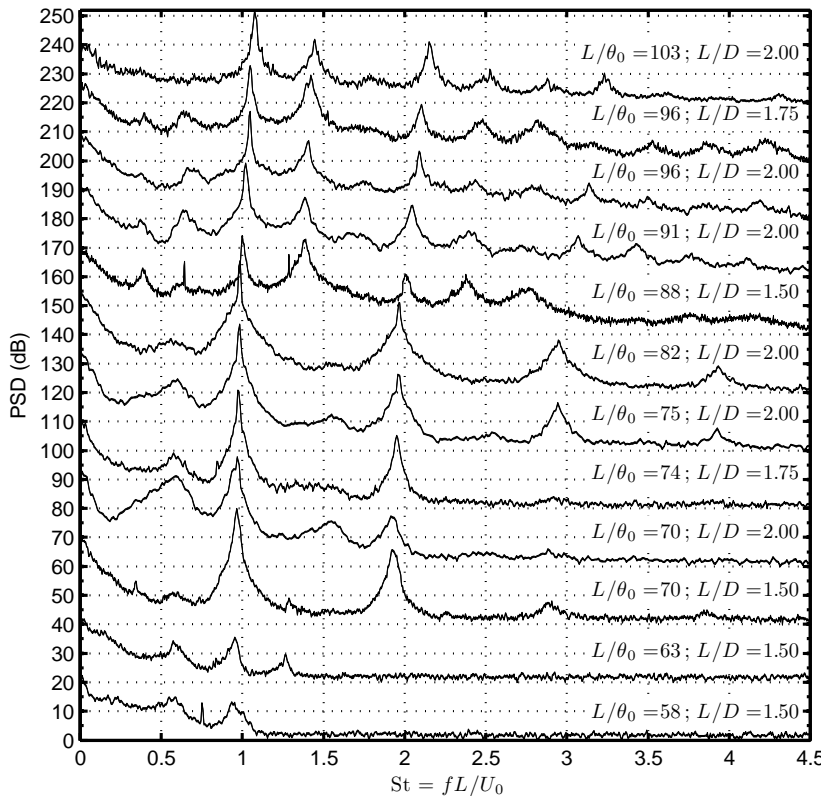


Figure B.2: Densités spectrales de puissance (composante longitudinale de vitesse légèrement en amont du coin impactant) pour différents cas ordonnés avec L/θ_0 croissant, en considérant le nombre de Strouhal basé sur la longueur de cavité L . Pour plus de clarté, chaque spectre est translaté de 20 dB. L'épaisseur des courbes correspond à un intervalle de confiance de 95%.

ainsi associés aux deux paramètres de contrôle, L/θ_0 et L/D , L et D désignant respectivement la longueur et la profondeur de la cavité. Plus particulièrement, pour différentes valeurs de ces paramètres, l'analyse spectrale (Figure B.2) met bien en évidence les *fréquences d'accrochage* classiquement observées. Ces fréquences satisfont la relation

$$St_n = \frac{f_n L}{U_0} = (n - \gamma) \frac{U_{kh}}{U_0}$$

où U_{kh}/U_0 est la vitesse des ondes de Kelvin-Helmholtz par rapport à la vitesse débitante, un rapport de l'ordre de 0.5 dans le régime incompressible. Le coefficient correctif γ a originellement été proposé pour modéliser les écarts de phase attribués à l'interaction des tourbillons avec le coin impactant.

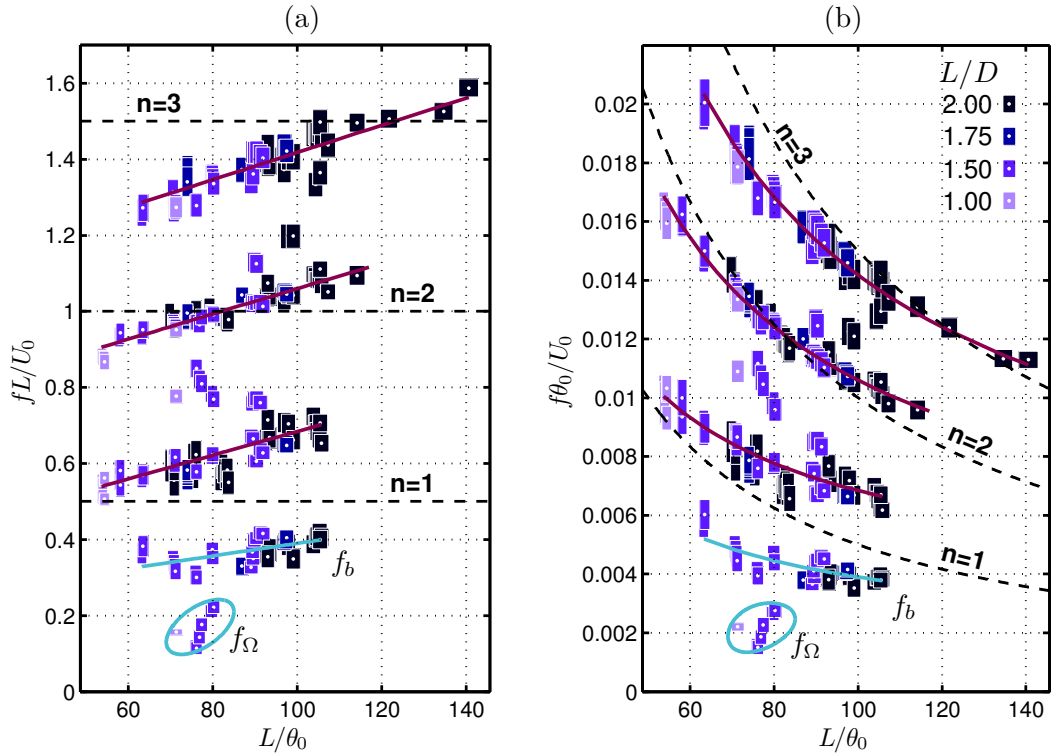


Figure B.3: Évolution paramétrique des fréquences principales des spectres en fonction du paramètre de contrôle L/θ_0 . Les données sont extraites des spectres LDV, pour de nombreux cas étudiés ces dernières années au LIMSI. Les fréquences sont normalisées en nombres de Strouhal basés sur la longueur de cavité L . Des régressions linéaires sont obtenues pour les trois modes d'accrochage, chacun autour d'un niveau $n/2$ avec $n = \{1, 2, 3\}$. Les couleurs indiquent les différentes géométries L/D et la dimension des rectangles représente les incertitudes de mesures.

Les interpolations linéaires effectuées en Figure B.3 permettent de proposer une expression empirique de ce coefficient.

$$\gamma_n(L/\theta_0) = \frac{41n - L/\theta_0}{10(17 - n)}$$

Cette expression dépend uniquement du niveau n et du paramètre de contrôle L/θ_0 . Une analyse de stabilité élémentaire de l'écoulement moyen permet de se convaincre que les fréquences observées sont compatibles avec un mécanisme d'instabilité de type Kelvin-Helmholtz, qui est donc logiquement le moteur dynamique des battements de la couche cisailée, la boucle de rétroaction appliquant une contrainte pour le choix du niveau d'accrochage. C'est ce couplage entre instabilité intrinsèque de la couche cisailée et longueur de cohérence entre décollement et impact, représenté par le paramètre L/θ_0 , qui conditionne principalement l'instabilité globale responsable des oscillations auto-entretenues.

La diversité des signatures spectrales (Figure B.2) pour les différentes configurations étudiées révèle la richesse de la dynamique non linéaire de l'écoulement. En particulier, on observe très souvent une modulation d'amplitude associée à la présence de fréquences latérales (*pics décalés*). Ces fréquences décalées forment des triades avec la fréquence dominante f_a et la basse fréquence f_b (appelée *fréquence de coin*), liées par une interaction non-linéaire. Dans l'espace spectral, cela correspond à une relation du type

$$f_{\pm} = f_a \pm f_b.$$

On peut observer une telle organisation dans le spectre donné en Figure B.4.

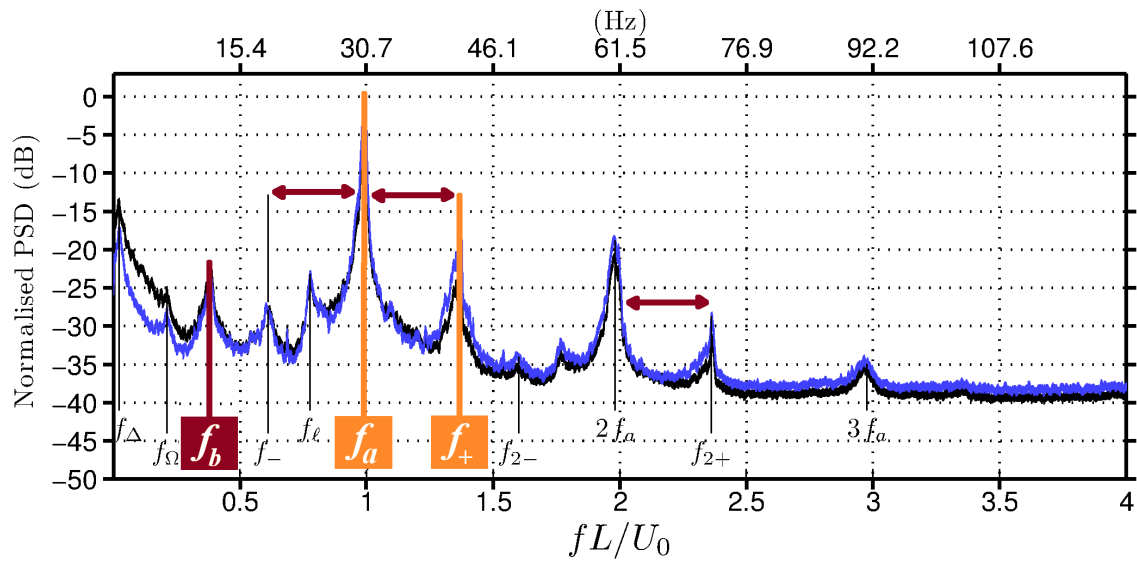


Figure B.4: Spectre de puissance normalisé, pour $L/\theta_0 = 79$ & $L/D = 1.5$, calculé à partir des fluctuations de vitesse longitudinale u' (noir) et normale v' (bleu).

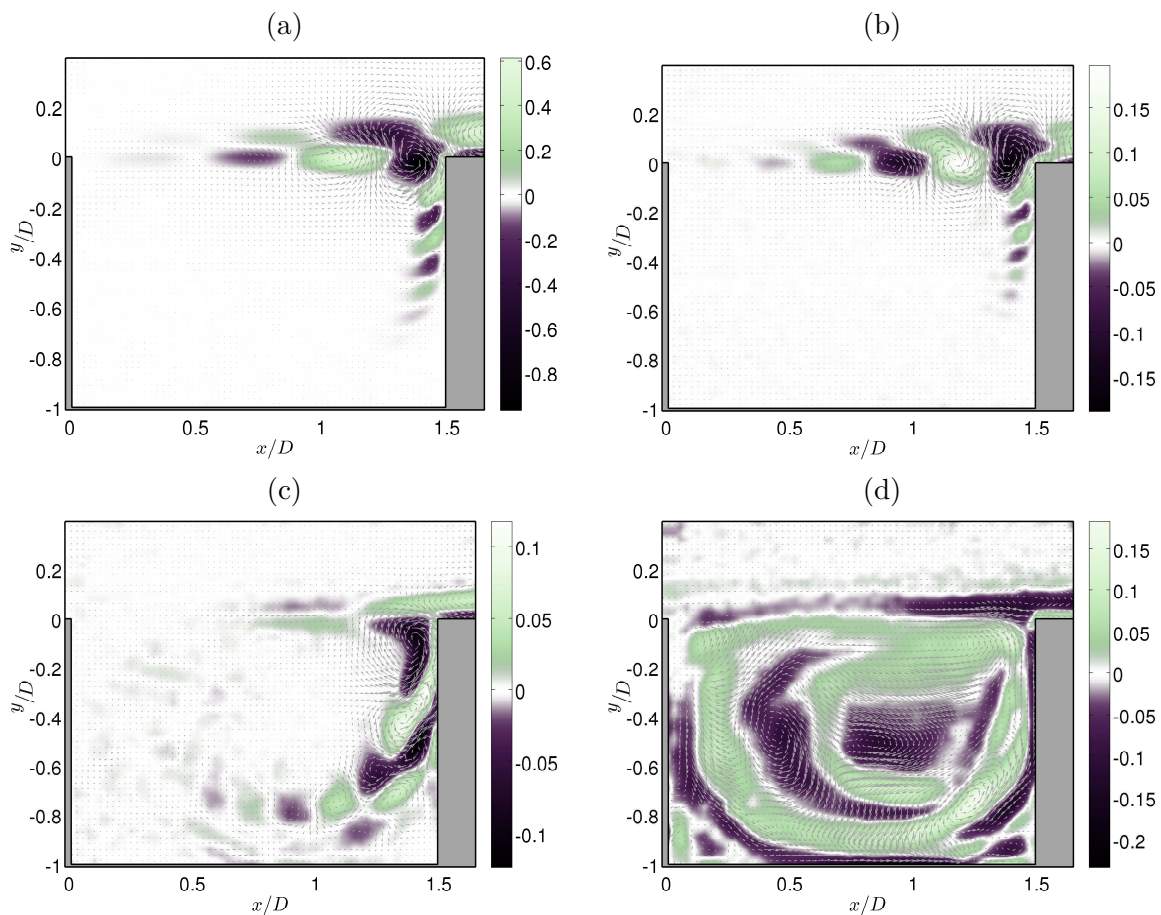


Figure B.5: Modes de Fourier globaux (partie réelle) associés aux fréquences $f_a = 30.7$ Hz ($f_a L/U_0 = 0.99$), (b): $f_+ = 42.2$ Hz ($f_+ L/U_0 = 1.37$), (c) $f_b = 11.5$ Hz ($f_b L/U_0 = 0.38$) et (d): $f_\Delta = 0.88$ Hz ($f_\Delta D/U_0 = 0.019$), pour $L/D = 1.5$, $L/\theta_0 = 79$. Les couleurs codent les fluctuations de vorticité ω_z' , les champs de vecteurs représentent les fluctuations de vitesse.

La Figure B.5 se compose des modes de Fourier globaux associés aux fréquences principales issues du spectre de la Figure B.4. Les deux modes de Fourier en Figures B.5.(a,b) fournissent les structures spatiales associées à la fréquence dominante f_a et à la fréquence décalée droite f_+ (Basley et al., 2011). Ces modes correspondent tous deux à des modes accrochés de la couche cisailée impactante. Ils présentent une allée de tourbillons contra-rotatifs se déplaçant et grossissant le long de la couche cisailée. On remarque que le rapport harmonique entre les fréquences se retrouve dans les nombres d'onde associés (taille des structures). Cela confirme qu'à la fois f_a et f_+ satisfont la même relation de dispersion de Kelvin-Helmholtz, se déplaçant à une même vitesse de phase, environ égale à $\frac{U_0}{2}$. En revanche, seul le mode à f_a est suffisamment puissant pour pouvoir créer des harmoniques $h f_a$ avec $h = 2, 3, 4$. En fait, la fréquence f_a peut être considérée comme la *porteuse* du signal et f_b la fréquence *modulante* décrivant les oscillations de l'enveloppe du signal. Ce modèle est illustré par le diagramme temps-fréquence et la série temporelle extraits en Figure B.6.

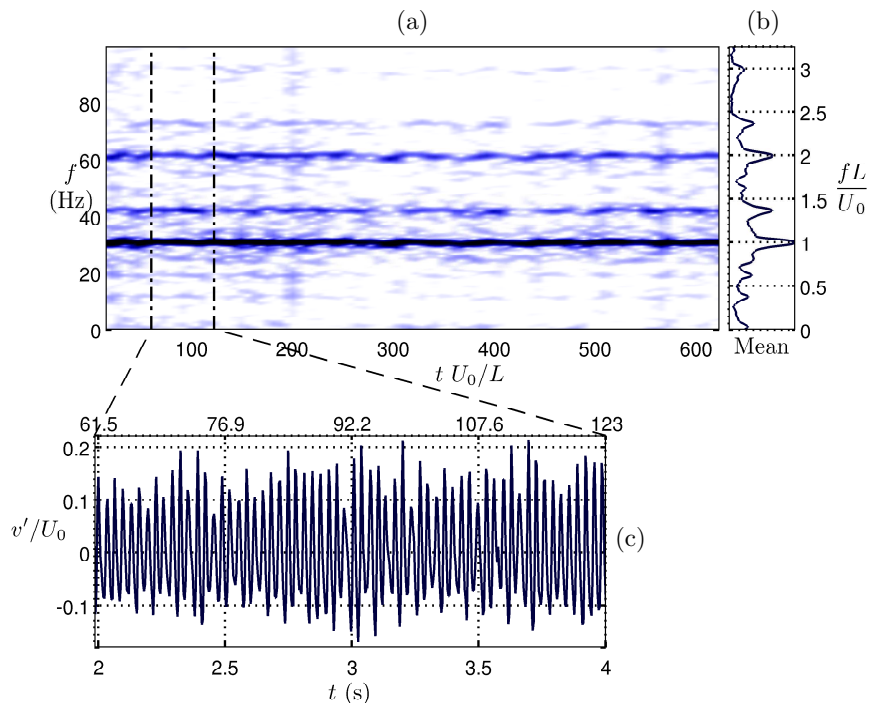


Figure B.6: Évolution temporelle des fluctuations de vitesse $v'(x_p, y_p, t)$ au point $(x_p/D = 1.35, y_p = 0)$, issues des champs de vitesse résolus en temps pour le cas $L/D = 1.5, L/\theta_0 = 79$. (a) Diagramme temps-fréquence pour l'enregistrement complet (21 s), les couleurs codant la densité spectrale; (b) le spectre moyen correspondant; (c) extrait de la série temporelle telle que $61 \leq t U_0/L \leq 123$ en unités sans dimension ($2 s \leq t \leq 4 s$).

L'analyse spectrale de ce type de régime met en effet toujours en évidence que la modulation de l'onde porteuse par la basse fréquence f_b peut être associée aux autres modes d'accrochage, qui s'interprètent alors comme des modes latéraux. Ces interactions ont été l'objet de nombreux travaux par Rockwell et ses co-auteurs (Rockwell and Knisely, 1979, 1980b; Knisely and Rockwell, 1982; Ziada and Rockwell, 1982; Tang and Rockwell, 1983). Ils avaient mis en évidence une interaction tourbillon-bord donnant lieu à des cycles plus longs que celui des oscillations auto-entretenues. Les tourbillons interagissent donc avec le bord impactant de façon quasi-périodique. Cette hypothèse se confirme au regard de la structure spatiale donnée en Figure B.5.c. Celle-ci montre que la basse fréquence f_b est portée par des structures tourbillonnaires qui descendent le long de la paroi aval au niveau de l'impact puis sont

advectées le long de la recirculation principale. La fréquence modulante traduit donc le cycle d'injections plus ou moins fortes induit par les tourbillons impactant dans la couche cisailée.

Les cas présentant deux modes d'accrochage en compétition et d'énergie équivalente sont particulièrement intéressants car ils peuvent conduire à un phénomène d'*intermittence*. La dynamique temporelle d'un tel cas ($L/D = 2.0$, $L/\theta_0 = 91$) montre clairement plusieurs occurrences de bascule d'un mode à l'autre, et la présence d'harmoniques bien identifiés pour les deux modes (Figure B.7).

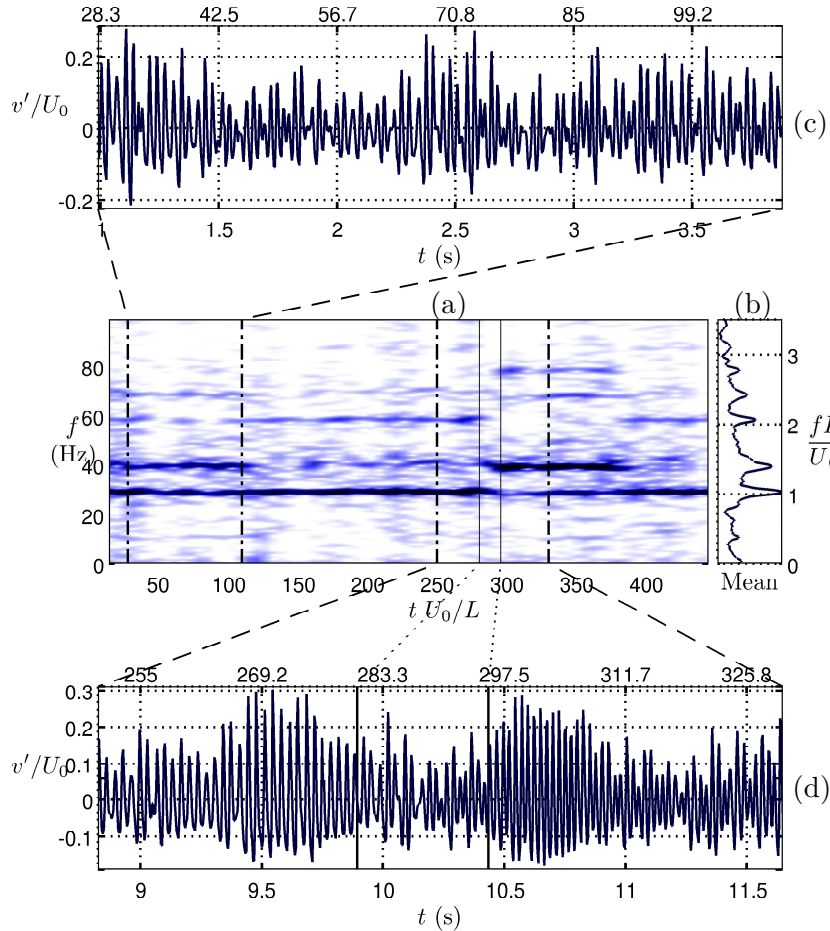


Figure B.7: Évolution temporelle des fluctuations de vitesse $v'(x_p, y_p, t)$ au point ($x_p/D = 1.35$, $y_p = 0$), issues des champs de vitesse résolus en temps pour le cas $L/D = 1.75$, $L/\theta_0 = 96$. (a) Diagramme temps-fréquence pour l'enregistrement complet (16 s), les couleurs codant la densité spectrale; (b) le spectre moyen correspondant (échelle logarithmique); extraits de la série temporelle tels que (c), $28 \leq t U_0/L \leq 110$ en unités sans dimension ($1 \text{ s} \leq t \leq 3.9 \text{ s}$); (d), $250 \leq t U_0/L \leq 330$ ($8.8 \text{ s} \leq t \leq 11.6 \text{ s}$).

Plus précisément, on se rend compte que les transitions de modes sont associées à une forte modulation d'amplitude des oscillations auto-entretenues: on parle de *surmodulation*. Au cours d'une transition, l'amplitude des oscillations diminue donc drastiquement et la fréquence porteuse n'est plus clairement définie mais se situe entre les deux fréquences f_a et f_+ des deux modes d'accrochage. Cette surmodulation résulte de la superposition des deux modes d'accrochage. Cette signature est riche d'enseignement car elle implique une continuité entre les

régimes modulés en amplitude et intermittents. L'évolution de la dynamique est uniquement conditionnée par la présence plus ou moins forte du deuxième mode d'accrochage.

Dans un autre registre, on peut s'intéresser à la dynamique plus lente de l'écoulement. L'analyse des spectres montre en effet une caractéristique constante pour tous les paramètres étudiés: un niveau d'énergie élevé pour les très basses fréquences, au moins un ordre de grandeur en dessous des fréquences des oscillations auto-entretenues. Un exemple du pic large-bande centré sur la fréquence notée f_Δ est donné en Figure B.8. Grâce à un comparatif entre la dynamique dans la couche cisailée et le fond de la cavité, on révèle que ces très basses fréquences règnent particulièrement dans la cavité mais interagissent avec la couche cisailée sous la forme d'une très forte modulation d'amplitude des oscillations auto-entretenues, pouvant même momentanément les annuler. Les nombres de Strouhal basés sur la profondeur de cavité et correspondant aux fréquences f_Δ sont tels que

$$0.010 \leq f_\Delta D/U_0 \leq 0.027.$$

Un exemple de mode spatial associé à ces fréquences est donné en Figure B.5.d. On observe une structure cohérente s'enroulant autour du tourbillon intra-cavitaire. Ces résultats rappellent ce qui a été observé dans les simulations numériques par Brès and Colonius (2008); de Vicente (2010), portant sur l'émergence d'instabilités centrifuges dans l'écoulement intra-cavitaire. On peut raisonnablement penser que les modes associées aux fréquences autour de f_Δ correspondent à la dynamique saturée d'ondes transverses issues des instabilités centrifuges. Afin d'étudier ces ondes en détails, la deuxième partie de l'analyse s'effectuera selon l'envergure de la cavité – dans un plan zx .

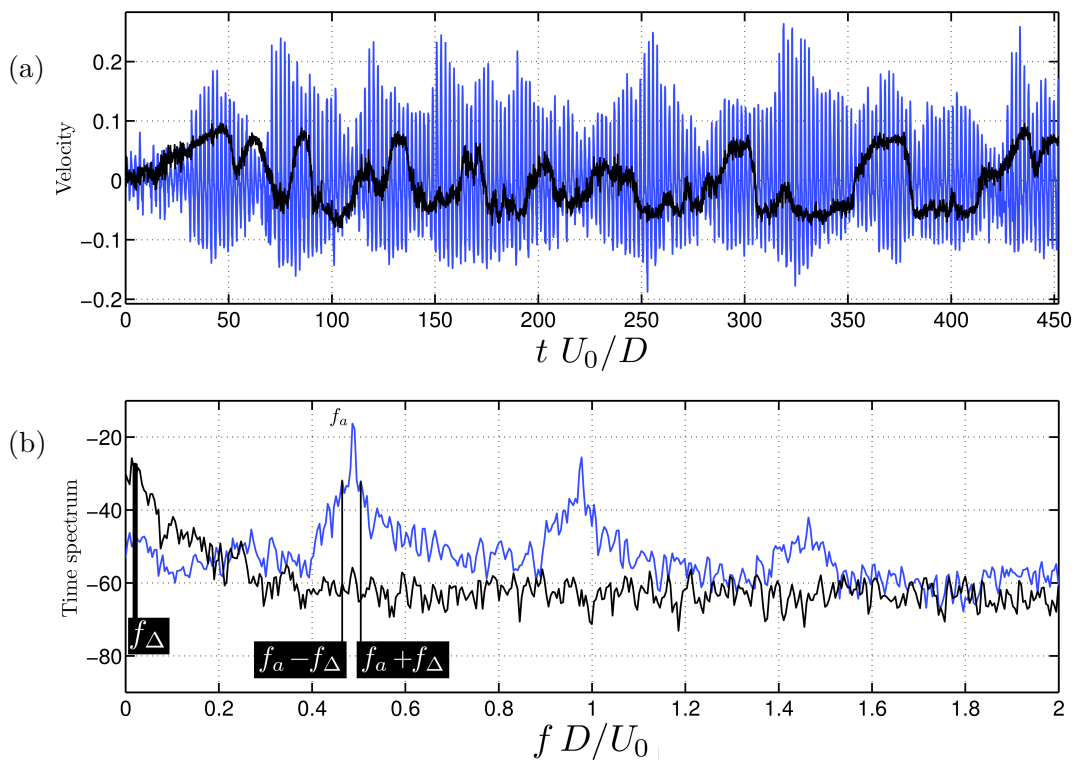


Figure B.8: Fluctuations de vitesse extraites des champs pour $L/D = 2.0$, $L/\theta_0 = 82$: (bleu clair) fluctuations v'/U_0 extraites dans la couche cisailée ($x_p/D = 1.70$, $y_p = 0$); (noir) fluctuations u'/U_0 extraites dans la cavité ($x_p/D = 1.0$, $y_p/D = -0.75$). (a) Série temporelle et (b) spectre correspondant.

B.5 La dynamique transverse de l'écoulement intra-cavitaire

Des mesures de vitesse sont effectuées dans un plan zx localisé à 10% de la profondeur d'une cavité de rapport d'aspect $L/D = 2$, pour trois configurations de paramètres. En première analyse, les champs instantanés de vitesse et de vorticité ω_y mettent en évidence une structuration tridimensionnelle de l'écoulement sur toute l'envergure de la cavité $S = 10D$ – voir Figure B.9. Des bandes périodiques de vorticité alternativement positive et négative sont associées à des zones de basse et haute vitesse longitudinale. Elle forment des ondes transverses – suivant la direction z – et la cohérence couvre toute la cavité entre les parois amont et aval. Ces structures cohérentes pourraient donc logiquement être la trace d'instabilités centrifuges se développant le long de la zone de recirculation intra-cavitaire.

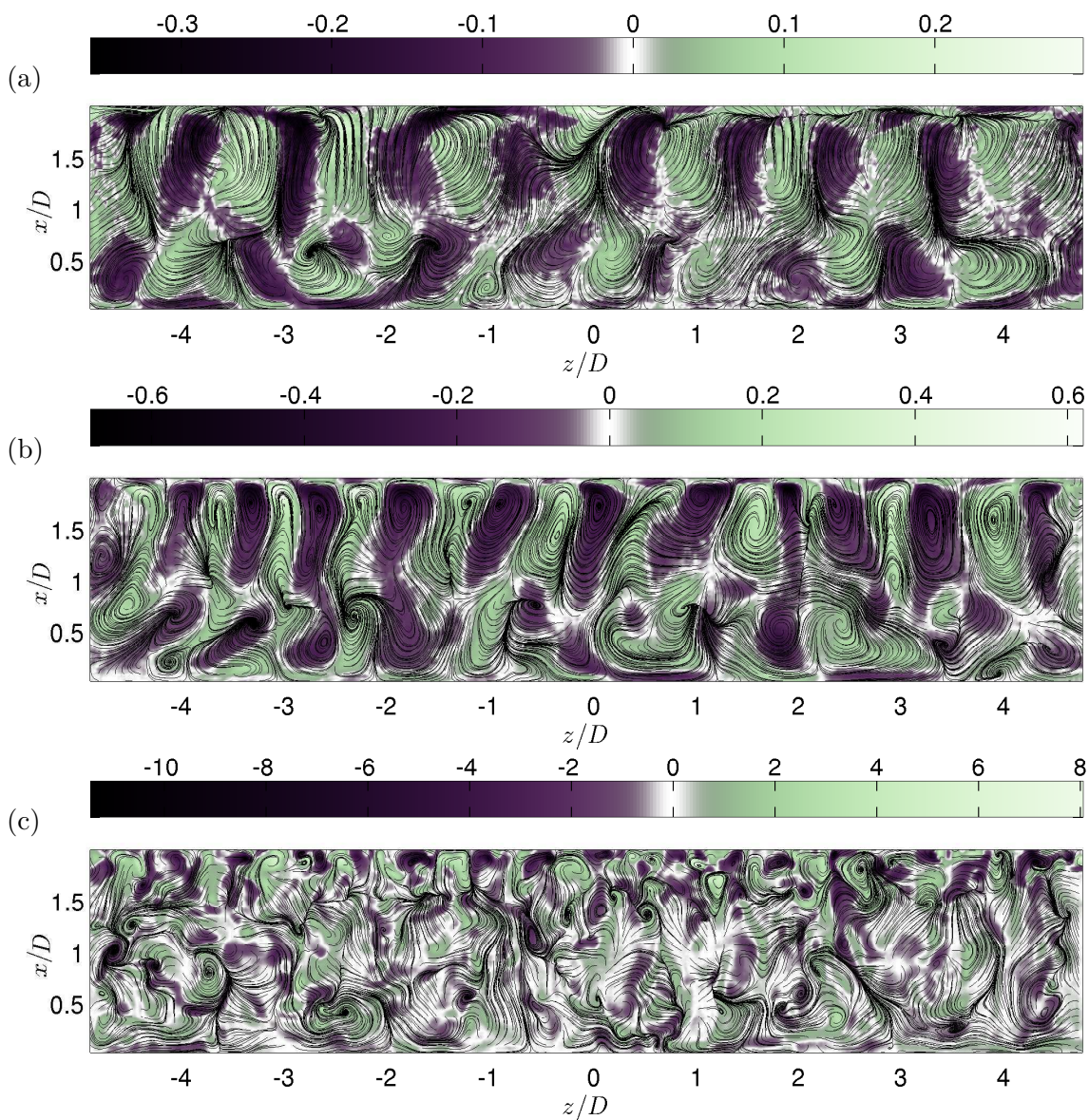


Figure B.9: Champs fluctuants instantanés dans le plan $(x, y/D = -0.1, z)$ pour trois configurations: (a), $Re_D = 1500$, $D/\theta_0 = 23.2$; (b), $Re_D = 2400$, $D/\theta_0 = 29.4$; (c), $Re_D = 5550$, $D/\theta_0 = 46.6$. Les couleurs codent la vorticité normalisée $\omega'_y D/U_0$ et les lignes de courants sont générées à partir des fluctuations de vitesse.

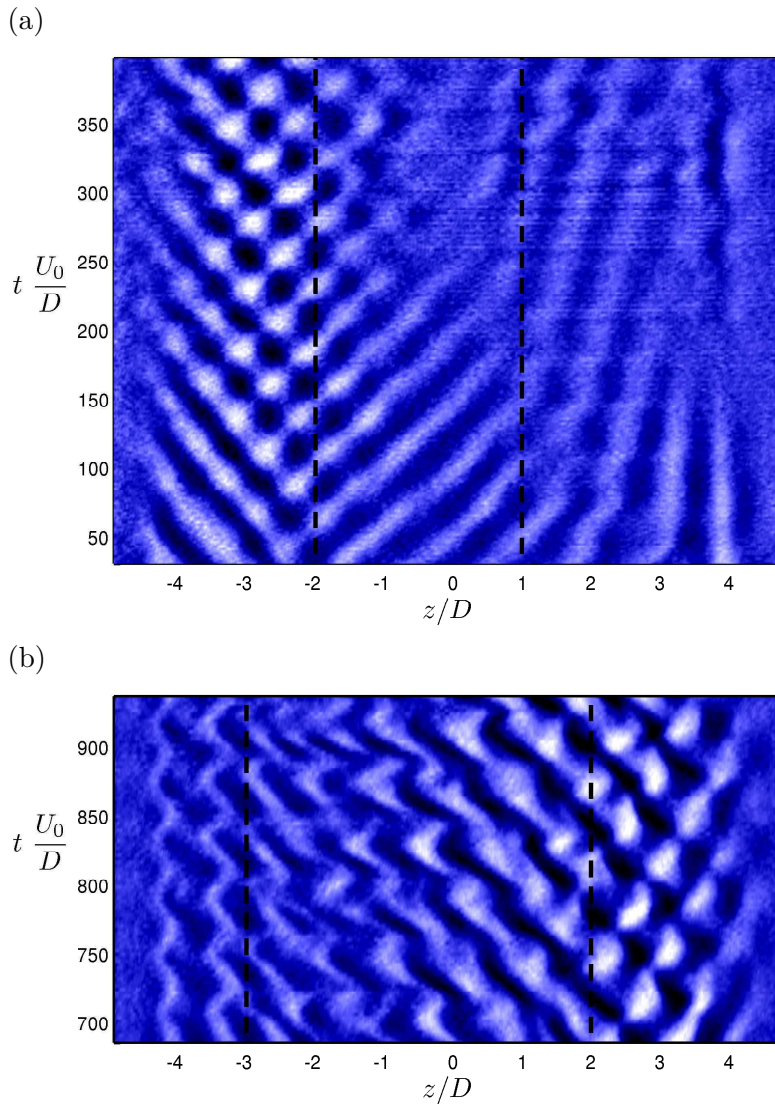


Figure B.10: Diagrammes spatio-temporels en $y/D = -0.1$ pour
 (a) $Re_D = 1500$, $D/\theta_0 = 23.2$,
 (b) $Re_D = 2400$, $D/\theta_0 = 29.4$.

Les fluctuations de vorticité ω_y' (valeurs négatives sombres) sont extraites de lignes suivant l'envergure pour $x/D = 1.5$ pour former des fonctions paramétriques des unités adimensionnées de temps $t \frac{U_0}{D}$ et de position z/D .

L'étude spatio-temporelle de l'écoulement révèle une dynamique très riche d'ondes tridimensionnelles. On note en particulier que la longueur d'onde qui prédomine dans les spectres de Fourier en z est proche de la profondeur de la cavité D , en accord avec une nature centrifuge. Phénoménologiquement, cette longueur d'onde principale est associée à des paires de tourbillons contra-propagatifs distribuées le long de l'envergure, comme précédemment observé dans les visualisations par Faure et al. (2007, 2009); Douay and Faure (2011) ou dans des simulations numériques telles que dans Pastur et al. (2012).

Plus précisément, on remarque que les structures cohérentes dominantes sont généralement constituées de paires d'ondes progressives gauche et droite pouvant s'exclure ou se superposer localement (Figure B.10). Dans le deuxième cas, les interférences des deux ondes produisent des oscillations quasi-stationnaires, qui apparaissent comme des damiers dans le diagramme spatio-temporel.

Une décomposition de Fourier en temps permet d'identifier les différentes ondes en fonction de leur fréquence temporelle. En Figures B.11.a et B.12.a sont affichées les parties réelles de deux ondes progressive opposées visibles dans le diagramme spatio-temporel de la Figure B.10.a.

De telles ondes progressives rappellent l'organisation spatiale et les caractéristiques des

modes globaux issus des analyses de stabilité linéaire d'un état de base uniforme transversalement. Ces modes globaux identifient en effet les ondes découlant des effets centrifuges dus à l'écoulement recirculatoire dans la cavité (Brès and Colonius, 2008; de Vicente, 2010; Meseguer-Garrido et al., 2011). Or, puisque ces ondes transverses correspondent aux modes intra-cavitaires observés dans le plan xy , on montre ainsi que les très basses fréquences responsables de la forte modulation d'amplitude des oscillations auto-entretenues proviennent d'instabilités d'origine centrifuge, y compris loin du seuil d'instabilité dans le régime permanent.

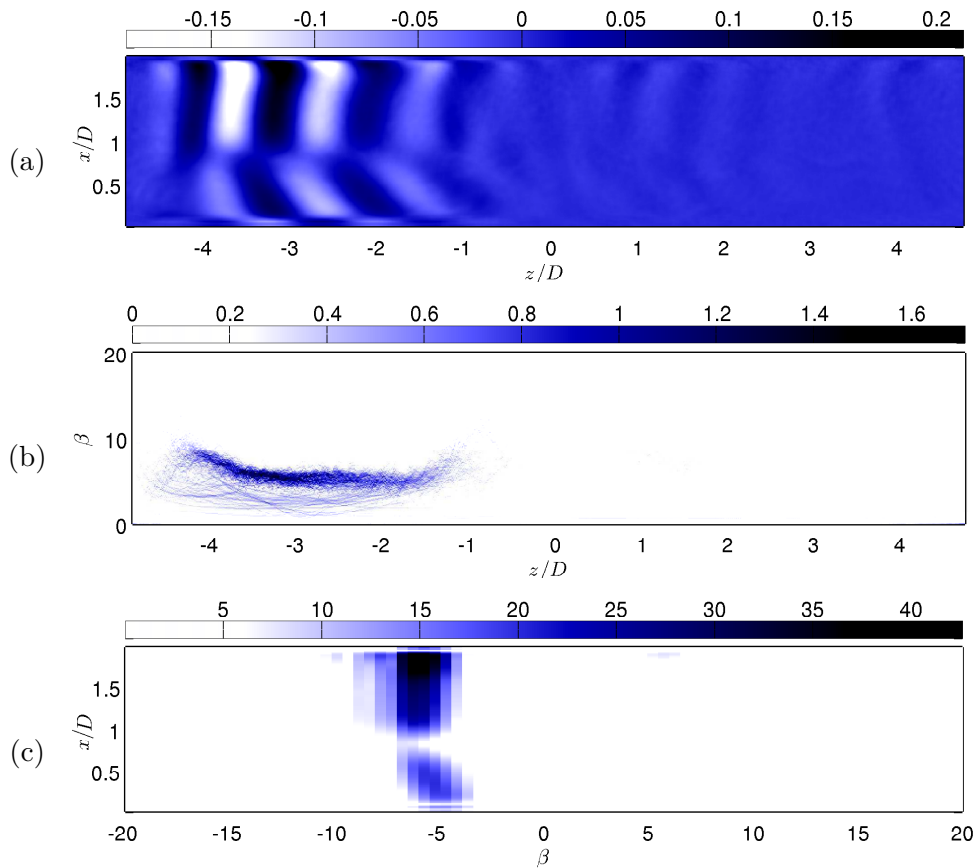


Figure B.11: Structure spatiale associée à $St = 0.019$ pour le cas $Re_D = 1500$, $D/\theta_0 = 23.2$. (a) Partie réelle, (b) Transformée de Hilbert-Huang, (c) transformée de Fourier.

En revanche, il reste des interrogations concernant la sélection des structures saturées parmi les modes propres instables. En effet, bien que les modes fournis par les analyses de stabilité linéaire (structures stationnaires ou ondes progressives) se retrouvent dans les mesures expérimentales de ce travail avec des caractéristiques similaires, les modes dominants dans le régime permanent ne correspondent pas aux modes les plus linéairement instables. Cette disparité pourrait être due aux conditions latérales non-périodiques. On observe d'ailleurs un ralentissement des ondes générées au voisinage des parois latérales (en $z/D = \pm 5$). Les interactions non-linéaires se produisant dans le régime saturé peuvent également induire de tels modifications et expliqueraient aussi les brisures de symétrie et les domaines d'ondes spatialement localisés, observés dans l'écoulement.

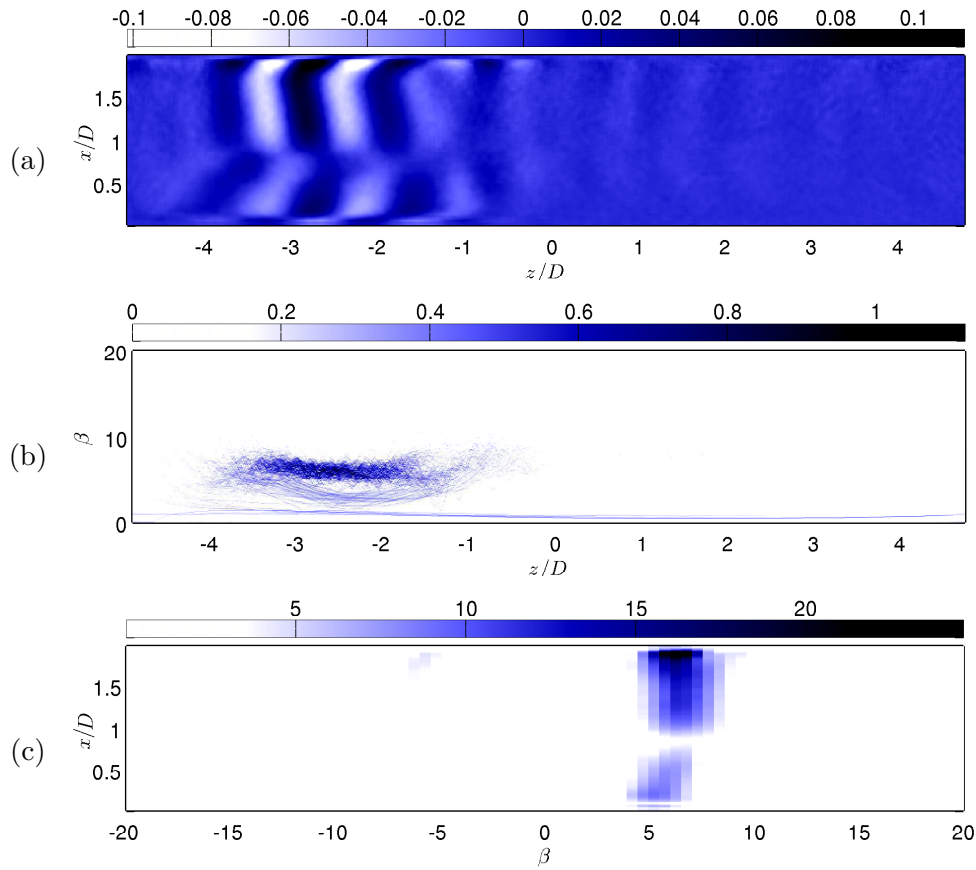


Figure B.12: Structure spatiale associée à $St = 0.023$ pour le cas $Re_D = 1500$, $D/\theta_0 = 23.2$. (a) Partie réelle, (b) Transformée de Hilbert-Huang, (c) transformée de Fourier.

B.6 Conclusions

Ce travail de recherche a eu pour objet l'écoulement passant une cavité ouverte de géométrie parallélépipédique dans le régime incompressible. La dynamique tridimensionnelle de ce système globalement instable et saturé non-linéairement a été étudié par une approche spatio-temporelle utilisant des données expérimentales résolues à la fois en temps et en espace. Ces données ont été acquises dans deux plans longitudinaux, respectivement perpendiculaire et parallèle au fond de la cavité, pour des nombres de Reynolds basés sur la profondeur de cavité de 1500 à 8000 environ, au cours de deux campagnes expérimentales effectuées au LIMSI (en soufflerie) et au LTRAC (dans une boucle en eau). A l'aide de méthodes de décompositions modales en temps et en espace – Fourier et Hilbert-Huang –, les ondes et les structures cohérentes constituant la dynamique dans le régime permanent ont été identifiées et caractérisées afin de pouvoir remonter aux différents mécanismes d'instabilités dont elles dérivent.

Dans un premier temps, l'objectif était d'approfondir notre compréhension de l'effet des non-linéarités sur les oscillations auto-entretenues de la couche cisailée impactante et leurs interactions avec l'écoulement intra-cavitaire. C'est notamment par une analyse spectrale d'une région de l'espace des paramètres qu'il a été possible de mettre en évidence un lien entre l'accrochage des modes d'oscillations auto-entretenues, la modulation d'amplitude au niveau

du coin impactant et l'intermittence de ces modes, encore très peu comprise. On a également pu caractériser en détails la signature spatio-temporelle des basses fréquences observées pour confirmer que les dynamiques lentes présentes dans l'écoulement intra-cavitaire sont toutes directement connectées à plusieurs mécanismes non-linéaires de modulation d'amplitude des modes d'oscillations auto-entretenu de la couche cisailée.

Par ailleurs, le rapprochement des structures spatiales associées à ces basses fréquences avec les modes propres transverses issus de simulations numériques a démontré l'existence d'une dynamique tridimensionnelle intrinsèque à l'intérieur de la cavité, indépendamment des perturbations causées par la couche cisailée instable. En effet, les analyses de stabilité linéaire globale, réalisées autour d'un écoulement de base 2D, c'est-à-dire avec conditions limites latérales périodiques, ont déjà mis en évidence que des instabilités centrifuges résultent de la courbure induite par la recirculation et produisent des ondes progressives selon l'envergure de la cavité.

On s'est donc intéressé à la dynamique transverse de l'écoulement intra-cavitaire dans le régime permanent pour discuter du devenir des instabilités centrifuges après que la saturation non-linéaire se soit produite et dans le cas de conditions limites réelles. L'étude de la dynamique saturée a ainsi révélé de nombreuses structures cohérentes se composant généralement de paires de tourbillons contra-rotatifs distribuées le long de l'envergure et s'organisant autour de la recirculation principale, rappelant les visualisations publiées précédemment, notamment par l'équipe du LIMSI. Les propriétés de cette dynamique tridimensionnelle ont été quantifiées et classées en s'appuyant sur la forme des instabilités sous-jacentes: des ondes transverses progressives ou stationnaires. Les nombres d'onde et les fréquences mis en jeu confirment la nature centrifuge de toutes les structures cohérentes observés dans le plan transverse.

Nous avons vu que la dynamique saturée découle bien des instabilités centrifuges décrites par les modes propres issus des analyses de stabilité globale. Pourtant, les modes dominant le régime permanent ne correspondent pas strictement aux caractéristiques des modes les plus linéairement instables. Il reste donc à déterminer les mécanismes responsables de la sélection et de la modification des modes instables dans le système réel saturé. Une collaboration est en cours avec l'Universidad Politecnica de Madrid sur les mêmes configurations que celles menées dans l'expérience. Le parallèle entre données expérimentales et stabilité linéaire n'a pas été exposé en détails dans ce travail mais apporte un complément primordial dans la caractérisation des mécanismes de sélection des structures tridimensionnelles organisant l'écoulement intra-cavitaire. Ces mécanismes pourraient être liés au changement de conditions limites ou à l'action des non-linéarités au cours du transitoire.

Il se trouve que le développement local des structures tridimensionnelles de l'écoulement saturé et leur forte sensibilité aux conditions initiales nous indiquent que les termes non-linéaires gouvernent l'état et l'évolution de la dynamique intra-cavitaire. Cela suggère qu'une approche faiblement non-linéaire et l'utilisation d'équations d'amplitude pourraient nous renseigner sur cette dynamique.

Bibliography

- Albensoeder, S. and Kuhlmann, H. C. (2005). Accurate three-dimensional lid-driven cavity flow. *J. Comp. Phys.*, 206:536–558. (In page 15.)
- Albensoeder, S. and Kuhlmann, H. C. (2006). Nonlinear three-dimensional flow in the lid-driven square cavity. *J. Fluid Mech.*, 569:465–480. (In pages 15, 122 and 124.)
- Albensoeder, S., Kuhlmann, H. C., and Rath, H. J. (2001). Three-dimensional centrifugal-flow instabilities in the lid-driven-cavity problem. *Phys. Fluids*, 13. (In pages 15, 16, 115, 121, 124 and 162.)
- Alizard, F., Basley, J., Robinet, J.-C., Faure, T., Pastur, L., Gloerfelt, X., Lusseyran, F., and Delprat, N. (2010). Flow dynamics in open square cavity: experimental and stability comparisons. Bad Reichenhall, Germany. 8th EUROMECH Fluid Mechanics Conference. (In page 16.)
- Amram, K. (1995). *Etude numérique des instabilités dans les couches de mélange compressibles*. PhD thesis, LadHyX, École Polytechnique, Palaiseau, France. (In pages 7, 74 and 76.)
- Ashcroft, G. and Zhang, X. (2005). Vortical structures over rectangular cavities at low speed. *Phys. Fluids*, 17. (In page 11.)
- Barbagallo, A., Sipp, D., and Schmid, P. J. (2009). Closed-loop control of an open cavity flow using reduced-order models. *J. Fluid Mech.*, 641:1–50. (In pages 11, 74 and 162.)
- Basley, J., Pastur, L. R., Lusseyran, F., Faure, T. M., and Delprat, N. (2011). Experimental investigation of global structures in an incompressible cavity flow using time-resolved piv. *Experiments in Fluids*. DOI: 10.1007/s00348-010-0942-9. (In pages 9, 42, 46, 71, 79, 86, 113, 176 and 181.)
- Betchov, R. and Szewczyk, A. (1963). Stability of a shear layer between parallel streams. *Phys. Fluids*, 6(10):1391. (In page 7.)
- Blackburn, H. M. and Lopez, J. M. (2003). The onset of three-dimensional standing and modulated travelling waves in a periodically driven cavity flow. *J. Fluid Mech*, 497:289–317. (In pages 15, 16 and 115.)
- Boppana, V. B. L. and Gajjar, S. B. (2010). Global flow instability in a lid-driven cavity. *Int. J. Numer. Methods Fluids*, 62:827–853. (In page 16.)
- Brès, G. A. and Colonius, T. (2007). Three-dimensional linear stability analysis of cavity flows. *AIAA J.*, page 1126. (In pages 16 and 122.)
- Brès, G. A. and Colonius, T. (2008). Three-dimensional instabilities in compressible flow over open cavities. *J. Fluid Mech.*, 599:309–339. (In pages 11, 16, 74, 112, 115, 116, 117, 121, 122, 123, 125, 132, 136, 162, 167, 168, 183 and 186.)
- Chatellier, L., Laumonier, J., and Gervais, Y. (2004). Theoretical and experimental investigations of low mach number turbulent cavity flows. *Experiments in Fluids*, 36:728–740. (In page 11.)

- Chiang, T., Sheu, W., and Hwang, R. (1998). Effects of the reynolds number on the eddy structure in a lid-driven cavity. *Int. J. Numer. Methods Fluids*, 26:557–579. (In page 15.)
- Chicheportiche, J., Merle, X., Gloerfelt, X., and Robinet, J.-C. (2008). Direct numerical simulation and global stability analysis of three-dimensional instabilities in a lid-driven cavity. *Comptes rendus. Mécanique*. (In pages 16 and 115.)
- Colonus, T., Basu, A. J., and Rowley, C. W. (1999). Numerical investigation of a flow past a cavity. *AIAA J.*, (27953). (In pages 9 and 13.)
- Colonus, T., Rowley, C. W., and Theofilis, V. (2001). Global instabilities and reduced-order models of cavity flow oscillations. In Theofilis, V., Colonius, T., and Seifert, A., editors, *Proceedings of the AFOSR/EOARD/ERCOFTAC SIG-33: Global Flow Instability and Control Symposium - I*, Crete, Greece. ISBN-13: 978-84-692-6244-3. Fundación General UPM. (In page 11.)
- de Vicente, J. (2010). *Spectral Multi-Domain Method for the Global Instability Analysis of Complex Cavity Flows*. PhD thesis, Universidad Politécnica de Madrid. (In pages 16, 74, 115, 116, 117, 121, 122, 123, 162, 167, 168, 183 and 186.)
- Delprat, N. (2006). Rossiter formula: a simple spectral model for a complex amplitude modulation process? *Phys. Fluids*, 18(071703). (In pages 9, 10 and 13.)
- Delprat, N. (2010). Low-frequency components and modulation processes in compressible cavity flows. *J. Sound Vibrat.*, 329(22):4797–4809. DOI: 10.1016/j.jsv.2010.05.013. (In pages 9, 13, 73, 113 and 115.)
- Dergham, G., Brion, V., Robinet, J.-C., and Sipp, D. (2008). The use of global modes to compute optimal transient growth. In *EUROMECH Fluid Mechanics Conference 7th*, Manchester, England. (In page 11.)
- Djenidi, L., Elavarasan, R., and Antonia, R. A. (1999). The turbulent boundary layer over transverse square cavities. *J. Fluid Mech.*, 395:271–294. (In pages 14 and 121.)
- Douay, C. L. and Faure, T. M. (2011). Secondary instability of centrifugal vortices in a cavity shear flow. (In page 185.)
- Duriez, T. (2009). *Application des générateurs de vortex au contrôle d'Écoulements décollés*. PhD thesis, Université Diderot (Paris 7). (In page 46.)
- Ehrenstein, U. and Gallaire, F. (2005). On two-dimensional temporal modes in spatially evolving open flows: the flat-plate boundary layer. *J. Fluid Mech.*, 536:209–218. (In pages 11 and 162.)
- Ehrenstein, U. and Gallaire, F. (2008). Two-dimensional global low-frequency oscillations in a separating boundary-layer flow. *J. Fluid Mech.*, 614:315–327. (In pages 11, 88 and 162.)
- Faure, T. M., Adrianos, P., Lusseyran, F., and Pastur, L. R. (2007). Visualizations of the flow inside an open cavity at medium range reynolds numbers. *Experiments in Fluids*, 42(2):169–184. (In pages 14, 121, 122, 124, 165 and 185.)

- Faure, T. M., Pastur, L. R., Lusseyran, F., Fraigneau, Y., and Bisch, D. (2009). Three-dimensional centrifugal instabilities development inside a parallelepipedic open cavity of various shape. *Experiments in Fluids*, 47(3):395–410. (In pages 14, 121, 122, 124, 125, 165 and 185.)
- Forestier, N., Jacquin, L., and Geffroy, P. (2003). The mixing layer over a deep cavity at high-subsonic speed. *J. Fluid Mech.*, 475:101–145. (In page 71.)
- Garg, S. and Cattafesta III, L. N. (2001). Quantitative schlieren measurements of coherent structures in a cavity shear layer. *Experiments in Fluids*, 30:123–134. (In pages 12 and 13.)
- Gloerfelt, X. (2006). Aeroacoustic computations of high-reynolds number cavity flows on staggered grids. *AIAA Paper*, (2433). (In pages 11, 12 and 113.)
- Gloerfelt, X. (2008). Compressible proper orthogonal decomposition/galerkin reduced-order model of self-sustained oscillations in a cavity. *Phys. Fluids*, 20. (In pages 11, 13 and 88.)
- Gloerfelt, X. (2009). *Aerodynamic noise from wall-bounded flows: Cavity noise*, chapter 0. VKI Lectures. (In page 9.)
- Gloerfelt, X., Bogey, C., and Bailly, C. (2003a). Numerical evidence of mode switching in the flow-induced oscillations by a cavity. *Int. J. Aeroacoustics*, 2:99. (In page 12.)
- Gloerfelt, X., Bogey, C., and Bailly, C. (2003b). Numerical investigation of the coexistence of multiple tones in flow-induced cavity noise. *AIAA Paper*, (3234). (In page 12.)
- Gonzalez, L. M., Ahmed, M., J., K., Kuhlmann, H. C., and Theofilis, V. (2011). Three-dimensional flow instability in a lid-driven isosceles triangular cavity. *J. Fluid Mech.*, 675:369–396. (In page 16.)
- Grace, S. M., Dewar, W. G., and Wroblewski, D. E. (2004). Experimental investigation of the flow characteristics within a shallow wall cavity for both laminar and turbulent upstream boundary layers. *Experiments in Fluids*, 36:791–804. (In page 13.)
- Guermond, J.-L., Migeon, C., Pineau, G., and Quartapelle, L. (2002). Start-up flows in a three-dimensional rectangular driven cavity of aspect ratio 1:1:2 at $re=1000$. *J. Fluid Mech.*, 450:169–199. (In pages 15 and 124.)
- Haigermoser, C., Scarano, F., and and, M. O. (2008). Investigation of the flow in a rectangular cavity using tomographic and time-resolved piv. Number 26. (In pages 11 and 76.)
- Hama, F. R. (1962). Streaklines in a perturbed shear flow. *Phys. Fluids*, 5(644). (In page 63.)
- Hart, D. P. (2000). PIV error correction. *Experiments in Fluids*, 29:13–22. (In pages 28 and 30.)
- Howe, M. S. (1997). Low strouhal number instabilities of flow over apertures and wall cavities. *J. Acoust. Soc. Am.*, 102:772–780. (In page 10.)
- Huang, N. E., Long, S. R., and Shen, Z. (1996). The mechanism for frequency downshift in nonlinear wave evolution. *Adv. Appl. Mech.*, 32:59–111. (In page 48.)
- Huang, N. E., Shen, Z., and Long, S. R. (1999). A new view of nonlinear water waves: the hilbert spectrum. *Ann. Rev. Fluid Mech.*, 31:417–457. (In pages 48, 128 and 129.)

- Huang, N. E., Shen, Z., Long, S. R., Wu, M. C., Shih, H. H., Zheng, Q., Yen, N.-C., Tung, C. C., and Liu, H. H. (1998). The empirical mode decomposition and hilbert spectrum for nonlinear and non-stationary time-series analysis. In *Proc. R. Soc. London, Ser. A*, volume 454, pages 903–995. (In pages 48, 49 and 58.)
- Huang, N. E., Wu, M. C., Long, S. R., Shen, S. S., Qu, W., Gloersen, P., and Fan, K. L. (2003). A confidence limit for empirical mode decomposition and hilbert spectral analysis. In *Proc. R. Soc. London, Ser. A*, volume 459, pages 2317–2345. (In page 58.)
- Huerre, P. and Monkewitz, P. A. (1985). Absolute and convective instabilities in free shear layers. *J. Fluid Mech.*, 159:151–168. (In pages 7 and 74.)
- Huerre, P. and Monkewitz, P. A. (1990). Local and global instabilities in spatially developing flows. *Ann. Rev. Fluid Mech.*, 22:473–537. (In pages 7 and 9.)
- Huerre, P. and Rossi, M. (1998). *Hydrodynamic instabilities in open flows*, chapter 2, pages 81–294. Hydrodynamics and Nonlinear Instabilities. Cambridge University Press. (In pages 7, 74 and 76.)
- Kegerise, M. A., Spina, E. F., Garg, S., and Cattafesta III, L. N. (2004). Mode-switching and nonlinear effects in compressible flow over a cavity. *Phys. Fluids*, 16:678–687. (In page 12.)
- Knisely, C. and Rockwell, D. (1982). Self-sustained low-frequency components in an impinging shear layer. *J. Fluid Mech.*, 116:157–186. (In pages 9, 10, 13, 67, 73, 74, 94, 122 and 181.)
- Koseff, J. R. and Street, R. L. (1984a). The lid-driven cavity flow: A synthesis of qualitative and quantitative observations. *Trans. ASME: J. Fluids Eng.*, 106:390–398. (In page 14.)
- Koseff, J. R. and Street, R. L. (1984b). On endwall effects in a lid-driven cavity flow. *Trans. ASME: J. Fluids Eng.*, 106:385–389. (In page 14.)
- Koseff, J. R. and Street, R. L. (1984c). Visualization studies of a shear driven three-dimensional recirculating flow. *Trans. ASME: J. Fluids Eng.*, 106:21–29. (In page 14.)
- Kuo, C.-H. and Huang, S.-H. (2001). Influence of flow path modification on oscillation of cavity shear layer. *Experiments in Fluids*, 31:162–178. (In pages 71 and 73.)
- Kuo, C.-H. and Jeng, W. I. (2003). Lock-on characteristics of a cavity shear layer. *J. Fluids Struct.*, 18:715–728. (In pages 10 and 73.)
- Larchevêque, L., Sagaut, P., and Labbé, O. (2007). Large-eddy simulation of a subsonic cavity flow including asymmetric three-dimensional effects. *J. Fluid Mech.*, 577:105–126. (In page 14.)
- Larchevêque, L., Sagaut, P., Lê, T. H., and Comte, P. (2004). Large-eddy simulations of a compressible flow in a 3d open cavity at high reynolds number. *J. Fluid Mech.*, 516:265–301. (In page 11.)
- Larchevêque, L., Sagaut, P., Mary, I., Labbé, O., and Comte, P. (2003). Large-eddy simulation of a compressible flow past a deep cavity. *Phys. Fluids*, 15(1). (In page 13.)
- Lee, S. B., Seena, A., and Sung, H. J. (2010). Self-sustained oscillations of turbulent flow in an open cavity. *J. Aircraft*, 47(3). (In page 11.)

- Lusseyran, F., Pastur, L., and Letellier, C. (2008). Dynamical analysis of an intermittency in an open cavity flow. *Phys. Fluids*, 20. 114101. (In pages 12 and 74.)
- Malomed, B. A. (1994). Domain wall between travelling waves. *Physical Review E*, 50(5). (In page 161.)
- Mamum, C. K. and Tuckerman, L. S. (2009). Asymmetry and hopf bifurcation in spherical couette flow. *Phys. Fluids*, 7:80–91. (In pages 11 and 162.)
- Meseguer-Garrido, F., de Vicente, J., Valero, E., and Theofilis, V. (2011). Effect of aspect ratio on the three-dimensional global instability analysis of incompressible open cavity flows. *AIAA Paper*, (3605). (In pages 16, 117, 123, 162 and 186.)
- Michalke, A. (1964). On the inviscid instability of the hyperbolic tangent velocity profile. *J. Fluid Mech.*, 19(4):543–556. (In pages 7, 74, 76, 87 and 88.)
- Michalke, A. (1965). On spatially growing disturbances in a shear layer. *J. Fluid Mech.*, 23:521–544. (In pages 7, 87 and 88.)
- Migeon, C. (2002). Details on the start-up development of the taylor-görtler-like vortices inside a square-section lid-driven cavity for $1000 < re < 3200$. *Experiments in Fluids*, 33:594–602. (In pages 15, 122 and 124.)
- Migeon, C., Pineau, G., and Texier, A. (2003). Three-dimensionality development inside standard parallelepipedic lid-driven cavities at $re=1000$. *J. Fluids Struct.*, 17:717–738. (In pages 15, 122 and 124.)
- Miksad, R. W. (1973). Experiments on nonlinear interactions in the transition of a free shear layer. *J. Fluid Mech.*, 59(1):1–21. (In page 8.)
- Moffat, R. J. (1988). Describing the uncertainties in experimental results. *Exp. Thermal Fluid Sci.*, 1:3 – 17. (In page 28.)
- Monkewitz, P. A. and Huerre, P. (1982). Influence of the velocity ratio on the spatial instability of mixing layers. *Phys. Fluids*, 25(7):1137–1143. (In pages 7, 8, 67, 74 and 76.)
- Monkewitz, P. A., Huerre, P., and Chomaz, J.-M. (1993). Global linear analysis of weakly non-parallel shear flows. *J. Fluid Mech.*, 251:1–20. (In pages 7 and 11.)
- Neary, M. D. and Stephanoff, K. D. (1987). Shear-layer-driven transition in a rectangular cavity. *Phys. Fluids*, 30(10):2936–2946. (In pages 14 and 115.)
- Oshkai, P., Rockwell, D., and Pollack, M. (2005). Shallow cavity tones: transformation from large- to small-scale modes. *J. Sound Vibrat.*, 280:777–813. (In pages 11 and 13.)
- Parker, K., von Ellenrieder, K. D., and Soria, J. (2007). Morphology of the forced oscillatory flow past a finite-span wing at low Reynolds number. *J. Fluid Mech.*, 571:327–357. (In page 26.)
- Pastur, L., Westra, M.-T., Snouck, D., van de Water, W., van Hecke, M., Storm, C., and van Saarloos, W. (2003a). Sources and holes in a one-dimensional traveling-wave convection experiment. *Phys. Rev. E*, 67. (In page 161.)

- Pastur, L., Westra, M.-T., and van de Water, W. (2003b). Sources and sinks in 1d traveling waves. *Physica D*, 174:71–83. (In page 161.)
- Pastur, L. R., Fraigneau, Y., Lusseyran, F., and Basley, J. (2012). From linear stability analysis to three-dimensional organisation in an incompressible open cavity flow. *arXiv*. (In pages 161, 162, 163, 166, 168 and 185.)
- Pastur, L. R., Lusseyran, F., Faure, T. M., Fraigneau, Y., Pethieu, R., and Debesse, P. (2008). Quantifying the non-linear mode competition in the flow over an open cavity at medium reynolds number. *Experiments in Fluids*, 44(4):597–608. (In pages 12, 49 and 74.)
- Podvin, B., Fraigneau, Y., Lusseyran, F., and Gougat, P. (2006). A reconstruction method for the flow past an open cavity. *J. Fluids Eng.*, 128:531–540. DOI: 10.1115/1.2175159. (In page 14.)
- Poliashenko, M. and Aidun, C. K. (1995). A direct method for computation of simple bifurcations. *J. Comput. Phys*, 121:246–260. (In pages 16 and 115.)
- Powell, A. (1953). On edge tones and associated phenomena. *Acustica*, 3. (In pages 9 and 11.)
- Powell, A. (1961). On the edgetone. *J. Acoust. Soc. Am.*, (33):395–409. (In pages 9 and 11.)
- Powell, A. (1990). Some aspects of aeroacoustics: From rayleigh’s until today. *ASME Journal of Vibration and Acoustics*, 112:145–159. (In page 9.)
- Powell, A. (1995). Lord rayleigh’s foundations of aeroacoustics. *J. Acoust. Soc. Am.*, 98:1839–44. (In page 9.)
- Quénot, G. M. (1992). The orthogonal algorithm for optical flow detection using dynamic programming. In *ICASSP 3*, page 252. IEEE. 249-61485. (In pages 25, 29 and 176.)
- Quénot, G. M., Pakleza, J., and Kowalewski, T. A. (1998). Particle image velocimetry with optical flow. *Experiments in Fluids*, 25:177–189. (In pages 25, 29 and 176.)
- Quénot, G. M., Rambert, A., Lusseyran, F., and Gougat, P. (2001). Simple and accurate piv camera calibration using a single target image and camera focal length. In *4th International Symposium on of Particle Image Velocimetry*, pages 17–19, Göttingen, Germany. Springer. (In page 29.)
- Raffel, M., Willert, C., Wereley, S., and Kompenhans, J. (2007). *Particle Image Velocimetry: A Practical Guide*. Springer, 2nd edition. (In page 32.)
- Ramanan, N. and Homsy, G. M. (1994). Linear stability of lid-driven cavity flow. *Phys. Fluids*, 6. (In pages 16 and 115.)
- Riecke, H. and Kramer, L. (2000). The stability of standing waves with small group velocity. *Physica D*, 137:124–142. (In page 160.)
- Rockwell, D. (1977). Prediction of oscillation frequencies for unstable flow past cavities. *Trans. ASME: J. Fluids Eng.*, pages 294–300. (In pages 9, 10, 67, 73 and 113.)
- Rockwell, D. (1983). Oscillations of impinging shear layers. *AIAA J.*, 21(5):645–664. (In page 44.)

- Rockwell, D. and Knisely, C. (1979). The organized nature of flow impingement upon a corner. *J. Fluid Mech.*, 93(3):413–432. (In pages 9, 42 and 181.)
- Rockwell, D. and Knisely, C. (1980a). Observations of the three-dimensional nature of unstable flow past a cavity. *Phys. Fluids*, 23(425). (In page 13.)
- Rockwell, D. and Knisely, C. (1980b). Vortex edge interaction: Mechanisms for generating low frequency components. *Phys. Fluids*, 23(239). (In pages 13, 73, 79, 94, 115 and 181.)
- Rockwell, D., Lin, J. C., Oshkai, P., Reiss, M., and Pollack, M. (2003). Shallow cavity flow tone experiments: onset of locked-on states. *J. Fluids Struct.*, 17(3):381–414. (In page 11.)
- Rockwell, D. and Naudascher, E. (1978). Review — self-sustaining oscillations of flow past cavities. *J. Fluids Eng.*, 100:152–165. (In pages 9, 10, 67, 73, 113 and 121.)
- Rockwell, D. and Naudascher, E. (1979). Self-sustained oscillations of impinging free shear layers. *Ann. Rev. Fluid Mech.*, 11:67–94. (In pages 9, 10, 11, 13, 14, 21, 67, 73, 121 and 122.)
- Rossiter, J. (1964). Wind-tunnel experiments on the flow over rectangular cavities at subsonic and transonic speeds. *Aeronautical Research Council Reports and Memoranda*, 3438. (In pages 9 and 10.)
- Rowley, C. W., Colonius, T., and Basu, A. J. (2002). On self-sustained oscillations in two-dimensional compressible flow over rectangular cavities. *J. Fluid Mech.*, 455:315–346. (In pages 9, 11, 13, 46, 76 and 176.)
- Rowley, C. W., Colonius, T., and Murray, R. M. (2000). Pod based model of self-sustained oscillations in the flow past an open cavity. *AIAA J.*, 1969. (In page 87.)
- Sarohia, V. (1977). Experimental investigation of oscillations in flows over shallow cavities. *AIAA J.*, 15. (In pages 73 and 76.)
- Shankar, P. N. and Deshpande, M. D. (2000). Fluid mechanics in the driven cavity. *Annu. Rev. Fluid Mech.*, 32:93–136. (In pages 125 and 158.)
- Sipp, D. and Lebedev, A. (2007). Global stability of base and mean flows: a general approach and its applications to cylinder and open cavity flows. *J. Fluid Mech.*, 593:333–358. (In pages 11, 88 and 162.)
- Soria, J. (1994). Digital cross-correlation particle image velocimetry measurements in the near wake of a circular cylinder. (In page 28.)
- Soria, J. (1996). An investigation of the near wake of a circular cylinder using a video-based digital cross-correlation particle image velocimetry technique. *Experimental Thermal and Fluid Science*, 12:221 – 233. (In pages 28 and 176.)
- Soria, J. (1998). Multigrid approach to cross-correlation digital piv and hpiv analysis. Sydney. 13th Australasian Fluid Mechanics Conference. (In pages 28 and 176.)
- Soria, J., Cater, J., and Kostas, J. (1999). High resolution multigrid cross-correlation digital piv measurements of a turbulent starting jet using half frame image shift @lm recording. *Optics & Laser Technology*, 31:3±12. (In page 28.)

- Stanislas, M., Okamoto, K., Kähler, C. J., Westerweel, J., and Scarano, F. (2008). Main results of the third international piv challenge. *Experiments in Fluids*, 45:27–71. (In page 29.)
- Stanislas, M., Okamoto, M., Kähler, C. J., and Westerweel, J. (2005). 2nd international piv challenge. *Experiments in Fluids*, 39:170–191. (In page 29.)
- Tang, Y.-P. and Rockwell, D. (1983). Instantaneous pressure fields at a corner associated with vortex impingement. *J. Fluid Mech.*, 126. (In pages 13 and 181.)
- Theofilis, V. (2003). Advances in global linear instability of nonparallel and three-dimensional flows. *Prog. Aerosp. Sci.*, 39(4):249–315. (In pages 11, 16 and 162.)
- Theofilis, V. (2011). Global linear instability. *Annu. Rev. Fluid Mech.*, 43:319. (In pages 16, 123 and 162.)
- Theofilis, V. and Colonius, T. (2003). An algorithm for the recovery of 2- and 3-D BiGlobal instabilities of compressible flow over 2-d open cavities. In *AIAA Paper 2003-4143*, 33rd Fluid Dynamics Conference and Exhibit, June 23 – 26, 2003, Orlando, FL. (In pages 11, 16 and 162.)
- Theofilis, V., Duck, P. W., and Owen, J. (2004). Viscous linear stability analysis of rectangular duct and cavity flows. *J. Fluid Mech.*, 505:249–286. (In pages 16 and 115.)
- van Hecke, M., Storm, C., and van Saarloos, W. (1999). Sources, sinks and wavenumber selection in coupled cgl equations and experimental implications for counter-propagating wave systems. *Physica D*, 134:1–47. (In page 161.)
- Vogel, M., Hirsra, A. H., and Lopez, J. M. (2003). Spatio-temporal dynamics of a periodically driven cavity flow. *J. Fluid Mech.*, 478:197–226. (In page 15.)
- von Ellenrieder, K., Kostas, J., and Soria, J. (2001). Measurements of a wall-bounded turbulent, separated flow using hpiv. *Journal of Turbulence*, 2:1–15. (In page 28.)
- Welch, P. D. (1967). *Modern spectrum analysis*, chapter The use of fast Fourier transform for the estimation of power spectra: a method based on time averaging over short, modified periodograms, pages 17–20. IEEE Press. (In page 41.)
- Westerweel, J. (1994). Efficient detection of spurious vectors in particle image velocimetry data sets. *Experiments in Fluids*, 16:236 – 247. (In page 28.)
- Williams, D. R. and Hama, F. R. (1980). Streaklines in a shear layer perturbed by two waves. *Phys. Fluids*, 23(442). (In pages 7, 63, 71 and 86.)
- Ziada, S. and Rockwell, D. (1982). Oscillations of an unstable mixing layer impinging upon an edge. *J. Fluid Mech.*, 124:307–334. (In pages 10, 13 and 181.)